Carla Fabris

Numerical Study on Pullout Tests of Ground Anchors Monitored with Fibre Optic Sensors

DOCTORAL THESIS

to achieve the university degree of

Doktor der technischen Wissenschaften

submitted to

Graz University of Technology

Supervisor

Ao.Univ.-Prof. Dipl.-Ing. Dr.techn. Helmut F. Schweiger, MSc.

Institute of Soil Mechanics, Foundation Engineering and Computational Geotechnics
Graz University of Technology

Prof. Janko Logar, MSc., PhD.

Faculty of Civil and Geodetic Engineering

University of Ljubljana

Graz, January 2020

Affidavit

I declare that I have authored this thesis independently, that I have not used other than the declared sources/resources, and that I have explicitly indicated all material which has been quoted either literally or by content from the sources used. The text document uploaded to TUGRAZonline is identical to the present doctoral thesis.

………………… ………………………………………………

Date Signature

Acknowledgements

I wish to express my gratitude to Prof. Helmut F. Schweiger for his continuous assistance and encouragement during the last three years. I am indebted to Helmut for giving me the opportunity to conduct my research at the Graz University of Technology and for his valuable guidance. The results presented in this thesis were developed within the framework of the FFG-Project (Bridge-24 No. 858505) with cooperation of Keller Grundbau, ÖBB Infrastruktur and Asfinag. The financial support is gratefully acknowledged.

Prof. Janko Logar from the University of Ljubljana is thanked for his constant collaboration and for accepting to be second reviewer. I extend my gratitude to Prof. Roman Marte for his stimulating discussions during the course of my thesis and to Prof. Franz Tschuchnigg for his encouragement.

I am very grateful to the team of the Institute of Engineering Geodesy and Measurement Systems, in special to Helmut Woschitz and Madeleine Winkler, for their great work when performing the in situ measurements and for their insights into the data analysis. Thanks are also due to Reinhard Kulmer and Václav Račanský from Keller Grundbau, from whom I learned much about anchor test.

I am indebted to Boštjan Pulko from the University of Ljubljana for the valuable discussions undertaken during his stay in Graz and for his continuous support, not limited to the research.

I would like to thank all my colleagues from the Institute of Soil Mechanics, Foundation Engineering and Computational Geotechnics, namely Kamchai Choosrithong, Laurin Hauser, Christopher Krammer, Simon Oberhollenzer, Patrick Pichler and Matthias Rebhan. Special thanks to Mirva Gega and Elisa Angelina Hübner for the great moments we shared. I appreciate all the help from the Institute's staff: Martin Brunner, Margit Rückert and Alexandra Taferner. The assistance from the team of the Soil Mechanics Laboratory and from the Rock Mechanics Laboratory is also acknowledged. Thanks in particular to Odalys Del Carmen Morales-Calderon, for her kindness and support, and to Manfred Blümel.

I thank my Austrian family, Attila and Melitta, for everything they have done for me.

This work is dedicated to my parents, without whom this thesis would never be possible.

Graz, January 2020 Carla Fabris

Kurzfassung

Numerische Studien zu Herausziehversuchen von mit Glasfasersensoren bestückten Freispielankern

Obwohl Freispielanker für Stabilisierungsmaßnahmen in Boden und Fels häufig eingesetzt werden, ist das Tragverhalten dieser Anker noch nicht vollständig erforscht und daher werden in der Dimensionierung meist vereinfachende Annahmen getroffen, wie zum Beispiel eine gleichförmige Verteilung der Schubspannungen zwischen Verpresskörper und Baugrund. Die Anwendung von Glasfasersensoren zur Überwachung geotechnischer Bauwerke hat in den letzten Jahren sehr stark zugenommen, Zugversuche an Ankern werden aber meist noch mit traditionellen Messmethoden am Ankerkopf durchgeführt.

In dieser Arbeit werden Zugversuche an 10 Freispielankern in unterschiedlichen Baugrundverhältnissen vorgestellt, wobei mindesten jeweils ein Anker mit Glasfaseroptik ausgerüstet war. Die Sensoren waren sowohl am Zugglied appliziert als auch in den Verpresskörper eingebettet und erlaubten eine kontinuierliche Messung von Dehnungen in einer hohen räumlichen Auflösung von etwa 1 cm. Damit konnte sowohl die Lastabtragung zwischen Zugglied und Verpressmörtel untersucht werden, als auch die Entwicklung von Rissen im Verpresskörper durch Spitzen in den Dehnungsmessungen veranschaulicht werden.

Numerische Simulationen mit Hilfe der Finite-Elemente-Methode wurden unter Einsatz hochwertiger Stoffgesetze durchgeführt und die Ergebnisse mit den faseroptischen Messungen verglichen. Es wurden auch Berechnungen vor den Versuchen durchgeführt (sogenannte class-A-predictions). Die numerischen Berechnungen stellen für die Interpretation der gemessenen Dehnungsprofile eine wertvolle Hilfe dar und führen zu einem besseren Verständnis verschiedener Aspekte der Lastabtragung. Der Einfluss der Baugrundsteifigkeit, des Mörtels in der Freispielstrecke, der Verpresskörperlänge sowie etwaig vorhandener Stützwände wurden in einer Studie separat untersucht. Die Auswirkungen von Verbundversagen zwischen Zugglied und Verpressmörtel auf das Dehnungsprofil werden diskutiert.

Der Autorin ist eine derart detaillierte Beschreibung der Lastabtragungsmechanismen von Freispielankern in der Fachliteratur bislang nicht bekannt. Es kann argumentiert werden, dass numerische Berechnungen im Zusammenspiel mit hochauflösenden Messsystemen eine verbesserte Interpretation der Lastübertragungsmechanismen Zugglied/Verpressmörtel und Verpresskörper/Baugrund ermöglichen und somit einen Beitrag zu einer wirtschaftlicheren Bemessung von Freispielankern im Grundbau leisten können.

Abstract

Numerical Study on Pullout Tests of Ground Anchors Monitored with Fibre Optic Sensors

Although ground anchors are widely employed for soil and rock stabilisation, the load transfer behaviour of these structures is not fully understood and anchor design usually relies on simplified assumptions such as a uniform shear stress distribution in the grout-ground interface. Despite the fact that the use of distributed sensors for monitoring geotechnical structures has been increasing over the last years, ground anchor pullout tests are traditionally monitored only at the anchor head.

In this thesis, 10 anchor pullout tests were performed under different ground conditions and, for each ground type, at least one anchor was monitored with distributed fibre optic sensors. The fibres were installed along the tendon and embedded in the grout and enabled continuous measurements of strains over depth with high spatial resolution of about 1 cm. The load transfer in the tendon-grout interface was evaluated and crack development was verified by measured peaks along the longitudinal strain profile.

Numerical simulations using the finite element method were carried out employing advanced constitutive models and the results compared with the fibre optic measurements. In some cases, numerical class-A predictions were undertaken prior to the anchor pullout test. The numerical simulations proved to be a valuable tool for interpreting the in situ strain distribution and for understanding specific aspects influencing the load transfer mechanism of anchors. In this respect, the influence of the grout in the anchor free length, of the anchor length, of the retaining wall and of the ground stiffness were analysed separately. Debonding and its effect on the strain profile were also discussed.

To the best of the author's knowledge, such detailed description of the load transfer mechanism of soil anchors has not been presented in literature before. It is argued that numerical analysis combined with high spatial resolution measurements may contribute to a better understanding of the skin friction mobilisation along the tendon-grout and grout-ground interfaces during pullout tests, eventually leading to a more economical design of ground anchors.

Table of contents

List of symbols and abbreviations

The symbols used in this thesis are listed below. Additional information is provided in the text at first appearance.

Small letters

a	[-]	increase of ε_{cp} with increase of p’ (Concrete model)
c	[stress]	cohesion
c'	[stress]	effective cohesion
c_{rock}	[stress]	rock cohesion
d	[length]	equivalent thickness
f_c	[stress]	compressive strength (Concrete model)
f_{c0n}	[-]	normalised initial strength (Concrete model)
f_{cap}	N/A*	volumetric part of yield function (MMS_HV model)
f_{cfn}	[-]	normalised failure strength in compression (Concrete model)
f_{cone}	N/A	deviatoric part of yield function (MMS_HV model)
f_{cun}	[-]	normalised residual strength in compression (Concrete model)
f_{cy}	[stress]	uniaxial compressive stress (Concrete model)
f_{HV}	N/A	Hvorslev yield function (MMS_HV model)
f_t	[stress]	uniaxial tensile strength (Concrete model)
f_{tens}	N/A	yield function in tension (tension cut-off) (MMS_HV model)
f_{tu}	[stress]	residual strength in tension (Concrete model)
f_{tun}	[-]	normalised residual strength in tension (Concrete model)
h_0	[length]	initial specimen height
h	[length]	specimen height
h_{soft}	[-]	softening parameter (MMS_HV model)
l_{cal}	[length]	internal length (MMS_HV model)
m	[-]	stress dependency index (power)
n_{cp}	[-]	number of integration planes (MMS_HV model)

p'	[stress]	mean effective stress; pressure in the cavity
p_{ref}	[stress]	reference pressure
s_a	[length]	tendon end displacement at time t_a
s_b	[length]	tendon end displacement at time t_b
t_a	[time]	start of the time interval during anchor test
t_b	[time]	end of the time interval during anchor test
$u_{free\ length}$	[length]	displacements due to the elastic elongation of the free length
$u_{top\ fixed\ length}$	[length]	displacements at the top of the fixed length
u_{total}	[length]	displacements measured at the anchor head

*N/A: not applicable

Capital letters

A_{mat}	[-]	deviatoric hardening parameter (MMS_HV model)
A_{tendon}	[length^2]	cross-sectional area of 1 strand
E	[stress]	Young’s modulus
E_1	[stress]	Young’s modulus in first axial direction
E_2	[stress]	Young’s modulus in second axial direction
$E_{50,ref}$	[stress]	primary loading modulus at reference pressure
E_M	[stress]	Ménard modulus
E_{oed}	[stress]	oedometer modulus
$E_{oed,ref}$	[stress]	oedometer modulus at reference pressure
E_R	[stress]	un/reloading modulus derived during pressuremeter test
E_{rock}	[stress]	rock Young’s modulus
E_{tendon}	[stress]	tendon elastic modulus
$E_{ur,ref}$	[stress]	un/reloading modulus at reference pressure
F	[force]	applied force at one strand
F_c	N/A*	Mohr-Coulomb yield surface (Concrete model)
F_t	N/A	Rankine yield surface (tension cut-off) (Concrete model)
G_0	[stress]	small-strain shear modulus

$G_{0,ref}$	[stress]	small-strain shear modulus at reference pressure
G_c	[force/length]	compressive fracture energy (Concrete model)
G_t	[force/length]	tensile fracture energy (Concrete model)
G_{ur}	[stress]	un/reloading shear modulus
$G_{ur,ref}$	[stress]	un/reloading shear modulus at reference pressure
H_c	[-]	normalised hardening/softening parameter in compression (Concrete model)
H_{cf}	[-]	normalised hardening/softening parameter in compression at failure strength (Concrete model)
H_{cu}	[-]	normalised hardening/softening parameter in compression at residual strength (Concrete model)
H_t	[-]	normalised softening parameter in tension (Concrete model)
H_{tu}	[-]	normalised softening parameter in tension at residual strength (Concrete model)
I_D	[-]	material index
K_0	[-]	lateral earth pressure coefficient at rest
$K_{0.nc}$	[-]	lateral earth pressure coefficient at rest for normally consolidated conditions
$L_{free\ length}$	[length]	distance between the anchorage point at the jack and the proximal end of the fixed length
M	[stress]	constrained modulus
R_f	[-]	failure ratio (MMS_HV model)
R_{inter}	[-]	strength reduction factor
V'	[length^3]	volume of the cavity
V_S	[length/time]	shear wave velocity

*N/A: not applicable

Small Greek letters

α	[length]	creep rate
γ	[force/length^3]	ground unit weight
$\gamma_{0.7}$	[-]	shear strain at 70% of G_0
ε_1	[-]	major principal strain
ε_1^p	[-]	major principal plastic strain (Concrete model)
ε_3^p	[-]	minor principal plastic strain (Concrete model)

ε_{cp}	[-]	total peak strain (Concrete model)
ε_{cp}^{p}	[-]	plastic peak strain in uniaxial compression (Concrete model)
ε_{cr}	[-]	creep strains (Concrete model)
ε_{e}	[-]	elastic strains (Concrete model)
ε_{n}	[-]	local normal strain on integration plane (MMS_HV model)
ε_{p}	[-]	plastic strains (Concrete model)
ε_{shr}	[-]	shrinkage strains (Concrete model)
ε_{tu}^{p}	[-]	plastic ultimate strain in uniaxial tension (Concrete model)
ε_{y}	[-]	vertical strain
φ	[°]	ground friction angle
φ_{max}	[°]	maximum friction angle (Concrete model)
φ'	[°]	effective friction angle
φ'_{cs}	[°]	effective friction angle at critical state (MMS_HV model)
φ'_{e}	[°]	inclination of Hvorslev surface in τ-σ'-diagram (MMS_HV model)
ν	[-]	Poisson’s ratio
ν'	[-]	drained Poisson’s ratio
ν'_{ur}	[-]	unloading-reloading drained Poisson’s ratio
ρ	[mass/length^3]	soil bulk density
σ_{1}	[stress]	major principal stress
σ_{3}	[stress]	minor principal stress
σ_{rot}	[stress]	intersection of the Mohr-Coulomb envelope and the isotropic axis (Concrete model)
σ'	[stress]	effective stress
σ'_{1}	[stress]	effective major principal stress
σ'_{i}	[stress]	effective stress vector in terms of micro level components of plane i (MMS_HV model)
σ'_{n}	[stress]	effective normal stress on integration plane (MMS_HV model)
σ'_{nc}	[stress]	local effective normal preconsolidation stress on integration plane (MMS_HV model)
$\sigma'_{nc,0}$	[stress]	initial effective normal preconsolidation stress on integration plane (MMS_HV model)

σ'_{ne}	[stress]	equivalent normal stress on local normal consolidation line (MMS_HV model)
τ	[stress]	local shear stress (MMS_HV model)
$\tau_{average}$	[stress]	average shear strength
$\tau_{grout\text{-}soil}$	[stress]	shear stress in the grout-soil interface
τ_{mob}	[stress]	mobilised shear stress
τ_{peak}	[stress]	peak shear strength
τ_{rel}	[-]	relative shear stress
$\tau_{residual}$	[stress]	residual shear strength
τ_s	[stress]	local shear stress in s-direction (MMS_HV model)
τ_t	[stress]	local shear stress in t-direction (MMS_HV model)
$\tau_{tendon\text{-}grout}$	[stress]	shear stress in the tendon-grout interface

Abbreviations

A10-test	test performed on the A10 Tauernautobahn
AASHTO	American Association of State Highway and Transportation Officials
BOTDA	Brillouin Optical Time Domain Analysis
BOTDR	Brillouin Optical Time Domain Reflectometer
CSL	Critical State Line
DMT	Dilatometer Test
DOFS	Distributed Optical Fibre Sensors
FO	Fibre Optic
HSsmall model	Hardening Soil model with small-strain stiffness
LJ-test	test performed in Ljubljana
LL	Liquid Limit
MC model	Mohr-Coulomb model
MMS_HV model	Multilaminate soil model with Hvorslev surface
MST	Multistage Triaxial Test
OBR	Optical Backscattered Reflectometer
OFDR	Optical Frequency Domain Reflectometry

OTDR	Optical Time Domain Reflectometer
PI	Plasticity Index
PL	Plastic Limit
POP	Pre-Overburden Pressure
sDMT	seismic Dilatometer Test
SK_1A-test	test performed in St Kanzian (Anchor 1A)
SK_1B-test	test performed in St Kanzian (Anchor 1B)
SK_2A-test	test performed in St Kanzian (Anchor 2A)
SK_2B-test	test performed in St Kanzian (Anchor 2B)
SK_2C-test	test performed in St Kanzian (Anchor 2C)
SK_3A-test	test performed in St Kanzian (Anchor 3A)
SK_3B-test	test performed in St Kanzian (Anchor 3B)
SÖ-test	test performed in Söding
TU Graz	Graz University of Technology
UCS	Uniaxial Compression Strength

1 Introduction

Although ground anchors are widely employed for soil and rock stabilisation, monitoring such structures during load tests are traditionally performed with local sensors installed at the anchor head. Therefore, the anchor behaviour along depth is rarely assessed and anchor design relies on simplified assumptions such as a constant shear stress distribution in the grout-ground interface. Alternatively, design curves such as the well-known diagrams proposed by Ostermayer & Scheele (1978) can be used in order to account for soil type and density when estimating the load carrying capacity of ground anchors.

The use of modern distributed fibre optic sensing systems allows for continuous and accurate measurements of strains with a high spatial resolution of about 1 cm, for Rayleigh based systems, using only one lead-in fibre optic cable (Monsberger et al. 2016). Additionally, compared to traditional sensors, fibre optic sensors are less intrusive due to the small dimension of the sensing cable and immune to electromagnetic interference (Palmieri & Schenato 2013). If the sensors are applied for monitoring anchor pullout tests, the detailed strain profile along the anchor length is a valuable information for understanding the load transfer behaviour of the system. The fibre optic sensors can be applied for strain measurements along the steel tendon and along the grouted section. For the case where strains are monitored along the tendon, the strain profile can be easily employed to calculate the load acting at the free and at the fixed length or integrated to obtain the displacements along depth. On the other hand, if measurements are performed along the grout, cracking during the pullout test can be evaluated and, if the grout is not cracked, displacements can be calculated without a significant amount of effort.

In this thesis fibre optic measurements of strains during anchor pullout tests are compared with simulations using the finite element method. The anchor pullout tests were performed in different ground types. The grouting technique and the grouted body geometry varied for each anchor. The numerical simulations were compared with the in situ measured strain profile and enabled a better understanding of the measurements. Advanced constitutive models were employed for simulating the ground and the grout and, in most cases, the material parameters were calibrated with laboratory and in situ tests. Emphasis is given to discuss the capabilities of the Concrete model, which was the constitutive model employed for the grout. Whenever possible class-A numerical predictions of the pullout tests were performed and, after the in situ results, the simulations were refined.

It is shown that, despite the complex non-linear soil behaviour and its interaction with the surrounding structures, reliable results can be achieved if standard laboratory tests are available and an appropriate choice of the constitutive model is made. Furthermore, additional numerical studies were carried out and some aspects such as the grout in the free length, the fixed length size and the ground stiffness were investigated separately to analyse their influence on the overall anchor behaviour.

The thesis is divided into the following parts:

- Chapter 2 is a literature review covering shortly the main aspects concerning ground anchors, such as the grouting technique, the main modes of failure and the European Standards applicable. The progressive failure mechanism of anchors is explained as well as some basic principles of optical fibre sensing. At the end of the chapter examples of distributed fibre optic sensors applied in geotechnical engineering are given;
- Chapter 3 concerns the constitutive models employed for the numerical simulations. The constitutive models are summarised and reference is given for further information;
- Chapter 4 gives a general overview of the anchor pullout tests and some preliminary information regarding the interpretation of the fibre optic data are presented;
- A detailed description of the anchor pullout tests follows. The Söding-test is described in chapter 5, the St Kanzian pullout tests in chapter 6, the test undertaken at the A10 Tauernautobahn in chapter 7 and the one carried out in Ljubljana in chapter 8. For each test, the ground and the anchor are described and, if applicable, the material parameter calibration is presented. The in situ results are discussed and compared with the numerical simulations;
- In chapter 9, additional discussion is addressed with respect to specific aspects influencing anchor pull out tests. At the beginning of the chapter, different debonding mechanisms observed during the anchor tests are discussed. Furthermore, numerical simulations were performed to understand the influence of the retaining wall, the contribution of the grout in the free length on the anchor ultimate capacity and the influence of the anchor length;
- The main conclusions are summarised in chapter 10 and references are found in chapter 11.

In order to facilitate the in situ results visualisation, the strain distribution along the tendon and the grout measured with the fibre optic cables is shown separately in the Appendix.

2 Literature review

2.1 Ground anchors

According to the Eurocode 7 (ÖNORM EN 1997-1:2014), a ground anchor is an installation capable of transmitting an applied tensile load to a load-bearing stratum. It is composed of an anchor head, a free length and a fixed length. Whereas the free length is unbonded and free to elongate, the fixed length of grouted anchors interacts with the grout and the ground in order to transfer the load.

A pioneer example of ground anchors application dates from 1934 when the French engineer Andre Coyne used rock anchors for strengthening a dam in Algeria. The improvement of grouting and drilling methods as well as the development of high quality steel wire and strand led to the post-war development of ground anchors mainly in France, Germany, Sweden and Switzerland, and later England (Xanthakos 1991). In 1958 the company Bauer showed for the first time that a bar could be anchored into gravel through a borehole with the aid of cement grout injection under pressure (Littlejohn 1980), thus leading to the invention of grouted anchors. According to Xanthakos (1991), in Austria prestressed rock and alluvium anchors have been used since the mid-1960s in the mountainous Alpine and western regions of the country, especially to stabilise rock formations.

The anchor capacity and performance depend mainly on three factors: the ground characteristics, the installation techniques and the workmanship attained in the field (Xanthakos 1991). Regarding the nature of foundation materials, ground anchors can be divided into soil anchors, rock anchors and marine anchors. Marine anchors are beyond the scope of this research and are not discussed herein.

2.1.1 Grouting technique

For a certain ground condition, the anchor pullout capacity is mainly affected by the anchor geometry and the construction technique. In this respect, the grouting method plays a major role. Littlejohn (1980) and Xanthakos (1991) divide grouted anchors into 4 types, as shown in Fig. 1:

- Type A: tremie-grouted straight shaft cylindrical hole of a uniform diameter, usually applied for rock and very stiff to hard cohesive layers;
- Type B: the borehole is grouted under low pressure, usually smaller than 10 bar, and the effective diameter of the fixed length is increased with minimal disturbance. The cement does not permeate the small pores and the grout compacts the soil locally while the diameter is increased. The method is in general employed for soft fissured rocks and coarse alluvium, and also for fine grained cohesionless soils;

- Type C: in this method, the borehole is grouted under high pressure, generally larger than 20 bar, and the grouted fixed length is enlarged by hydrofracturing the ground mass. The cement penetrates the ground irregularly. This technique is usually employed in cohesionless soils;
- Type D: the borehole is tremie-grouted with a series of enlargements in the fixed anchor length. It is commonly employed in stiff to hard cohesive deposits.

For type C anchors, the effect of the injection pressure on the pullout capacity depends, among other things, on the soil type. In general, if the in situ permeability of the soil increases, more of the injection pressure is dissipated. For this reason, the ultimate capacity is often estimated by means of design curves for different kinds of soils instead of relying on theoretical or empirical equations (Littlejohn 1980). Other techniques that are not included into types A to D can be undertaken, such as jet grouting techniques.

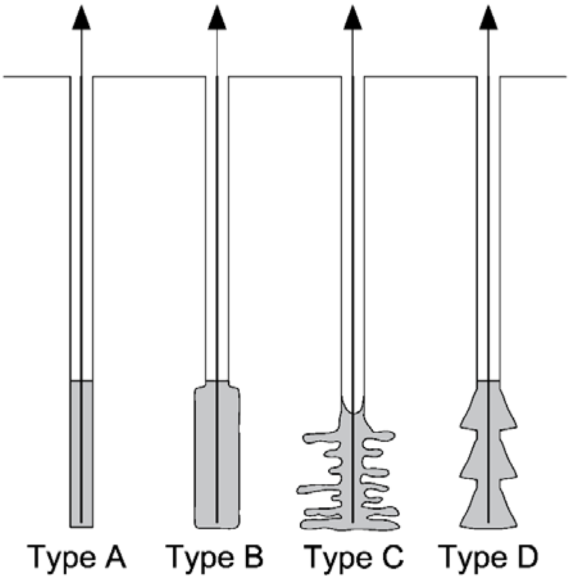

Fig. 1: Main types of cement grout injection (after Littlejohn 1980)

2.1.2 Mode of failure

According to Xanthakos (1991) failure of grouted anchors occurs in one of the following ways:

- Failure of the ground mass;
- Shear failure along the contact surface of grout and ground;
- Bond failure along the tendon-grout interface;
- Failure of the tendon or anchor head;
- Crushing or bursting of the grout column around the tendon;
- Gradual long-term deterioration.

Because the strength and toughness of the steel are much larger than the corresponding parameters of the ground and the grout, failure is often observed at the tendon-grout or grout-ground interface (Akisanya & Ivanović 2014).

Regarding rock anchors, Ivanović & Neilson (2009) performed pullout tests to investigate the bond between the interfaces and observed that failure occurred along the grout-rock interface. On the other hand, Benmokrane et al. (1995) carried out laboratory and field tests on rock anchors and observed failure in the tendon-grout interface. Ren et al. (2010) developed an analytical model and validated it with pullout experiments of grouted rockbolts that showed debonding in the bolt-grout interface. According to Xanthakos (1991), the tendon-grout bond of a ground anchor under working conditions is usually assumed to be appropriate for the load transfer and emphasis is often given to the grout-ground interface.

Due to the fact that soils exhibit much softer behaviour than rocks, slippage between grout and soil is more prone to occur than between grout and rock. Therefore, studies performed on soil anchors under pullout condition usually show failure mode in the grout-soil interface (Ostermayer 1975, Ostermayer & Scheele 1978, Wernick 1978).

2.1.3 Standards

The execution of ground anchors is mainly covered by three European Standards: general information such as materials, design, execution and testing is found in ÖNORM EN 1537:2015; the execution of grouted anchors tension tests is further detailed in ÖNORM EN ISO 22477-5:2019; the anchor design is described by ÖNORM EN 1997-1:2014 (Eurocode 7).

The Standards recognise three types of anchor load tests: investigation test for determining the ultimate load resistance of an anchor and for establishing the characteristics of the anchor in the working load range; suitability test to confirm that a particular design is adequate in particular ground conditions; and acceptance test to check if the anchor is in accordance with its acceptance criteria. Acceptance tests must be carried out for each working anchor (ÖNORM EN 1997-1:2014, ÖNORM EN 1537:2015).

None of the above-mentioned European Standards clearly specifies design methods of ground anchorages for determining the ultimate load holding capacity. Instead, Eurocode 7 states that investigation or suitability tests have to be performed in order to measure the geotechnical ultimate limit state resistance of an anchor. However, it is common practice to assume uniform shear distribution along the fixed length for anchor design. Alternatively, design curves such as the charts presented by Ostermayer & Scheele (1978) for cohesionless soils are traditionally employed to determine the ultimate load carrying capacity of anchors. In fact, the stress conditions acting along the interface where failure occurs are rarely accessible and usually only the ultimate load capacity is obtained during anchor tests.

In ÖNORM EN ISO 22477-5:2019, in addition to load tests, test methods are defined for each type of anchor test, namely method 1, method 2 and method 3. In method 1, the anchor is loaded up to a proof load in cycles. The tendon end displacement is measured for each load and, at the maximum load of each cycle, the displacement is measured during a certain time period. In method 2, the anchor is loaded to the proof load stepwise and in cycles and the load loss is measured at each load step during a time period. In method 3, the anchor is loaded in steps up to a maximum test load. The tendon end displacement is measured for each load stage and during a specified time period. For each method, different loading sequences and time periods are established in ÖNORM EN ISO 22477-5:2019.

The creep rate (α) is often the limiting criterion that determines the pullout resistance of the load tests. The ÖNORM B 1997-1-1:2013 establishes a maximum creep rate value of 2 mm. The creep rate at a certain anchor load is determined according to Eq. 1 (ÖNORM EN ISO 22477-5:2019) as follows:

$$\alpha = (s_b - s_a)/log(t_b/t_a) \tag{1}$$

In Eq. 1, s_a and s_b are the tendon end displacements at times t_a and t_b, respectively, t_a being the start of the time interval and t_b the end.

2.2 Progressive failure mechanism in soils

The progressive failure in soils is a widely recognised phenomenon. Terzaghi & Peck (1948) describes the progressive failure of natural clay strata as "*the spreading of the failure over the potential surface of sliding from a point or a line toward the boundaries of the surface. While the stresses in the clay near the periphery of this surface approach the peak value, the shearing resistance of the clay at the area where the failure started is already approaching the much smaller ultimate value*".

According to Taylor (1948), progressive action occurs during all shear failures, in nature and in laboratory tests. Therefore, if a soil mass is loaded until failure is incipient, failure will not be reached at all points at the same time. Progressive effects are larger in clays that have structure and in dense sands in comparison with loose sands and soft clays.

During drained shear, dense sands and overconsolidated stiff clays show gradual loss of strength after peak. These soils first decrease in volume and then increase. The stress-strain behaviour of a normally consolidated clay is similar to that of a loose sand and volume decrease is observed. The final range of the stress-strain curve during which the strength is constant with increasing the strain is called the ultimate condition. Fig. 2 shows the results of drained triaxial tests performed in loose and dense sands and in normally and overconsolidated clays (extracted from Lambe & Whitman 1969).

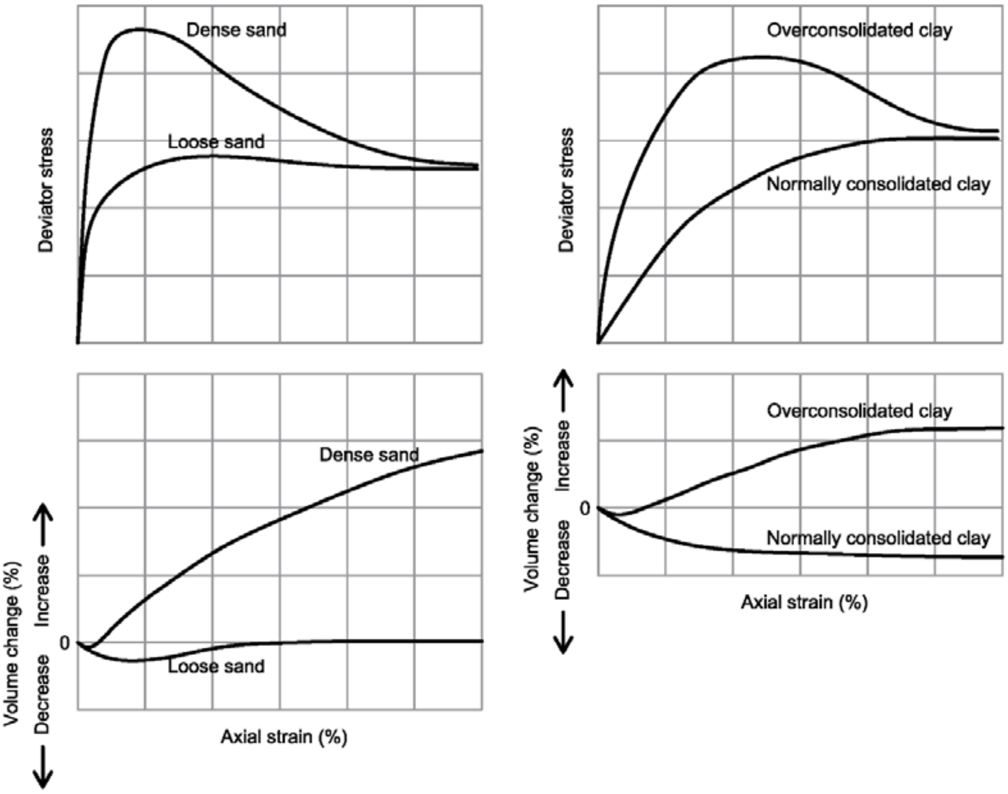

Fig. 2: Stress-strain curves for loose and dense sands and for normally consolidated and overconsolidated clays (after Lambe & Whitman 1969)

Taylor (1948) and Lambe & Whitman (1969) divide the shear resistance of a sand in two components: one part is the frictional resistance between grains and the second part is governed by the degree of interlocking. The loss of strength after peak observed in dense sands may be attributed to a gradual decrease in interlocking that occurs because the density of the sample decreases. In this case, shear failure occurs when the frictional resistance is overcome and when particles move up and over one another, i.e. the sample increases in volume. Additionally, Taylor (1948) explains interlocking in terms of strain energy, and states that "*the part of the shearing stress that is acting to overcome interlocking may also be said to be supplying the energy that is being expended in volume increase*".

For overconsolidated clays, the additional strength, which is usually attributed to cohesion and arises from precompression, is in part caused by resistance to volume increase as observed for dense sands (Taylor 1948). The post-peak drop off in strength is more pronounced as the degree of overconsolidation increases. Normally consolidated clays may also show peak strength but, in contrast with overconsolidated clay specimens that show volume increase at peak, for normally consolidated clays decrease of volume occurs at the peak point. According to

Lambe & Whitman (1969), the decrease in strength after peak is the result of decreasing structural strength due to remolding of the specimen.

The selection of peak values or ultimate values for analyses and design of structures is a delicate issue. According to Taylor (1948), the use of peak values may lead to unsafe procedures, whereas the use of ultimate values is generally too conservative.

2.3 Progressive failure mechanism in soil anchors

The progressive failure mechanism in soil anchors was already recognised in the 1970s, when it was observed that the skin friction in the grout-soil interface was non-uniform during anchor pullout tests in dense soils (Ostermayer 1975, Ostermayer & Scheele 1978, Wernick 1978). Ostermayer & Scheele (1978) performed strain gauge measurements at anchors in dense sand during pullout tests and observed that, as the test load was increased, the skin friction calculated from the measurements showed peak values that moved from the proximal end of the fixed length to the distal end. On the other hand, strain gauge measurements performed in loose and medium dense sands indicated that the skin friction was approximately uniform along the anchor fixed length. The peak values observed in dense soils were attributed to interlocking due to soil dilation, as also shown by Wernick (1978).

The progressive failure of anchors is illustrated in Fig. 3, which was adapted from Ostermeyer & Barley (2003). Fig. 3 shows the shear stress distribution during an anchor load test in the grout-soil interface: initially, stress concentration is observed at the proximal end of the fixed length and, with increasing load, this stress concentration moves towards the distal end of the fixed length. As the peak strength moves, progressive displacement evolves in the grout-soil interface at the area where failure started, leading to a decrease in the shear strength up to a residual value.

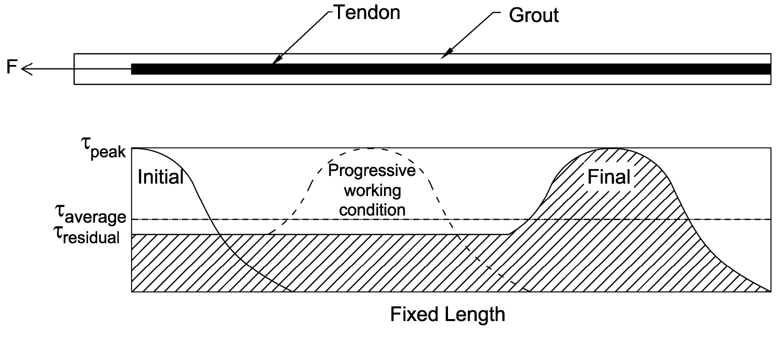

Fig. 3: Progressive failure mechanism in anchors (adapted from Ostermeyer & Barley 2003)

It is noteworthy that another mechanism of stress concentration was reported by Ostermayer & Scheele (1978) in the tendon-grout interface. This mechanism is illustrated in Fig. 4 and is explained by the fact that, because the strands were isolated with plastic tubes along the free length, the bond length of the grout-soil interface is longer than the one of the tendon-grout interface. For this reason, the forces resulting from the skin friction in the grout-soil interface ($\tau_{\text{grout-soil}}$) in the front part of the grouted body are transmitted back to the front part of the tendon at the fixed length. Therefore, stress concentration is observed at the proximal end of the fixed length in the tendon-grout interface ($\tau_{\text{tendon-grout}}$). This skin friction distribution is especially important if shear stresses along the grout-soil interface are calculated from measurements performed on the tendon. In this case, high values of skin friction at the proximal end of the fixed length might be obtained due to the stress concentration in the tendon, which in reality are distributed along the grout-soil interface.

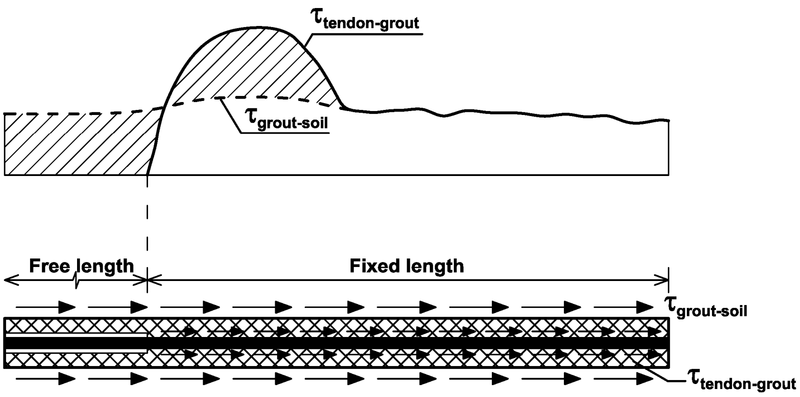

Fig. 4: Skin friction and stress concentration in the tendon-grout interface (adapted from Ostermayer & Scheele 1978)

2.4 Optical fibre sensing

When a light wave is launched into an optical fibre, the light interacts with the constituent atoms and molecules and the electric field induces a dipole. This dipole generates a secondary electromagnetic wave, which is called light scattering (Bao & Chen 2012). Whereas in a homogeneous medium a forward scattered beam is allowed, in an inhomogeneous medium such as the optical fibre some protons return towards the light source producing backscattering (Barrias et al. 2016). Three scattering processes are identified: Raman, Brillouin and Rayleigh scattering. Whereas Rayleigh scattering has frequency components close to the forward propagating light, Raman and Brillouin scattering effects show different spectral characteristics. Raman scattered light is caused by thermally influenced molecular vibrations and the backscattered light carries information on the local temperature. Brillouin scattering is caused by interaction between the propagating optical signal and thermally excited acoustic waves. Due to frequency shifted components, local temperature and strain variations can be obtained from Brillouin scattering (Leung et al. 2015). Rayleigh scattered light has been used to measure propagation effects such as attenuation and gain, phase interference and polarisation variation (Barrias et al. 2016).

In Optical Time Domain Reflectometer technique (OTDR), an optical pulse is launched into the fibre and the amount of light that is backscattered is detected. The spatial resolution of an OTDR instrument is of the order of 1 m. This spatial resolution can be increased by reducing the pulse width, leading to a decrease in the launched pulse energy which would weaken the signal-to-noise ratio (Barrias et al. 2016). Despite that, Brillouin Optical Time Domain Reflectometer (BOTDR) and Brillouin Optical Time Domain Analysis (BOTDA) are capable of long distance distributed sensing and a sensing range of more than 20 km is achieved.

In order to obtain measurements with higher spatial resolution, distributed fibre optic sensors based on Rayleigh scattering and Optical Frequency Domain Reflectometry (OFDR) were developed and are called Optical Backscattered Reflectometer (OBR). In comparison to OTDR that reads the intensity of the Rayleigh backscattered signal, OFDR measures the interference fringes of the Rayleigh scattered light from a tunable laser source and a static reference fibre in the frequency domain (Leung et al. 2015). In this way, the spatial resolution of the OFDR is independent on the bandwidth of the detector or digitizer and it is determined by the optical frequency sweep range of the tunable laser source. By increasing the frequency scanning range, the spatial resolution can be of less than 1 mm. However, the sensing length is usually less than 100 m.

2.4.1 Distributed optical fibre sensors in geotechnical engineering

Distributed Optical Fibre Sensors (DOFS) provide sensing points along the entire fibre length, thus enabling measurements in a truly distributed way. Moreover, distributed sensing requires a single connection cable from the acquired data to the reading unit (Barrias et al. 2016). OTDR technique has been used for monitoring geotechnical structures over approximately the last 15 years. Some examples of in situ applications are listed below.

- Bennett et al. (2006) described the use of BOTDR technique for strain monitoring during pile load tests and during the construction of a building. In the first case, the fibres were attached to steel reinforcing bars and, in the second case, they were attached to a pile reinforcement cage. Conventional vibrating wire strain gauges were also installed and the measurements were compared. The agreement between fibre optic and strain gauges measurements was very good and cracks could be identified with the BOTDR technique;

- Iten et al. (2008) employed an optical fibre cable to estimate the position of the boundary between a landslide and the stable part of the slope. The fibres were embedded into a trench cut along a road and 89 m of the road were monitored. BOTDA technology was used and the spatial resolution was about 1 m and strain measurements were carried out at different periods and compared. The measurements were in good agreement with the observed landslide displacements and with geodetical data;
- The use of BOTDR technique for monitoring strains in a tunnel was described in Mohamad et al. (2010). The fibres were attached to the surface of the tunnel and the strains were induced by the construction of another tunnel, close to the monitored one. The fibre was fixed around the tunnel circumference and 12 tunnel rings were monitored. The strains induced by the excavation of the adjacent tunnel were successfully monitored;
- Mohamad et al. (2011) used a distributed fibre optic strain sensing technique to monitor a secant pile wall. BOTDR technology was used. The optical cable was installed along two opposing sides of a pile reinforcement cage. The strain measurements were converted into curvature and the inclination and lateral displacement of the pile were calculated. The results were then compared with inclinometer data from adjacent piles.

In contrast with OTDR, the use of OFDR technique for monitoring in situ geotechnical structures was only recently reported. Examples of distributed fibre optic system employing OFDR for monitoring geotechnical structures are given below. This technique was employed for monitoring the anchor pullout tests described in the next chapters and it enables spatial resolutions of millimetre scale.

- Hauswirth et al. (2014) employed distributed fibre optic sensors for monitoring horizontal ground strains during the passage of earth pressure balance shield tunnel boring machines. The sensors were embedded in shallow ground surface trenches perpendicular and parallel to the tunnel axis and the measurements were validated against micrometer stick measurements. The strains were integrated in order to obtain the displacements transversely to the tunnel direction;
- Monsberger et al. (2016) applied a fibre optic system to measure the strains during a static load test of a driven pile. In this study, it was challenging to ensure the integrity of the fibre during the installation process and, although the fibre was protected, it broke during the pile installation. The authors employed the strain sensing cable Brugg BRUsens V4, with an outer diameter of 3.2 mm. During the test, cracking evolution in the grout was evaluated;
- Bersan et al. (2018) used a fibre optic sensing system for measuring the strains along the reinforcement bars during a static pile load test. The fibre optic cable was embedded in the pile shaft, fastened to the vertical bars of the reinforcement. The cable used was the Brugg BRUsens V9, with an outer diameter of 3.2 mm. In order to obtain the vertical displacements along the

pile, the strain profile was integrated. The load distribution and the shaft friction were also obtained from the strain data;

- Rabaiotti & Malecki (2018) conducted pullout tests of barrette foundations which were instrumented by distributed fibre optical measurements. The fibre optic cables were employed inside the test barrettes, namely cable Brugg BRUsens V9, and were interrogated by BOTDA and OFDR technologies. The vertical strains measured with OFDR technology allowed to identify cracks in the test barrettes, which increased with increasing load. Due to the spatial resolution of 1 m, the cracks position was not detected by the BOTDA technology;
- Monsberger et al. (2018) described the use of distributed fibre optic sensing for monitoring strains in the shotcrete lining at a railway tunnel. Measurements were performed during the shotcrete curing and during the advance of the tunnel drive and the sensor cables had a total length of more than 230 m. The results were compared with vibrating wire sensors and geodetic measurements. An Optical Backscattered Reflectometer was employed. The measurements performed with the vibrating wire sensors compared well with the fibre optic results and some deviations were observed with respect to the geodetic measurements. Cracks inside the shotcrete were also captured by the fibre optic measurements;
- Smet et al. (2019) employed an optical fibre for monitoring strains during an anchor pullout test. The strains were monitored along the anchor grouted body and the measurement technique was based on Brillouin Optical Frequency Domain Analysis. The anchor was monitored along the anchor free and fixed lengths and the spatial resolution varied from about 20 to 40 cm. The measurements indicated that debonding occurred between the tendon and the grout at the proximal end of the fixed length. A numerical 1D simulation was carried out and the anchor load-displacement behaviour compared well with the simulation.

3 Constitutive models

In this chapter, the constitutive models employed in the numerical simulations of the anchor pull out tests are presented. Describing the constitutive models in detail is beyond the scope of this thesis and for more information on the models the reader is referred to the literature mentioned below.

3.1 Mohr-Coulomb model

The well-known Mohr-Coulomb model (MC model), a linear elastic perfectly plastic constitutive model, is a simple model that describes soil behaviour based on Hooke's law and employs the Mohr-Coulomb failure criterion. The yield surface is fixed and not affected by plastic straining. This constitutive model does not account for stiffness dependency on the stress path, stress level and strain level. The MC model was only employed in the numerical calculations for describing rock behaviour or for soil layers that were located close to the ground surface and thus had no significant influence on the behaviour of the anchor fixed length. The MC model is described in Brinkgreve et al. (2019a).

3.2 Hardening soil model with small strain stiffness

The Hardening Soil model with small-strain stiffness (HSsmall model) is an elasto-plastic constitutive model that considers shear and compression hardening by implementing a cone yield surface and a cap yield surface (Schanz et al. 1999). The model also takes into account the stiffness at small-strain levels (Benz 2007). Four stiffness parameters must be set in order to use this material model: the secant stiffness for deviatoric loading ($E_{50,ref}$), the tangent stiffness for oedometer loading ($E_{oed,ref}$), the unloading/reloading stiffness ($E_{ur,ref}$) and the small-strain shear modulus ($G_{0,ref}$). In addition to $G_{0,ref}$, the small-strain behaviour is controlled by a threshold shear strain ($\gamma_{0.7}$), at which the secant shear modulus is reduced to about 70% of the small-strain shear modulus. The stiffness parameters are related to a reference pressure, which is usually taken as 100 kPa. Failure is governed by the Mohr-Coulomb failure criterion. More information on the HSsmall model is found in Brinkgreve et al. (2019a).

3.3 Multilaminate constitutive model

The development of the multilaminate framework relates macro-mechanical behaviour of materials to the micro-mechanical scale and dates back to the slip theory of Taylor (1938), describing the sliding phenomena in metals with contact planes of different orientations. The multilaminate material models are based on the concept that the material behaviour can be formulated on a distinct number of local planes with varying orientation. The stress–strain state varies from plane to plane, and the global behaviour is obtained by integration of the contributions of all planes (Bažant & Oh 1986).

Local stress increments σ'$_i$ are a projection of the global stresses into the integration planes (Fig. 5) and yield surfaces are defined in terms of local shear stress τ and normal stress σ'$_n$.

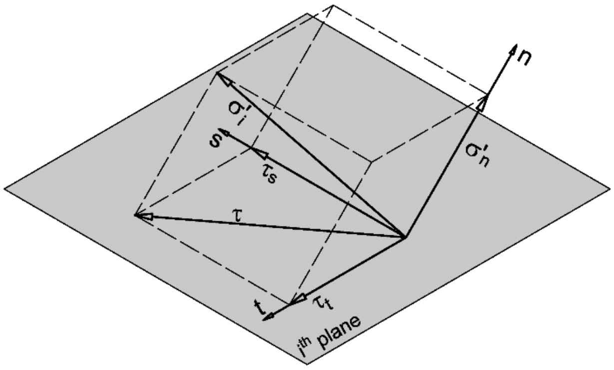

Fig. 5: Local stress components (after Schädlich & Schweiger 2014b)

The original Multilaminate model for clay as proposed by Pande & Sharma (1983) was extended by Schweiger et al. (2009) for modelling the behaviour of loose to medium dense sand or normally to slightly overconsolidated clays. The model features an elliptical volumetric hardening surface f_{cap} for loading in compression, a linear shear hardening surface f_{cone} for deviatoric loading and a tension cut-off surface f_{tens} and takes into account small strain stiffness.

This Multilaminate model was extended further by Schädlich & Schweiger (2014b) in order to reproduce specific features of overconsolidated clays and is refereed herein as the MMS_HV model. A Hvorslev failure envelope f_{HV} is introduced in order to describe peak shear strength of heavily overconsolidated clays (Fig.6a). Therefore, the Hvorslev surface definition was adapted to the integration plane level by normalising the local stresses with the equivalent normal stress σ'$_{ne}$, as shown in Fig.6b.

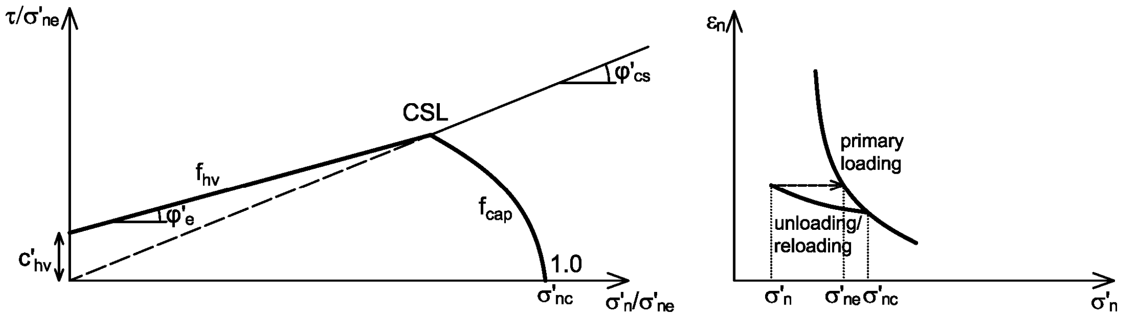

a) b)

Fig.6: MMS_HV model – a) normalised Hvorslev surface on integration plane level and b) equivalent normal stress definition (after Schädlich & Schweiger 2014b)

Because σ'_{ne} decreases with reduction of the normal stress σ'_n, the Hvorslev yield surface is a curved line in the non-normalised τ-σ'_n plot of the yield surfaces and only gets activated when the local stress path reaches the Hvorslev surface. Plastic strains are obtained also from the strain hardening deviatoric yield surface (Schädlich & Schweiger 2014b). A regularization technique, namely a non-local formulation (Galavi & Schweiger 2010) is introduced in order to avoid the well-known mesh dependency when modelling strain softening behaviour by means of standard finite element formulations. For more details on the MMS_HV model the reader is referred to Schädlich (2012) and to Schädlich & Schweiger (2014b).

3.4 Concrete model

The constitutive model employed for the grout, the Concrete model, is a nonlinear model originally developed for modelling time dependent behaviour of shotcrete for NATM tunnelling applications. The Concrete model is a standard material model in Plaxis from the version 2018 onwards (Brinkgreve et al. 2019a).

The model is capable of considering the time-dependent strength and stiffness development, strain hardening and softening, creep, and shrinkage. In this study, no time dependency is considered as the grout is assumed cured at the time of loading. This is justified because the pullout tests were carried out several weeks after the anchors installation. Strain softening is governed by the fracture energies in tension (G_t) and in compression (G_c), which are input parameters. A regularisation technique is implemented to avoid mesh dependency due to softening.

The model decomposes the total strain ε into elastic strains ε_e, plastic strains ε_p, creep strains ε_{cr} and shrinkage strains ε_{shr}. Plastic strains are calculated according to strain hardening/softening elastoplasticity. Creep and shrinkage are not taken into account herein.

For deviatoric loading, a Mohr-Coulomb yield surface F_c is employed and, in the tension regime, a Rankine yield surface F_t is assumed (Fig.7). The behaviour in compression and in tension are shown in Fig.8 and Fig.9. In compression, it is divided in four parts:

- Quadratic strain hardening (part 1): located between the normalised initial strength f_{c0n} and the uniaxial compressive strength of cured concrete f_c;
- Linear strain softening (part 2): between the uniaxial compressive strength and the normalised failure strength f_{cfn};
- Linear strain softening (part 3): between the normalised failure strength and the normalised residual strength $f_{cun;}$
- Constant residual strength (part 4): starts after residual strength f_{cun} is reached.

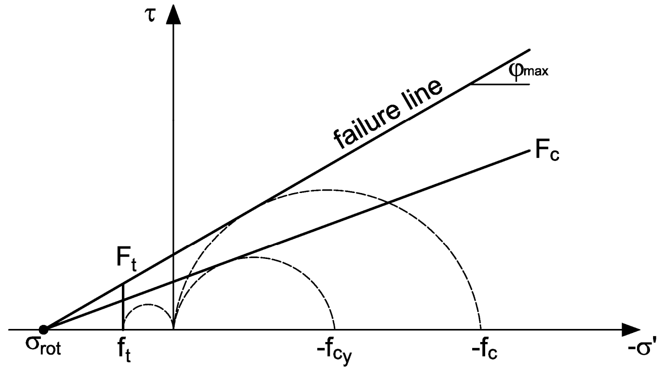

Fig.7: Yield surfaces and failure envelope (after Schädlich & Schweiger 2014a)

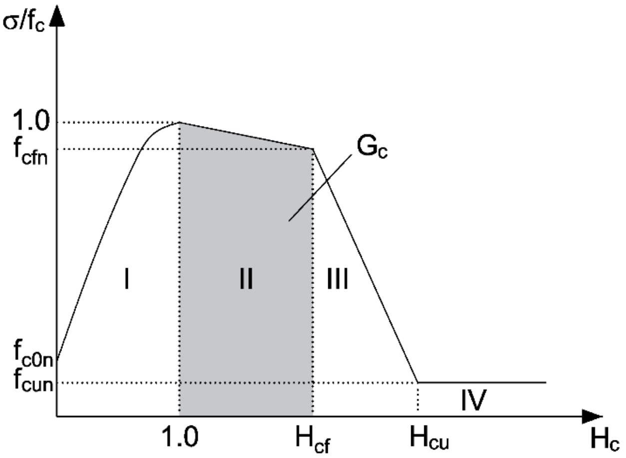

Fig.8: Normalised stress-strain curve in compression (after Schädlich & Schweiger 2014a)

In Fig.8, H_c is a normalised hardening/softening parameter equal to $\varepsilon_3{}^p / \varepsilon_{cp}{}^p$, where $\varepsilon_3{}^p$ is the minor principal plastic strain and $\varepsilon_{cp}{}^p$ is the plastic peak strain in uniaxial compression. Full mobilisation of f_c coincides with $H_c = 1$ and failure strength is reached at H_{cf}.

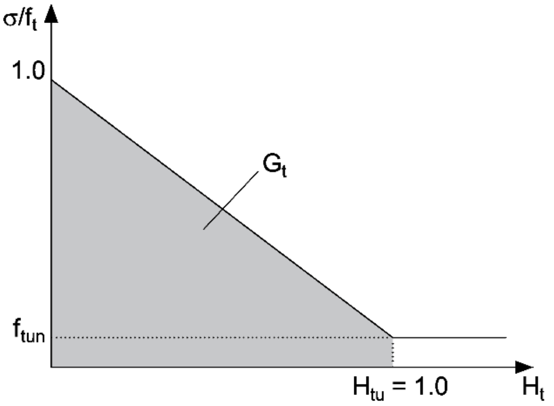

Fig.9: Normalised stress-strain curve in tension (after Schädlich & Schweiger 2014a)

The model behaviour in tension is linear elastic up to the tensile strength f_t, followed by linear strain softening (Fig.9). The tensile strength is governed by a softening parameter H_t, equal to $\varepsilon_1{}^p / \varepsilon_{tu}{}^p$, where $\varepsilon_1{}^p$ is the major principal plastic strain and $\varepsilon_{tu}{}^p$ is the plastic ultimate strain in uniaxial tension. Values of H_t larger than 0 indicate softening, which takes place until the residual strength $f_{tu} = f_{tun}.f_t$ is reached and H_t is larger than 1.

More details on the Concrete model can be found in Schädlich & Schweiger (2014a), Schädlich et al. (2014) and in Brinkgreve et al. (2019a).

4 Pullout tests: general remarks

4.1 Overview of the anchor pullout tests

With the main purpose of evaluating anchor performance under various ground conditions, a research program was carried out in which 10 in situ full scale pullout tests were undertaken. Additionally, the anchor behaviour was compared if different grouting techniques and geometries were employed.

During the pullout tests selected anchors were equipped with distributed fibre optic sensors. The fibre optic cables were attached along the tendon length and embedded in the grout. The reading unit used (Optical Backscatter Reflectometer, OBR) is capable to record sensing information with a very high resolution of about ± 1 µm/m for strain and about ± 0.1 °C for temperature measurements (Luna 2014). The reading unit emits laser light into a passive optical sensing fibre and analyses the backscattered light which is generated along the sensing fibre due to Rayleigh backscattering. Measurements are carried out continuously along the fibre and show a typical spatial resolution of 10 mm, depending on the quality of the signal. One single optical fibre is used for both, sensing and signal transmission.

The strain profile along the entire tendon and grout was obtained, thus allowing for a detailed assessment of the anchors performance, such as: the evaluation of the fixed length activation for every load step; the load transfer behaviour between the tendon, the grout and the soil; the cracking evolution in the grout during the test and its influence on the anchor performance. In addition to the fibre optic sensors, the anchors were monitored with linear transducers at the anchor head.

Sensing cables from Solifos, Switzerland (formerly Brugg Cables) were used. Except for the pullout test undertaken in 2015, the strands were equipped with a 0.9 mm thick fibre optic cable (FiMT), which corresponds to the inner part of the steel armoured BRUsens Strain V4 and V9, but without the outer polyamide sheath. This cable was used because of the limited space between the individual wires. It was glued along two separate strands using special epoxy, following the torsion of the wires, which protects the sensing cable well. However, the increased length due to the torsion must be considered during data analysis. Regarding the pullout test carried out in 2015, the cable employed was type BRUsens Strain V4, with an outer diameter of 3.2 mm.

For the embedment into the grout, the more robust cables BRUsens Strain V9 and BRUsens Strain V3 were used. The V9 and the V3 cables have an outer diameter of 3.2 mm and 7.2 mm, respectively, and are refereed herein as “thin” and “thick” cables. Both have a structured surface at the outside, which provides good coupling to the grout, and the V3 cable additionally contains a steel armour. The cables were attached outside the corrugated plastic sheath using an adhesive tape and conducted in loops. Due to this redundancy, the robustness of the measuring system was increased and thus measurements may be continued in the case of one single fibre breakage and possible outliers may be identified. Because of the short duration of the tests, which was approximately half a day, and due to the essentially constant temperature a few metres below the ground that emerges after hardening of the grout, a separate cable for temperature compensation was not used. Fig. 10 shows the fibres being installed along the tendon and the grout. Fig. 11 shows the cables from Solifos types FiMT, V9 and V3. The calibration, installation and data acquisition of the fibre optic monitoring system was performed by the Institute of Engineering Geodesy and Measurement Systems of the Graz University of Technology. Results on the calibration of the measuring system are shown in Woschitz et al. (2016).

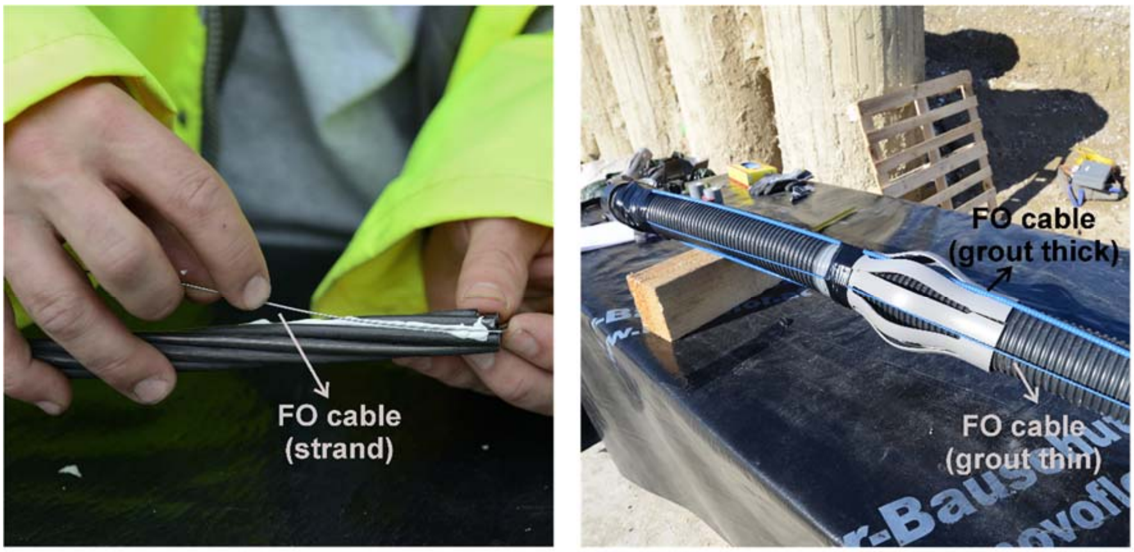

a) b)

Fig. 10: Installation of the fibre optic cables – a) for the tendon measurements and b) types V9 and V3 for the grout measurements

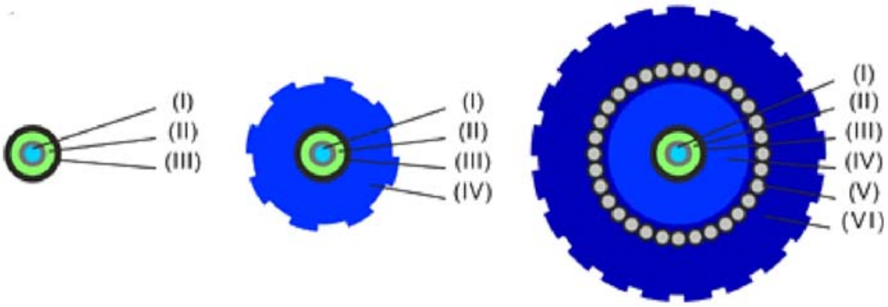

a) b) c)

Fig. 11: Structure of different strain sensing cables from Solifos GmbH - a) type FiMT; b) type V9 and c) type V3. (I) strain sensing single mode fibre (∅ 250 µm), (II) multi-layer buffer with strain transfer layer, (III) metal tube, (IV) polyimide protection layer, (V) special steel armouring and (VI) polyimide outer sheath

The pullout tests were conducted in different soil types and, additionally, one anchor in rock was tested. Tab. 1 shows an overview of the in situ tests. More information on the anchor tests are addressed separately in the following chapters, where the anchor geometry, the grouting technique and the ground description are given in detail.

Tab. 1: Overview of the anchor pullout tests

Test name	**Date**		**FO system?**	**Location**	**Ground type**[1]
	Installation	**Test**			
SÖ	August 2015	08.09.2015	Yes	Söding, Austria	Overconsolidated, silty sand (Opok)
SK_1A	24.10.2017	06.12.2017	Yes	St Kanzian, Austria	Clayey silt (Seeton)
SK_1B	24.10.2017	07.12.2017	No		
SK_2A	25.10.2017	30.11.2017	Yes		
SK_2B	25.10.2017	04.12.2017	No		
SK_2C	30.10.2017	05.12.2017	No		
SK_3A	25.10.2017	29.11.2017	Yes		
SK_3B	25.10.2017	28.11.2017	No		
A10	03.07.2018	19.07.2018	Yes	A10 Tauernautobahn km 50.6-50.9, Austria	Fragmented claystone
LJ	11.02.2019	28.02.2019	Yes	Ljubljana, Slovenia	Gravel

[1] Predominant material along the anchor fixed length

4.2 Preliminary considerations for data interpretation

4.2.1 Load-displacement curves interpretation

Unless it is mentioned in the text, the load-displacement curves are presented with respect to the displacements measured with the linear transducer (u_{total}). Test method 1 (ÖNORM EN ISO 22477-5:2019) was employed during the pullout tests. The curves obtained numerically are compared with the in situ curves considering the displacements at the top of the fixed length ($u_{\text{top fixed length}}$). This type of presentation was chosen because the tendon end displacements are mainly due to the elastic elongation of the free length ($u_{\text{free length}}$), i.e. they are highly dependent on the free length size. Therefore, the elastic elongation of this part was subtracted from the total displacement measured with the linear transducer, according to Eq. 2 and Eq. 3:

$$u_{top\ fixed\ length} = u_{total} - u_{free\ length} \tag{2}$$

$$u_{free\ length} = \frac{F}{A_{tendon}} \Big/ E_{tendon} \ x \ L_{free\ length} \tag{3}$$

The tendon free length considered in Eq. 3 ($L_{\text{free length}}$) is the distance between the anchorage point at the jack and the proximal end of the fixed length. This length was obtained by measuring the distance from the anchorage point to the tendon end, and then subtracting it from the total designed free length (including the section above the ground level). In Eq. 3, F is the applied force at one strand; A_{tendon} is the cross-sectional area of one strand, normal to F; E_{tendon} is the elastic modulus of the tendon. Fig. 12 shows a sketch of a ground anchor during a pullout test using a conventional displacement monitoring system. In this figure, the position considered for evaluating the numerical and in situ displacements during the test ($u_{\text{top fixed length}}$) is depicted.

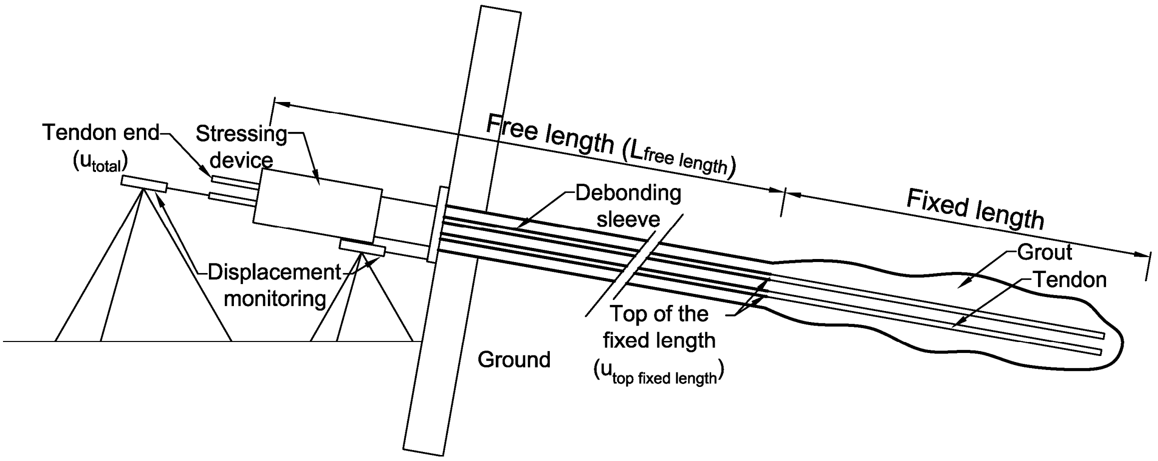

Fig. 12: Schematic presentation of a ground anchor and conventional monitoring system

4.2.2 Fibre optic measurements interpretation

The fibre optic strain profile provides valuable information on the anchor behaviour during the pullout test. In this respect, discussion is addressed to enable the interpretation of such results, with focus on the load transfer mechanism developed during the test. Positive values denote tensile strains and negative values imply compressive strains.

Whereas an approximate constant strain distribution indicates no load transfer, a decrease of strain along depth from the proximal end of the fixed length to the distal end indicates load transmission from the tendon to the grout. Therefore, a sharp decrease of strain along depth implies higher shear stresses in the tendon-grout interface and a moderate decrease implies lower shear stresses values.

In order to facilitate the evaluation of the load transfer mechanism from the fibre optic strain profile, one example is given in Fig. 13. The free length section is located at the first 12 m and the fixed length at the last 8 m depth. The strain profile can be divided in 4 parts:

1. Anchor free length: along the tendon free length, the strands were isolated with plastic tubes (debonding sleeves in Fig. 12). For this reason, if perfectly isolated, within this section no load transfer is expected between the tendon and the grout and the strains along the tendon free length show a constant value for a certain load in the strain profile. The strains along the grout within part 1 usually increase with depth and are negative (compressive stresses).
2. Transition zone: the transition between compressive and tensile zones in the grout is not exactly on top of the fixed length, but it extends to the proximal end of the fixed length. Usually, the width of this transition zone is located between the fixed length top and the first tensile crack or, in case no crack develops, the point where the tensile strain stop to increase at the fixed length. Along the tendon, part 2 usually shows the highest rate of strain decrease. The transition zone is discussed further in section 4.2.3.
3. Cracked area: in comparison to part 2, the strain decrease along the tendon in part 3 is less abrupt but is still remarkable. In the grout, cracks are observed in this area, which explain the high values of strains in the tendon.
4. Undamaged area: from -3 up to -7.5 m the load transfer in the tendon is reduced. In the example, the tendon is not completely activated at the fixed length and, within the last 1.5 m, almost no strains develop. The grout in part 4 is not cracked and the strain profile is essentially the same as the one along the tendon.

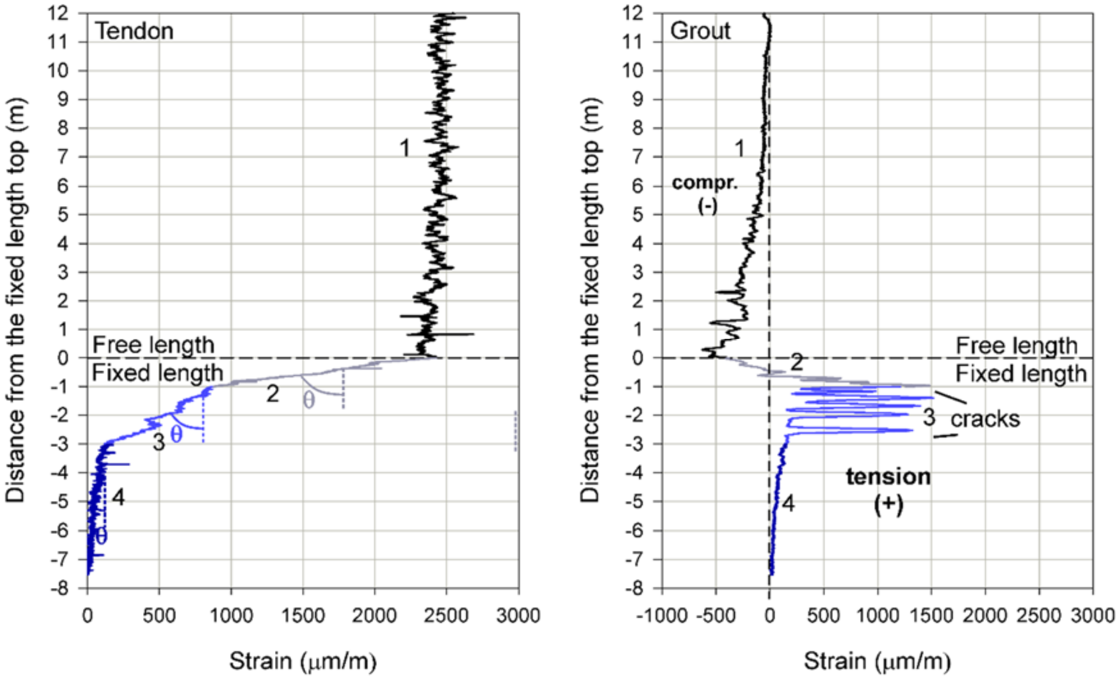

Fig. 13: Strain distribution along the tendon and the grout: load transfer behaviour

4.2.3 Transition zone

The transition between tensile and compressive stresses in the grout verified in Fig. 13, herein called “transition zone”, is discussed in more detail in this section. Within this zone, the strains in the tendon exhibit a sharp decrease along the strain profile at the fixed length, thus leading to high shear stress concentration in the tendon-grout interface at the proximal end of the fixed length. Stress concentration was verified by Ostermayer & Scheele (1978) during field tests on anchors monitored with strain gauges on the steel bar. Fig. 14 shows the transition zone at the fixed length along the tendon and along the grout verified by fibre optic strain measurements.

Due to the stress concentration in the tendon at the proximal end of the fixed length, debonding along the tendon-grout interface is more likely to initiate at this area. Weerasinghe & Littlejohn (1997) investigated the load transfer behaviour of anchors installed in mudstone and showed that the load transfer at the proximal end decreases as the load increases. The same was observed by Benmokrane et al. (1995), when performing laboratory and in situ experiments in rock anchors, and by Ivanović & Neilson (2009) during laboratory tests undertaken to investigate debonding along rock anchors.

In Fig. 14, it can be verified that the transition zone width increases as the pullout load increases. As the compressive stresses increase within the transition zone on top of the fixed length from loading stage 1 to loading stage 2, positive strains become negative and tensile cracks appear to close. Furthermore, although not shown in Fig. 14, debonding in the tendon-grout interface would lead to a vertical strain distribution along the tendon at the fixed length if the grout was subjected to tensile stresses. The amount of skin friction concentration is highly dependent on the ground stiffness: stiff soil or rock shows higher stress concentration than a soft material and therefore debonding is more likely to occur in the former case.

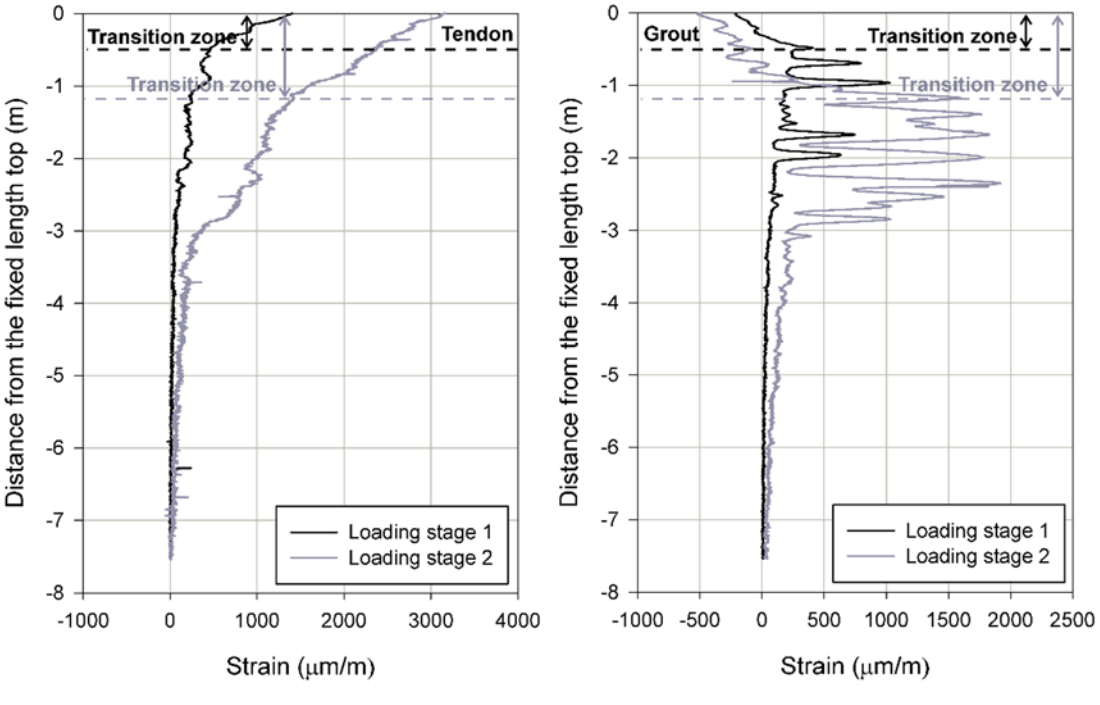

Fig. 14: Transition zone at the fixed anchor length along the tendon and along the grout

5 Söding-test

5.1 Anchor and soil description

The pullout test was undertaken in 2015 by Keller Grundbau in Söding, Austria, and described in Racansky et al. (2016). The anchor was vertically installed and the borehole diameter was 178 mm. The free length was 12 m and the fixed length was 8 m long. The grout at the free and fixed length was only gravity grouted and 11 strands were used. The water/cement ratio was 0.5.

A core drilling was carried out and the soil condition was inspected. In a simplified profile, three different soil layers are considered: the first layer is a fill and is identified within the first 5.5 m; the second layer is 2 m thick and is an overconsolidated soil characterised as sandy gravel, located between 5.5 and 7.5 m; the third layer is also an overconsolidated soil characterised as silty sand that extends up to the bottom of the fixed length. The second layer is referred as “Opok upper layer” and the third layer as “Opok lower layer”.

5.2 In situ pullout test results

The load-displacement curve considering the displacements at the top of the fixed length is presented in Fig. 15, where unloading steps are not depicted. The creep rate did not exceed 2 mm during the test, i.e. the limiting criterion was not achieved. During the last loading step of 2700 kN the creep rate was 1.97 mm.

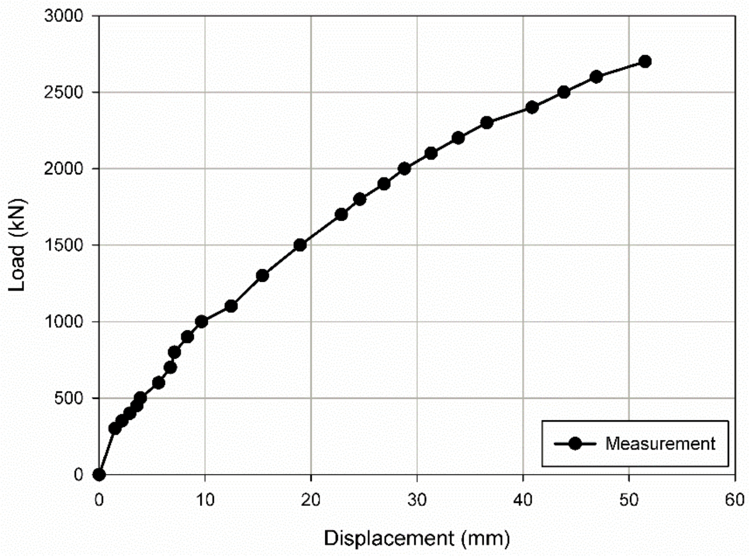

Fig. 15: In situ load-displacement curve

The in situ strain distribution along the tendon and the grout is shown in Fig. 16 and Fig. 17, respectively. The free length is located along the first 12 m and the fixed length along the last 8 m. In order to look in more detail at the strain profile, Fig. 18 presents only the results of the 500 and 1000 kN loading steps. The profile can be divided according to the above-mentioned parts (section 4.2.2): anchor free length; transition zone; cracked area; undamaged area. However, it is also remarkable that the strains along the tendon at the fixed length within the cracked area in Fig. 18 show different inclinations along depth.

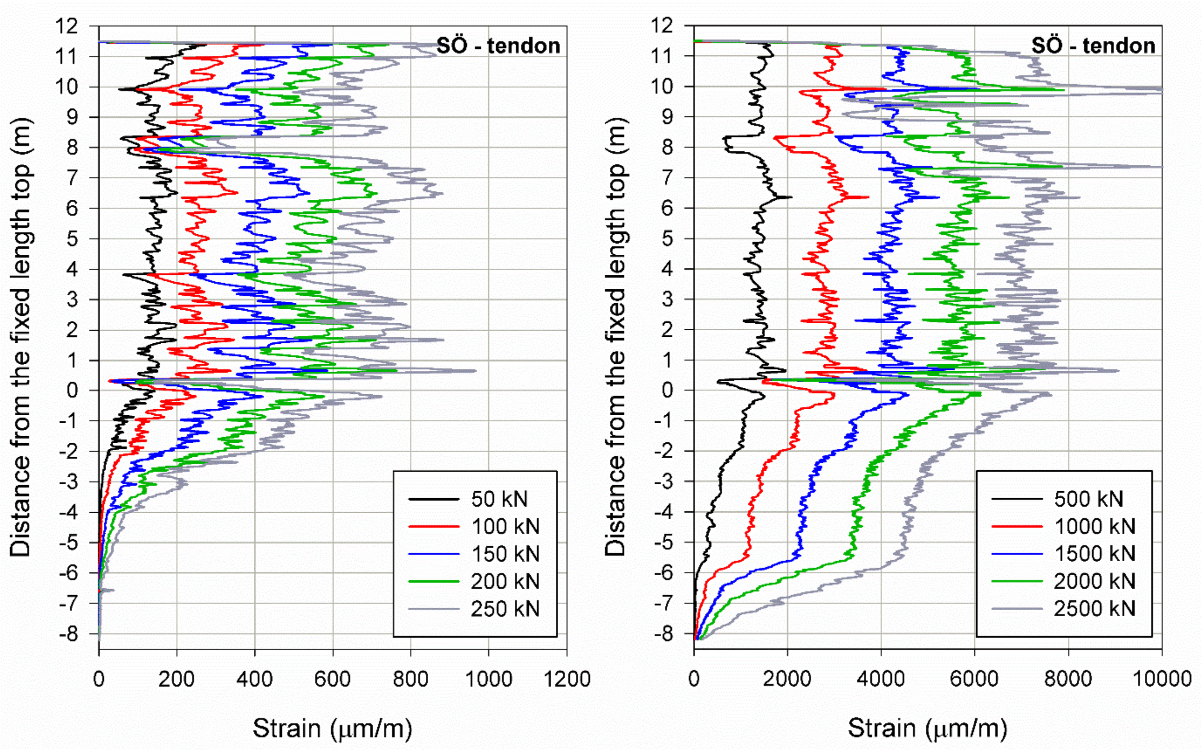

Fig. 16: Strains along the tendon

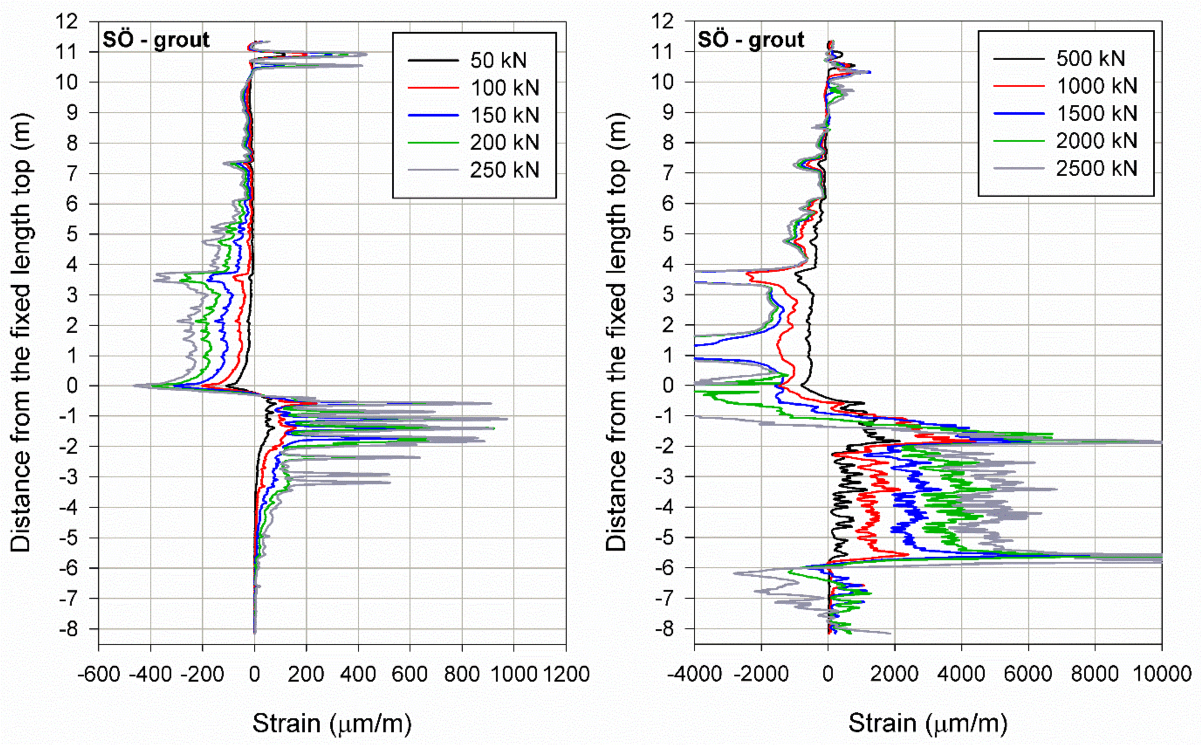

Fig. 17: Strains along the grout

In Fig. 18, within the first 0.8 m of the fixed length, at the transition zone, the strains in the tendon show a sharp decrease whereas the strains in the grout are compressive. Although the grout within this area is probably cracked, the compressive stresses acting in the grout lead to crack closure and load transfer is high. Below -0.8 and up to -1.8 m, tensile cracks in the grout evolve and, along the tendon, the strains show a remarkable vertical profile, thus indicating load transfer decrease. It is believed that in this area debonding occurred between the tendon and the grout. Between 2000 and 2500 kN, tensile cracks appear to close due to the development of compressive stresses at the proximal end of the fixed length in the grout and load transfer is regained. For this reason, in the last two load steps shown in Fig. 16, the inclination of the tendon strain profile with respect to the vertical axis between -0.8 and -1.8 m increases.

Between approximately -3.4 and -5.6 m, the slope of the tendon strain curve is different from the slope observed below -5.6 m. This can also be explained by local debonding between the tendon and the grout up to -5.6 m. From 1000 kN onwards a large crack is observed at -5.6 m and, at 1500 kN, compressive strains start to develop below this crack. The same phenomenon observed at the proximal end of the fixed length is then verified below -5.6 m: where compressive strains in the grout develop, the slope of the strains in the tendon with respect to the vertical axis increases, resulting in a second transition zone. This is shown in Fig. 19 for the 1500 kN load step and considering the strain profiles along the anchor fixed length.

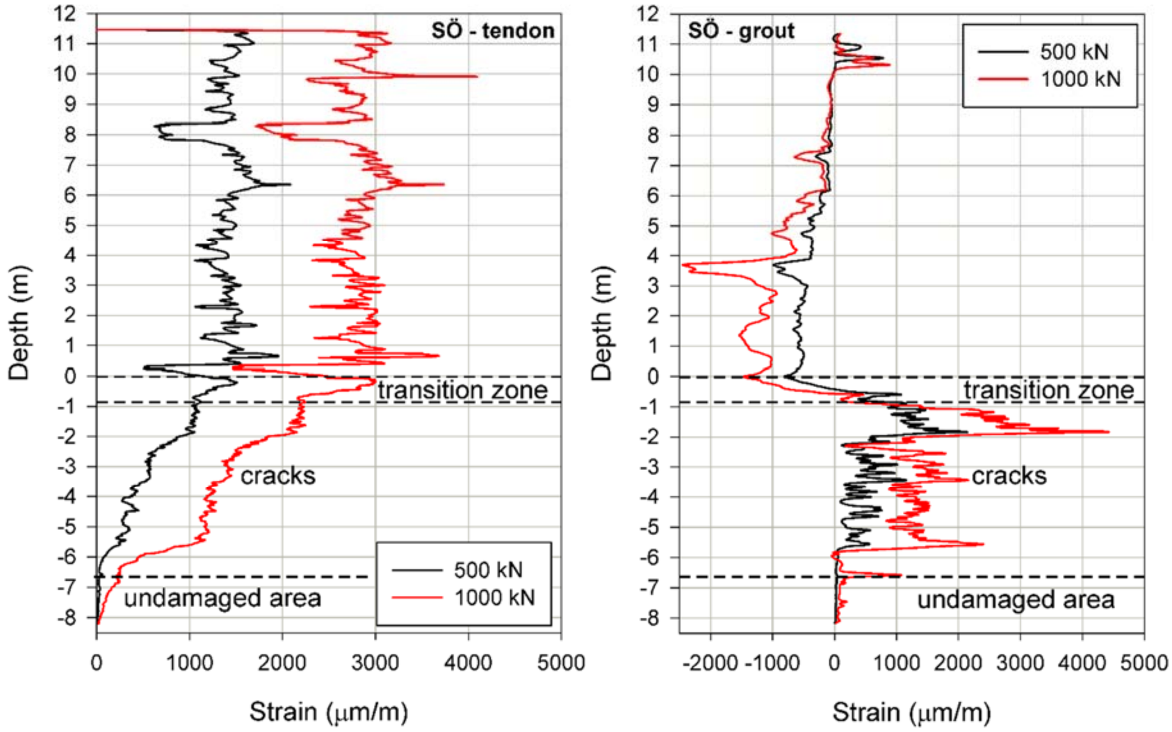

Fig. 18: Strain distribution along the tendon and the grout – different grout conditions

As expected, the fibre optic measurements show that the strains along the tendon are influenced once cracking in the grout starts. The distal end of the fixed length being the last part of the grout that cracks, at this position in Fig. 18 the strains in the tendon are significantly smaller than within the cracked area.

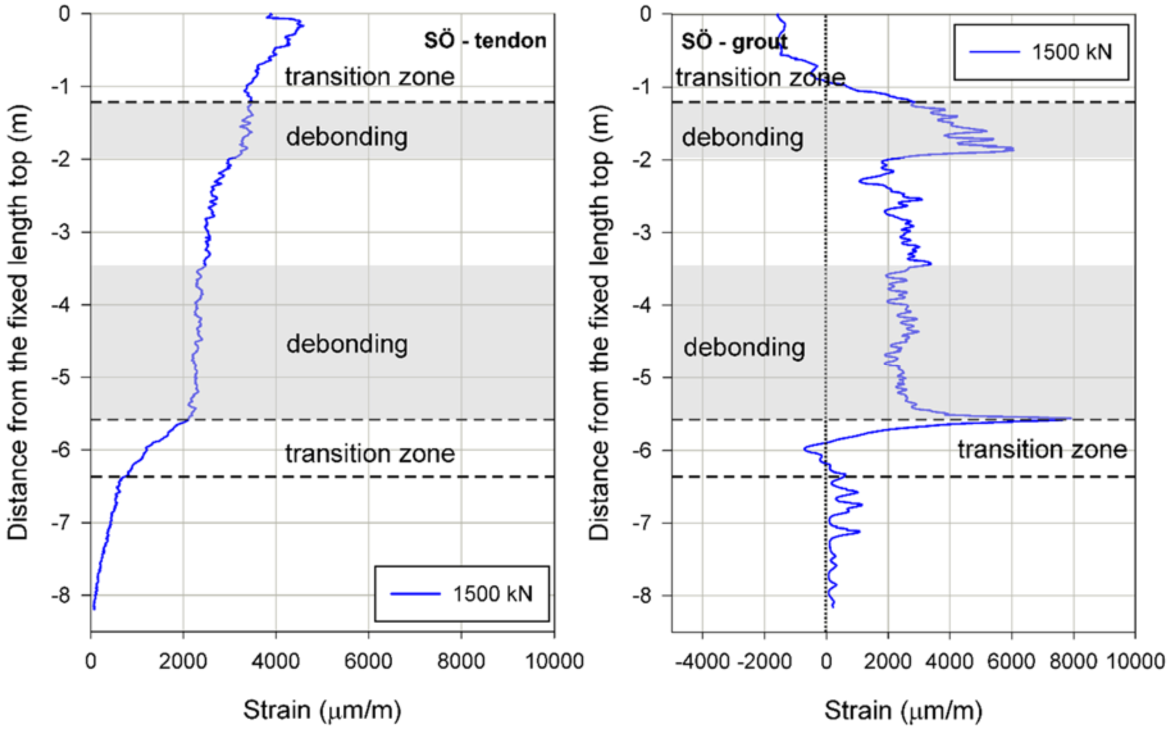

Fig. 19: Strain distribution along the tendon and the grout at the fixed length – transition zones

5.3 Numerical simulations

The numerical simulations were axisymmetric with respect to the vertical axis, thus taking advantage of the fact that the anchor was vertically installed. In order to save calculation time, the first two soil layers where the initial 7.5 m of the anchor free length were positioned (fill and Opok upper layer) were modelled with the Mohr-Coulomb model. The other soil layer, where the remaining part of the free length and the entire fixed length were located (Opok lower layer), was simulated either with both, the HSsmall model and the MMS_HV model, or only with the HSsmall model. In the case that the MMS_HV model was employed, this constitutive model was assigned only within a soil cluster located 0.5 m from the axis of symmetry.

The pullout load was simulated by means of prescribed displacements applied at the top of the tendon and the tendon was modelled only along the fixed length. This is justified by the fact that along the free length the strands are isolated and no load transfer is expected to occur. The strands were modelled as one equivalent strand with continuum finite elements and, for this purpose, the equivalent transversal area was calculated considering the diameter of a single strand as 15.7 mm. The geometry of the numerical simulation is shown in Fig. 20a and Fig. 20b, where the soil layers and the detail of the fixed length top are depicted, respectively. Tab. 2 shows general information of the Söding-test numerical simulations.

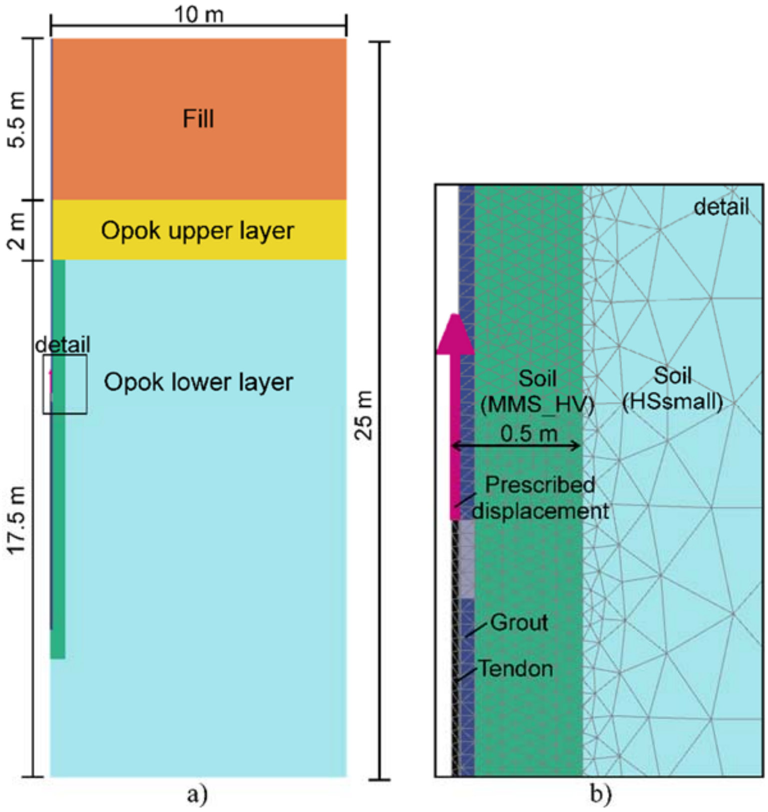

Fig. 20: Geometry of the numerical simulation – a) soil layers and b) top of the fixed length detail

Tab. 2: General information of the numerical simulations

Simulation	**Software**	**Number of elements**	**Element type**
Simulation 1	Plaxis 2D – 2018	7623	15-noded
Simulation 2	Plaxis 2D – 2018	7625	15-noded
Refinement 1	Plaxis 2D – 2018	7623	15-noded
Refinement 2	Plaxis 2D – 2018	7625	15-noded

5.3.1 Material parameters

Laboratory investigations were undertaken on a sample located between 12.80 and 13.85 m and the soil parameters of the third layer were calibrated based on triaxial tests. Because the soil was overconsolidated, except for the fill the lateral earth pressure coefficient at rest (K_0) was set as 1.5 for all soil layers. Additionally, the pre-overburden pressure of the layers modelled with the HSsmall model and the MMS_HV model was considered as 3500 kPa. The soil unit weight in all cases was 21 kN/m^3. The soil parameters are shown in Tab. 3, Tab. 4 and Tab. 5.

The Concrete model was employed for simulating the grout. A uniaxial compression test was conducted to determine the grout strength and stiffness parameters. The tensile strength and the post-peak parameters of the grout were assumed based on experience and the grout unit weight was 25 kN/m³. The steel tendon was modelled as a linear elastic material (E_{tendon} = 160 GPa and ν = 0.2) with unit weight set as 78.5 kN/m³. The grout parameters are shown in Tab. 6.

Tab. 3: Material parameters (Mohr-Coulomb model, fill and upper layer)

Parameter	**Description**	**Fill**	**Opok upper layer**
		Value	**Value**
E (kN/m²)	Youngs's modulus	15 000	40 000
ν'	Poisson's ratio	0.3	0.35
c' (kN/m²)	Effective cohesion	2	100
φ' (°)	Effective friction angle	27.5	35
K_0	Earth pressure coefficient at rest	0.54	1.5

Tab. 4: Material parameters (HSsmall Model, Opok lower layer)

Parameter	**Description**	**Value**
$E_{50,ref}$ (kN/m²)	Reference primary loading stiffness	6000
$E_{oed,ref}$ (kN/m²)	Reference oedometric stiffness	6000
$E_{ur,ref}$ (kN/m²)	Reference un/reloading stiffness	29 000
ν'_{ur}	Poisson's ratio un/reloading	0.2
c' (kN/m²)	Effective cohesion	200
φ' (°)	Effective friction angle	35
m	Stress dependency index	0.85
$K_{0,nc}$	Earth pressure coefficient for normal consolidation	0.426
POP (kN/m²)	Pre-overburden pressure	3500
$\gamma_{0.7}$	Shear strain at 70% of G_0	1.50e-4
G_{0ref} (kN/m²)	Small strain shear modulus	48 300
K_0	Earth pressure coefficient at rest	1.5

Tab. 5: Material parameters (Multilaminate model, Opok lower layer)

Parameter	**Description**	**Value**
$E_{oed,ref}$ (kN/m²)	Reference oedometric stiffness	6000
$E_{ur,ref}$ (kN/m²)	Reference un/reloading stiffness	29 000
m	Power	0.85
ν'_{ur}	Poisson's ratio in un-/reloading	0.2
A_{mat} (10^{-3})	Shear hardening parameter	2.5
R_f	Failure ratio	0.95
$K_{0,nc}$	Earth pressure coefficient for normal consolidation	0.47
n_{cp}	Number of integration planes	21
φ'_e (°)	Hvorslev surface Inclination	24
$\sigma'_{nc,0}$ (kN/m²)	Initial value of σ_{nc}	-3500
φ'_{cs} (°)	Critical state friction angle	32
h_{soft}/l_{calc} (m^{-1})	Ratio h_{soft}/l_{cal}	10 000
K_0	Earth pressure coefficient at rest	1.5

Tab. 6: Material parameters (Concrete model, grout)

Parameter	**Description**	**Value**
E (GPa)	Young's modulus of cured grout	16.26
ν	Poisson's ratio	0.2
f_c (MPa)	Uniaxial compressive strength	32.12
f_t (MPa)	Uniaxial tensile strength	1.5
f_{c0n}	Normalized initially mobilised strength	0.15
f_{cfn}	Normalized failure strength (compression)	0.95
f_{cun}	Normalized residual strength (compression)	0.1
$\varepsilon_{cp}{}^{p}$	Uniaxial plastic peak strain	-0.0035
G_c (kN/m)	Compressive fracture	3
f_{tun}	Ratio of residual *vs*. Peak tensile strength	0.05
G_t (kN/m)	Tensile fracture energy	0.01
a	Increase of ε_{cp} with increase of p'	16
φ_{max} (°)	Maximum friction angle	40

5.3.2 Numerical results

The results of the first two numerical simulations are presented below. For the numerical calculations, the interface parameters were not modified. Simulation 1 considered only the HSsmall model for the Opok lower layer and in simulation 2 the HSsmall model and the MMS_HV model were employed (Fig. 20). The numerical load-displacement curves are plotted in Fig. 21 as well as the in situ curve.

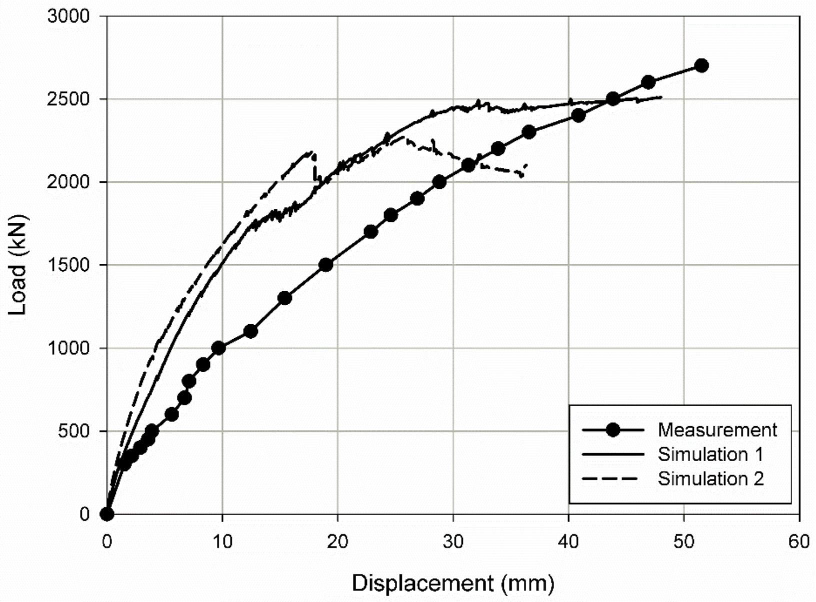

Fig. 21: In situ load-displacement curve *vs* simulations 1 and 2

The load-displacement curves obtained with simulations 1 and 2 showed stiffer behaviour and lower ultimate capacity than the in situ curve. The curve obtained with the HSsmall model (simulation 1) was softer than the one that considers the HSsmall model and the MMS_HV model (simulation 2). This is due to the stiffness definition in the MMS_HV model, which in general results in stiffer behaviour in comparison to the HSsmall model. The kink observed in simulation 2 at 18 mm of anchor displacement is due to soil instability when residual state is achieved. When softening takes place in the soil, the zone around it unloads elastically. The instability is observed if the unloading energy is larger than the energy released during softening. In this case, load and displacement must decrease to reach equilibrium. Due to the fact that the simulation is displacement-controlled, the load drops at constant displacement.

The strains along the tendon at the fixed anchor length are compared in Fig. 22 for the 1000 kN load step and considering simulation 1. The grey arrows at the proximal end of the fixed length show strains decreasing due to compressive stresses in the grout. It is remarkable that this decrease is more pronounced in the numerical simulation than in the in situ measurements. Because at this part of the anchor stress concentration occurs, it is believed that this area is a damaged area in the grout under compressive stresses. The sharper decrease of strains obtained numerically indicates that the numerical compressive stresses are larger than the in situ stresses. Below the compressive stress concentration area, tensile stresses in the grout follow and debonding possibly occurs, indicated by the vertical in situ strain distribution. A second debonding area is observed between -3.4 and -5.6 m from the fixed length top. It is worth noting that cracking evolution is reproduced by the Concrete model but it does not account for the load transfer decrease within the debonded area under tensile stresses.

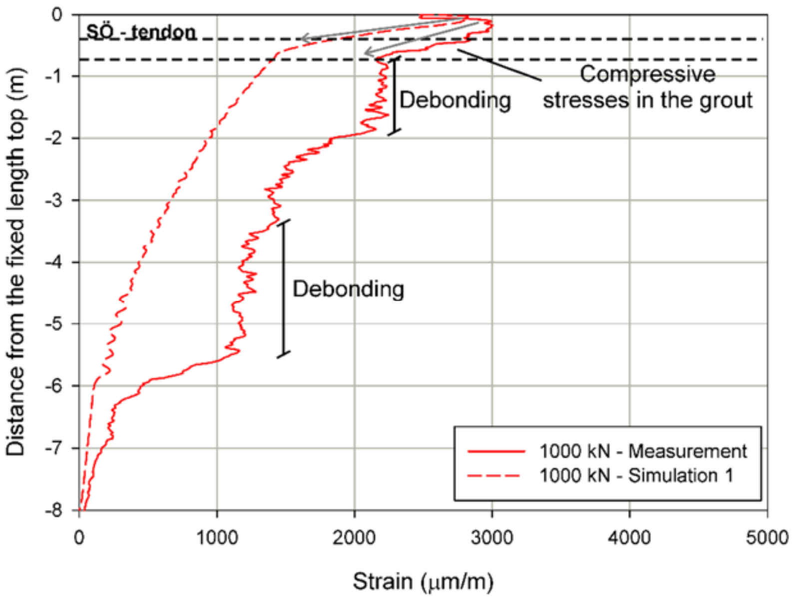

Fig. 22: Strain distribution along the tendon – in situ *vs* simulation 1 (1000 kN)

In order to improve the calculation, additional simulations were carried out. For these simulations, a cluster within the grouted body at the proximal end of the fixed length was considered in order to account for the damaged area in compression. This cluster was activated since the first prescribed displacement increment was applied and was located within the first 0.3 m of the fixed length. The height of this cluster was chosen according to the extension of compressive strains at the fixed length in the grout observed in the first load step. The parameters of this damaged area were selected assuming that the tensile strength was at residual state due to cracking in the grout ($f_t = 75$ kPa). Because the slope of the numerical strain distribution (Fig. 22) was more pronounced than the in situ one, the compressive strength and the stiffness of the grout were reduced until a similar slope was obtained, leading to $f_c = 10$ MPa and E = 5 GPa.

In order to account for debonding due to tensile cracks as observed in Fig. 22, the stiffness of the grout had to be decreased, so to reduce the load transfer between the tendon and the grout in this area. The stiffness reduction was carried out below the 0.3 m cluster up to -2 m from the fixed length top and between -3.4 and -5.5 m. The change of material was undertaken after this part of the grout was cracked. The same set of parameters assumed for the intact grout was considered for this damaged area in tension, except for the stiffness that was reduced to 10 MPa. The stiffness reduction accounts for the partial contact between tendon and grout that occurs when the cracked grout is subjected to tensile stresses. It is important to mention that the Concrete model, when used as a user defined soil model, memorises cracking even if the material is replaced. Therefore, after changing the grout material, softening is maintained according to the state before the change. Fig. 23 shows the geometry of the numerical simulation with the clusters to account for the damaged grout.

The first numerical refinement (refinement 1) was undertaken only with the HSsmall model assigned to the Opok lower layer. The second numerical refinement (refinement 2) was carried out considering both, the MMS_HV model and the HSsmall model for this layer, as presented in Fig. 20.

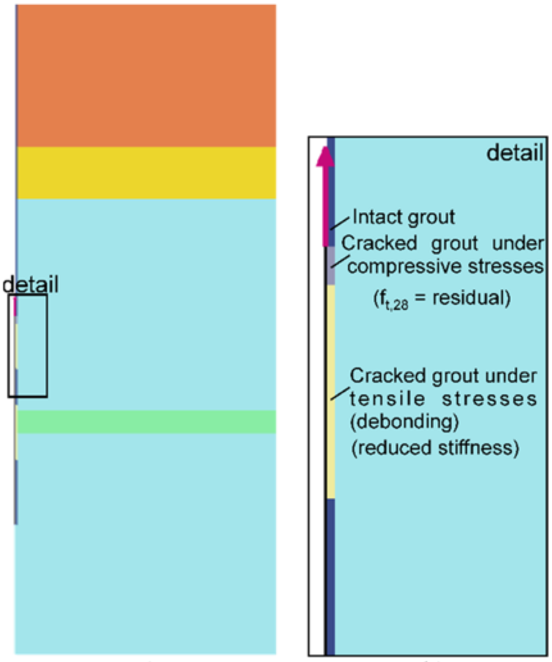

a) b)

Fig. 23: Geometry of the numerical simulation (refinements) – a) soil layers and b) top of the fixed length detail

The load-displacement curves obtained with refinements 1 and 2 are shown in Fig. 24. The results achieved with the HSsmall model agreed almost perfectly with the measurements, whilst stiffer behaviour was obtained with the MMS_HV model. Despite the capability of the MMS_HV model to reproduce the post-peak behaviour of overconsolidated soils and therefore to simulate the progressive failure mechanism of anchors, in this specific case the load-displacement behaviour was only slightly different from the behaviour observed with the HSsmall model.

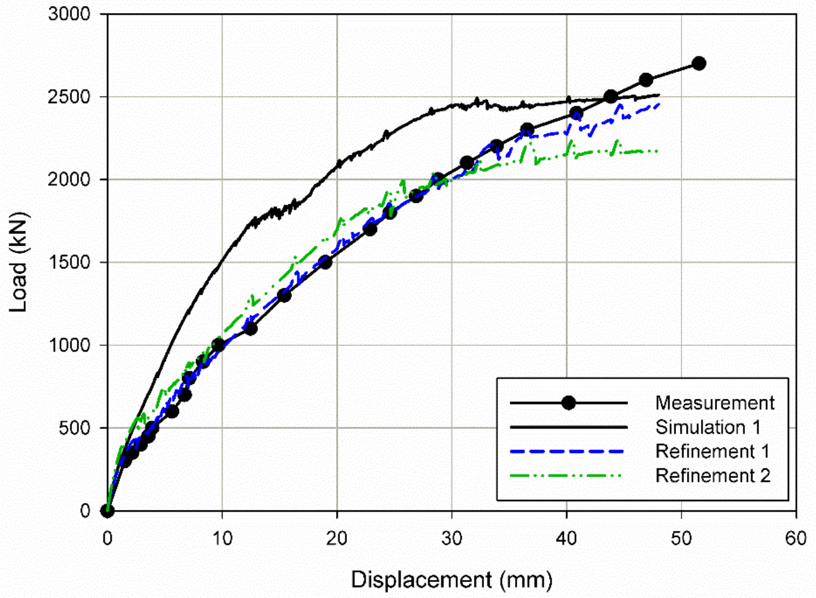

Fig. 24: In situ load-displacement curve *vs* refinements 1 and 2

The strain distribution along the tendon at the fixed length is compared with the numerical results of refinements 1 and 2 in Fig. 25. The in situ measurements are depicted with solid lines and the numerical results with dashed lines. The agreement between the numerical refinement and the in situ measurements was good up to 1000 kN. For the last two load steps shown in Fig. 25 the numerical results did not capture the vertical strain distribution between -3.4 and -5.6 m. This difference indicates that, despite the stiffness reduction performed manually for the Concrete model, as the pullout load increases the amount of load being transferred from the tendon to the grout in the numerical model increases significantly. At the 2000 kN step, the tendon in the numerical model is fully activated. Because at this position the grout is subjected to tensile stresses, unless compressive stresses evolve and close the cracks, the numerical load transfer within the debonded area should remain very low. Therefore, in order to improve the numerical agreement using the Concrete model, the stiffness must be further reduced. However, due to the development of high displacements in the soft grout material if the Young's modulus of the Concrete model is very low, this procedure leads to numerical problems. Comparing refinement 1 and 2, the strain distribution for both refinements was similar.

In Fig. 26 the contours plot of the H_t parameter and of the mobilised shear stresses in the grout for refinement 1 at the 1000 kN load step are depicted. Two cracked areas were selected, the first one (detail 1) is located within the cluster where the grout stiffness was reduced, i.e. where debonding occurs. The second one (detail 2) is positioned in the grout where no debonding is observed. The softening parameter H_t indicates cracking once it is larger than 0 and residual state if it is larger than 1 and, in both cases, the cracks were already at residual state.

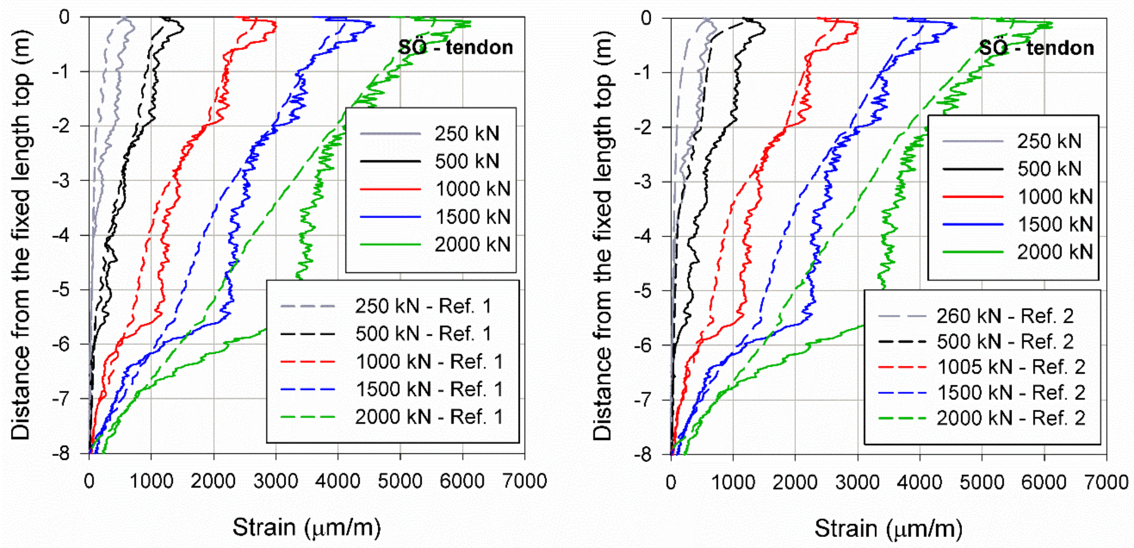

Fig. 25: Strain distribution along the tendon – in situ *vs* refinements 1 and 2

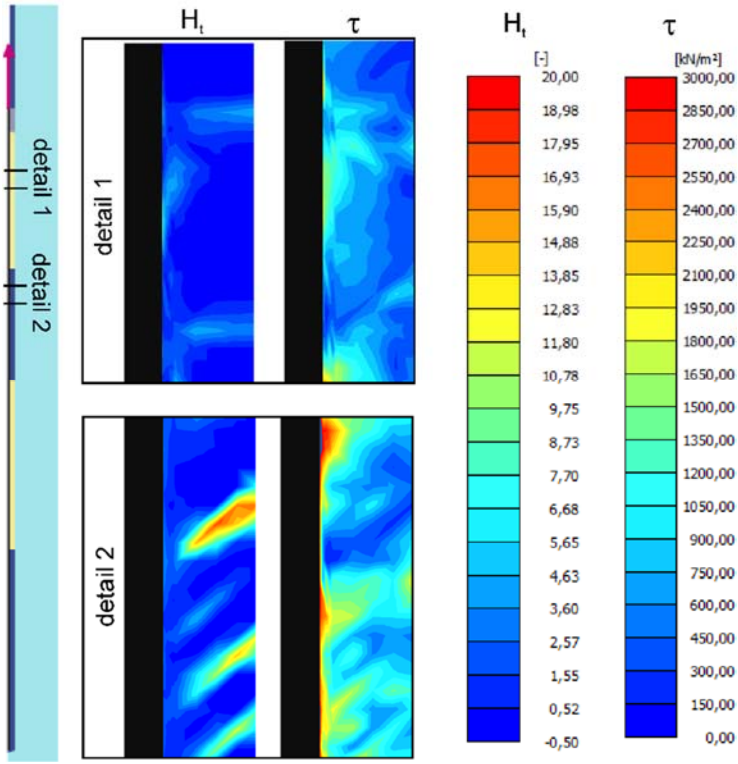

Fig. 26: Cracks details in the grout for refinement 1 (1000 kN load step)

Although the mobilised shear stresses within the cracked area are reduced in comparison to the area surrounding the cracks, the stresses are not zero. If the area in the grout where the stiffness was manually reduced is compared with the area where no debonding occurs, the stresses are smaller but, even in this case, the values can reach up to 900 kPa in the stress point located at the damaged grout. This figure confirms that, even if manual material replacement is performed, modelling the load transfer decrease with the Concrete model due to debonding in tension is not straightforward.

Regarding the capabilities of the MMS_HV model to account for the post-peak behaviour of overconsolidated soils, the mobilised shear stresses along a cross-section in the soil, adjacent to the anchor fixed length, are plotted in Fig. 27. The shear stresses obtained with the HSsmall model (Fig. 27a) are compared with the stresses calculated using the MMS_HV model (Fig. 27b). The cross-section was located 6 cm away from the grouted body. In order to facilitate the results interpretation, simulations 1 and 2 were selected for plotting the shear stress distribution. Both simulations did not account for the damaged grout clusters employed in the numerical refinement and shown in Fig. 23.

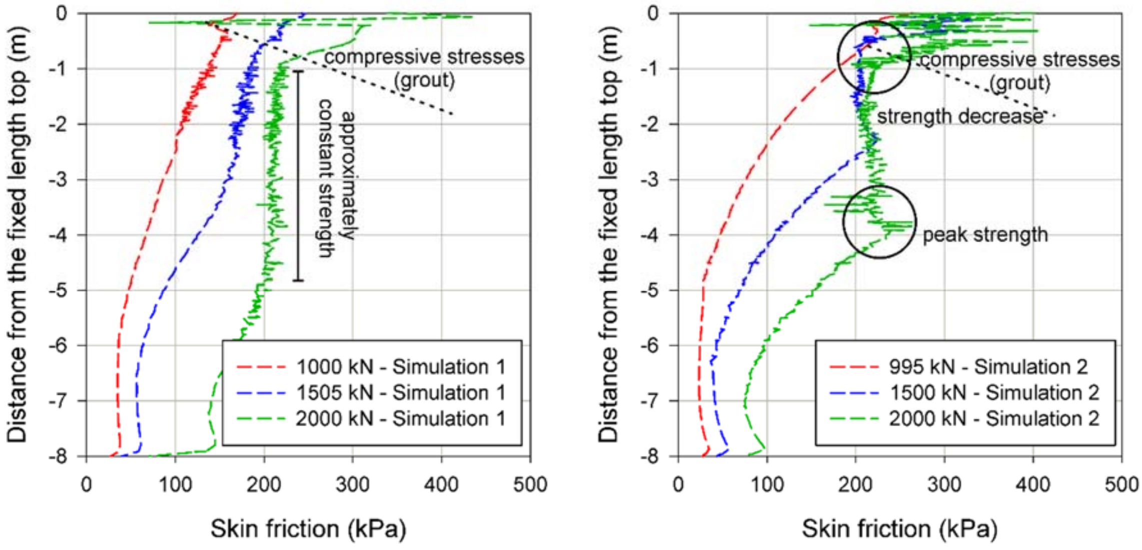

a) b)

Fig. 27: Skin friction in the soil (numerical results) – a) HSsmall model and b) MMS_HV model

In Fig. 27 it is clear that, if the MMS_HV model is employed, the peak strength is observed and is larger than the shear strength reached with the HSsmall model. Additionally, the shear strength of the soil decreases within the first metres of the anchor fixed length whereas the peak value moves towards the distal end. At the proximal end of the fixed length stress concentration is observed with both constitutive models. The stress concentration area is located within the transition zone, where compressive stresses in the grout at the fixed length occur. Within this area the numerical results show shear failure in the tendon-grout interface, thus indicating debonding in shear.

Fig. 28 shows the in situ crack development compared with H_t obtained in the simulation (refinement 1). The numerical cracks distribution is in good agreement with the in situ measurements. As observed for the in situ strain profiles, the numerical results showed that if the grout is undamaged, the strains in the tendon reach very low values.

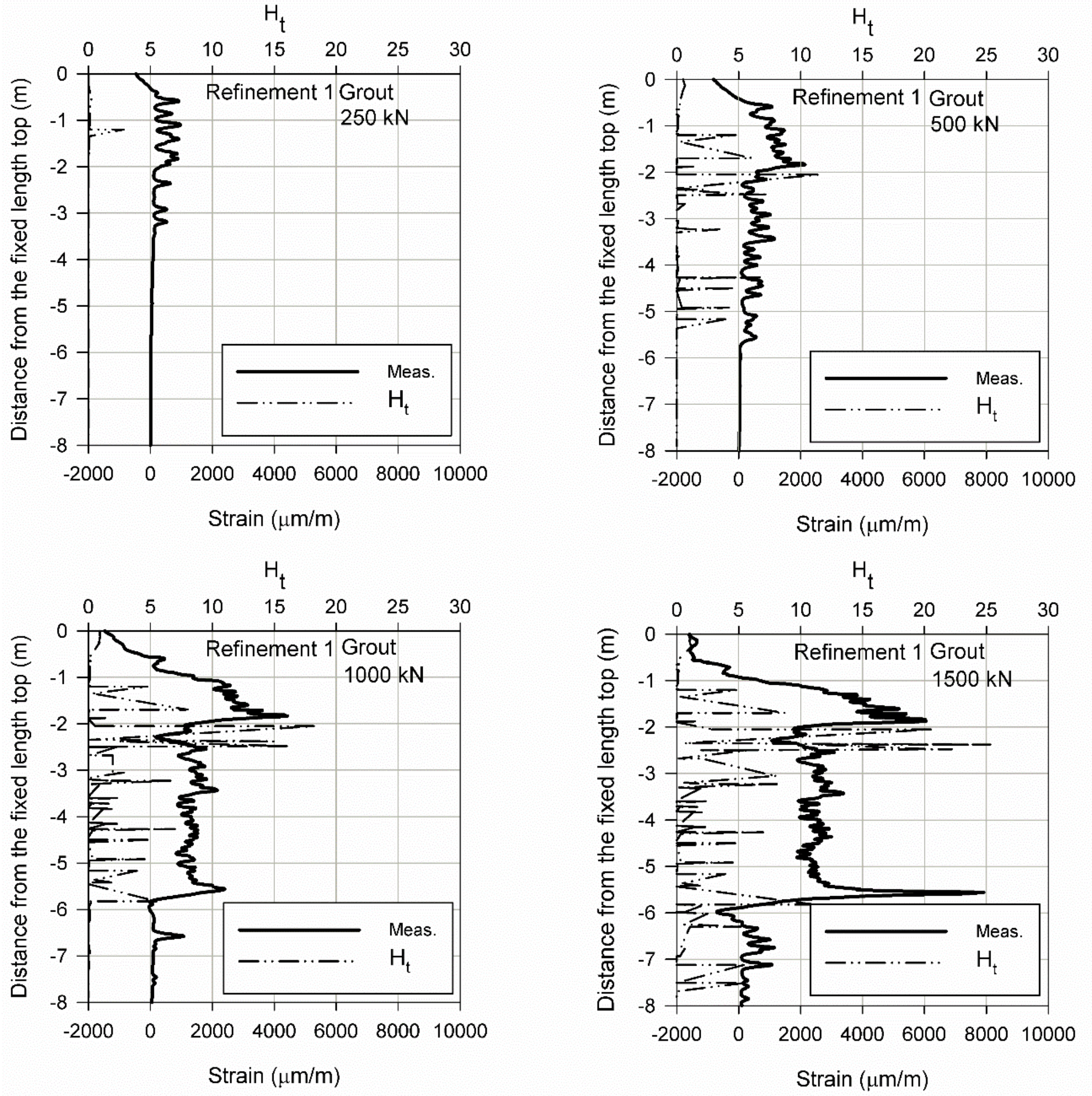

Fig. 28: Measured strain distribution along the grout at the fixed length and comparison with the numerical parameter H_t

5.4 Summary

An anchor pullout test was carried out in Söding, Austria, in an overconsolidated silty sand. The fibre optic measurements along the anchor tendon and along the grout were shown. The slope of the measured strain distribution along the tendon varied along depth, indicating distinct load transfer behaviour in the tendon-grout interface. Some important observations were addressed:

- At the proximal end of the fixed length shear stress concentration occurred in the tendon-grout interface. Within this area, the grout was possibly cracked but, because it was subjected to subsequent compressive stresses, cracking closure occurred and the load transfer was high;

- Below the stress concentration region, the strain decrease at the tendon was reduced and, because the grout was cracked and subjected to tensile stresses, the load transfer was very low at this area. The load transfer reduction was indicated by an almost constant strain distribution along the tendon strain profile. A similar behaviour was observed between -3.4 and -5.6 m and it is believed that debonding between the tendon and the grout occurred in both areas;
- At the distal end of the anchor, a sharp strain decreased was observed, i.e. the load transfer was higher. At this area a large crack in the grout was identified and, below the crack, the grout was subjected to compressive stresses. Similar to the proximal end of the fixed length, the transition between tensile and compressive stresses in the grout led to high shear stress concentration in the tendon-grout interface.

Numerical simulations of the anchor pullout test were undertaken and compared with the measurements. The first simulation considered the HSsmall model for the soil layer where the anchor fixed length was located. The second simulation was carried out with the HSsmall model and the MMS_HV model for this soil layer. The numerical load-displacement curves were similar and showed stiffer behaviour than the in situ one. Due to soil softening reproduced by the MMS_HV model, the load-displacement curve of the second simulation indicated load decrease after peak.

Because the first simulations did not capture the load transfer decrease due to tensile cracks, additional simulations were undertaken where damaged grout clusters were manually activated. The load transfer decrease was accounted by decreasing the grout stiffness and, after the numerical refinements, the agreement between in situ measurements and numerical calculations improved. Despite that, development of shear stresses in the damaged grout was observed in the numerical simulations and, with increasing pullout load, the load transfer increased whereas the in situ one remained very low. The in situ cracking evolution was well captured by the Concrete model.

The skin friction obtained numerically showed that the MMS_HV model was able to reproduce the post-peak behaviour of overconsolidated soils. However, comparing the MMS_HV model with the HSsmall model, the differences observed with respect to the anchor load-displacement behaviour and to the strain distribution along the tendon were not pronounced.

6 St Kanzian-tests

6.1 Anchor description

The soil anchors were installed in late October 2017 and approximately one month later they were pulled out. Three types of anchors were installed:

- Type 1 – Conventional anchor and post-grouted;
- Type 2 – Jet grouted anchor;
- Type 3 – Jet grouted anchor with plate at the bottom.

The differences between the three types were the length of the fixed length, the grouted body diameter, the grouting technique and the load transfer mechanism between the tendon and the grout. Regarding anchor type 1, the fixed length was 8 m and was post-grouted. With respect to anchor type 2, the fixed length was 3 m and its diameter was increased before it was jet grouted. An additional anchor was considered for type 2 with a 6 m long fixed length. Anchor type 3 was also jet grouted but a plate was attached at the bottom of the fixed length. For this last anchor type, it was planned to install the debonding sleeves along the entire anchor length, thus compressing the grouted body at the fixed length. To enable the load transfer between the strands and the grout in type 3, a 2 m long Gewi bar was inserted in the centre of the anchor, at its distal end.

Except for the additional anchor type 2, 6 strands were used. For the additional type 2, 9 strands were employed. The borehole diameter was 178 mm. Two anchors were installed for each type, one monitored with a linear transducer at the anchor head and with fibre optic sensors and another only with the linear transducer. The monitored anchors with fibre optic sensors are referred herein with the letter “A” and the anchors monitored only with the linear transducer with the letter “B”. The additional anchor type 2 was only monitored with the linear transducer and is referred with the letter “C”. Tab. 7 summarizes the characteristics of each anchor type.

Tab. 7: Anchors characteristics

Anchor name	**Grouting**	**Fixed length**	**Monitoring system**
SK_1A	Post-grouted	8 m – 6 strands	Fibre optic: tendon and grout. Linear transducer
SK_1B	Post-grouted	8 m – 6 strands	Linear transducer
SK_2A	Jet grouted	3 m – 6 strands	Fibre optic: tendon and grout. Linear transducer
SK_2B	Jet grouted	3 m – 6 strands	Linear transducer
SK_2C	Jet grouted	6 m – 9 strands	Linear transducer
SK_3A	Jet grouted	3 m – 6 strands	Fibre optic: grout. Linear transducer
SK_3B	Jet grouted	3 m – 6 strands	Linear transducer

The distance between the anchors was 4 m and no group effect was expected. An overview of the anchors is shown in Fig. 29. Due to an error in the delivery of the debonding sleeves for the strands encapsulation, anchor type 3 was not installed as planned. The strands were not encapsulated along the entire length, but only at the free length. As a result, the differences between anchor types 2 and 3 were only the plate and the Gewi bar at the bottom, as shown in Fig. 29. Fig. 30 and Fig. 31 show, respectively, the installation and pullout test of anchor 1A. The anchors were pulled out after at least 30 days of the installation date.

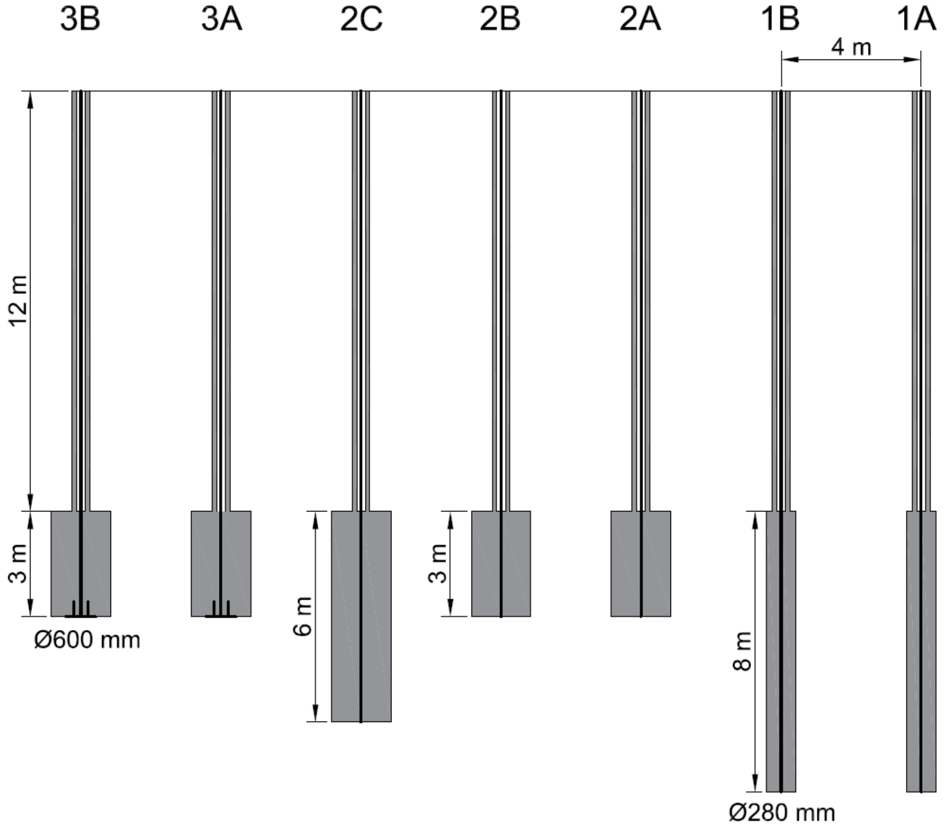

Fig. 29: Overview of the anchors in St Kanzian

Regarding anchor 1A, the diameter of the fixed length was estimated according to the volume of grout injected and was approximately 280 mm. The post-grouting pressure in this case varied between 20 and 60 bar. During post-grouting of anchor type 1B, the planned volume of grout was not fully applied and, instead of 300 L of grout, only 184 L were injected. The equivalent diameter of the fixed length for anchor type 1B was then 250 mm instead of 280 mm. The ground during installation of anchor types 2 and 3 was pre-cut with water and the diameter of the bond length was expected to be about 600 mm.

a) b)

Fig. 30: Anchor 1A – a) fibre optic sensors for grout measurements and b) anchor installation

Fig. 31: Pullout test of anchor 1A

6.2 Soil description and calibration

Prior to the anchor pullout tests, the oedometer stiffness at reference pressure was determined by calibrating it against laboratory oedometer tests, carried out in 2008 and 2009. Additionally, in situ testing such as seismic dilatometer test (sDMT) was undertaken in October 2017 and the shear wave velocity profile was also used for the estimation of the unloading/reloading stiffness at reference pressure and the small strain shear modulus. The shear wave velocity profile was also applied for determining the position of silty sand layers identified during the in situ test.

Following the pullout tests, additional soil samples were collected at the pullout tests area and oedometer tests, direct shear tests, grain size distribution and Atterberg limits were performed at the Graz University of Technology (TU Graz). The same tests were carried out at the University of Ljubljana, as well as a cyclic simple shear test with bender elements for the measurement of the soil shear wave velocity. The soil laboratory and in situ results are presented below.

6.2.1 Grain size distribution

The soil is a clayey, sandy silt locally known as Seeton and the grain size distribution is approximately 60-70% silt, 15-30% clay and 10-15% sand. The laboratory results are shown from Tab. 8 to Tab. 10. Silty sand layers were identified in the laboratory tests carried out in 2008-2009 and in the tests undertaken in 2018 at the TU Graz. These layers are marked with the colour grey.

Tab. 8: Grain size distribution – Laboratory tests conducted in 2008-2009

Seeton Klagenfurt		**Sample: 76-B34-08**			
		Depth (m)			
		11.2-11.6[1]	**17.0-17.4**	**20.0-20.4**	**24.4-24.8**
Grain Size (%)	**gravel**	1	0	0	0
	sand	58	15	2	11
	silt	39	68	72	73
	clay	2	17	26	16

[1]Silty sand soil

Tab. 9: Grain size distribution – Laboratory tests conducted in 2018 (TU Graz)

Seeton Klagenfurt		**Sample: 1A**					**Sample: 2A**		**Sample: 3B**	
		Depth (m)					**Depth (m)**		**Depth (m)**	
		10-11	**11-12**	**12-13**	**16-17**	**17-18**	**13-14**	**14-15[1]**	**14.9-15.2**	**15.2-15.5**
Grain Size (%)	**gravel**	-	-	2.9	-	-	2.8	6.6	0.2	-
	sand	12.3	17.0	9.9	10.9	11.2	22.2	52.1	12.3	19.0
	silt	61.2	70.5	64.7	60.0	64.3	62.3	36.8	62.6	61.5
	clay	26.5	12.5	22.5	29.1	24.5	12.7	4.5	24.9	19.5

[1]Silty sand soil

Tab. 10: Grain size distribution – Laboratory tests conducted in 2018 (University of Ljubljana)

Seeton Klagenfurt		**Sample: 1A**	
		Depth (m)	
		16.45-16.75	**17.50-17.75**
Grain Size (%)	**gravel**	-	-
	sand	10	17
	silt	66	58
	clay	24	25

The particle size determination performed in 2008-2009 followed ÖNORM CEN ISO/TS 17892-4:2005. The tests undertaken at the TU Graz were based on ÖNORM EN ISO 17892-4:2014. The grain size distribution carried out at the University of Ljubljana was in accordance with ISO 17892-4:2016.

6.2.2 Atterberg limits

The Atterberg limits are found between 28.0-35.5% (liquid limit - LL), 15.0-18.0% (plastic limit - PL) and 10.5-17.5% (plasticity index - PI). Only the sample 2A between 14.0-15.0 m, composed mainly by sand and analysed at the TU Graz, was out of this range. The results are presented from Tab. 11 to Tab. 13.

The determination of the Atterberg limits carried out in 2008-2009 and at the TU Graz followed ÖNORM B 4411:2008 and ÖNORM B 4411:2009, respectively. The tests undertaken at the University of Ljubljana were according to ISO 17892-12:2004.

Tab. 11: Atterberg limits – Laboratory tests conducted in 2008 - 2009

Seeton Klagenfurt		**Sample: 76-B34-08**		
		Depth (m)		
		17.0-17.4	**20.0-20.4**	**24.4-24.8**
Atterberg limits (%)	**LL**	28.0	33.0	28.5
	PL	15.0	15.5	15.5
	PI	13.0	17.5	13.0

Tab. 12: Atterberg limits – Laboratory tests conducted in 2018 (TU Graz)

Seeton Klagenfurt		**Sample: 1A**			**Sample: 2A**
		Depth (m)			**Depth (m)**
		10-11	**16-17**	**17-18**	**14.0-15.0**[1]
Atterberg limits (%)	**LL**	28.0	34.5	29.0	25.5
	PL	17.5	18.0	17.0	22.0
	PI	10.5	16.5	12.0	3.5

[1] Silty sand soil

Tab. 13: Atterberg limits – Laboratory tests conducted in 2018 (University of Ljubljana)

Seeton Klagenfurt		**Sample: 1A**	
		Depth (m)	
		16.45-16.75	**17.50-17.75**
Atterberg limits (%)	**LL**	29.0	28.0
	PL	16.0	15.0
	PI	13.0	13.0

6.2.3 Direct shear test

The results obtained from direct shear tests assuming the Mohr-Coulomb failure criterion are shown in Tab. 14. The friction angle varied between 24.5-35.5° and the cohesion intercept between 6-20 kPa.

The tests undertaken in 2008-2009 and at the TU Graz were based on ÖNORM B 4416:1978. The tests performed at the University of Ljubljana were in accordance with ISO/TS 17892-10:2004.

Tab. 14: Direct shear tests

Sample	**2008 - 2009**	**TU Graz - 2018**		**University of Ljubljana - 2018**	
	76-B34-08	**3B**		**1A**	
Depth (m)	**17.0-17.4**	**14.9-15.2**	**15.2-15.5**	**16.45-16.75**	**17.50-17.75**
φ’ (°)	29.4	35.5	29.5	24.5	30.0
c’ (kN/m^2)	10	6.1	19.7	14	11

6.2.4 Oedometer test

The results from oedometer tests and the numerical calibrations are presented below. The calibrations were performed using the Plaxis SoilTest tool (Brinkgreve et al. 2017a) and the HSsmall model. Tab. 15 shows the values of the reference stiffness after calibration with laboratory oedometer tests that were carried out in 2008-2009. Tab. 16 shows the parameters obtained after calibration against oedometer tests performed at the TU Graz and Tab. 17 presents the values obtained after calibrating the model with laboratory results from the University of Ljubljana. The calibrated parameters for the sample located between 24.4 and 24.8 m (Fig. 32) and shown in Tab. 15 ($E_{oed,ref}$, $E_{50,ref}$ and m) were employed for the numerical predictions of the pullout tests. These parameters were assigned to the Seeton material.

The oedometer tests undertaken in 2008-2009 and at the TU Graz were according to ÖNORM B 4420:1989. The tests carried out at the University of Ljubljana followed ISO/TS 17892-5:2004.

Tab. 15: Oedometer tests – Laboratory tests conducted in 2008 - 2009

Sample	**76-B34-08**	
Depth (m)	**20.0-20.4**	**24.4-24.8**
$E_{50,ref}$ (kN/m²)	4375	6625[1]
$E_{oed,ref}$ (kN/m²)	3500	5300[1]
$E_{ur,ref}$ (kN/m²)	12 500	19 200
m	1	0.9[1]
$G_{0,ref}$ (kN/m²)	20 900	32 000

[1] Parameters employed for the numerical predictions

Tab. 16: Oedometer tests – Laboratory tests conducted in 2018 (TU Graz)

Sample	**1A**			**2A**	**3B**	
Depth (m)	10.60-10.62	16.24-16.26	17.34-17.36	14.60-14.62[1]	14.94-14.96	15.42-15.44
$E_{50,ref}$ (kN/m²)	6625	7550	6250	16 000	6750	6875
$E_{oed,ref}$ (kN/m²)	5300	6200	5000	16 000	5400	5500
$E_{ur,ref}$ (kN/m²)	25 000	25 000	20 000	32 000	20 000	20 000
m	0.9	0.9	0.9	0.6	0.9	0.9
$G_{0,ref}$ (kN/m²)	62 500	62 500	50 000	80 000	50 000	50 000

[1] Silty sand soil

Tab. 17: Oedometer tests – Laboratory tests conducted in 2018 (University of Ljubljana)

Sample	**1A**	
Depth (m)	**16.45-16.75**	**17.50-17.75**
$E_{50,ref}$ (kN/m²)	5250	4375
$E_{oed,ref}$ (kN/m²)	4200	3500
$E_{ur,ref}$ (kN/m²)	25 000	20 000
m	1	1
$G_{0,ref}$ (kN/m²)	62 500	50 000

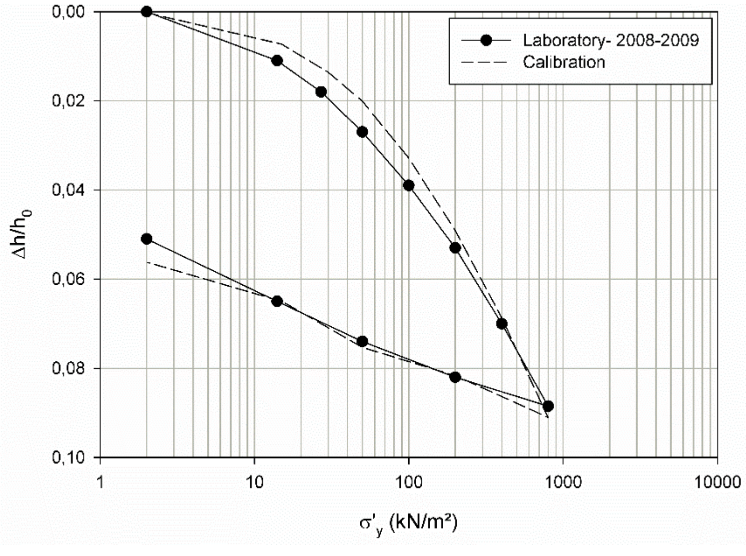

Fig. 32: Oedometer test calibration (2008-2009, 24.4-24.8 m depth)

6.2.5 Seismic dilatometer test

The shear wave velocity distribution (V_S), the material index (I_D) and the constrained modulus (M) over depth are shown in Fig. 33. The silty sand layers identified during the core drilling were also observed with the sDMT, as indicated by the material index I_D (Fig. 33b). I_D values larger than 1.8 suggest sandy materials, values between 0.6 and 1.8 designate silty materials, and I_D values smaller than 0.6 indicate clayey materials (Marchetti 1980). In Fig. 33b, one can notice that I_D values obtained for the Seeton suggest a clayey material and not a silty material, although the grain size distribution indicates about 60-70% silt. Due to the partial drainage of the clayey silt material, excess pore pressure dissipation occurs during the penetration phase and the membrane expansion, thus reducing DMT pressure readings in comparison to measurements performed during DMT tests in soils that show fully undrained response (Schnaid et al. 2018). The constrained modulus M is a DMT correlation that depends on soil type and stress history. In Fig. 33c this modulus varies from about 2 to 5 MPa within the Seeton material. However, the partial drainage has to be taken into account when estimating stiffness parameters from DMT readings and therefore a careful interpretation is necessary.

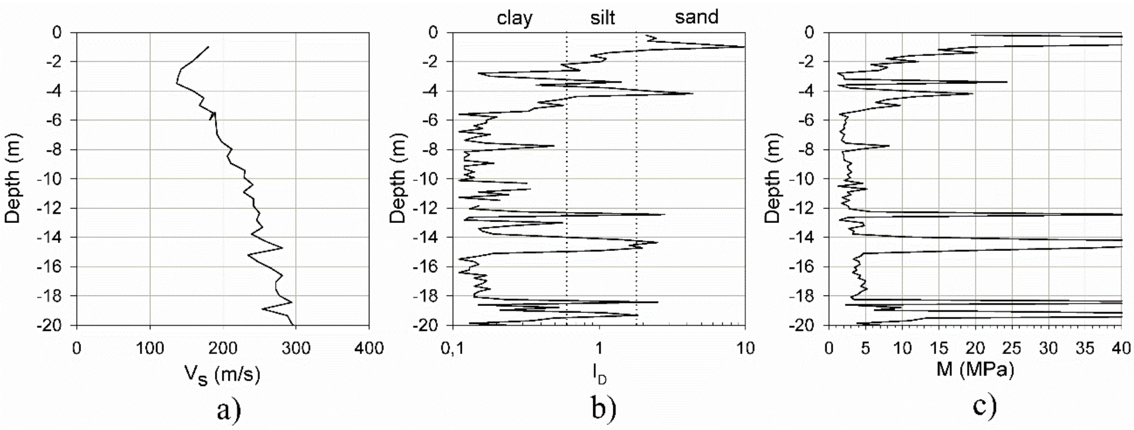

Fig. 33: sDMT results – a) shear wave velocity; b) material index and c) constrained modulus

Regarding the small-strain shear modulus (G_0), it was determined based on the measured shear wave velocity distribution during the sDMT. G_0 is related to the shear wave velocity (V_S) according to Eq. 4, where ρ is the material bulk density:

$$G_0 = \rho V_S^2 \tag{4}$$

G_0 was calibrated in Plaxis 2D 2017 by determining V_S along depth according to Eq. 4 and comparing the numerical V_S profile with the in situ one. For this calibration, the same soil layers considered in the numerical simulations of the pullout tests were assumed and the position of the silty sand layers was selected based on the material index (Fig. 33b). The soil constitutive model was the

HSsmall model. The soil bulk density was determined during the sDMT and was approximately 1.7 g/cm³. The shear wave velocity calibration is shown in Fig. 34. Although the in situ shear wave velocity was lower within the first 10 m depth, in the last 10 m, where the anchor fixed length was located, the agreement improved.

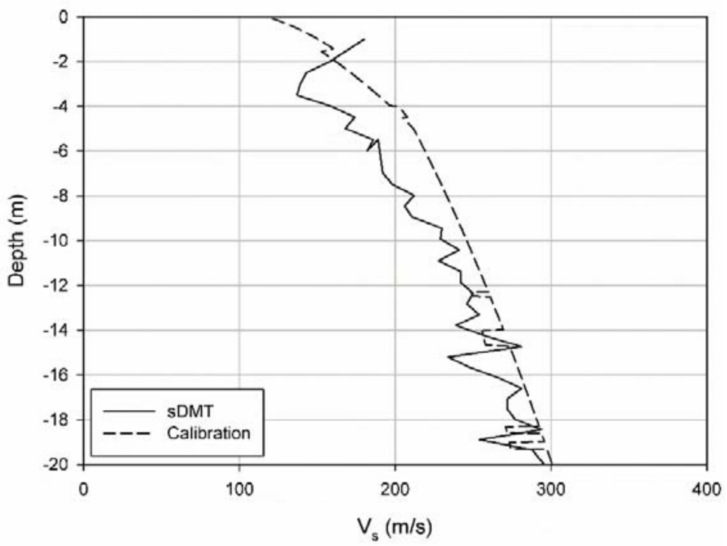

Fig. 34: Calibration of the shear wave velocity profile

For the Seeton material, based on experience from similar ground conditions, the unloading/reloading shear modulus was adopted as $G_{ur,ref} = G_{0,ref}/6$ and $E_{ur,ref}$ was then back calculated, leading to $E_{ur,ref} \approx 9E_{oed,ref}$. Because the silty sand layers showed similar shear wave velocity distribution, the reference small-strain shear modulus $G_{0,ref}$ for these layers was kept the same as for the Seeton material. The unloading/reloading shear modulus was assumed as $G_{ur,ref} = G_{0,ref}/4$ for the silty sand soil layers.

6.2.6 Bender element test

Bender element tests were undertaken at the University of Ljubljana. The shear wave velocities were measured after the specimen consolidation (K_0 consolidation), for the effective vertical stresses of about 50 kPa, 100 kPa and 200 kPa. The comparison between laboratory results, numerical calibration and in situ results is shown in Tab. 18. In order to compare the numerical and in situ values with the laboratory tests, the values were selected for the same vertical stresses applied during the sample consolidation. The soil unit weight was assumed as 21 kN/m³ and the water table was considered at 5 m depth.

Tab. 18: Shear wave velocity – comparison

	University of Ljubljana						**In situ sDMT**			**Numerical calibration**		
Sample	**1A**											
Depth (m)	**16.45-16.75**			**17.50-17.75**								
σ' (kPa)	53	109	214	53	108	213	53	111	212	53	109	214
V_s (m/s)	193	220	275	172	217	278	143	186	281	172	215	275

The sample corresponding to the depth 16.45-16.75 m showed higher shear wave velocity than the sample collected at 17.50-17.75 m for the 53 kPa consolidation stage. The shear wave velocity obtained at this stage also showed the highest deviation in comparison with the in situ and the numerical values. Nevertheless, the laboratory values showed very good agreement with the in situ and numerical values.

6.2.7 Soil parameters employed in the numerical simulations

Tab. 19 shows the parameters assumed before the pullout tests (numerical predictions) and after the tests (numerical refinements). The parameters adopted before the pullout tests were based on the soil investigations carried out in 2008-2009 and on the sDMT. The vales assumed after the pullout tests also took into account the laboratory tests undertaken in 2018.

Due to the good agreement between the previous and the new laboratory tests, the Seeton parameters were not modified. The unloading/reloading stiffness and the small strain shear modulus were determined based on the sDMT. Because previously no data of the silty sand layers was available, the parameters of this material were changed after the tests carried out in 2018.

Tab. 19: Previous and new soil parameters (HSsmall model, Seeton and silty sand)

Parameter	**Seeton**	**Sand**	
	Parameters were not modified	**Prediction**	**Refinement**
$E_{50,ref}$ (kN/m²)	6625	24 000	16 000
$E_{oed,ref}$ (kN/m²)	5300	24 000	16 000
$E_{ur,ref}$ (kN/m²)	48 000	72 000	48 000
c' (kN/m²)	10	5	5
φ' (°)	29.4	35	35
m	0.9	0.6	0.6
$G_{0,ref}$ (kN/m²)	120 000	120 000	120 000
$\gamma_{0.7}$	0.15e-3	0.15e-3	0.15e-3

6.3 Grout laboratory results

During the installation of the anchors, cement samples were prepared for laboratory experiments. Three samples were sent to the Graz University of Technology (Institute of Rock Mechanics and Tunnelling) with the cement used for primary grouting and post-grouting of anchor type 1. The density of the freshly mixed cement measured in situ with an areometer was 1.75 kg/L and the back-calculated water-cement ratio was approximately 0.6. This grout material is referred as the “conventional grout”. Another 3 samples were sent to the Brno University of Technology (Faculty of Civil Engineering) with Soiljet binder used during the installation of the jet grouted anchors (types 2 and 3). The water-cement ratio was about 0.6.

The laboratory results obtained at the TU Graz and at the Brno University of Technology are shown below. The samples were tested after about 28 days of curing time and the laboratory results were available only after the pullout tests. Therefore, the calibrated parameters were employed for the numerical refinements of the tests and not for the numerical predictions. The uniaxial compression tests and the splitting tensile tests were executed in accordance with ÖNORM EN 12390-3:2012 and ÖNORM EN 12390-6:2010, respectively.

Softening is a size-dependent phenomenon and it has been extensively studied by means of fracture mechanics (Bažant & Oh 1983; Van Mier 1984; Bažant 1986; Vonk 1992). In this respect, the tensile and the compressive fracture energies (G_t and G_c, respectively) are dependent on the size of the specimens and extrapolations of laboratory results to large structures must be performed with care. For this reason, the post-peak behaviour was not calibrated against the laboratory tests and the post-peak parameters were assumed based on literature and on the evaluation of the in situ fibre optic measurements.

6.3.1 Conventional grout

Displacement-controlled uniaxial compression test (UCS) and multistage triaxial test (MST) were carried out. The laboratory tests were numerically calibrated in order to estimate the Concrete model parameters and the calibrations are shown in Fig. 35. The calibration of the multistage triaxial test was undertaken only for the first stage of the test ($\sigma_3 = 2.0$ MPa). The Mohr-Coulomb shear strength parameters obtained were a friction angle of 48° and a cohesion intercept of 6 MPa. The calibrated parameters are presented in Tab. 20.

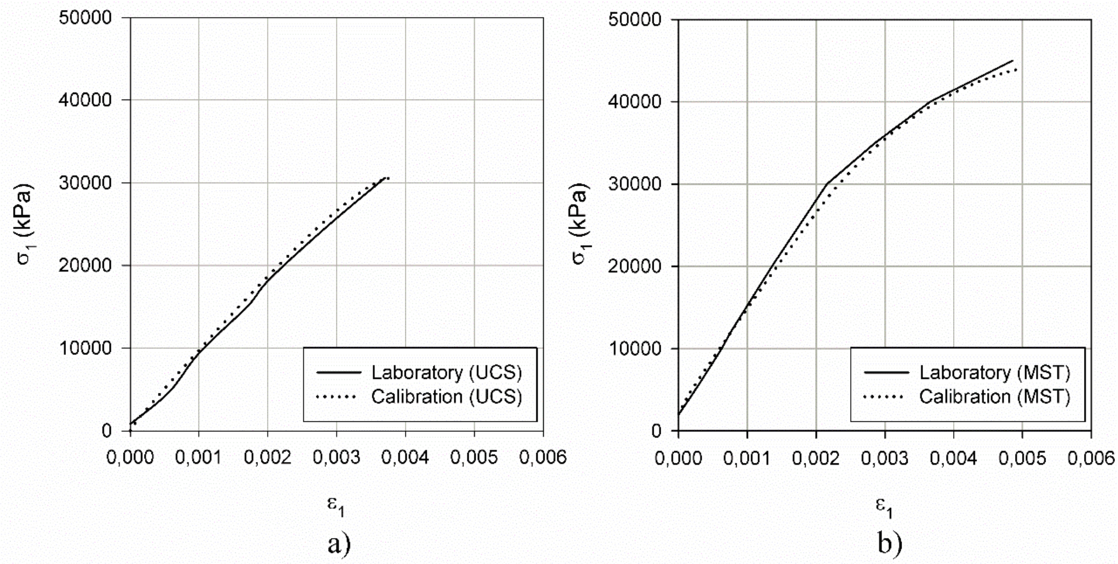

a) b)

Fig. 35: Numerical calibration against laboratory tests (conventional grout) – a) uniaxial compression test and b) multistage triaxial test

Tab. 20: Conventional grout parameters after calibration (Concrete model)

Parameter	**Value**	
	UCS	**MST**
E (kPa)	12.2E6	16.5E6
f_c (kPa)	30.58E3	32E3
f_{c0n}	0.05	
f_{cfn}	0.95	
a	19	
φ_{max} (°)	48°	
ε_{cp}^{p}	-1.3e-3	

Uniaxial tensile tests are the most direct method of tensile strength and fracture energy determination. However, these tests are difficult to execute reliably and therefore two indirect splitting tensile tests were carried out. The measured grout tensile strengths were 1.0 MPa and 1.2 MPa. It is important to mention that some judgement is required when defining the input parameters for the model. Some authors report that the tensile strength obtained from splitting tensile tests is lower than the strength obtained from direct tests (Berenbaum & Brodie 1959; Lin & Wood 2003), and a tensile strength of 1.5 MPa was adopted for the numerical refinement.

The fracture energy in tension was assumed herein as 0.01 kN/m and, after numerical evaluation of the crack development along the grout, this value matched well with the in situ measurements. The fracture energy in compression was adopted as 3 kN/m. However, due to the fact that the grout at the fixed length is subjected mainly to tensile stresses, G_c has little effect on the results in this particular case.

6.3.2 Jet grout

The uniaxial compressive strength (f_c) and the peak friction angle (φ_{max}) were taken directly from the laboratory results and were 21.1 MPa and 18°, respectively. The remaining parameters were calibrated with the Concrete model as presented in Fig. 36 and Fig. 37. The parameters are shown in Tab. 21.

Fang et al. (1994) performed laboratory tests in jet grout specimens mixed with silty sand and clay soils and obtained similar values for the uniaxial compressive strength (varying from about 5 MPa to 24 MPa) and Young's Modulus (from 1.0 to 6.5 GPa). The tensile strength obtained by the authors varied from 0.4 to 1.7 MPa and the friction angle was 35° for the silty sand and 40° for the clay. Toraldo et al. (2018) summarized the strength parameters found in the literature for jet grout material after it was mixed with soil, and the friction angle varied from 25° to 58°, depending on the soil and cement types, the density of the specimen, etc.

The tensile strength of the jet grout was set as 700 kPa. For a jet grout material, the fracture energy in tension depends not only on cement type and on cement content, but also on soil type and content. Lee (2014) studied the post-peak behaviour of a cement-treated Singapore marine clay and obtained G_t values between 0.0026 N/m and 0.0044 kN/m, for a cement content between 20 and 40%. However, it is important to mention that for the jet grouted anchors, the fixed length was pre-cut with water so that the final material was composed mainly by cement. Schweiger et al. (2014) suggest values for G_t between 0.01 to 0.05 kN/m for jet grout material. Therefore, the tensile fracture energy was assumed as 0.015 kN/m and the compressive fracture energy was adopted as 4.2 kN/m.

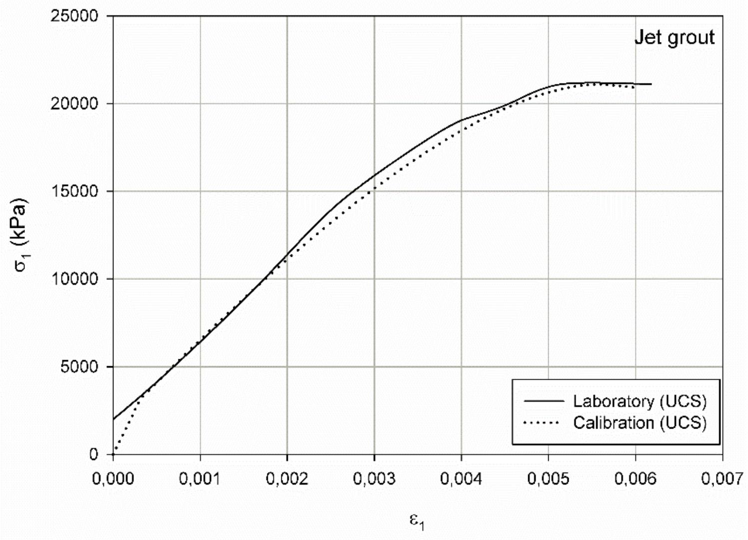

Fig. 36: Numerical calibration against uniaxial compression test (jet grout)

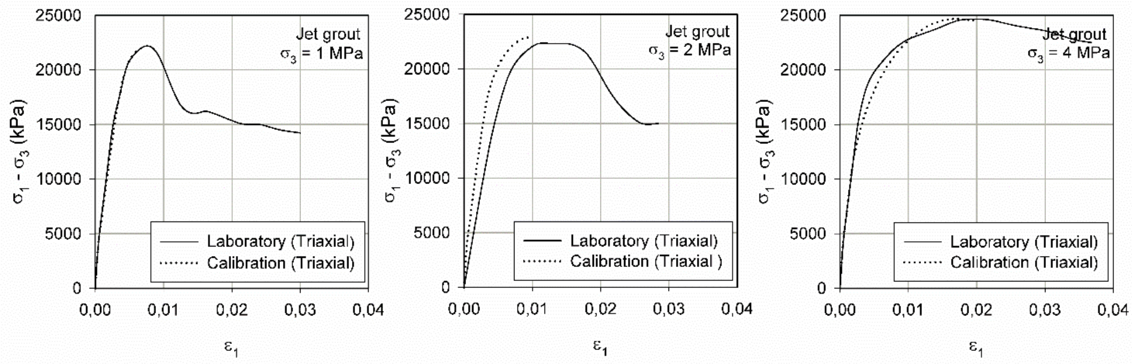

Fig. 37: Numerical calibration against triaxial tests (jet grout)

Tab. 21: Jet grout parameters after calibration (Concrete model)

Parameter	**Value**
E (kPa)	10E6
f_c (kPa)	21.1E3
f_{c0n}	0.15
f_{cfn}	0.95
a	19
φ_{max} (°)	18
ε_{cp}^{p}	-0.0035

6.3.3 Grout parameters employed in the numerical simulations

The parameters assumed in the numerical simulations carried out before the pullout tests and after refinement are presented in Tab. 22. Whilst before the calibration the jet grout parameters were assumed the same as the conventional grout, after the laboratory results distinction was made between both grout materials.

Tab. 22: Previous and new grout parameters (Concrete model, grout)

Parameter	**Previous grout parameters**	**New grout parameters – conventional grout**	**New grout parameters – jet grout**
E (kPa)	16 260 000	15 500 000	7 000 000
ν	0.20	0.20	0.20
f_c (kPa)	32 120	30 600	15 000
f_t (kPa)	2000	1500	700
f_{c0n}	0.15	0.05	0.15
f_{cfn}	0.95	0.95	0.95
f_{cun}	0.10	0.10	0.10
ε_{cp}^{p}	-0.0035	-0.0013	-0.0035
G_c (kN/m)	50	3	4.2
f_{tun}	0.05	0.05	0.05
G_t (kN/m)	0.15	0.01	0.015
a	16	19	19
φ_{max} (°)	40	48	18

The Young's modulus and the compressive strength of the jet grouted anchor were assumed as 70% of the original calibrated values shown in Tab. 21. This is justified by the fact that during its application the grout was mixed with soil and the cement samples were prepared without soil.

6.4 In situ pullout tests results

6.4.1 Load-displacement curves

The monitored load-displacement curves, considering the tendon end displacements, are presented from Fig. 38 to Fig. 44. The dashed line shows the load step at which the creep rate was larger or equal to 2 mm, which was not observed during the pullout test of anchor 2C. It is worth noting that, regarding anchor 3A, after the unloading step of 400 kN an additional load step of 700 kN was undertaken before the end of the test. However, before this load step the creep was very high and, at the 700 kN load step the anchor displacement was already above 200 mm. For this reason, the load-displacement curve in Fig. 43 is plotted with and without the 700 kN load step.

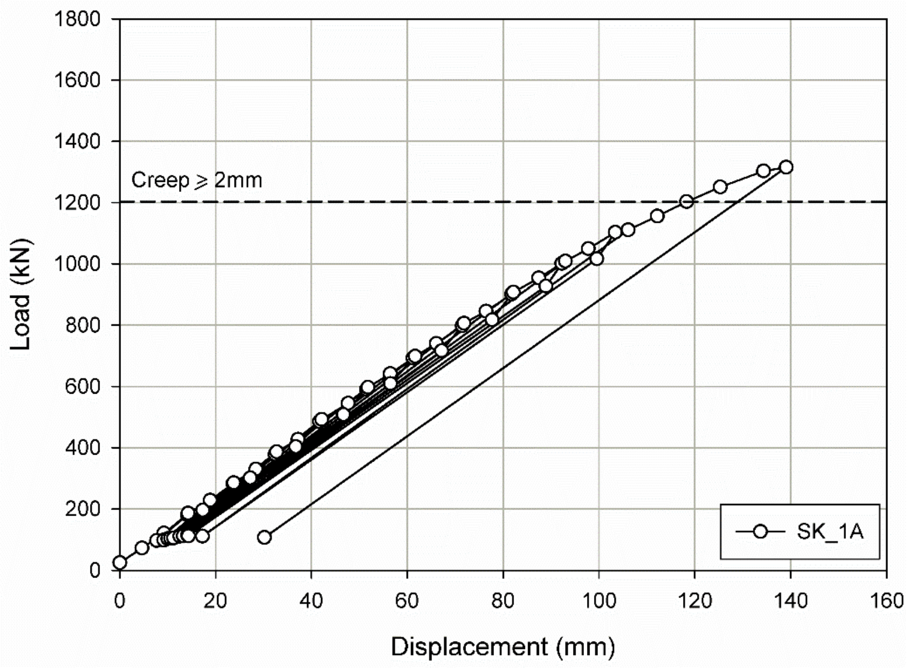

Fig. 38: Load-displacement curve (tendon end displacements) - anchor 1A

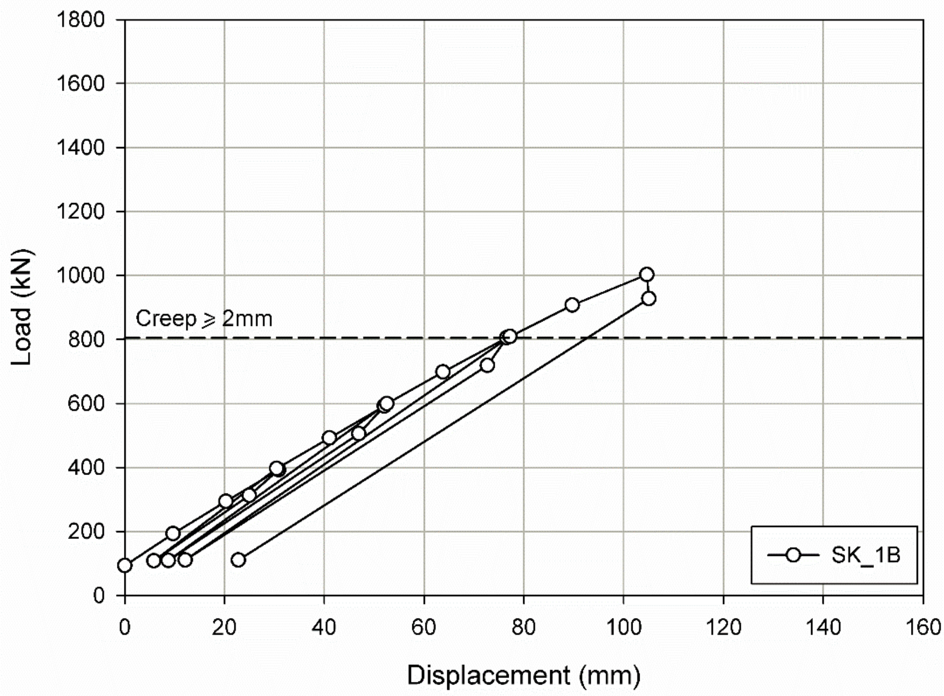

Fig. 39: Load-displacement curve (tendon end displacements) - anchor 1B

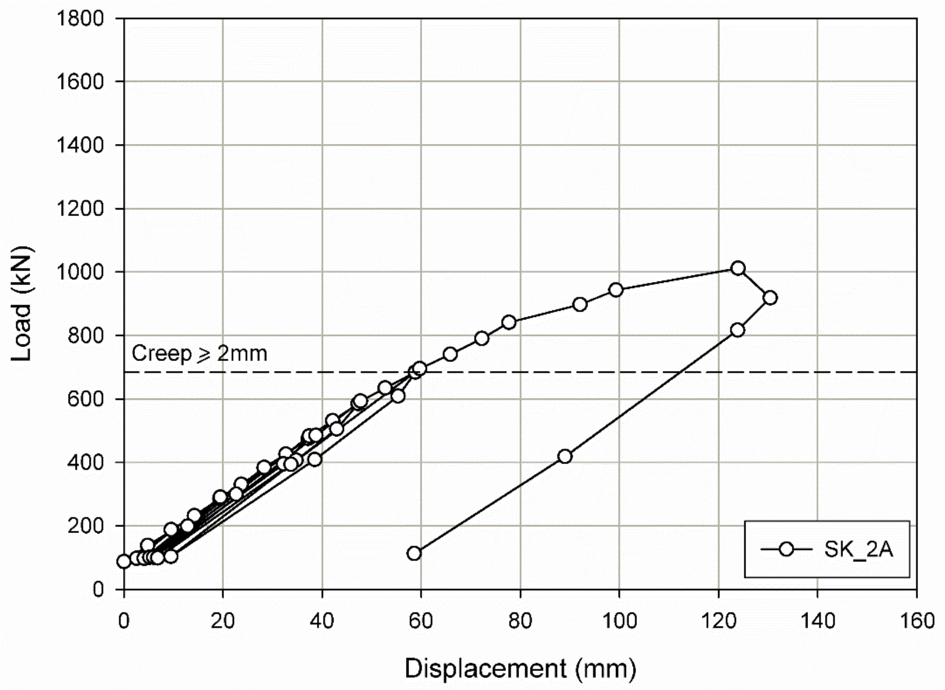

Fig. 40: Load-displacement curve (tendon end displacements) - anchor 2A

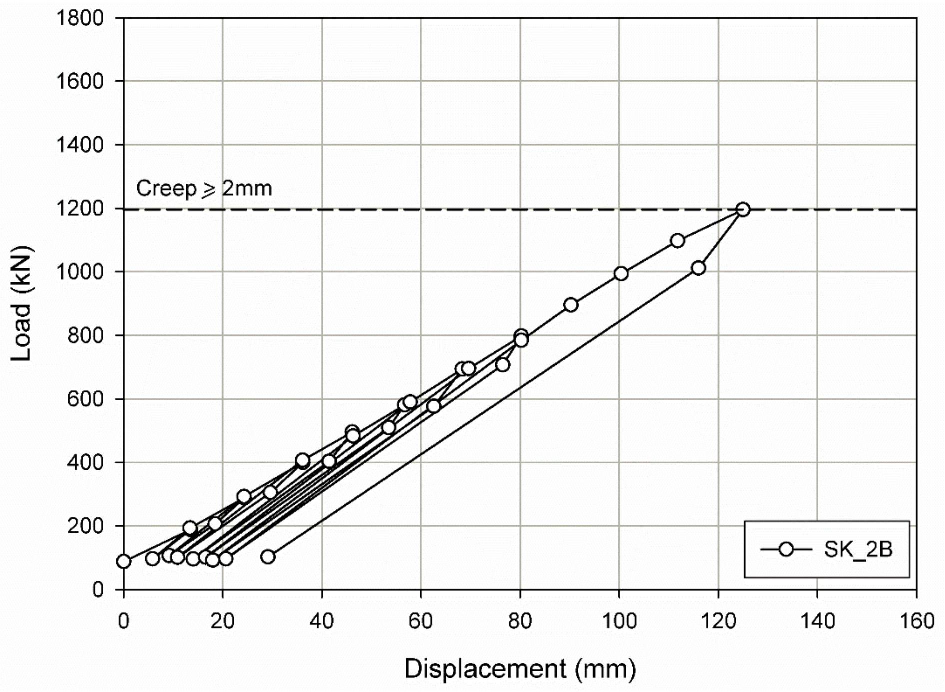

Fig. 41: Load-displacement curve (tendon end displacements) - anchor 2B

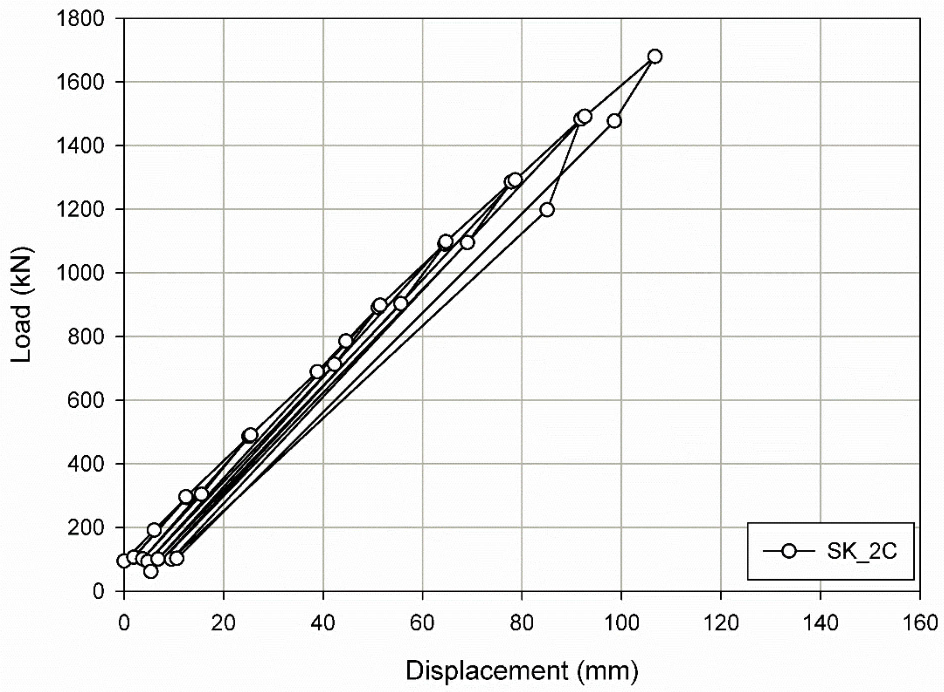

Fig. 42: Load-displacement curve (tendon end displacements) - anchor 2C

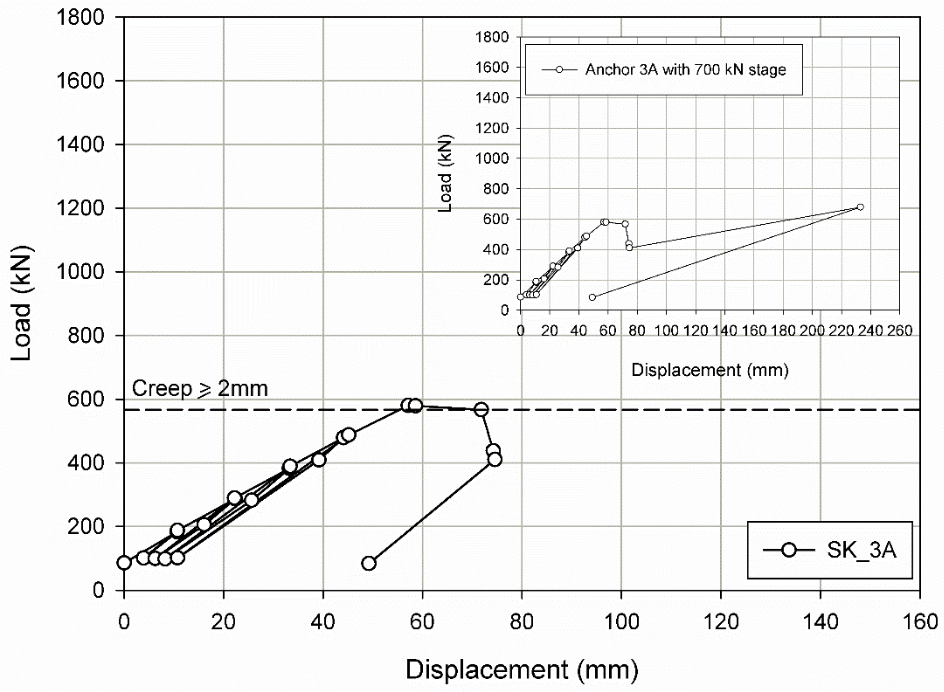

Fig. 43: Load-displacement curve (tendon end displacements) - anchor 3A

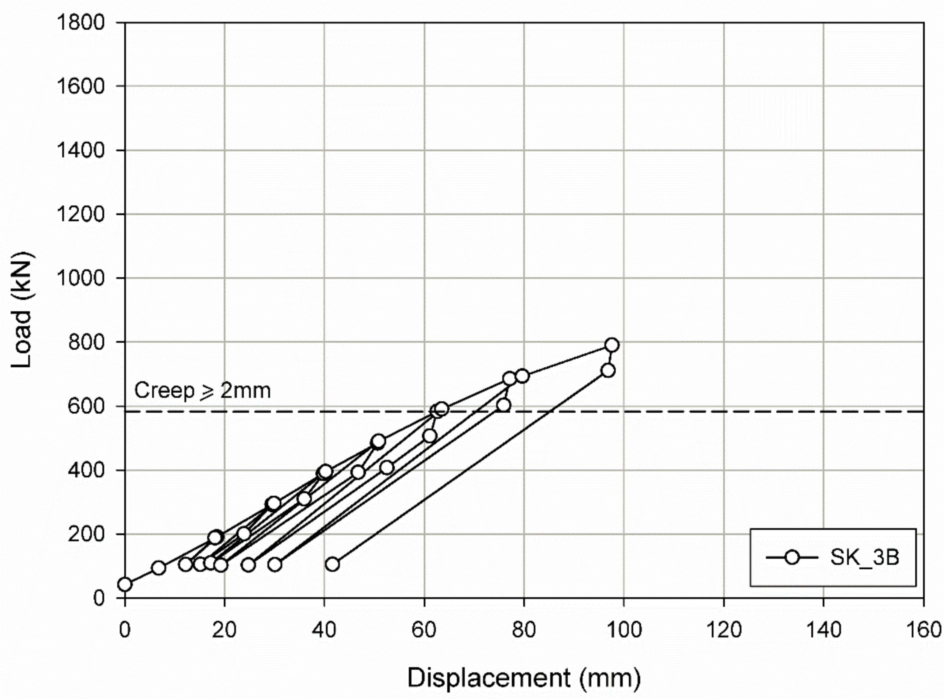

Fig. 44: Load-displacement curve (tendon end displacements) - anchor 3B

The load-displacement curves considering the displacements at the top of the fixed length are shown from Fig. 45 to Fig. 48. Unloading and reloading steps are not depicted. The horizontal bars plotted in these figures show the displacement values if the creep rate is subtracted from the displacement. The in situ measurements showed different behaviour for every anchor, even for the same anchor type. This can be explained by inhomogeneities in the grout or in the soil. In the particular case of anchor type 1B, which showed softer behaviour and lower ultimate capacity in comparison to anchor type 1A, the post-grouting was not satisfactorily applied and the volume of grout initially planned was not injected.

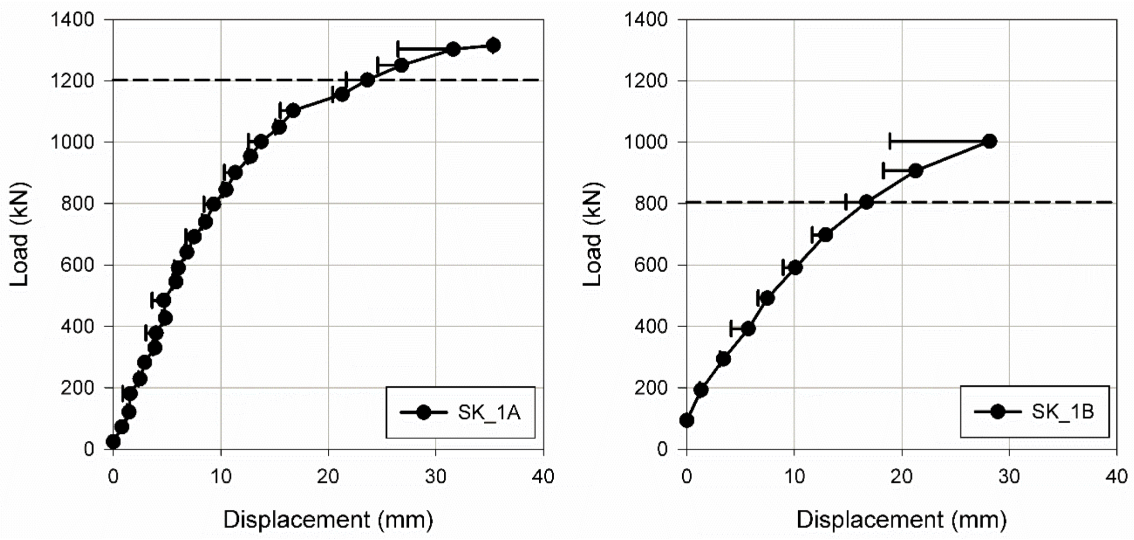

Fig. 45: In situ load-displacement curves (types 1A and 1B)

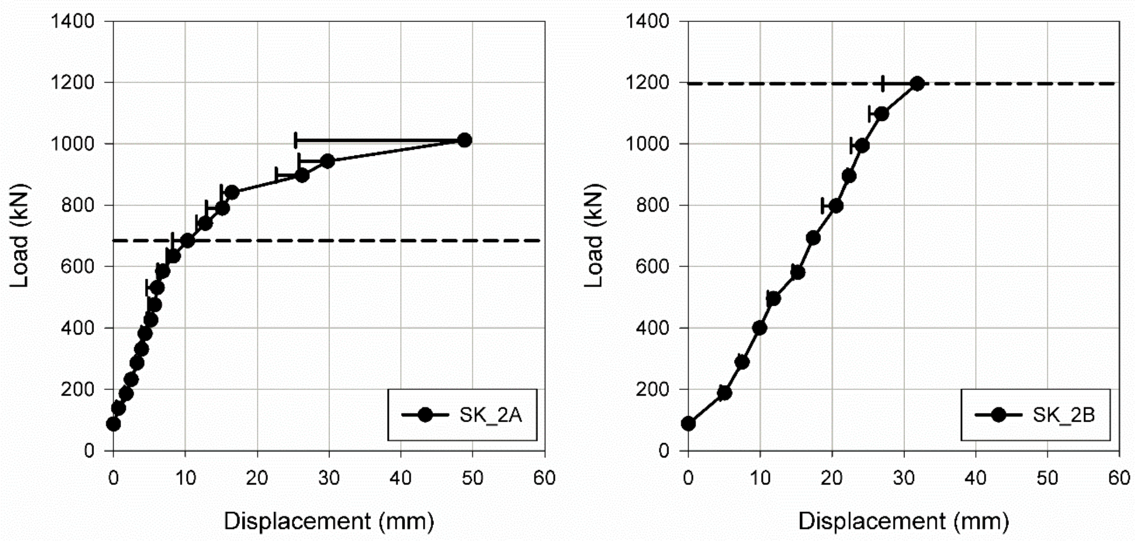

Fig. 46: In situ load-displacement curves (types 2A and 2B)

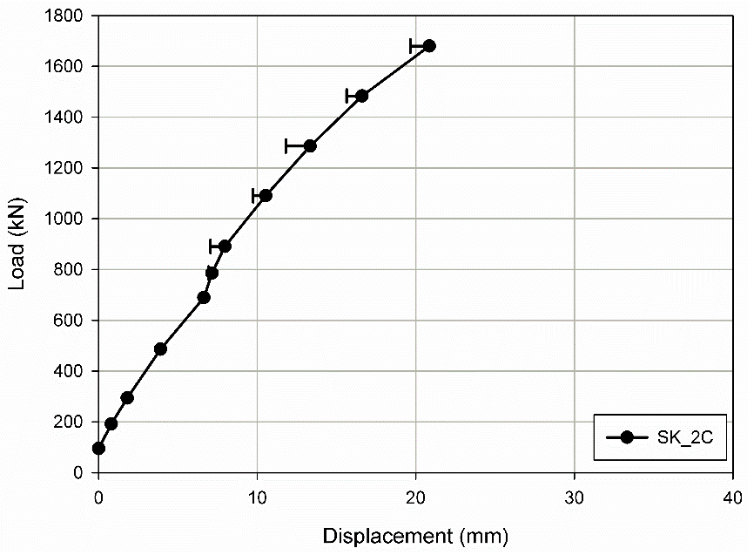

Fig. 47: In situ load-displacement curve (type 2C)

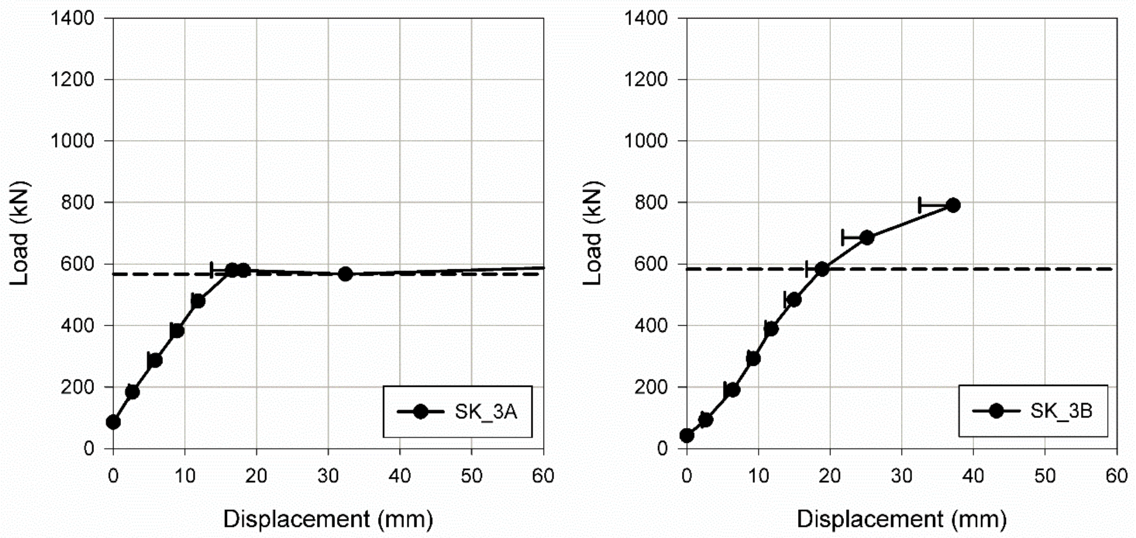

Fig. 48: In situ load-displacement curves (types 3A and 3B)

Regarding anchor type 3, both in situ results showed softer behaviour in relation to anchor types 2A and 2B. This was somehow unexpected, since the differences between them were the plate and the Gewi bar employed in type 3 and, for this reason, a stiffer behaviour was expected. Anchors 3A and 3B showed similar behaviour up to the sudden failure of the anchor 3A. It is believed that structural failure occurred in this case, possibly due to high stress concentration between the plate and the bottom of the grout or to insufficient steel-grout bonding.

6.4.2 Fibre optic strain measurements

Anchor 1A

The free length was 12 m and the fixed length was 8 m long. Regarding the measurements carried out along the tendon, only the results of one strand are presented because both measurements were very similar. Due to the fact that cracks in the grout are easier distinguished with the thin fibre results, only these measurements are shown. The strains along the tendon and the grout are shown in Fig. 49 and Fig. 50. The strains are relative values, i.e. the values are relative to the initial load of 25 kN, which was the “zero” measurement.

The development of the transition zone is very clear and the slope of the strain profile within this zone along the tendon fixed length is maximum with respect to the vertical axis. At the ultimate capacity of 1200 kN almost the entire tendon is activated and the grout is cracked along 6 m below the proximal end of the fixed length. The different grout conditions and their effect on the strain distribution along the tendon are presented in Fig. 51 for the 485 and 1000 kN load steps.

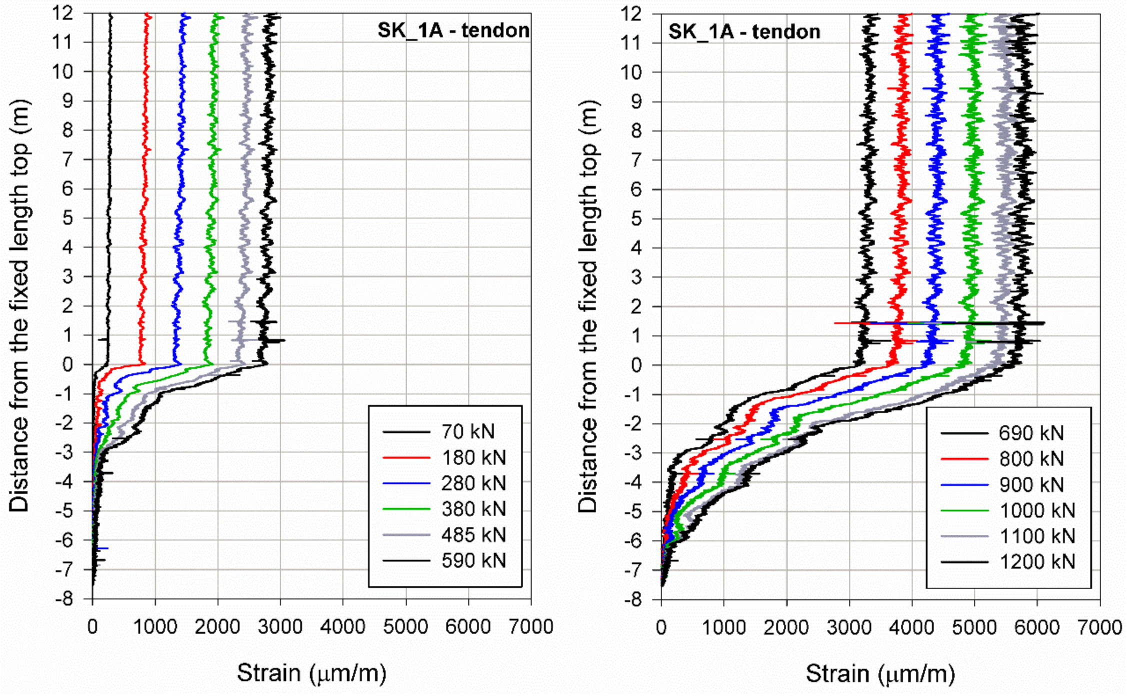

Fig. 49: Strains along the tendon (anchor 1A)

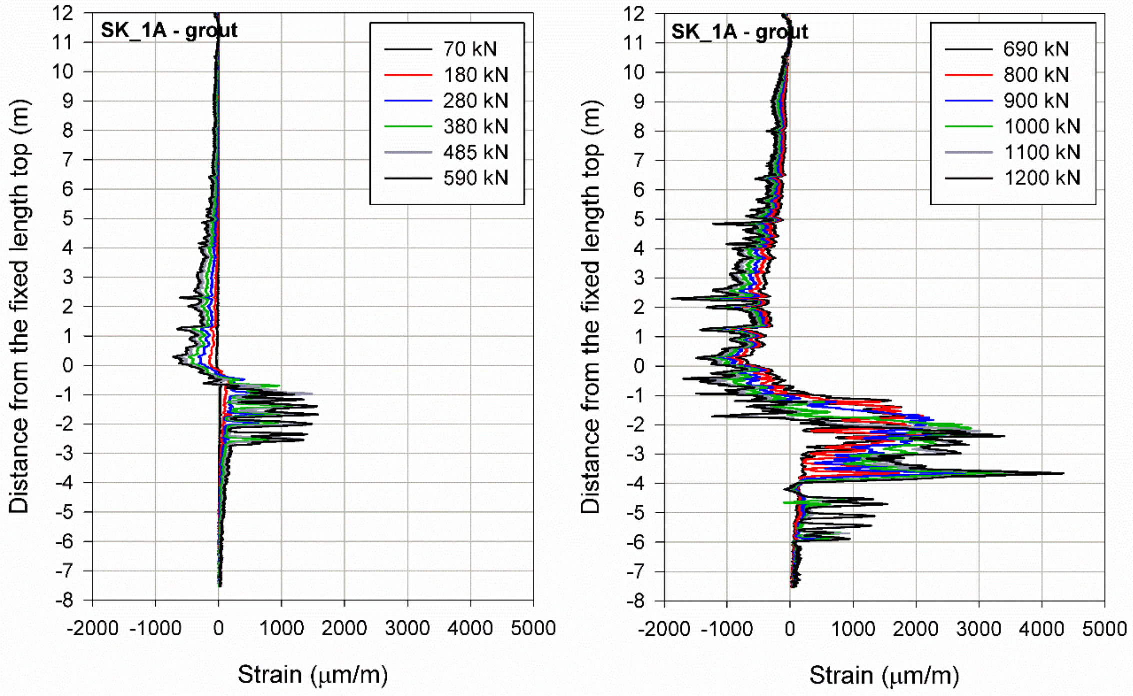

Fig. 50: Strains along the grout (anchor 1A)

At 1000 kN, the same phenomenon as observed during the Söding-test was noticed for anchor 1A: a large crack develops at -3.7 m and compressive strains are measured below the crack. In this case, however, compressive strains do not spread significantly and are observed only locally at about -4.2 m.

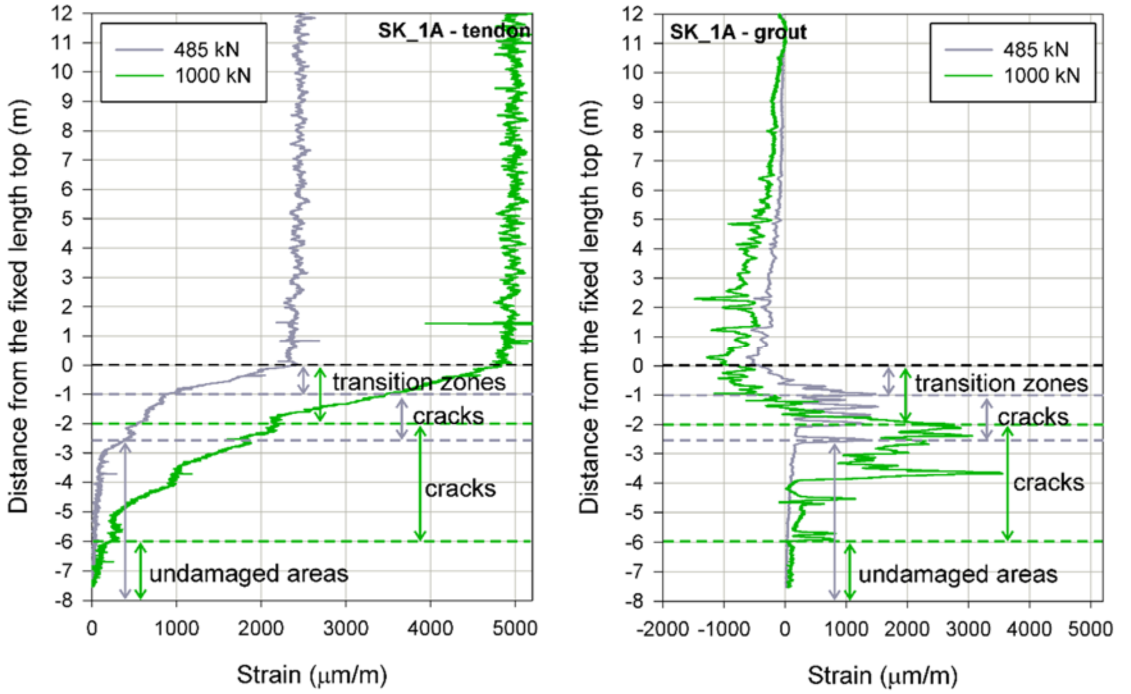

Fig. 51: Strain distribution along the tendon and the grout (anchor 1A) – different grout conditions

Through the fibre optic strain profile along the tendon, it is possible to determine the shear stress distribution in the grout-soil interface. For this purpose, the force was calculated for every 40 cm and the difference between the force values was divided by the circumference area of the grouted body. This is however an approximation because it neglects local effects of the load transfer through the grout. The skin friction along the fixed length is shown in Fig. 52.

As expected, the shear stress increases with increasing load step and, for a certain load, the stress is maximum at the proximal end of the fixed length, within the transition zone. It is however important to mention that the procedure employed for calculating the skin friction leads to high shear stress in this area due to the stress concentration in the tendon. As shown in Fig. 4, this stress concentration effectively takes place in the tendon-grout interface but, in the grout-soil interface, the actual skin friction is distributed along the front part of the grouted body (Ostermayer & Scheele 1978).

The shear stress drops with crack development, leading to a non-uniform distribution of shear stress in the grout-soil interface. From 900 kN onwards, the maximum shear stress moves from the top of the fixed length to approximately 1.8 m below it. Although it is recognised that the shear stress distribution along the fixed length of a ground anchor is non-uniform (Ostermayer & Scheele 1978; Littlejohn 1980; Ostermeyer & Barley 2003), it is common practice to assume uniformly distributed shear stresses along the grout-soil interface at the fixed length.

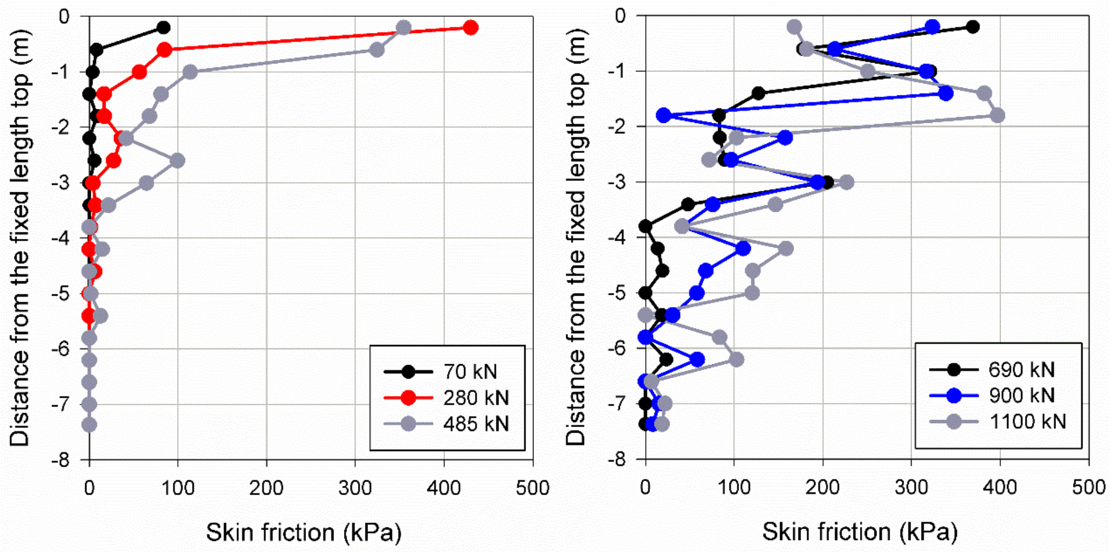

Fig. 52: Shear stress along the grout-soil interface at the fixed length (anchor 1A)

Anchor 2A

The fibre optic measurements along the tendon and the grout for anchor 2A are presented below. The free length is located within the first 12 m and the fixed length in the last 3 m. Because the strain profiles were different for the measurements performed along the strands, both monitored data are shown (Fig. 53 and Fig. 54). The "zero" measurement was 90 kN and the pullout loads are relative to this initial load step.

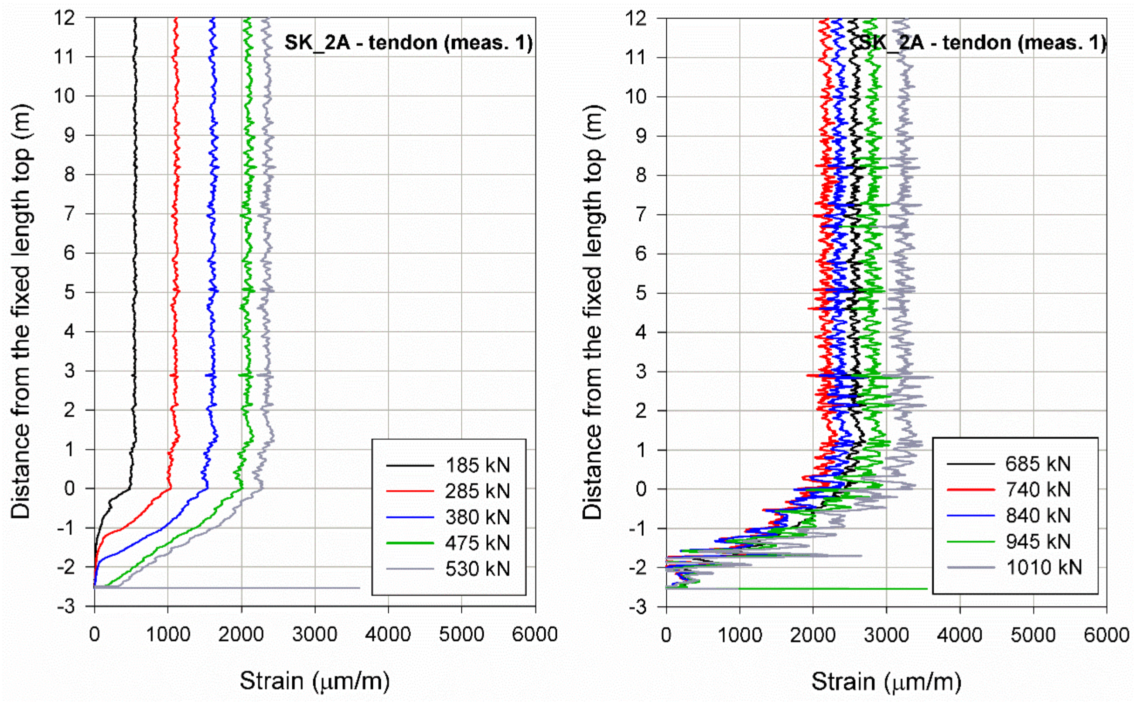

Fig. 53: Strains along the tendon (anchor 2A – measurement 1)

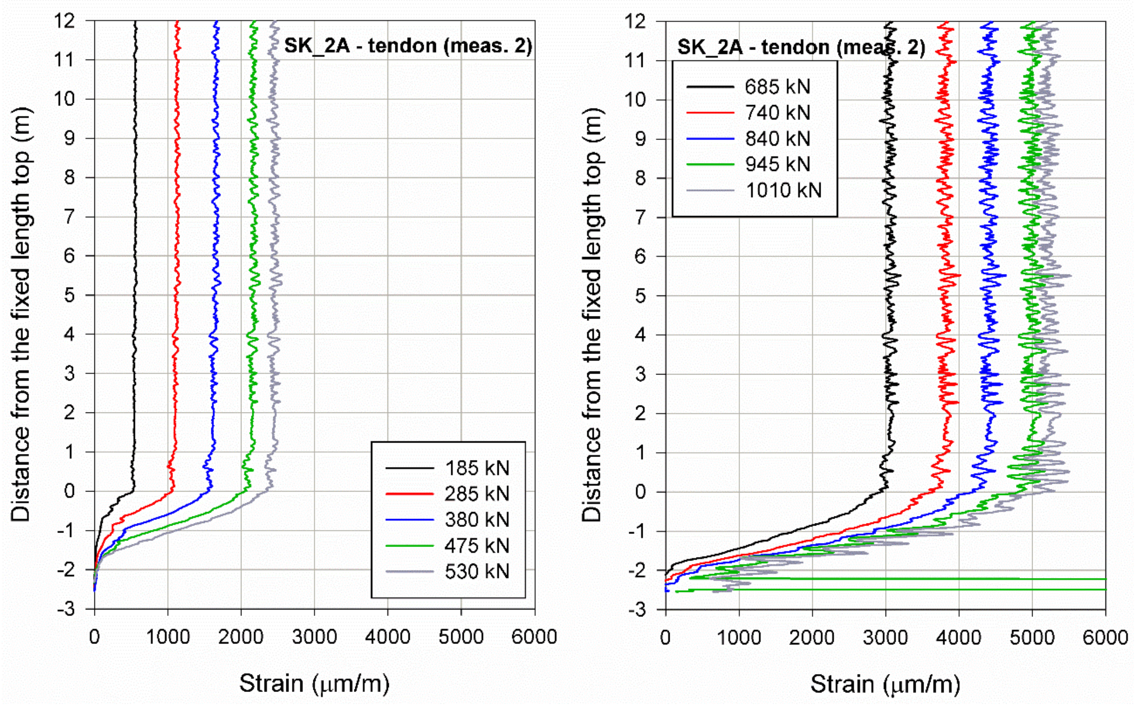

Fig. 54: Strains along the tendon (anchor 2A – measurement 2)

After 530 kN and considering measurement 1, the pullout load at this strand reduces and then increases again. It is important to mention that although the load at the strand decreases, the applied load increases from 530 kN to 685 kN, indicating load redistribution during the pullout test. In Fig. 55 the strains along the tendon are plotted (measurements 1 and 2) along the fixed length and up to the load step of 685 kN. Whereas at the 475 kN load step the entire strand correspondent to measurement 1 is activated, if measurement 2 is taken into account only 1.6 m of the strand is transferring load. At this load step the bottom of the strand monitored as measurement 1 detaches from the grout.

At 530 kN for measurement 1, the strand is still capable of sustaining the load, although the displacement at the bottom increases. At 685 kN the oscillations start at the bottom of the strand and unloading is observed only at this region. With increasing pullout load, the entire strand unloads and the oscillations are observed along the entire fixed length.

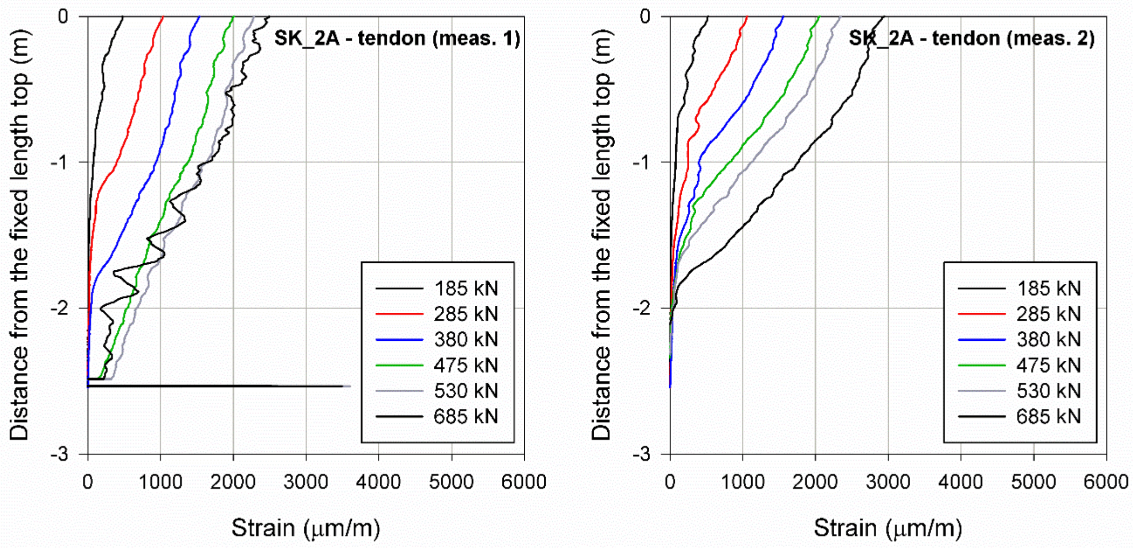

Fig. 55: Strains along the tendon fixed length (anchor 2A – measurements 1 and 2)

With respect to measurement 2, the strains increase continuously with increasing pullout load and the tendon is fully activated at about 840 kN. The measurements also show that the bottom of the strand is moving upwards from 945 kN onwards. At this step the strains start to oscillate substantially and, as observed for measurement 1, the oscillations start at the bottom and progresses during the pullout test. The failure criterion was reached at the load step of 685 kN. At this load step measurement 1 indicated that the strand was partially detached from the grout. At the 1010 kN load step the creep rate was larger than 23 mm and both monitored strands showed debonding from the grout.

Concerning the grout measurements, only the measurements obtained with the thin fibre are presented (Fig. 56). The fibre optic profile was also significantly different from the strain distribution verified in anchor 1A. The strain distribution in the grout shows compressive strains at the top of the free length possibly as a result of the reaction from the test apparatus, which compresses the grout when the anchor is loaded. Following these negative strains, tensile cracks are observed at the free length up to about 5.5 m depth and, below it, the expected negative strains are verified up to the fixed length top. Along the fixed length cracks are identified and, at the end of the test, cracking occurs at the entire fixed length.

In contrast with anchor 1A, the strains in anchor 2A along the grout were significantly smaller than the strains along the tendon, indicating that, at the position where the fibres were installed, load transfer between tendon and grout was reduced. This feature was already observed for the first non-zero strain measurement of 185 kN.

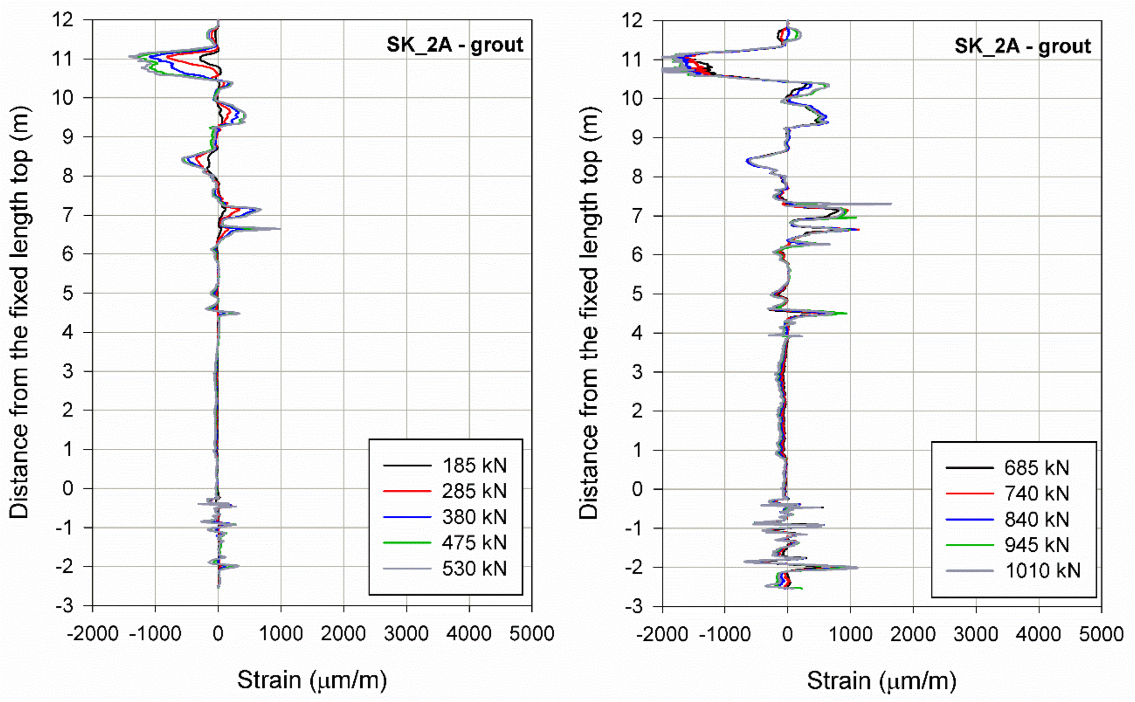

Fig. 56: Strains along the grout (anchor 2A)

Anchor 3A

The fibre optic cables of anchor 3A were installed only along the grout and the results obtained with the thin fibre are shown in Fig. 57. Although the strains along the grout were larger than the values measured in anchor 2A, it is not straightforward to interpret the measurements obtained with this anchor because the strains along the tendon were not monitored. The “zero” measurement was 85 kN.

The strains along the grout free length are compressive but at certain locations they are approximately zero, probably due to inhomogeneities in the grout. Tensile strains develop along the free length and they are larger than the positive strains observed at the fixed anchor length. This could indicate that the strands were not perfectly isolated at the free length, thus leading to load transfer above the proximal end of the bond length. Moreover, the strains along about 2.5 m of the fixed length were mainly compressive instead of tensile strains.

Because the Gewi bar was 2 m long (between -1 and -3 m), one possible explanation for the development of compressive strains at the fixed length in the grout is that the tendon-grout bond was somehow damaged along the Gewi bar. This would justify the high values of compressive strains at the distal end of the anchor because, in this case, the load would be transferred from the tendon to the grout mainly at the plate position, thus compressing the grout above the plate. From the proximal end of the fixed length up to about -1 m, where the Gewi bar started, the contact between tendon and grout was possibly not damaged and tensile stresses developed.

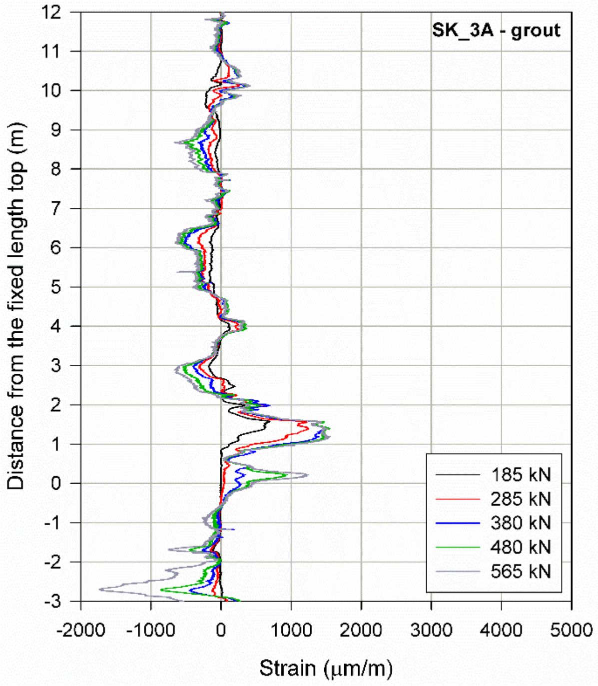

Fig. 57: Strains along the grout (anchor 3A)

6.5 Numerical simulations

As already mentioned, numerical simulations were undertaken prior to the anchor pullout tests (numerical predictions) and, after the tests, the simulations were refined (numerical refinements). The numerical simulations geometry was similar to the one employed for the Söding-test. Because the anchor was vertically installed, 2-D axisymmetric numerical models were developed. In all cases, the free length was 12 m long with a diameter of 178 mm, which corresponds to the borehole diameter. The soil unit weight for both soil materials, Seeton and silty sand, was assumed as 21 kN/m³. The tendon and the grout unit weight were, respectively, 78.5 and 25 kN/m³. The tendon was simulated as a linear elastic material (E_{tendon} = 160 GPa and ν = 0.2).

For anchor type 1, only one numerical prediction was carried out. The equivalent grout diameter at the fixed length was increased according to the volume of cement injected in anchor type 1A. The increase of the fixed length diameter based simply on the volume of cement injected is a simplification. The fixed length grouted body after cement injection is possibly formed by a mix of soil and cement and its shape will depend for instance on the soil porosity and on the injected pressure. The bond length diameter of anchor types 2 and 3 was increased to 600 mm for the numerical predictions.

In order to account for the post-grouting of anchor type 1, in addition to the diameter increase along the anchor fixed length the radial stresses along this section were increased by setting the lateral earth pressure coefficient at rest (K_0) to 1. Because the ground along the fixed length of the jet grouted anchor types 2 and 3 was cut before the grout injection, K_0 was not increased in these cases. The geometry of the numerical simulation for anchor type 1 is shown in Fig. 58.

Fig. 59 shows the numerical model of anchor types 2 and 3. The soil layers dimensions are the same as the values shown in Fig. 58. Anchor type 2C (Fig. 59b) is longer than anchors 2A and 2B. Regarding anchor type 3, the tendon diameter at its bottom is increased so to account for the Gewi bar and the plate is introduced at the end of the tendon (Fig. 59c, detail 2).

After the anchor pullout tests the numerical refinements were carried out and, in some cases, not only the material parameters were changed but also the geometry of the numerical simulation. In all cases the silty sand and the grout parameters were modified after calibration with the laboratory tests (Tab. 19 and Tab. 22). Other modifications performed are summarised below:

- Anchor type 1B: because the anchor post-grouting was not fully applied, the fixed length diameter was decreased to 250 mm instead of 280 mm and the lateral earth pressure coefficient at rest was decreased to 0.6 instead of 1;
- Anchor type 2A: in addition to the conventional grout, the jet grout material was taken into account (Tab. 22). During the installation of the in situ anchor, the jet grout was injected outside the corrugated pipe. Although the corrugated pipe was not simulated, a cluster was created at the same position where the pipe was installed to separate conventional grout and jet grout.
  The bond length diameter of the in situ anchor was inspected and determined between 730 and 830 mm. For this reason, the diameter that was initially assumed as 600 mm was increased to 780 mm. Interfaces between tendon and grout and grout and soil were introduced;
- Anchor type 2C: in the same way as performed for anchor type 2A, the jet grout material was taken into account. Although only the diameter of anchor type 2A was inspected, due to the high in situ bearing capacity of anchor 2C, the same range of values observed for anchor 2A was assumed for the numerical refinement of this anchor and the bond length diameter was set as 840 mm. An interface between grout and soil was added.

Tab. 23 shows the Plaxis version used for the numerical simulations, the number of elements employed and the element type.

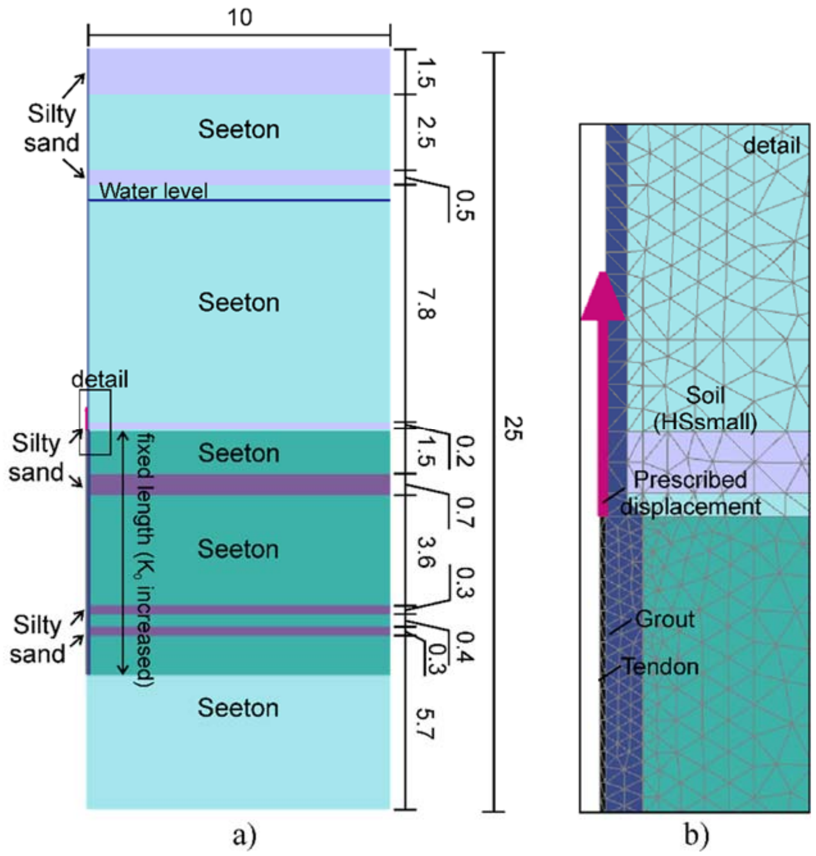

Fig. 58: Geometry of the numerical simulation (anchor type 1) – a) soil layers (dimensions in metres) and b) top of the fixed length detail

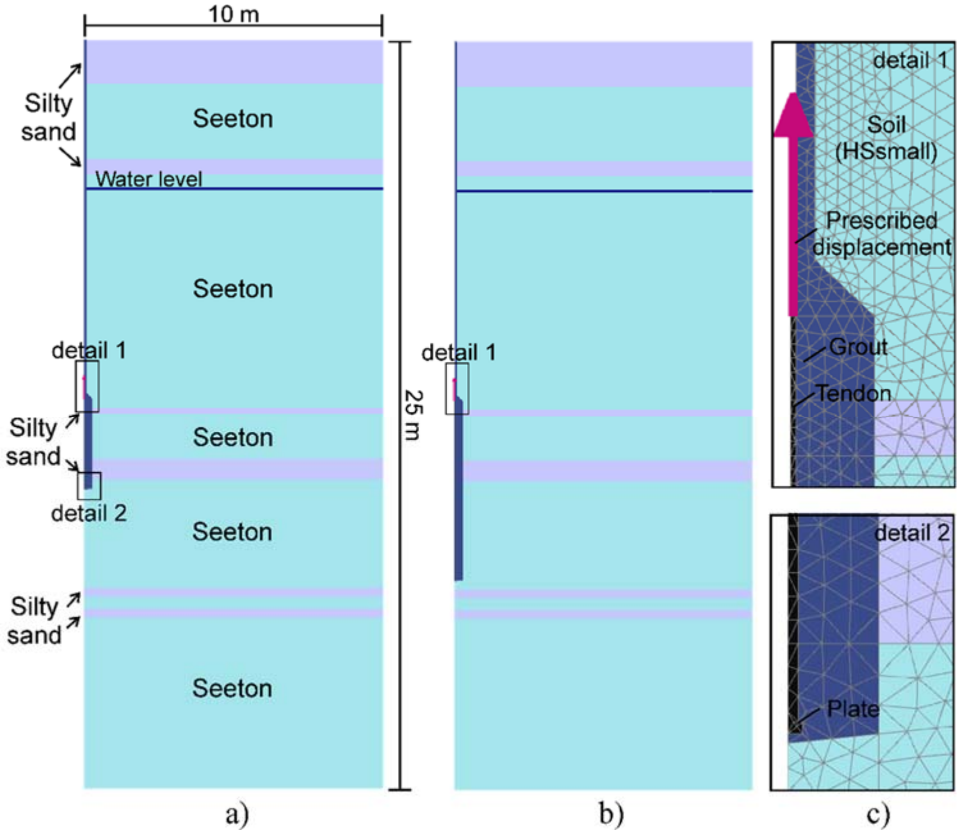

Fig. 59: Geometry of the numerical simulation (anchor types 2 and 3) – a) overview of anchor types 2A, 2B, 3A and 3B; b) overview of anchor type 2C and c) detail 1 (top of the fixed length) and detail 2 (bottom of anchor type 3)

Tab. 23: General information of the numerical simulations

Simulation	Software	Number of elements	Element type
Anchor 1A - prediction	Plaxis 2D – 2017	7901	15-noded
Anchor 1A – refinement	Plaxis 2D – 2017	7935	15-noded
Anchor 1B - refinement	Plaxis 2D – 2017	7938	15-noded
Anchor 2A – prediction	Plaxis 2D – 2017	9920	15-noded
Anchor 2A – refinement	Plaxis 2D – 2018	9765	15-noded
Anchor 2C – prediction	Plaxis 2D – 2017	10 408	15-noded
Anchor 2C - refinement	Plaxis 2D – 2018	10 511	15-noded
Anchor 3A - prediction	Plaxis 2D – 2017	8655	15-noded
Anchor 3A - refinement	Plaxis 2D – 2018	9892	15-noded

6.5.1 Numerical results

Anchor type 1

The measured and simulated load-displacement curves are compared in Fig. 60, where only the displacements with respect to the top of the fixed length are presented. The solid curve (anchor 1A) refers to the class-A prediction and the dashed curve to the numerical simulation with refined material parameters. The parameters employed for both simulations are shown in Tab. 19 and Tab. 22.

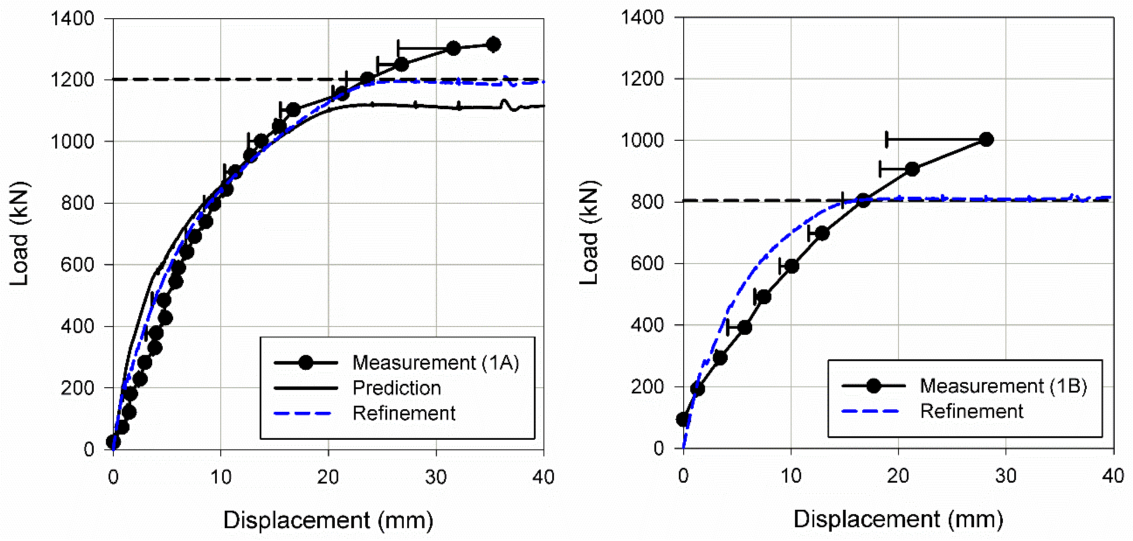

Fig. 60: In situ load-displacement curve *vs* prediction and refinements (anchors 1A and 1B)

The predicted load-displacement curve of anchor 1A showed a very good agreement with the measured one. The numerical ultimate capacity was approximately 1100 kN and the failure criterion of the in situ test was achieved at 1200 kN. Both, predicted and refined curves, were slightly stiffer than the measured curve. The same ultimate capacity as in the in situ test was obtained after the parameters were refined and, if the creep is subtracted from the displacement, the differences between measurements and both numerical results were not significant.

With respect to anchor 1B, after the simulation was refined to account for the partial post-grouting, the agreement with the in situ curve was good. However, although the same ultimate capacity of 800 kN was obtained, the numerical simulation was stiffer than the in situ curve.

The strain distribution along the tendon at the fixed length for anchor 1A is compared with the in situ measurements in Fig. 61. Only the results from the refined numerical simulation are discussed. The numerical oscillations observed from 280 kN onwards are the result of snap-back instability generated when cracking in the grout starts. This phenomenon, which is observed in displacement-controlled problems, is also referred in Carpinteri & Colombo (1989) and in Brinkgreve et al. (2019a). In the particular case of anchor 1A, numerical instability occurs due to the brittle behaviour of the cracking phenomenon and the instability increases if residual state is achieved. Although the effect of the snap-back instability is easily observed in Fig. 61, in the numerical load-displacement diagram of anchor 1A this effect is small.

Analysing the strain distribution along the tendon, it is clear that the transition zone is not well captured numerically, not agreeing with the in situ measurements. In fact, whilst for the in situ measurements this zone increases along the fixed length and thus leads to a change of slope along the tendon (Fig. 51), the transition zone in the numerical simulation is restricted to the first 0.4 m of the fixed length. As mentioned previously, the in situ measurements along the grout indicate that after tensile cracking starts, the compressive stresses transferred within the transition zone lead to crack closing. However, the smeared crack approach employed in the Concrete model cannot take this into account realistically and this numerical limitation explains the differences between in situ measurements and numerical distributions in Fig. 61.

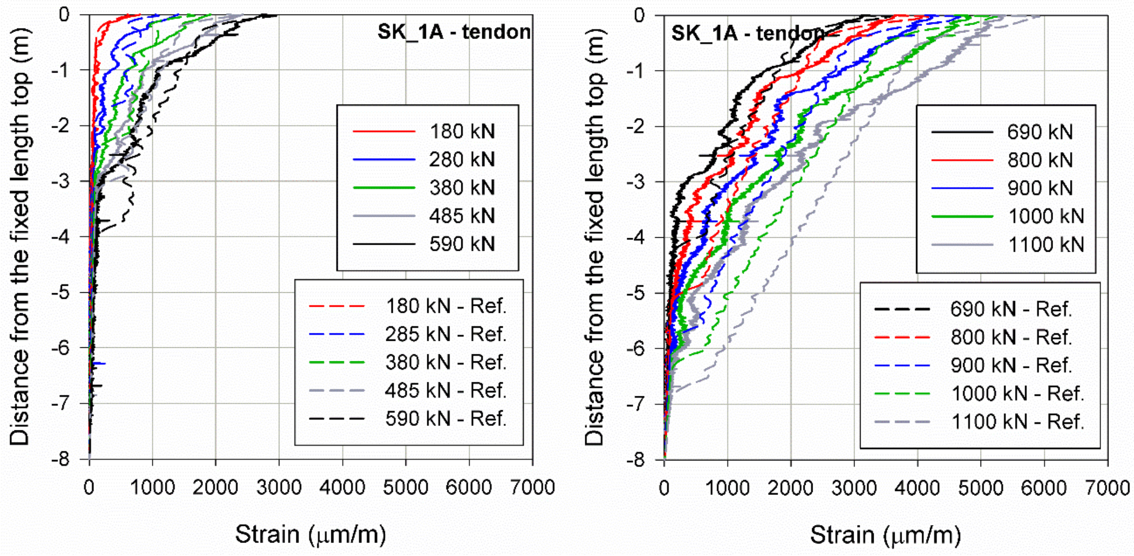

Fig. 61: Strain distribution along the tendon – in situ *vs* refinement (anchor 1A)

The numerical shear stress distribution along the grout-soil interface is compared with the calculated stresses obtained through the fibre optic measurements in the tendon in Fig. 62. The stress concentration that occurs at the proximal end of the fixed length, represented by the hatched area, is not observed numerically along the grout-soil interface. This confirms that, as stated by Ostermayer & Scheele (1978), if strain measurements performed in the tendon are considered for calculating the skin friction along the grout-soil interface, this bond stress concentration must be somehow equalised to obtain the actual values of shear stress. The sharp decrease of skin friction observed from the strain measurements due to cracking in the grout was not reproduced numerically. Instead, the numerical results show a more uniform shear stress distribution along the grout-soil interface in comparison to the values derived from the tendon fibre optic measurements. Moreover, because failure occurs in the grout-soil interface, relative displacements between grout and soil develop but not between tendon and grout. For this reason, at the bottom of the fixed length the shear stresses obtained numerically are higher than the stresses calculated from the fibre optic measurements.

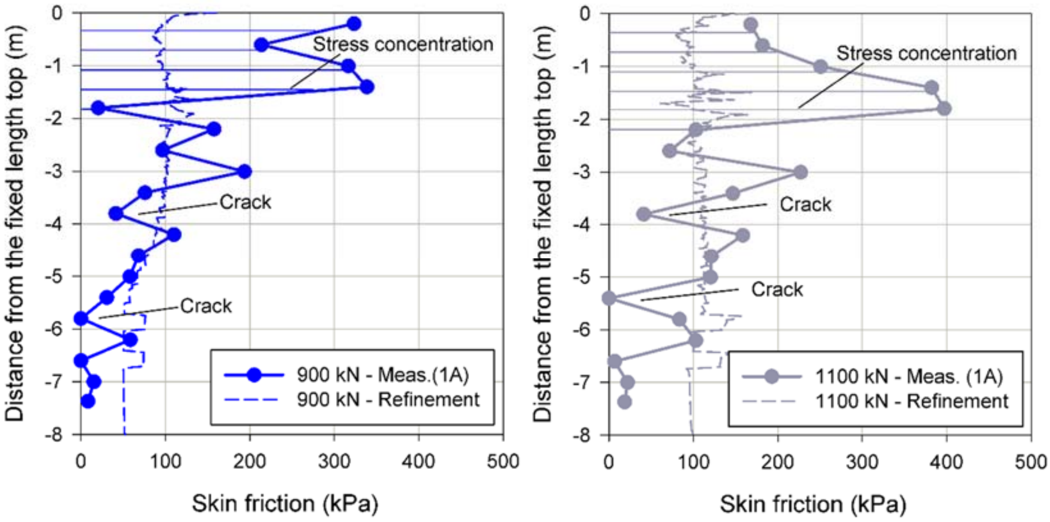

Fig. 62: Shear stress obtained with the fibre optic measurements compared with the numerical results (grout-soil interface, anchor 1A)

In Fig. 63, the tension softening parameter H_t is used as a measure to compare the numerical results with the in situ cracking. Fig. 63 presents the evolution of H_t for each load step from 280 kN onwards, the load at which cracking has started. H_t is plotted along the fixed length and compared with the in situ measured strain distribution in the grout. The peaks along the H_t profile indicate that cracking is, at least qualitatively, captured very well. However, crack closing observed in the in situ measurements led to negative strains on top of the fixed length and this was not captured in the numerical simulation for the above-mentioned reasons. Therefore, at the proximal end of the fixed length, more spikes (tensile cracking) are observed numerically than in the measurements. As observed for the in situ measurements, cracking in the grout influences the strains along the tendon.

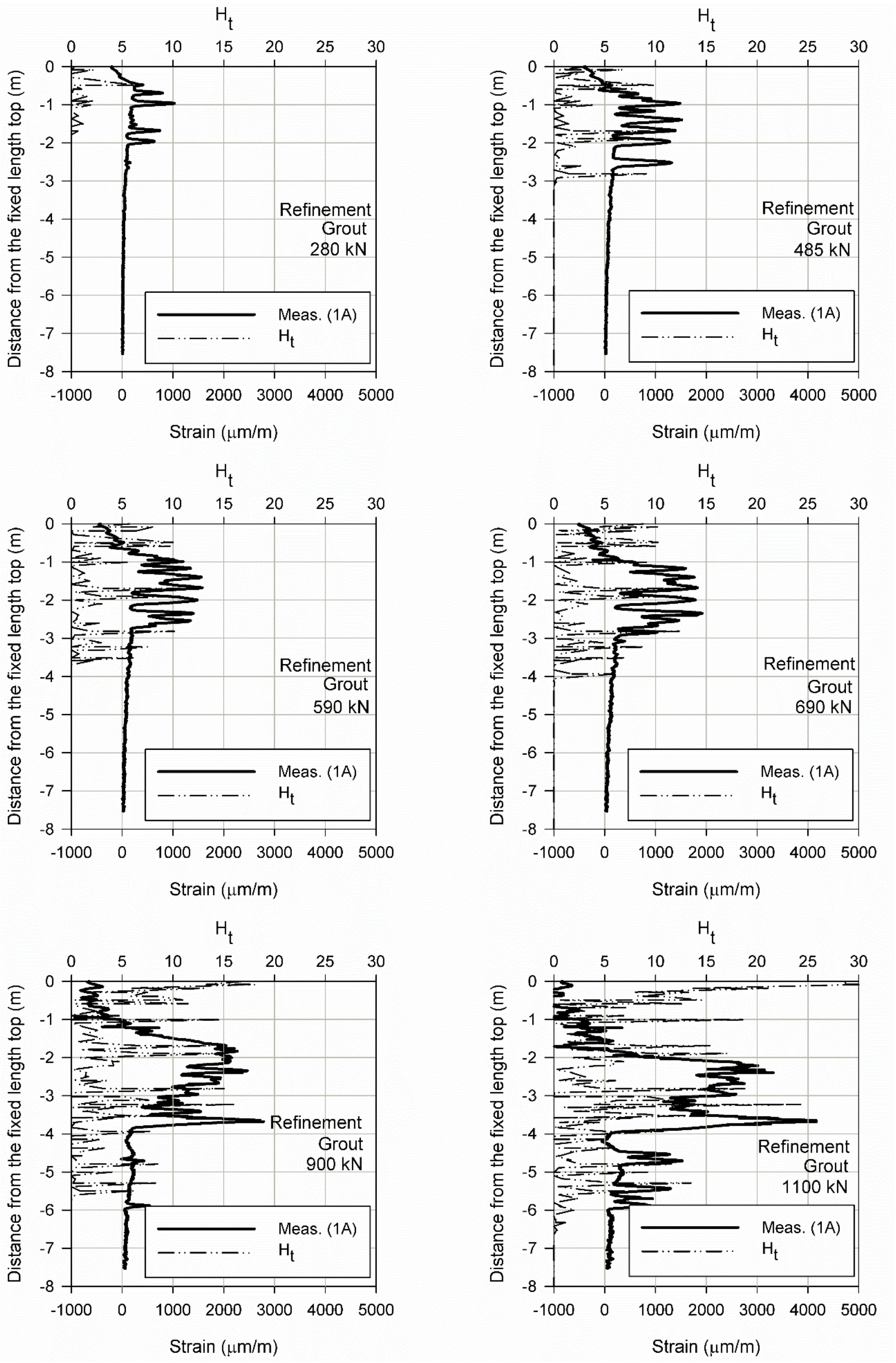

Fig. 63: Measured strain distribution along the grout at the fixed length and comparison with the numerical parameter H_t (anchor 1A)

Anchor type 2

The load-displacement curves of anchor 2A are presented in Fig. 64. Although the predicted curve agreed reasonably well with the measurements, the diameter at the grout along the fixed length was assumed as 600 mm whilst the grout inspection showed that actually it was between 730 mm and 830 mm. Moreover, the fibre optic measurements indicated that the failure mechanism was possibly along the tendon-grout interface whereas the numerical prediction led to failure along the grout-soil interface.

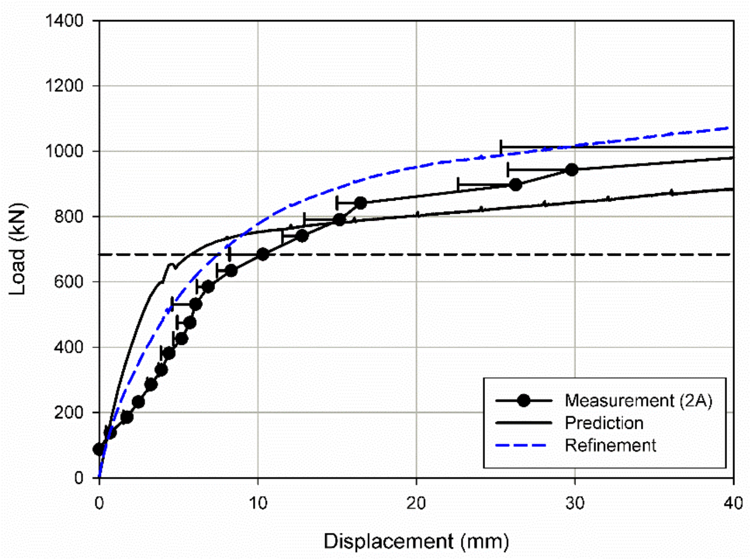

Fig. 64: In situ load-displacement curve *vs* prediction and refinement (anchor 2A)

In order to capture the correct failure mechanism, for the numerical refinement soil volume elements with reduced strength and stiffness parameters were introduced adjacent to the tendon, so to act as an interface. The tendon-grout interface was modelled with the Concrete model and, in order to determine the interface strength and stiffness parameters, the uniaxial strength in tension and in compression and the Young's modulus were progressively reduced until a failure mechanism along the tendon-grout interface was obtained. A reduction to 1/6 of the conventional grout parameters was then applied.

In addition to the tendon-grout interface, Plaxis interface elements were introduced between the grout and the soil and the strength reduction factor R_{inter} was set as 0.9 instead of 1.0. This assumption accounts for the fact that, during the in situ jet anchors installation, the ground at the fixed length was pre-cut with water and therefore the grout-soil interface was not as rough as for anchor type 1. The different grout materials and the interfaces assumed in the numerical refinement of anchor 2A are shown in Fig. 65. Furthermore, for this simulation the bond length diameter was increased to 780 mm and distinction was made between jet grout and conventional grout parameters. Once the interface is introduced so that failure occurs along the contact tendon-grout, the load-displacement curve obtained with the simulation approaches the measured one.

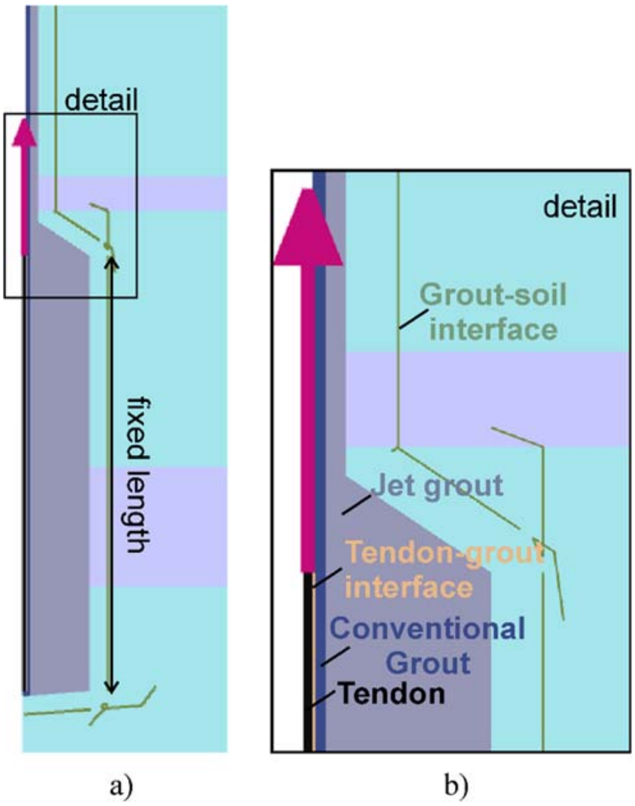

Fig. 65: Numerical refinement of anchor 2A – a) fixed length and b) detail of the grout materials and interfaces

The strain distribution along the tendon fixed length obtained with the numerical refinement is shown in Fig. 66. Due to the strain decrease observed for measurement 1, only the results of measurement 2 are compared. As previously explained, whereas after 530 kN the monitored strand referred as measurement 1 indicated unloading, the strand monitored as measurement 2 showed a continuous strain increase. In Fig. 66 it is clear that after this load step the numerical strains were smaller than the measured values, therefore confirming that load redistribution occurred during the test.

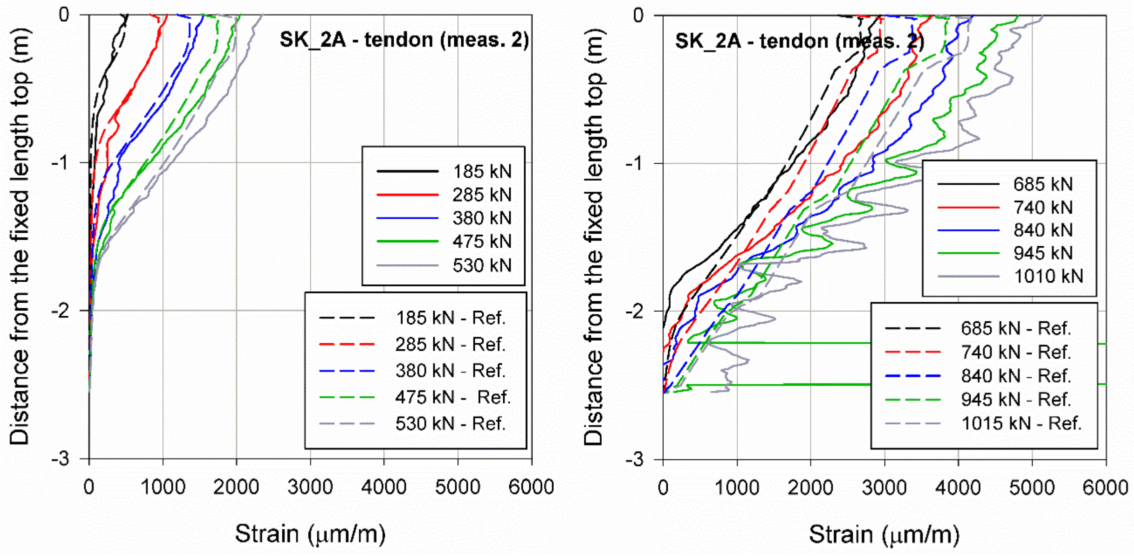

Fig. 66: Strain distribution along the tendon – in situ *vs* refinement (anchor 2A)

As already shown for anchor 1A, the numerical development of the strain along the tendon is strongly influenced by the grout condition. In comparison with the undamaged area, in the region where the grout is cracked the strains in the tendon are significantly larger. This is shown in Fig. 67, which compares the strain profile along the tendon with the distribution of the tension softening parameter H_t for the load steps of 475 and 740 kN. The parameter H_t was plotted along a cross-section located within the interface at the contact with the tendon. Once cracking occurs ($H_t > 0$), the strains in the tendon increase and residual state in tension ($H_t > 1$) was only achieved at the top of the fixed length.

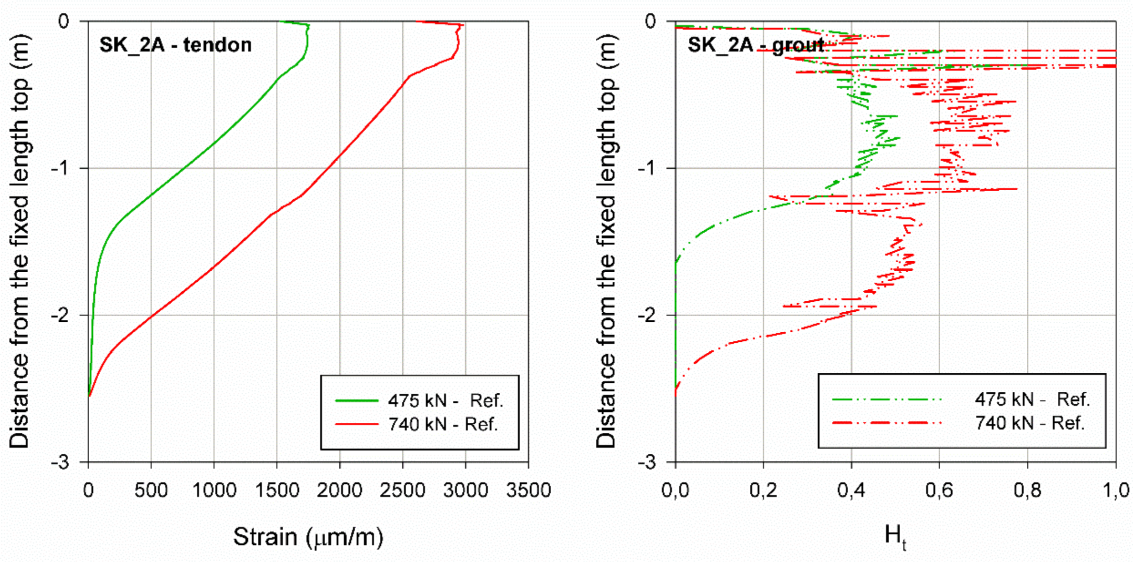

Fig. 67: Strain distribution and grout condition (anchor 2A) – a) strains along the tendon and b) H_t parameter

The numerical strain distribution in the grout was plotted along a cross-section located 5 cm away from the axis of symmetry, at approximately the same position where the fibres were installed. The cross-section position is shown in Fig. 68a. Because shear failure occurs along the tendon-grout interface, which was located between 1.9 and 2.5 cm away from the axis of symmetry, load is only partially transferred up to the cross-section position. The mobilised shear stresses for the 740 kN load step at the proximal end of the fixed length in the grout are presented in Fig. 68b, where it is possible to note that shear stresses concentrate along the tendon-grout interface. The strains in the grout at the fibre optic cables position are plotted in Fig. 69. In the same way as the monitored strains (Fig. 56), the values were very small.

Due to the fact that anchor 2B was not monitored with fibre optic sensors and because its load-displacement behaviour was very different from the one observed for anchor 2A, this numerical simulation was not refined.

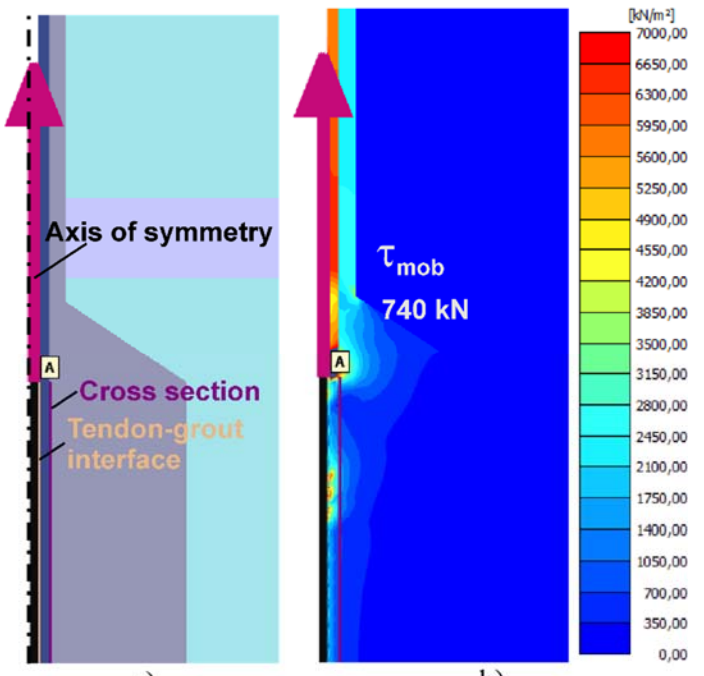

a) b)

Fig. 68: Proximal end of the fixed length (anchor 2A) – a) interface and cross-section position and b) mobilised shear stresses

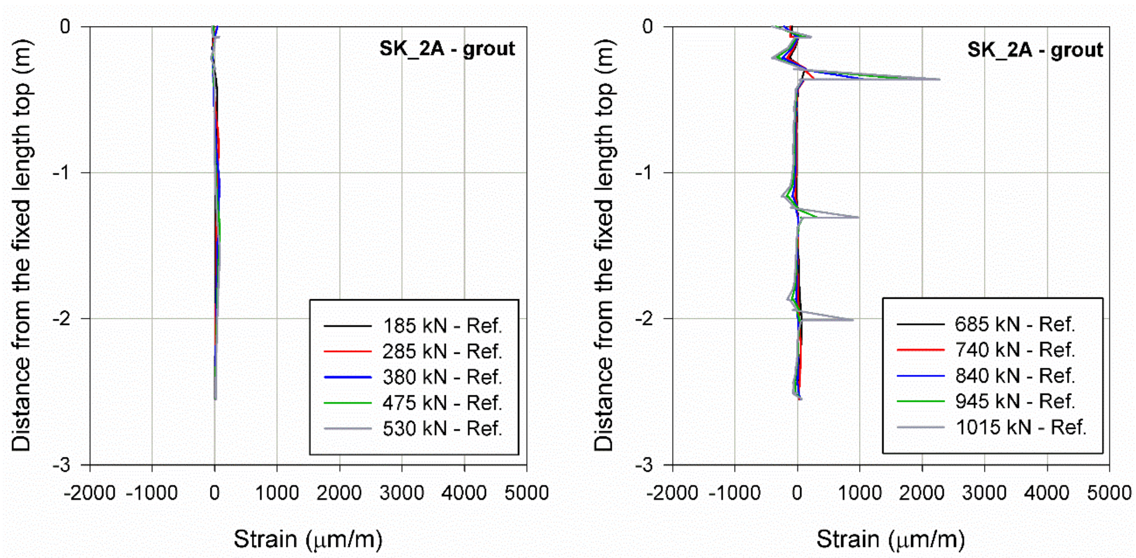

Fig. 69: Strain distribution along the grout – refinement (anchor 2A)

Regarding anchor 2C, the load-displacement curve obtained with the numerical prediction (Fig. 70) showed stiffer behaviour and lower ultimate capacity than the in situ curve. In order to refine the numerical model, the diameter of the grout at the fixed length was increased from 600 mm to 840 mm. Besides increasing the diameter, during the refinement the grout parameters were modified according to Tab. 22 and the jet grout material was taken into account. Because it is believed that the failure mechanism developed along the grout-soil interface, no tendon-grout interface was employed. Likewise anchor 2A, R_{inter} (grout-soil interface) was set as 0.9.

After refinement, the numerical load-displacement curve still showed stiffer behaviour than the measured one. Considering the same displacement value, from 15 mm onwards the diameter increase along the fixed length led to an increase in the load of about 35% in comparison with the predicted load. The kinks in the numerical curves occur when the grout reaches residual state in tension, which leads to numerical snap-back instability.

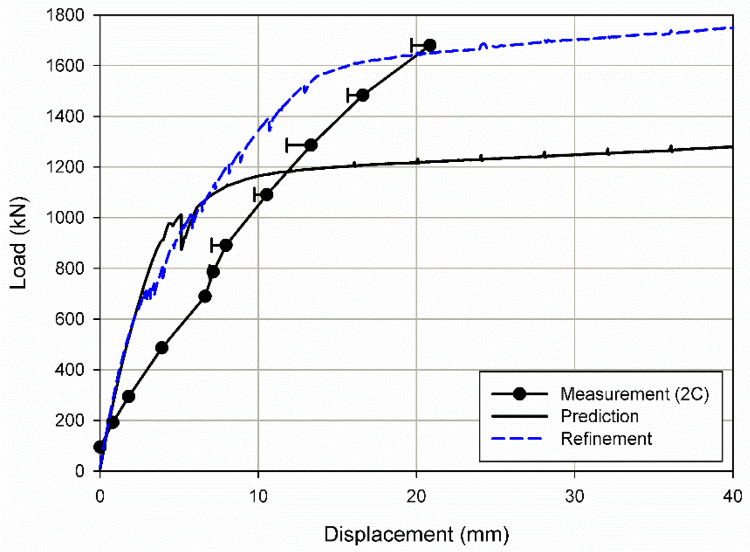

Fig. 70: In situ load-displacement curve *vs* prediction and refinement (anchor 2C)

Anchor type 3

Initially, it was assumed that the only differences between anchors 2A and 2B and anchors 3A and 3B were the plate and the Gewi bar at the distal end of the fixed length. In this respect, the numerical prediction of anchor type 3 led to a load-displacement curve almost identical to the curve obtained for anchors 2A and 2B. However, the in situ measurements showed significant different results in comparison with the measurements performed for anchor type 2.

It was already pointed out that probably the Gewi bar at the fixed anchor length contributed to the anchor failure. Therefore, the numerical refinement was carried out considering a gap between the steel and the grout along the anchor section where the Gewi bar was located (Fig. 71), thus simulating no steel-grout bonding in this area. After this assumption, the agreement between numerical simulation and in situ results improved, as presented in Fig. 72. The first kink in the curve occurs when tensile cracks develops in the jet grouted section, at the position where the Gewi bar starts (1 m below the fixed length top), as shown in Fig. 73. When this occurs, tensile stresses are not fully transferred from the region above the crack to the area below it and the grout column undergoes mainly compressive stresses coming from the distal end of the fixed length. The compressive stresses (negative values) before and after the crack development are depicted in Fig. 73 with coloured contours.

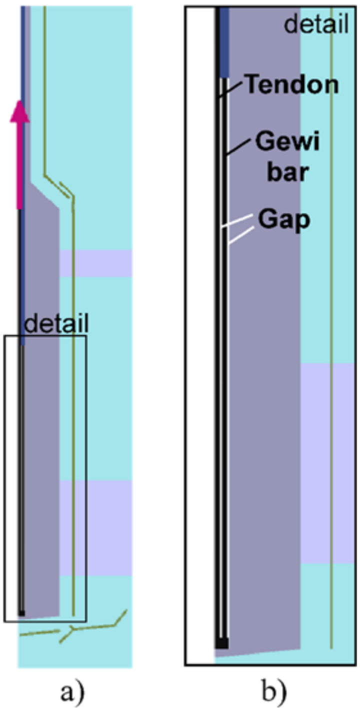

Fig. 71: Numerical refinement of anchor 3A – a) fixed length and b) detail of the contact Gewi bar-grout

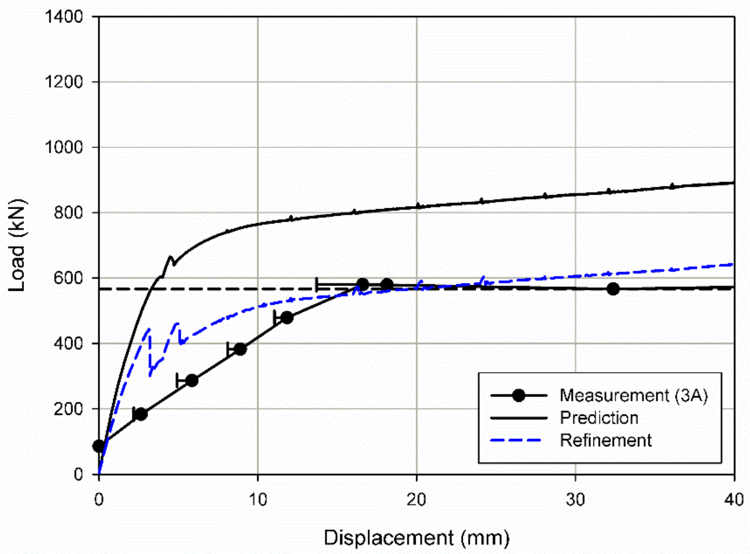

Fig. 72: In situ load-displacement curve vs prediction and refinement (anchor 3A)

Crack development at the top of the Gewi bar could explain why the in situ measurements of strains showed compressive strains below -1 m depth and tensile strains above it (Fig. 57). In this case, the tensile stresses would be confined to the region above the crack whereas the load below the crack would be transferred only at the plate position, thus compressing the grout column.

In the same way as anchor 2B, the numerical simulation of anchor 3B was not refined due to insufficient information concerning the anchor behaviour.

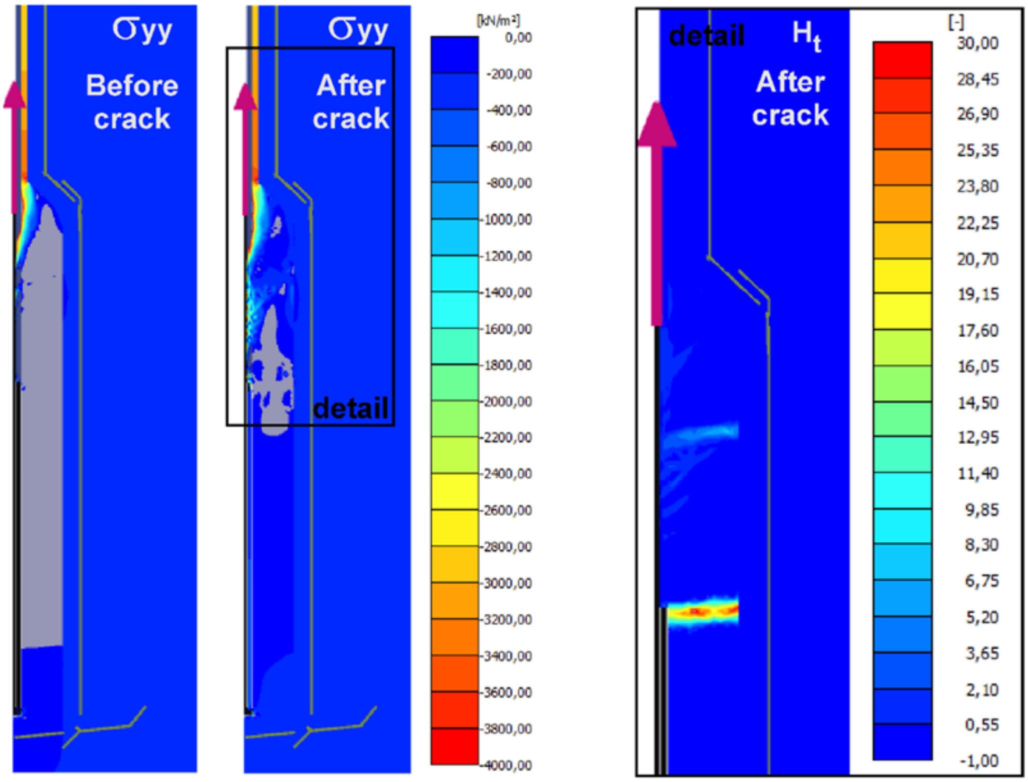

a) b)

Fig. 73: Numerical refinement of anchor 3A – a) compressive stresses before and after the crack formation b) crack position

6.6 Summary

In December 2017, 7 soil anchors were pulled out and 3 of them were monitored with fibre optic sensors. The anchors were divided into types 1, 2 and 3. The fibre optic monitored anchors are referred with the letter A, e.g. anchor 1A, and the anchors which were only monitored at the anchor head are referred with the letter B, e.g. anchor 1B. Anchor type 1 was post-grouted and anchor types 2 and 3 were jet grouted. The soil was a clayey silt and it was characterised prior to the anchor pullout tests, therefore the main strength and stiffness parameters were numerically calibrated with in situ and laboratory tests. After the pullout tests, additional laboratory tests were carried out on soil and grout samples and new numerical calibrations were undertaken.

The in situ load-displacement behaviour varied for each anchor, even if the anchors were designed to have the same geometry. Regarding anchor type 1, the differences were expected because one anchor was not successfully post-grouted. With respect to anchor types 2 and 3, it is believed that different failure mechanisms developed due to insufficient steel-grout bonding.

The numerical simulations were divided into predictions and refinements. The numerical predictions were carried out before the anchor pullout tests. The numerical refinements were undertaken after additional soil and grout laboratory tests were performed and after the in situ fibre optic measurements were interpreted.

The class-A prediction of anchor 1A agreed very well with the in situ load-displacement curve and the agreement was further improved in the numerical refinement. Regarding anchor 1B, after the insufficient post-grouting was taken into account by decreasing both, the radial stresses along the fixed length and the grout diameter, the differences between the in situ anchor and the numerical model decreased. The measured tendon strain distribution compared well with the numerical refinement results of anchor 1A and the tension softening parameter profile in the grout was in good agreement with the in situ crack development.

The in situ skin friction of anchor 1A was calculated through the fibre optic measurements in the tendon and it varied over depth: at the proximal end of the anchor stress concentration occurred and, at certain positions where cracking in the grout developed, the shear stresses dropped significantly. On the other hand, a more uniform shear stress distribution in the grout-soil interface was obtained numerically and numerical cracks did not affect the skin friction profile significantly.

Modelling the pullout tests of anchor types 2 and 3 was not straightforward. The in situ measurements of strains along the tendon and along the grout of anchor 2A suggested that the pullout load was not equally distributed between the strands and that failure occurred in the tendon-grout interface. With respect to the last remark, the fibre optic strain profile along the grout showed very small strain values, indicating that load transfer between tendon and grout was reduced. Although the predicted load-displacement curve of anchor 2A agreed reasonably well with the measurements, the prediction did not account for failure in the tendon-grout interface. Therefore, in the numerical refinement, an interface between tendon and grout was considered with reduced strength and stiffness parameters of the grout material. After the interface assumption, shear failure between tendon and grout occurred and the load-displacement curves agreement improved.

The fibre optic strain measurements in the grout of anchor 3A indicated compressive stresses development at the fixed anchor length within about the last 2 m. The compressive stresses were observed along approximately the same grouted section where the Gewi bar was installed. Additionally, a plate was placed at the distal end of the fixed length which might have contributed to compress the grouted body. Therefore, a numerical simulation was carried out in which no contact between the steel bars and the grout was assumed along the last 2 m of the anchor fixed length. The numerical results indicated that, under this assumption, tensile stresses develop at the first metre of the fixed length and a large tensile crack evolves at the top of the Gewi bar. Above the crack the grout undergoes tensile stresses and below it compressive stresses develop.

7 A10 Tauernautobahn-test

7.1 Anchor description

The installation and pullout test of the monitored anchor were undertaken in July 2018, at approximately 65 km from Salzburg, Austria (A10 Tauernautobahn km 50.6-50.9, Fig. 74). The anchor installation was part of the second construction phase of the renovation of existing anchors of a retaining wall located along the highway.

Fig. 74: Retaining wall where the monitored anchor was installed

The monitored anchor was situated at the top of the wall and was 15 m long at the free length and 10 m long at the fixed length. 8 strands were employed (8 x 15.7 mm using high grade steel Y1860). During drilling, a 178 mm casing was used up to about 15 m. From about 15 m until 25 m no casing was employed and the diameter was 150 mm.

The anchor was installed on July 3 2018 and the pullout test was on July 19 2018. In addition to primary grouting, post-grouting of the anchor was planned. However, due to the high rock stiffness, the post-grouting was not fully accomplished and only 2 L of cement were injected. Therefore, in this case the anchor behaved as a gravity grouted anchor. Fig. 75 shows the fibres being glued along the tendon and Fig. 76 the fibre optic cables employed for the grout measurements, attached outside the corrugated pipe.

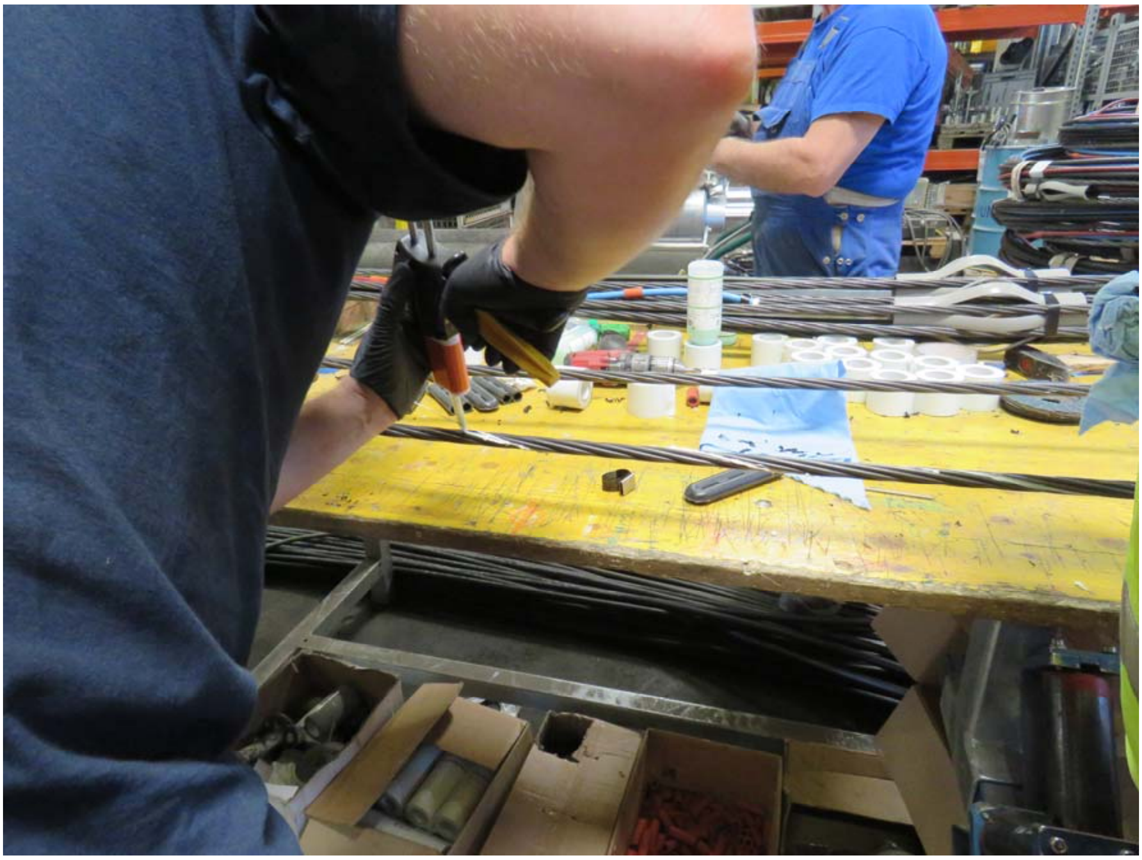

Fig. 75: Attachment of the fibre on the strand

Fig. 76: Installation of the fibres along the corrugated pipe

7.2 Ground description

The area where the anchor was installed is composed of three ground layers. The first is an upper layer varying from about 0.5 to 3.3 m. A fragmented claystone (Rock Quality Designation 30-60%) lies below the upper layer and is the transition between the upper layer and the rock. The fragmented claystone is located between about 5 and 15 m. Below it a better quality claystone layer (Rock Quality Designation 50-75%) and sandstone are found, the uniaxial compressive strength varying from 50 to 75 MPa. The layers and the monitored anchor position are shown in Fig. 77.

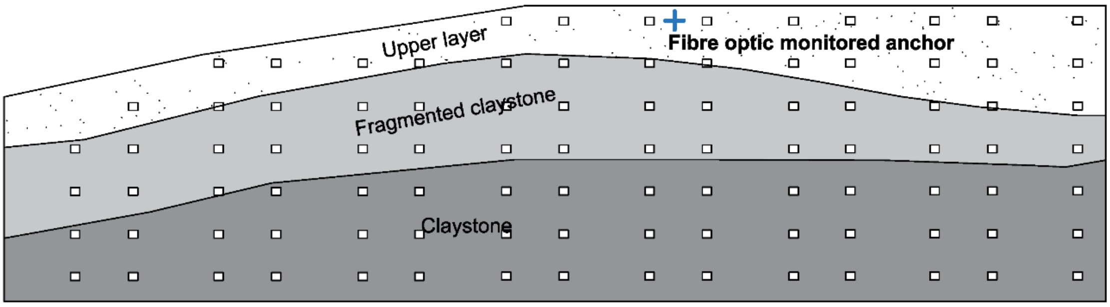

Fig. 77: Ground layers and monitored anchor position

The cross-section showing the monitored anchor and the soil and rock layers is shown in Fig. 78. The ground surface has an inclination of about 40° with respect to the horizontal direction. Due to the gradual transition between the upper layer and the rock, the separation of the soil layers is not straightforward and a simplified representation was employed. Therefore, in Fig. 78 the upper layer and the transition material are considered as a unique 6 m depth soil layer above the rock material. The geotechnical report recommends the parameters for the upper layer and the rock as shown in Tab. 24.

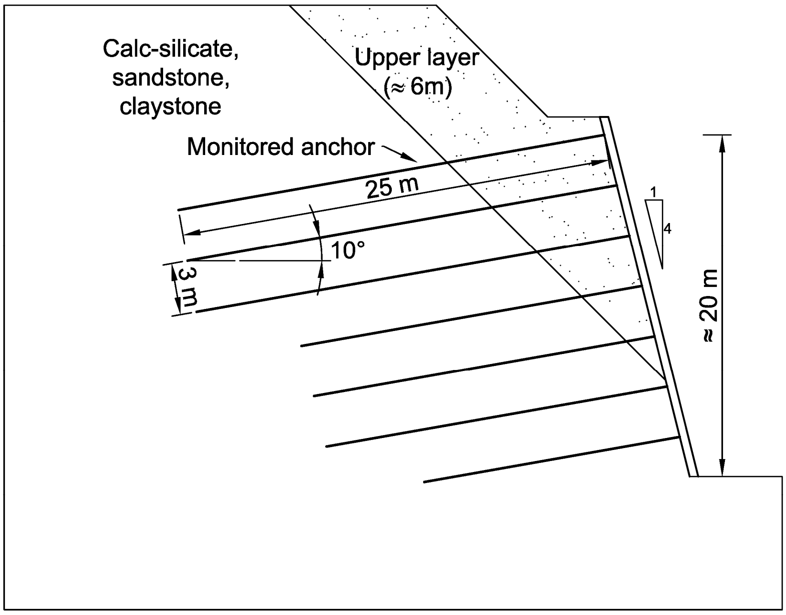

Fig. 78: Cross-section with monitored anchor

In Tab. 24, the low values of stiffness estimated in the geotechnical report for the claystone are remarkable. According to the American Association of State Highway and Transportation Officials (AASHTO 2002), the elastic modulus of a sandstone is found between 620 and 39200 MPa, whilst for a siltstone the range varies from 2620 to 32800 MPa. Although the elastic modulus for claystone is not mentioned, the AASHTO suggests values for the typical range of uniaxial compressive strength for claystone from about 1.4 to 8.3 MPa. Therefore, although the rock material presents uniaxial compressive strength varying from 50 to 75 MPa, the elastic modulus recommended in the geotechnical report is way below the range suggested by the AASHTO for sandstone and siltstone, even if local deviations from average values cited in literature are often found in practice.

Tab. 24: Soil and rock parameters

Material	**γ (kN/m³)**	**φ (°)**	**c (kN/m²)**	**E (MPa)**
Upper layer	21	35	0	70
Rock	24	40	40	150-500

7.3 In situ pullout test results

The load-displacement curve is shown in Fig. 79, where the displacements at the anchor head are depicted. From the unloading 100 kN steps, it is possible to evaluate the plastic deformation of the anchor, which did not exceed 4 mm. Because the anchor was designed to contribute to the retaining wall stability, the failure criterion was not reached in this case. After loading the anchor to 1495 kN, it was reloaded to the permanent load of 835 kN.

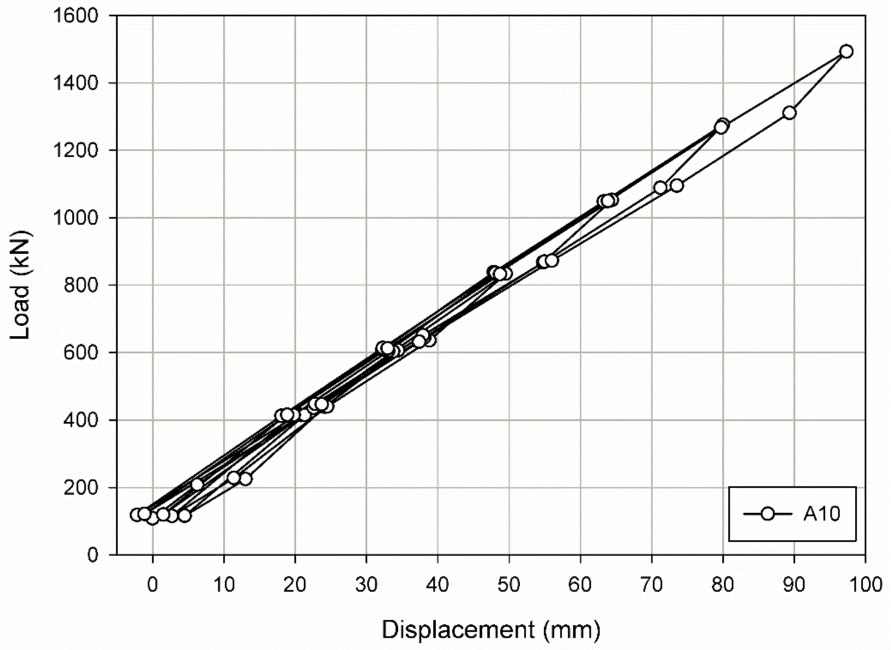

Fig. 79: Load-displacement curve (tendon end displacements)

If Eq. 2 is applied and the elongation of the free length is subtracted from the tendon end displacement, for certain load steps the calculated values at the top of the fixed length were negative, thus the elongation of the free length was larger than the measured total displacement. In order to understand the negative values, discussion is addressed in the following paragraphs where the fibre optic strain measurements are shown.

The fibre optic measurements for each load step, considering the measurements performed along one strand, are shown in Fig. 80. The strains along the tendon and the grout are relative values and the zero measurement corresponds to the first 110 kN load step. During the pullout test, it was observed that the tendon strain profile along the free length did not follow a constant distribution during the load steps. Considering the load step of 1050 kN, the strain is about 3900 µm/m within the first 7 m and it drops to approximately 3200 µm/m at the proximal end of the fixed length. If the strain distribution along the free length is integrated in order to calculate the elongation of the free length, the elongation is 3 mm smaller than the value obtained if a constant strain distribution along the free length is assumed. The boundary condition assumed for the integration was that the bottom of the anchor did not move. Because in Eq. 2 and Eq. 3 the anchor free length was assumed as completely free to elongate, this strain decrease was not taken into account.

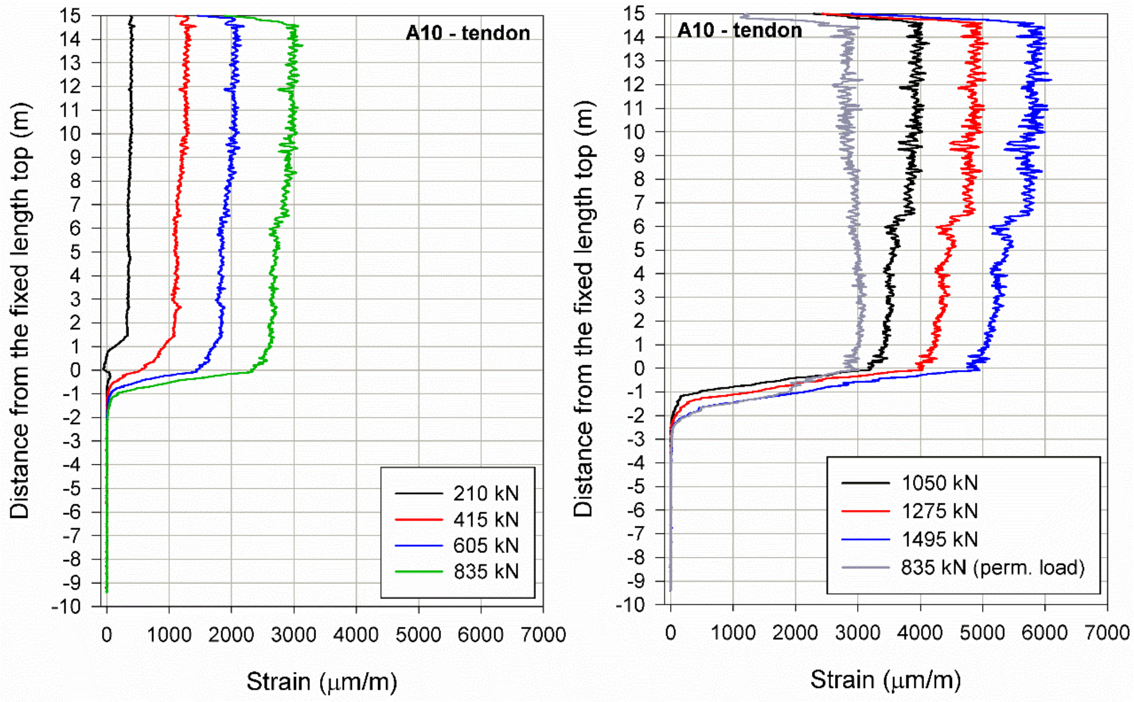

Fig. 80: Strains along the tendon

Still regarding the 1050 kN load step, only 2 m of the tendon is activated along the fixed length. As a result, the elongation of the fixed length is very small and, after integrating the strain profile along the tendon, the displacement at the top of the fixed length was about 2 mm. Since the elongation of the free length is 3 mm lower if the decrease of the strain is taken into account, the negative displacements obtained from Eq. 2 probably arise from the fact that the strains along the free length were assumed constant.

The strain decrease occurs because the strands were not perfectly isolated along the free length and friction developed between the strand and the grout. Intrusion of cement between the steel and the debonding sleeve and imperfections during the application of the grease could explain this behaviour. Another possible explanation for the decrease of the strains along the free length is that the rock might be so stiff that the cement along the free length restrains the strands movement at this section. This assumption is plausible since the fibre optic measurements indicate that the decrease is less significant within the first 7 m of the anchor, which is approximately the depth where the upper soil layer is located. Finally, because during drilling no casing was used below 10 m of the anchor and the borehole diameter decreased from 178 to 150 mm, below 10 m the rock was tighter to the anchor than within the first 10 m.

When the anchor was unloaded to the permanent load of 835 kN, the strains along the free length within the first 7 m almost coincided with the strains measured at the primary loading step of 835 kN, as shown in Fig. 81. From 7 m depth until the proximal end of the fixed length the strains at the permanent load were larger, indicating that friction between the tendon and the grout was probably destroyed as the load increased. From 1 until 2.5 m below the proximal end of the fixed length the strains at the permanent load coincided perfectly with the values measured at 1495 kN, suggesting that the deformation within this depth was purely plastic.

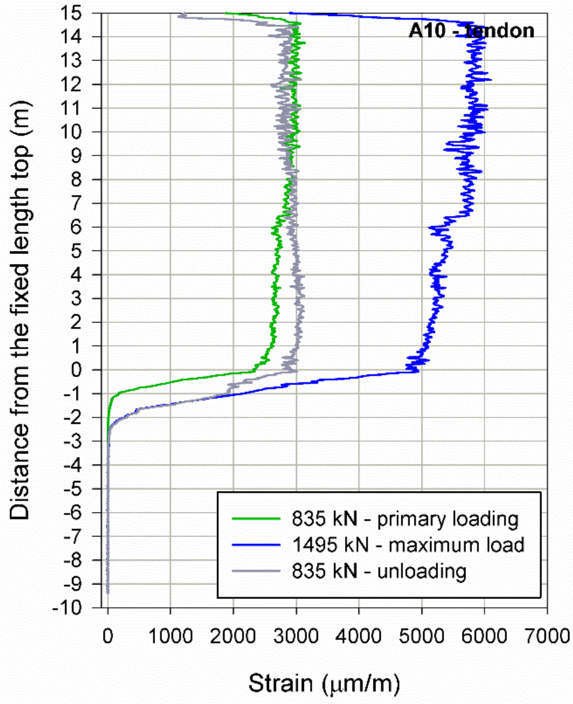

Fig. 81: Strains along the tendon (comparison between 835 kN load steps and maximum load)

The strains along the grout obtained with the thin fibre are shown in Fig. 82. The development of the strains is mostly restricted to the proximal end of the fixed length. Compressive strains (negative) are observed above the top of the fixed length and tensile strains (positive) are identified below it. Additionally, negative strains are observed at the top of the free length, possibly as a result of the reaction from the retaining wall. Tensile cracks develop in the grout and can be observed along the strain profile. The various grout conditions and their influence on the tendon strains are presented in Fig. 83 for the 415 and 1050 kN load steps.

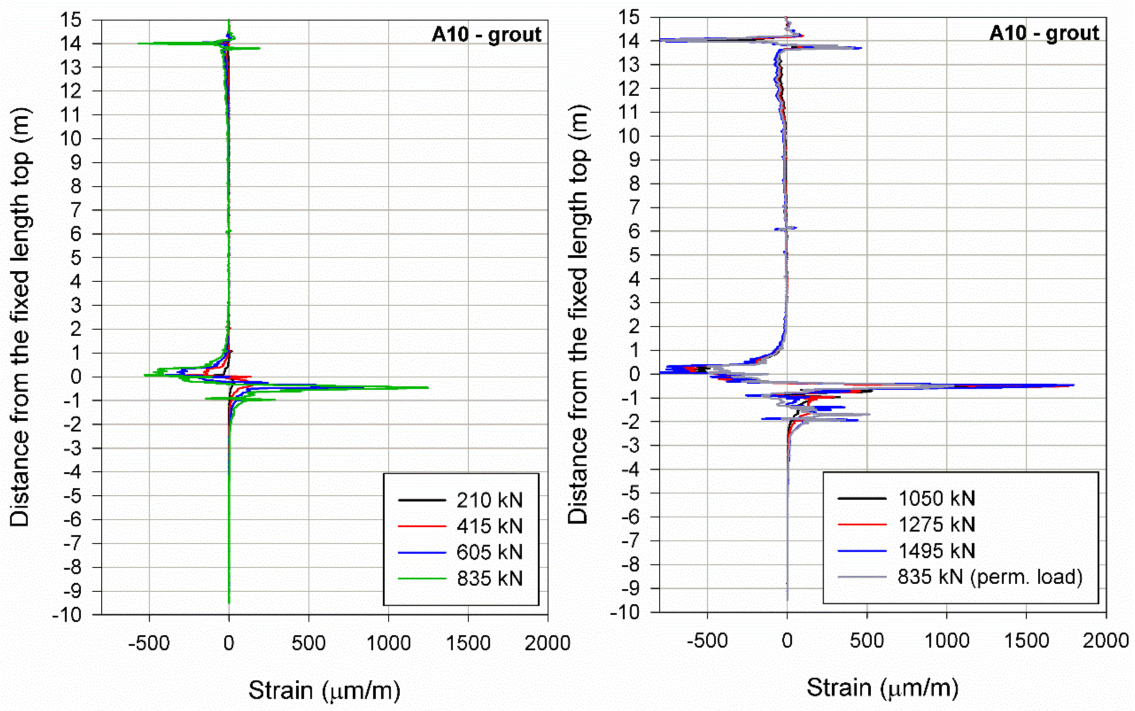

Fig. 82: Strains along the grout

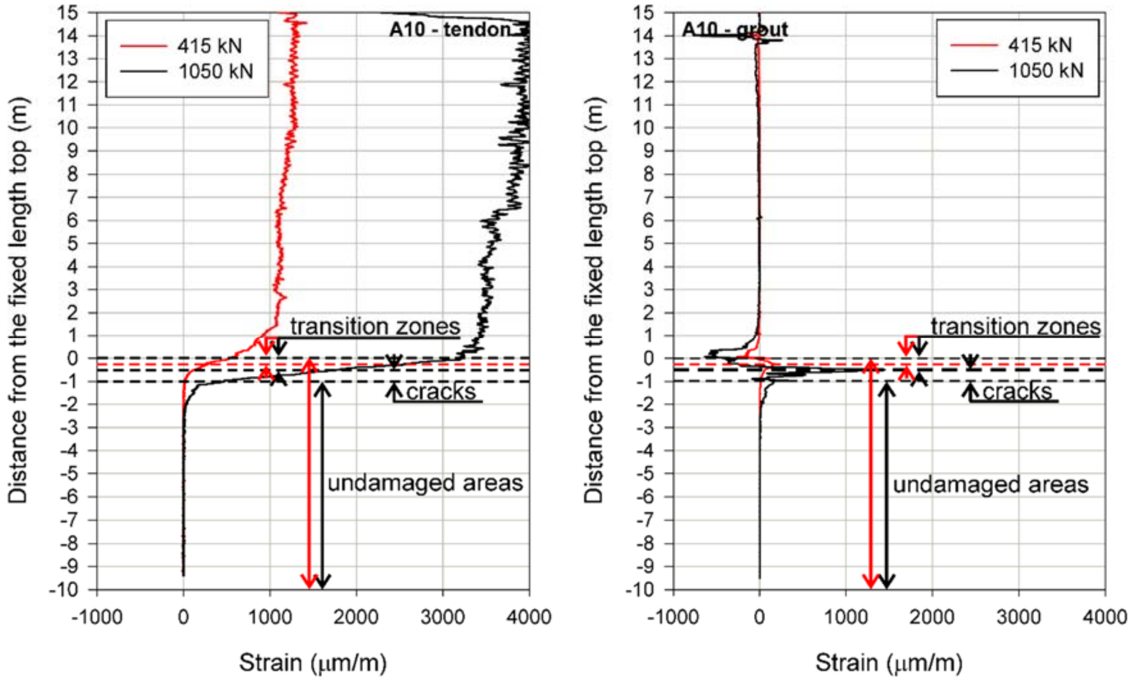

Fig. 83: Strain distribution along the tendon and the grout – different grout conditions

In Fig. 83, the transition zone is limited to 0.5 m below the proximal end of the fixed length. It is worth mentioning that, in St Kanzian, this zone extended up to 2 m considering approximately the same pullout load. Whereas for the load step of 415 kN cracking was not observed, regarding the 1050 kN step it developed within the first metre below the top of the fixed length. Below the cracked region, where the undamaged area is observed, almost the entire tendon and grout section were not activated.

In order to plot the load-displacement curve with respect to the displacements at the top of the fixed length, instead of applying Eq. 2 the strains along the tendon at the fixed length were integrated. The curve is shown in Fig. 84.

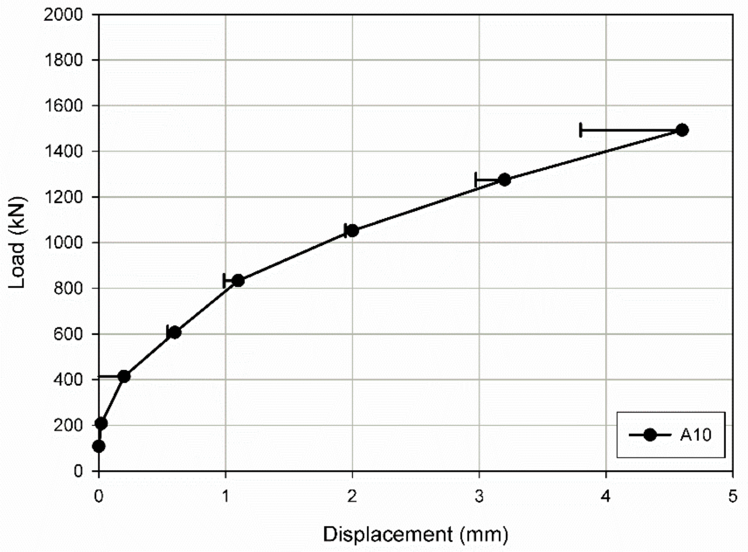

Fig. 84: In situ load-displacement curve

7.4 Numerical simulations

Numerical simulations were undertaken using the finite element software Plaxis 3D 2017 (Brinkgreve et al. 2017b). The monitored anchor was simulated with volume elements and the remaining anchors with node-to-node structural elements. Only one column of anchors was modelled and the first five anchors along the column, from the top to the bottom, were considered. The slope above the retaining wall was taken into account by an equivalent distributed load. In the numerical model, the node-to-node anchors were prestressed before the monitored one reflecting the actual in situ procedure, since the monitored anchor was the last anchor from the column to be tested. From the top to the bottom, the prestress was set to 810 kN for the second and the third anchors and to 610 kN for the last two anchors.

Regarding the monitored anchor, the grout was considered along the free and the fixed length and a gap was introduced at the tendon position along the free length. The load was applied directly at the fixed length, at the top of the tendon, by means of prescribed displacements. With respect to the node-to-node anchors, the length of these structural elements corresponded to the size of the free length. Therefore, the load was transferred directly to the rock at the end of the free length, without considering the grout material and the fixed length section. The overview of the model is shown in Fig. 85. In order to achieve a sufficiently fine mesh, cylindrical clusters were created surrounding the monitored anchor. The clusters with the materials at the free and fixed length are visualised in Fig. 86. Fig. 87 shows the 3D model geometry with the monitored anchor. In Tab. 25 general information of the calculations are presented.

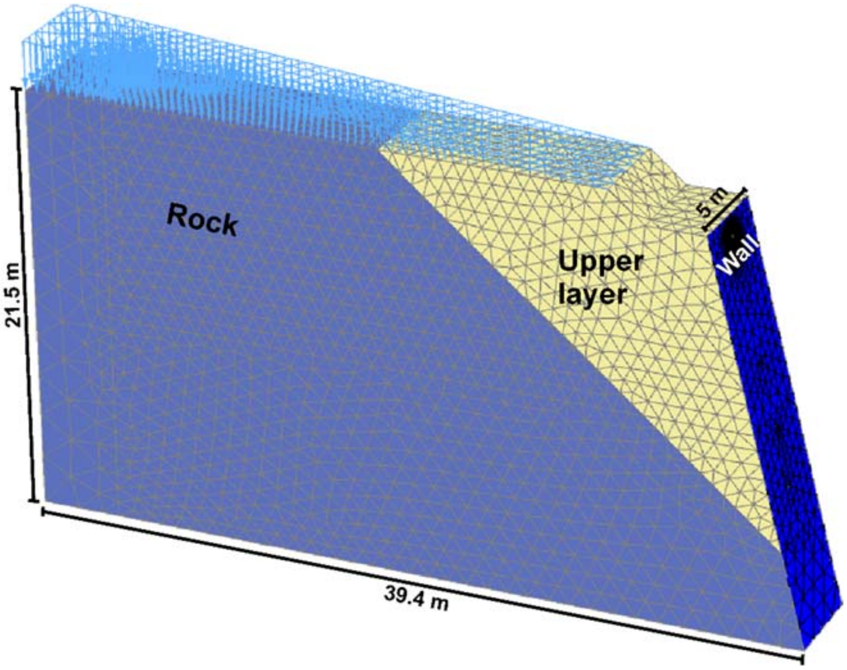

Fig. 85: Overview of the soil layers and retaining wall

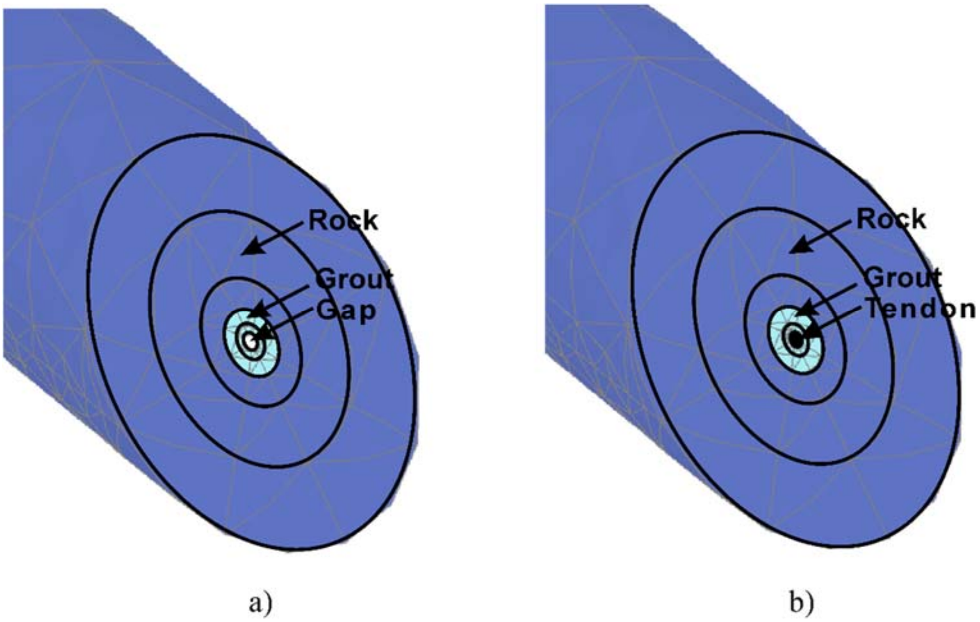

a) b)

Fig. 86: Cylindrical clusters for mesh refinement – a) free length and b) fixed length

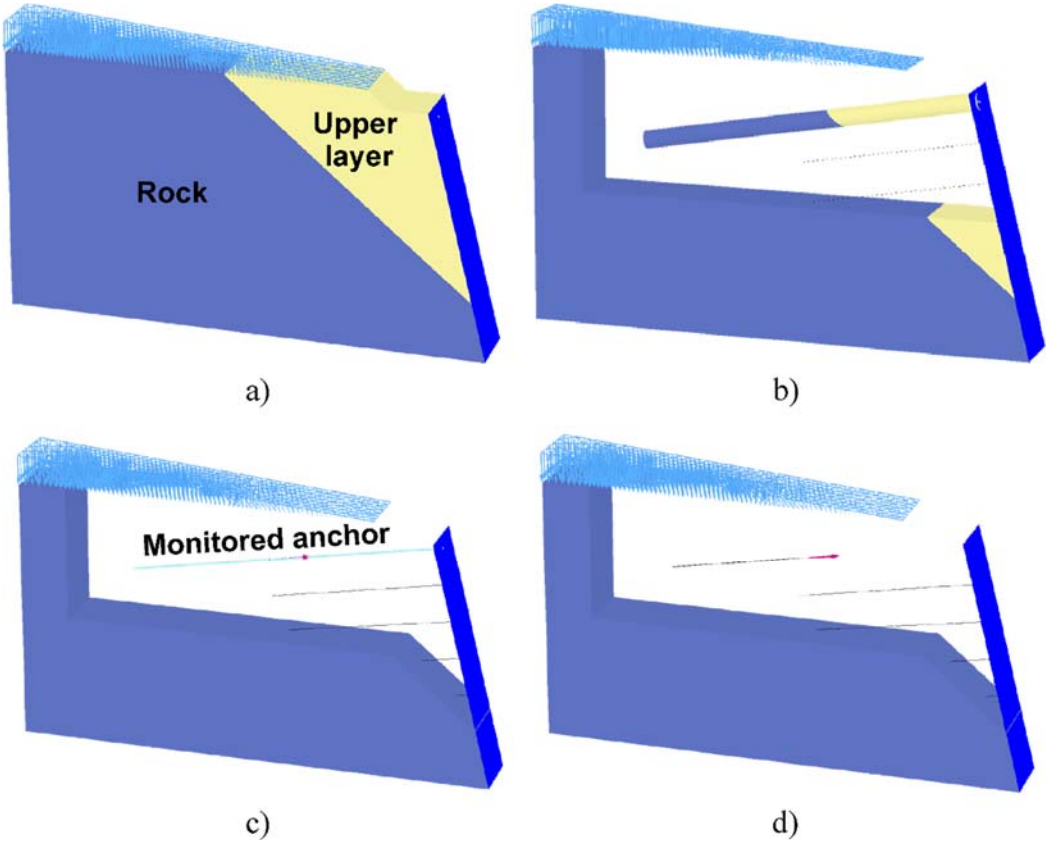

Fig. 87: Model geometry – a) ground layers; b) ground cluster for mesh refinement; c) monitored anchor (grout) and d) monitored anchor (tendon)

Tab. 25: General information of the numerical simulations

Simulation	**Software**	**Number of elements**	**Element type**
Simulation 1	Plaxis 3D – 2017	320 293	10-noded
Simulation 2	Plaxis 3D – 2017	320 293	10-noded
Simulation 3	Plaxis 3D – 2017	320 293	10-noded
Simulation 4	Plaxis 3D – 2017	320 293	10-noded
Simulation 5	Plaxis 3D – 2017	320 293	10-noded

7.4.1 Material parameters

Two ground layers were considered and they are referred herein as upper soil layer and rock. The parameters suggested in the geotechnical report for the upper layer (Tab. 24) were maintained but, with respect to the rock material, a parametric study was carried out. The Mohr-Coulomb constitutive model was selected for the soil and the rock and, concerning the rock, the option “Tension cut-off” was enabled and the tensile strength was determined considering the ratio between uniaxial tensile strength (f_t) and uniaxial compressive strength (f_c) as 0.1. After defining the cohesion intercept and the friction angle, the rock uniaxial compressive strength was determined by drawing the Mohr circle ($\sigma'_3 = 0$) that touches the failure envelope. The rock and the upper soil layer unit weight were 24 and 21 kN/m^3, respectively.

With regard to the grout and tendon materials of the monitored anchor, the Concrete model was assigned to the grout and the steel tendon was simulated using a linear elastic material (E_{tendon} = 160 GPa). In the same way as it was performed for the other simulations, the strands were modelled as one equivalent strand, leading to an equivalent diameter of 44.4 mm. Because the second and the third anchors had 8 strands and the fourth and the fifth had 6 strands, the normal stiffness assigned to the node-to-node anchors varied accordingly. The wall was modelled as a plate element. The tendon and the grout unit weight were 78.5 and 25 kN/m³, respectively. The parameters adopted are shown from Tab. 26 to Tab. 29.

Tab. 26: Material parameters (Concrete model, grout)

Parameter	**Value**
E (GPa)	16.5
ν	0.20
f_c (MPa)	32.0
f_t (MPa)	2
f_{c0n}	0.05
f_{cfn}	0.95
f_{cun}	0.10
$\varepsilon_{cp}{}^{p}$	-0.0013
G_c (kN/m)	3
f_{tun}	0.05
G_t (kN/m)	0.01
a	19
φ_{max} (°)	48

Tab. 27: Material parameters (Mohr-Coulomb model, upper layer and rock)

Parameter	**Value – Upper layer**	**Value – Rock**
E (MPa)	70	500/5000/10 000
ν'	0.3	0.3
c' (kN/m²)	2	40/100
φ' (°)	35	40
f_t (kN/m²)	0	17/40

Tab. 28: Material parameters (Plate, wall)

Parameter	**Description**	**Value**
d (m)	Equivalent thickness	1
E_1 (GPa)	Young’s modulus in first axial direction	30
E_2 (GPa)	Young’s modulus in second axial direction	30

Tab. 29: Material parameters (Node-to-node anchors, adjacent anchors)

Parameter	**Description**	**Value**
EA (kN)	Normal stiffness	250 000[1]/200 000[2]

[1] Second and third anchors from top to bottom

[2] Fourth and fifth anchors from top to bottom

7.4.2 Numerical results

The numerical results are presented below. The first simulation was carried out taking into account the rock parameters suggested in the geotechnical report. However, after comparing the calculated results with the in situ measurements, it was observed that the model behaviour was significantly softer than the in situ one. Therefore, the rock Young's modulus was increased to 5000 and 10 000 MPa. Additional simulations were undertaken assuming the cohesion as 100 kPa instead of 40 kPa and the tension cut-off was adjusted accordingly. Tab. 30 shows the parameters combination employed in the calculations.

Tab. 30: Rock parameters employed in the numerical model

Numerical simulation	**E_{rock} (MPa)**	**c_{rock} (kN/m²)**	**f_t (kN/m²)**
Simulation 1	500	40	17
Simulation 2	5000	40	17
Simulation 3	5000	100	40
Simulation 4	10 000	40	17
Simulation 5	10 000	100	40

The load-displacement curves are shown in Fig. 88. The displacements are referred to the fixed length top and the in situ curve was obtained by integrating the fibre optic measurements along the fixed length.

The best agreement was achieved if the Young's modulus is set as 10 000 MPa and the cohesion as 100 kPa. However, it is notable that the difference between the numerical curves employing E_{rock} = 5000 MPa and E_{rock} = 10 000 MPa is not very significant. This aspect will be further discussed below.

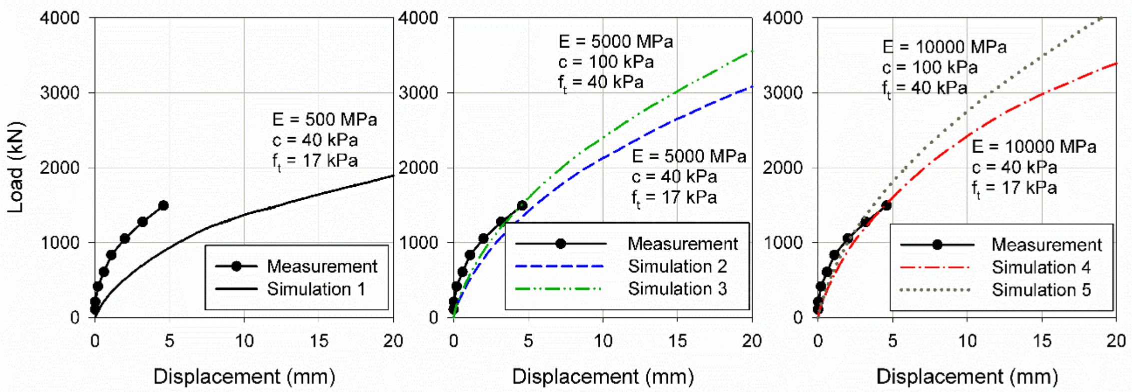

Fig. 88: In situ and numerical load-displacement curves

The measured strain distribution along the tendon is compared with the numerical simulations from Fig. 89 to Fig. 93. In comparison with the in situ measurements, the active portion of the tendon is significantly larger if the recommended parameters are employed. The best fit was obtained with simulation 5. However, as observed for the load-displacement behaviour, the difference between the strains profile obtained with E_{rock} = 5000 and 10 000 MPa is almost negligible for the same cohesion intercept.

The tension softening parameter H_t is plotted against the in situ grout strains. The H_t parameter evolution is shown from Fig. 94 to Fig. 98 for four selected load steps and the peaks observed in the fibre optic measurements are interpreted as cracking.

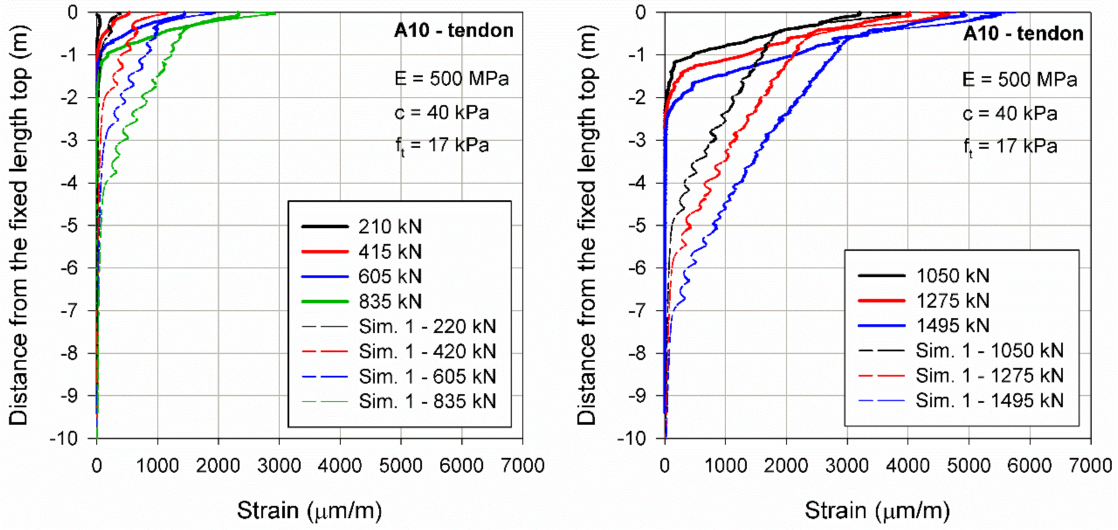

Fig. 89: Strain distribution along the tendon – in situ *vs* simulation 1

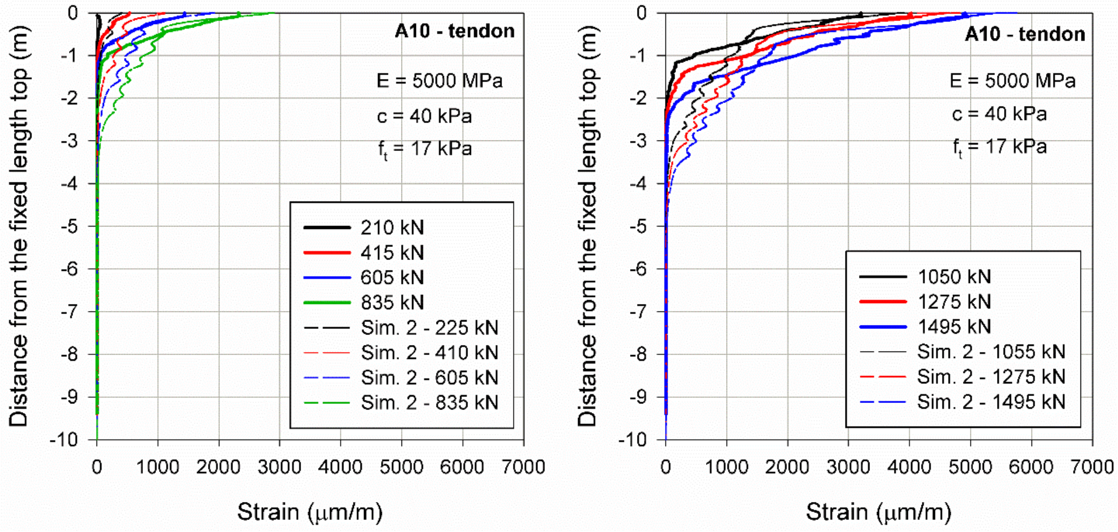

Fig. 90: Strain distribution along the tendon – in situ *vs* simulation 2

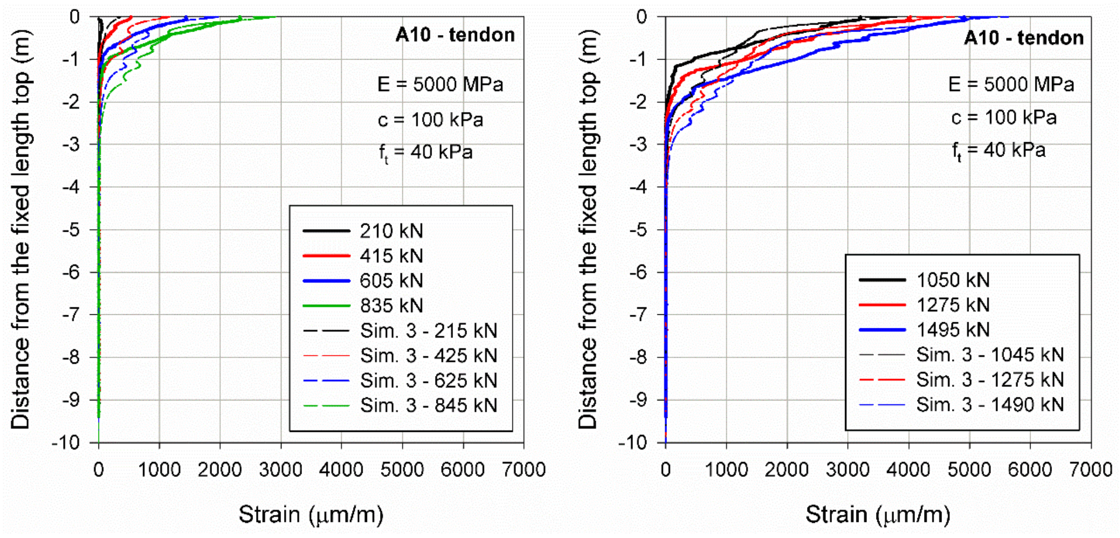

Fig. 91: Strain distribution along the tendon – in situ *vs* simulation 3

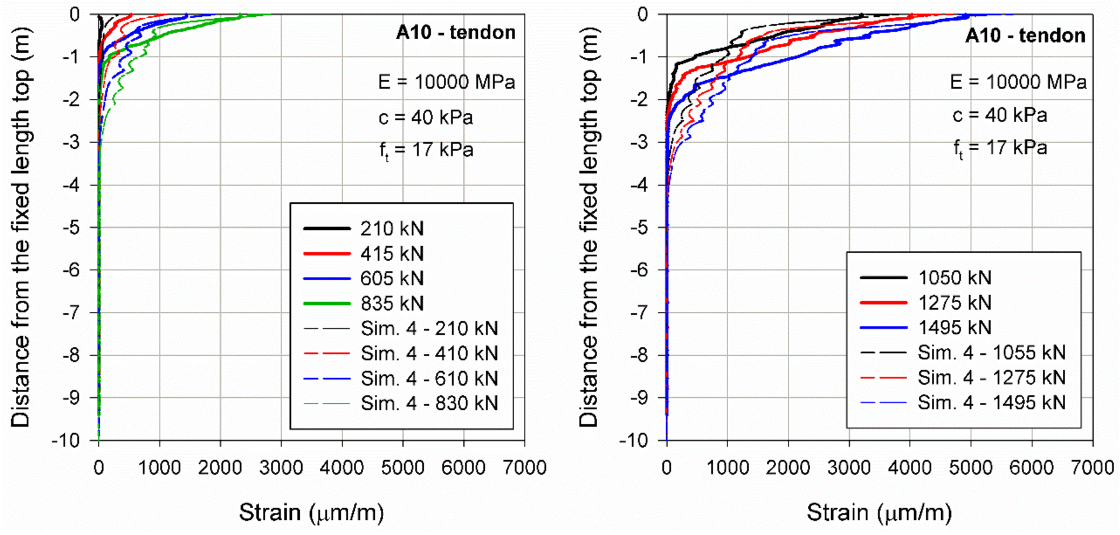

Fig. 92: Strain distribution along the tendon – in situ *vs* simulation 4

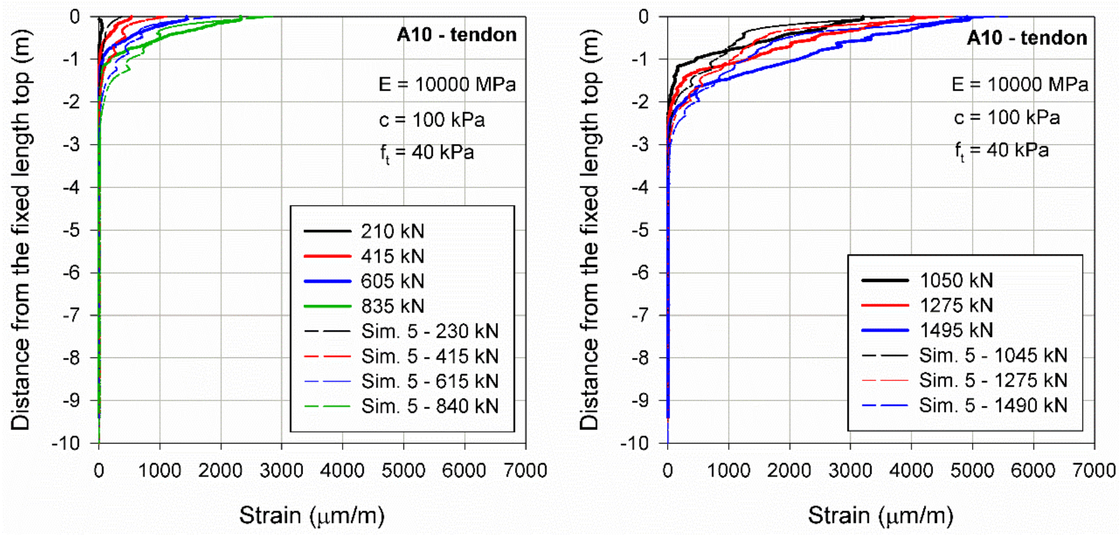

Fig. 93: Strain distribution along the tendon – in situ *vs* simulation 5

It is clear from Fig. 94 that the grout section where numerical cracking is observed is too large if the recommended parameters are employed. The results obtained with these parameters are significantly different from the results achieved with the increased parameter values. However, comparing the simulations with the same cohesion value and the stiffness set as 5000 and 10 000 MPa, the cracking evolution is only slightly different. With regard to the cohesion increase from 40 to 100 kPa, cracking is more pronounced for 40 kPa and the effect on the numerical result is more significant than the effect of the stiffness increase, indicating that failure in the rock is reached at some points.

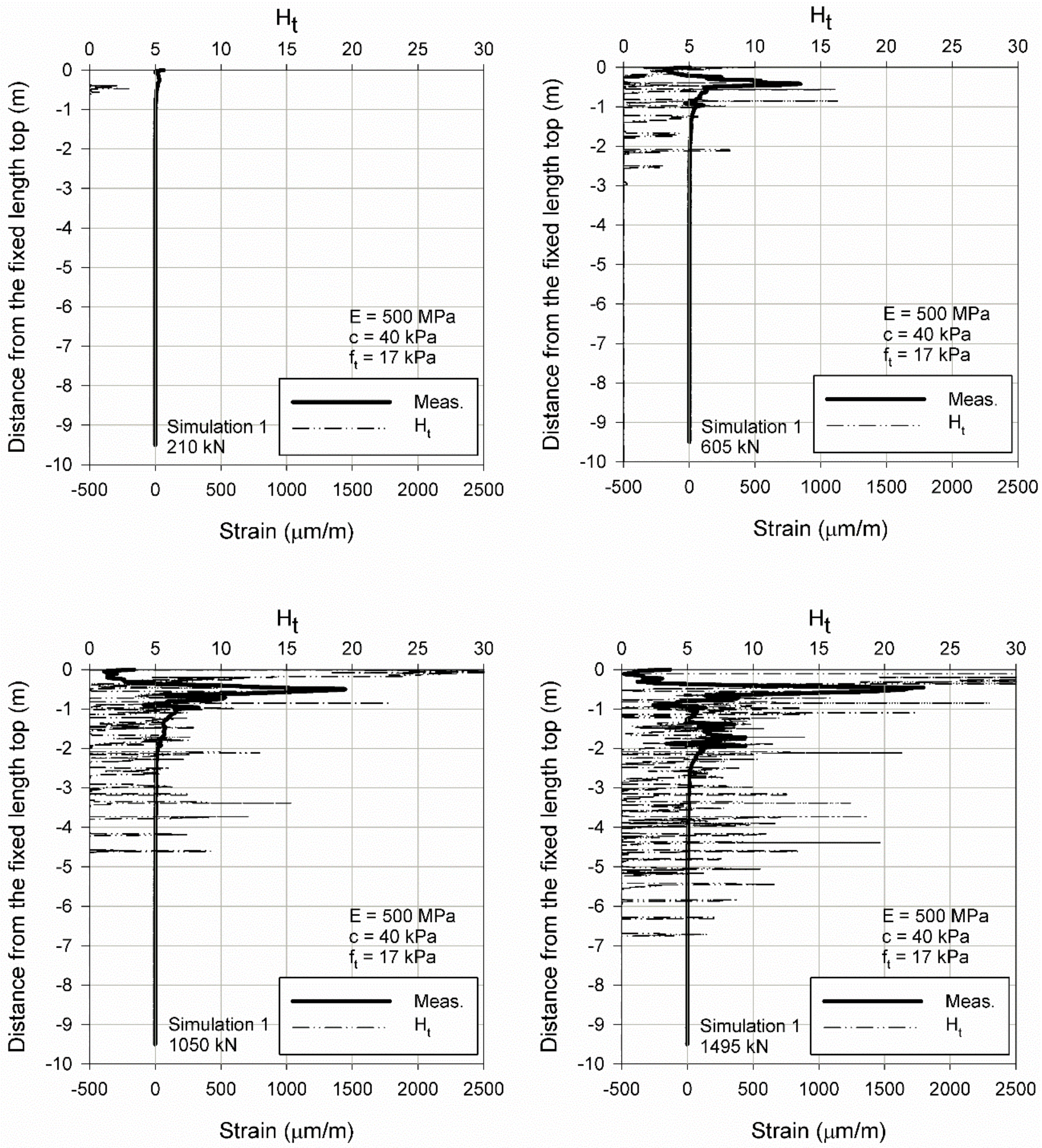

Fig. 94: Measured strain distribution along the grout at the fixed length and comparison with the numerical parameter H_t (simulation 1)

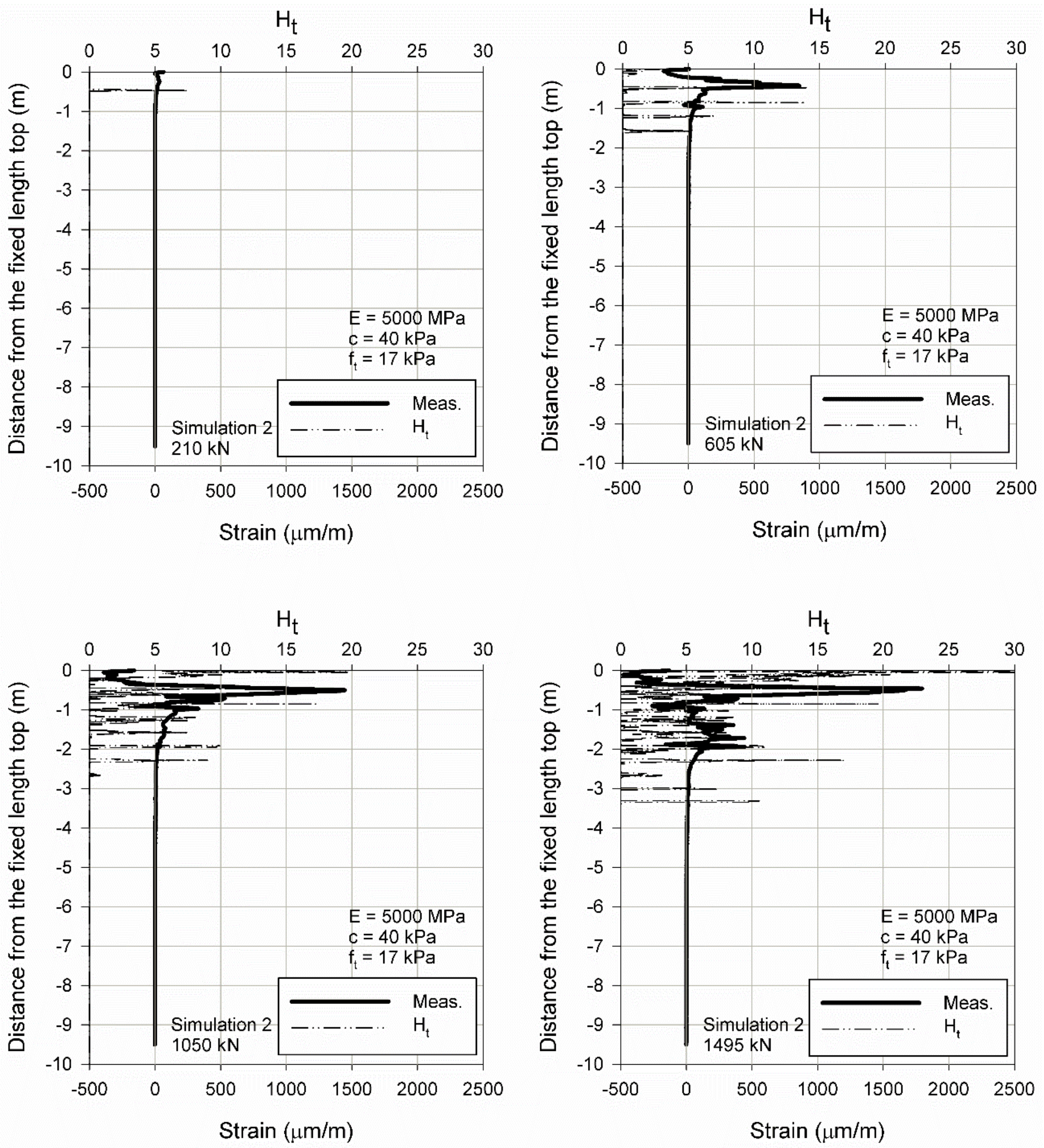

Fig. 95: Measured strain distribution along the grout at the fixed length and comparison with the numerical parameter H_t (simulation 2)

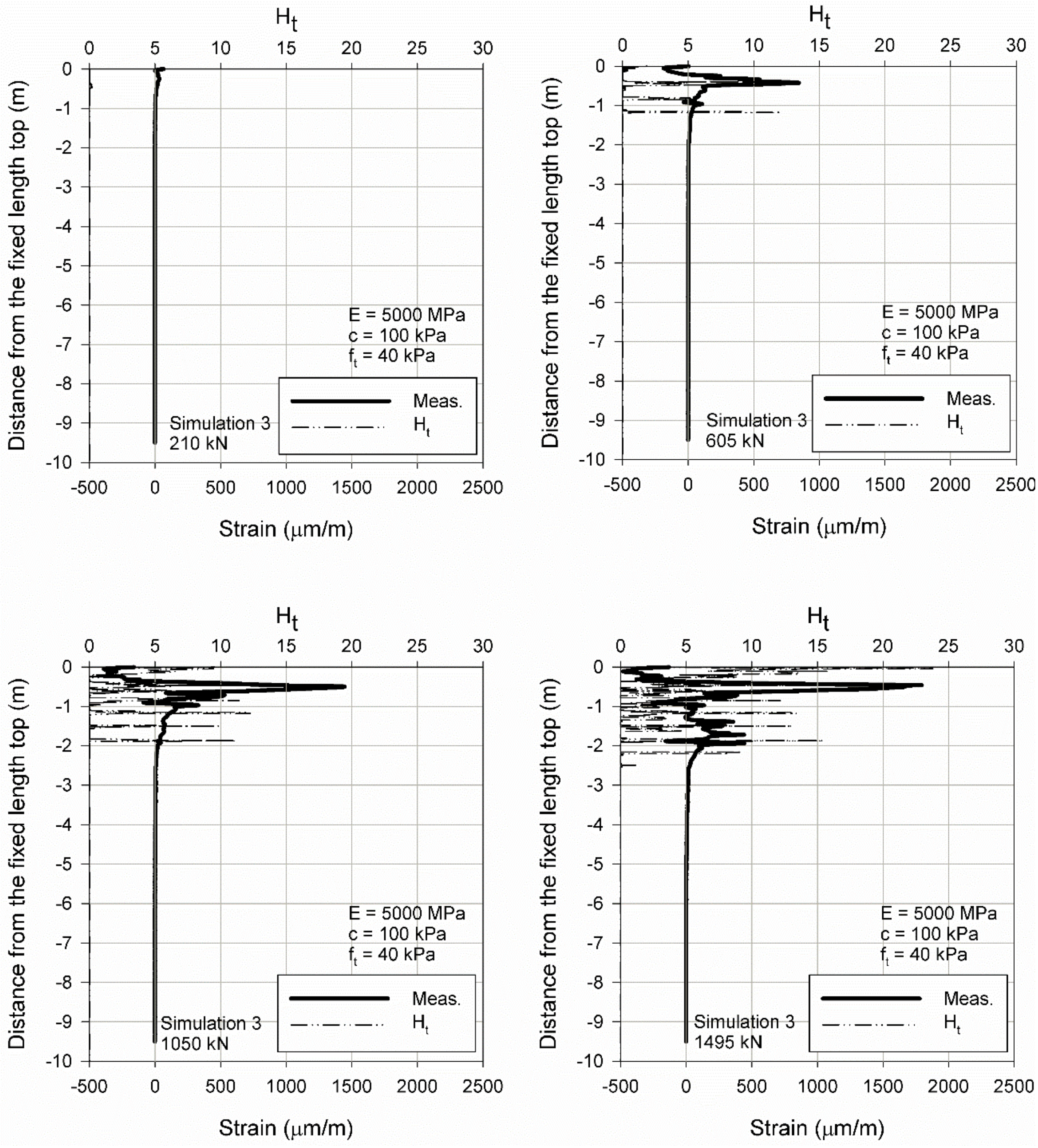

Fig. 96: Measured strain distribution along the grout at the fixed length and comparison with the numerical parameter H_t (simulation 3)

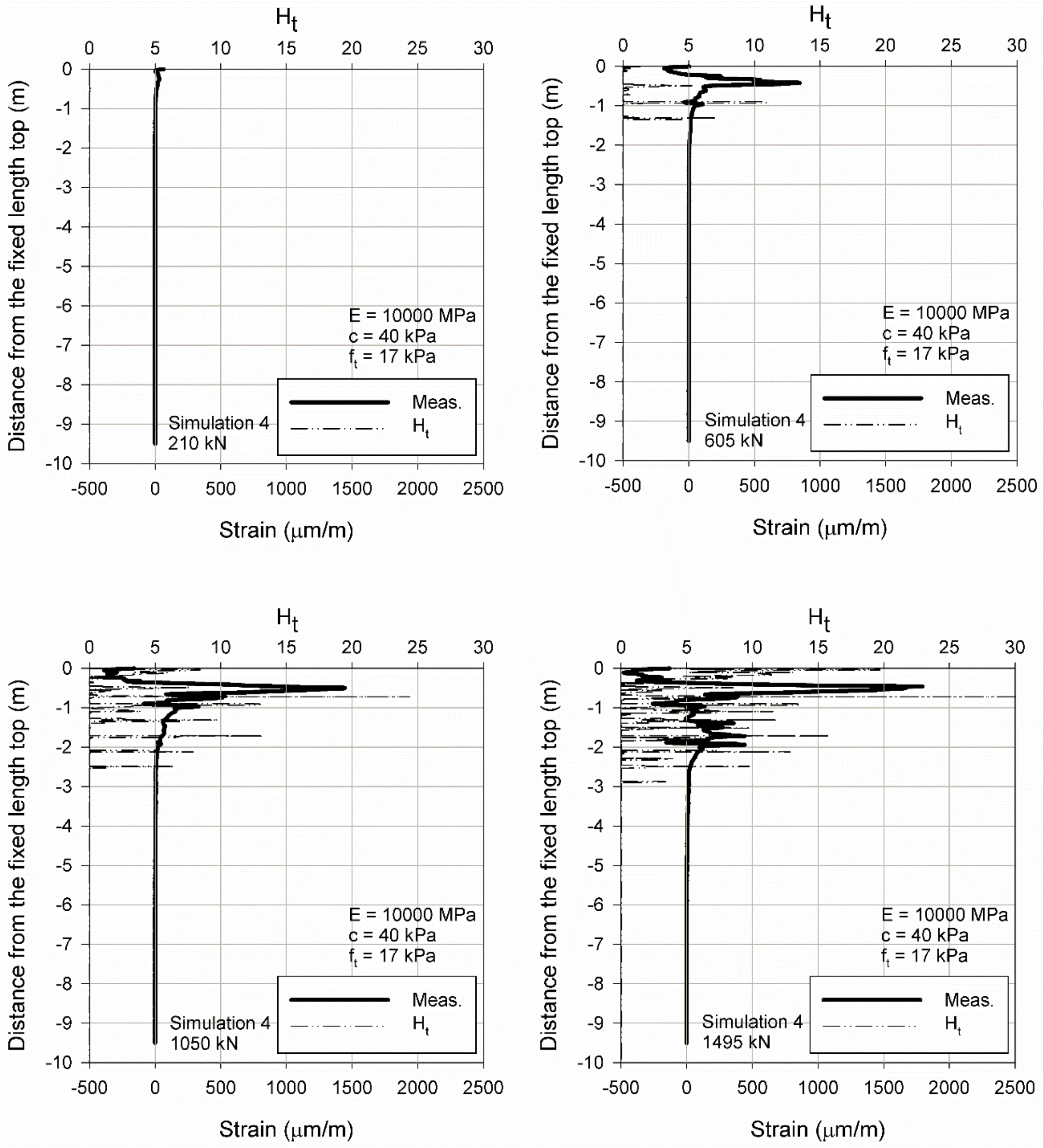

Fig. 97: Measured strain distribution along the grout at the fixed length and comparison with the numerical parameter H_t (simulation 4)

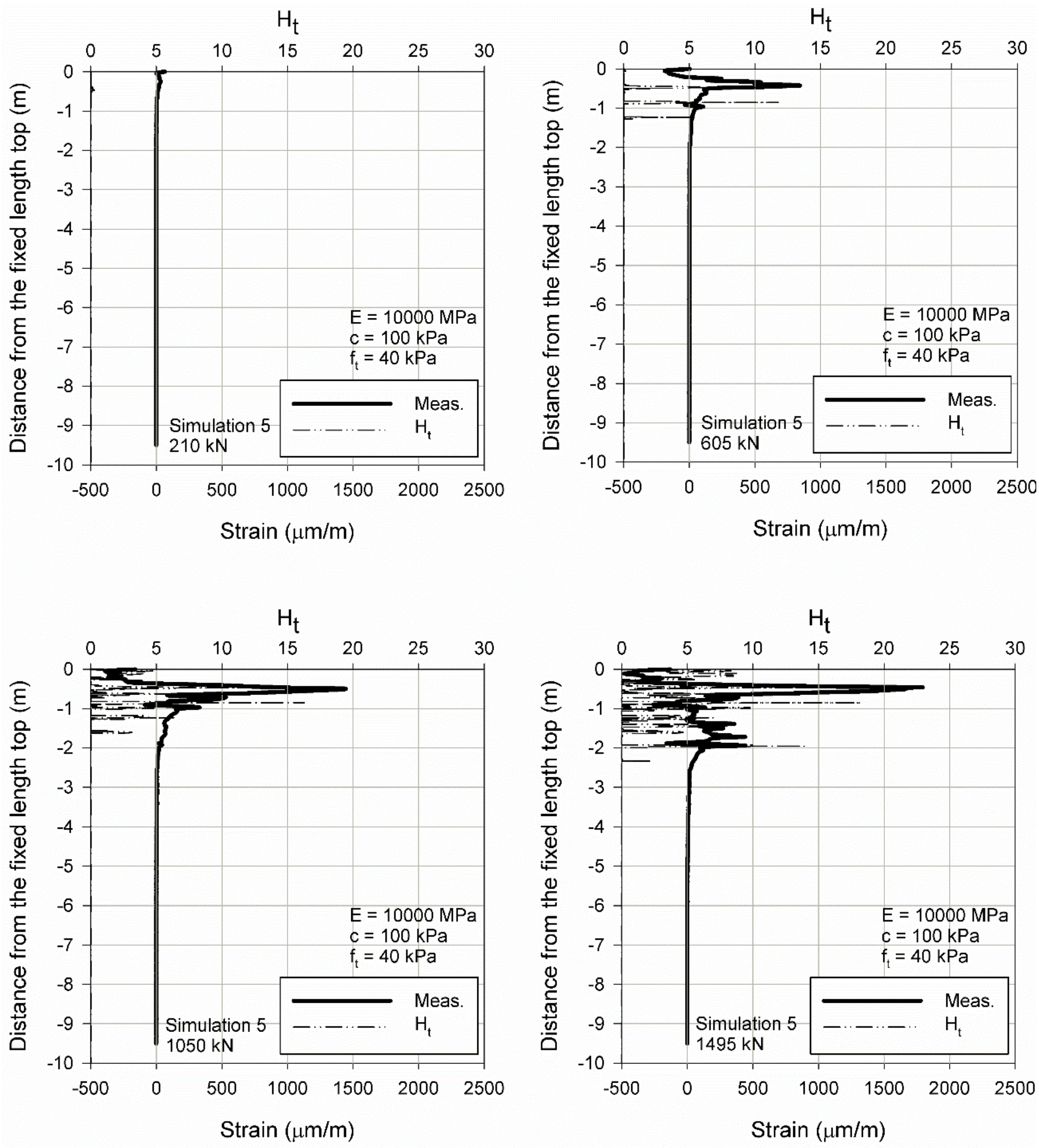

Fig. 98: Measured strain distribution along the grout at the fixed length and comparison with the numerical parameter Ht (simulation 5)

The relative shear stress is the mobilised shear stress divided by the maximum value of shear stress for the case where the Mohr's circle is expanded to touch the Coulomb failure envelope. This parameter indicates the proximity of the stress point to the failure envelope (Brinkgreve et al. 2019b).

In order to plot the relative shear stress, the distance between the stress points and the fixed length top was calculated. Because the stress points are distributed along the cylindrical interface surface, some oscillations occur if two or more stress points have approximately the same distance to the top of the fixed length but show different shear stresses values. This situation is illustrated in Fig. 99, where the stress points (purple dots) and the relative shear stresses are depicted along the interface at the anchor fixed length. In this figure detail, two stress points that have the same X coordinate and differ slightly with respect to the Y and Z coordinates were selected. Both points have approximately the same distance to the proximal end of the fixed length but the relative shear stresses are significantly different.

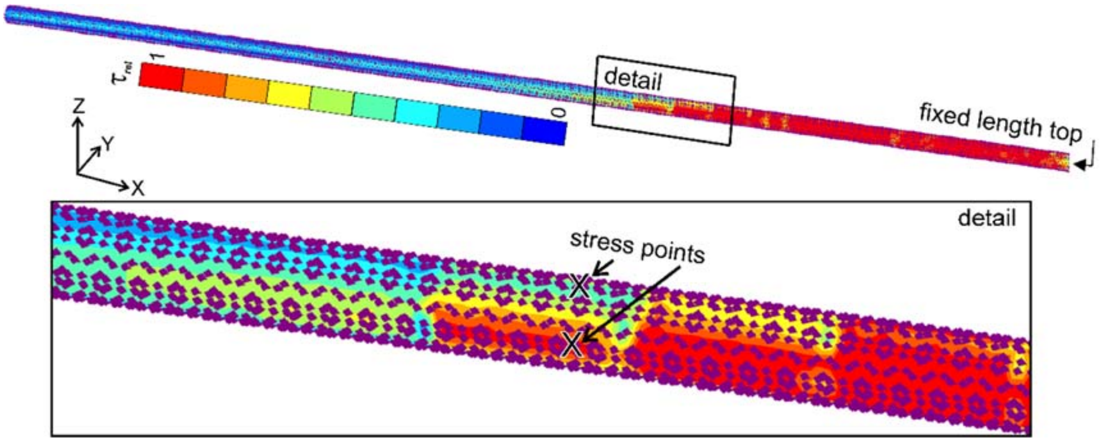

Fig. 99: Relative shear stresses along the interface and stress points

In Fig. 100 to Fig. 102 the relative shear stress along the grout-rock interface at the fixed length is presented. Above every plot and for each load step, the section of the fixed length at which the maximum shear stress is reached ($\tau_{rel} = 1$) is given. Considering simulation 1, the part of the rock-grout interface where cracking in the grout evolves is almost the same as the part where the maximum shear stress is reached. Comparing simulations with the same strength parameters as simulation 1, the interface section where shear stresses are fully mobilised is larger for the lower stiffness value employed. Therefore, in this case cracking evolution and maximum shear stress mobilisation are not only dependent on strength parameters but also on the rock stiffness.

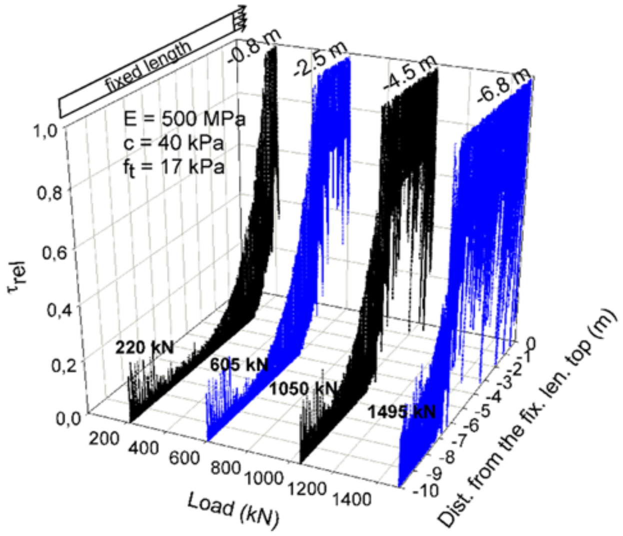

Fig. 100: Relative shear stresses along the grout-rock interface (simulation 1)

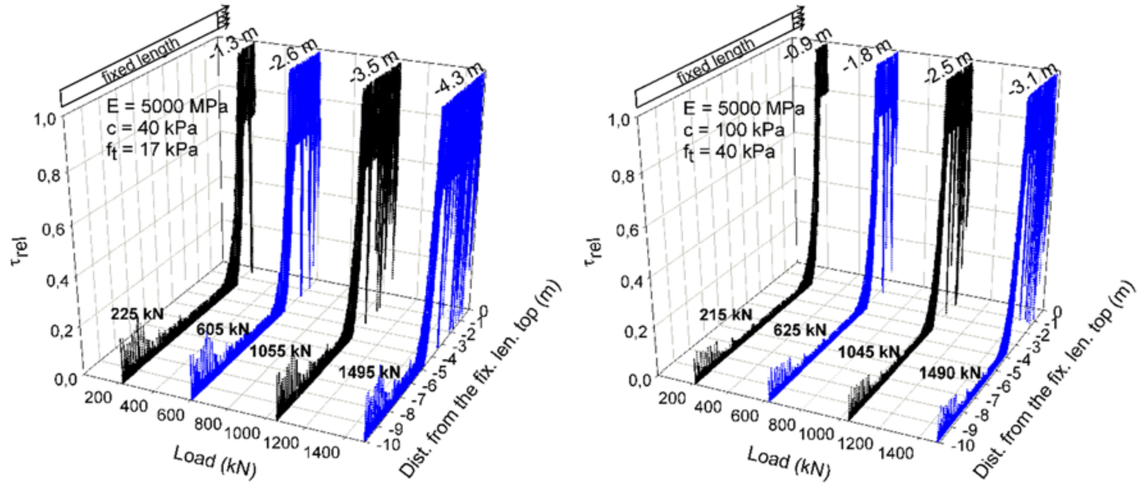

Fig. 101: Relative shear stresses along the grout-rock interface (simulations 2 and 3)

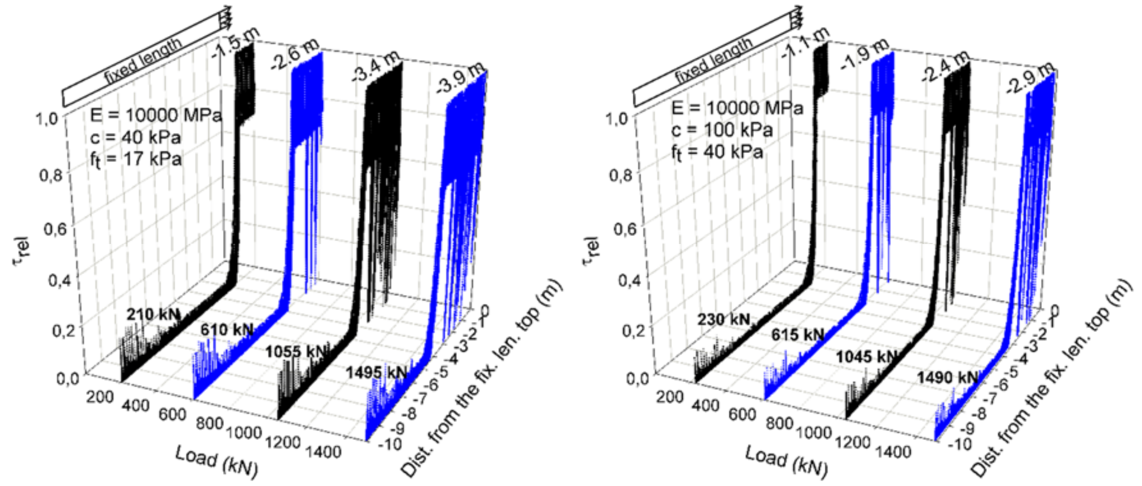

Fig. 102: Relative shear stresses along the grout-rock interface (simulations 4 and 5)

Regarding the other simulations, the part of the fixed length where the maximum shear stress evolves is larger than the one where cracking occurs. It is also remarkable that, taking into account the same cohesion intercept, for simulations with E_{rock} = 5000 and 10 000 MPa, $\tau_{rel} = 1$ is reached along almost the same interface section. In cases where the rock stiffness is within the same order of magnitude as the ground stiffness, the maximum shear stress mobilisation remains essentially the same. It is also worth mentioning that increasing the cohesion intercept from 40 kPa to 100 kPa not only results in a decrease of relative shear stress by increasing the maximum shear stress, but also cracking propagation in the grout was reduced.

7.5 Summary

In July 2018 a fibre optic monitored rock anchor was tested. The anchor was installed on a retaining wall and during the pullout test the anchor was not brought to failure because it was part of the construction. Although the anchor was 10 m long at the fixed length, the active portion of the bond length at the maximum load step was only 2.5 m and cracking in the grout was restricted to the first 2 m of the fixed anchor length.

Due to insufficient information concerning the rock parameters, a parametric study was undertaken after the anchor pullout test to adjust the numerical results according to the in situ measurements. Therefore, the rock Young's modulus and the cohesion were modified and the results compared with the in situ measurements.

The first numerical simulation was carried out assuming E_{rock} = 500 MPa and c_{rock} = 40 kPa and the numerical model showed considerable softer behaviour if compared to the measurements. For this simulation, the section where shear strength in the grout-rock interface was reached was approximately the same section where cracking in the grout was observed. A satisfactory agreement was obtained after increasing the Young's modulus to 5000 and 10 000 MPa and the cohesion to 100 kPa. Increasing the rock cohesion from 40 to 100 kPa reduced cracking propagation in the grout. Moreover, although the grout parameters were maintained, cracking was more pronounced for the softer rock condition employed in the first simulation. Therefore, the results showed that shear failure in the grout-rock interface is reached along a larger section for softer ground materials. Because cracking in the grout increases if shear failure in the interface occurs, the grout condition is dependent on the ground stiffness.

Despite this stiffness dependency observed in the numerical results, the results were not very different if the rock Young's modulus was increased from 5000 to 10 000 MPa. In these cases, the rock stiffness is within the same order of magnitude as the grout stiffness and the relative movement between both materials is reduced. For this reason, comparing the same load step, the section at which shear strength in the grout-rock interface is reached is almost the same for both numerical simulations.

8 Ljubljana-test

8.1 Anchor description

During a deep excavation in the centre of Ljubljana, the installation of a fibre optic monitored anchor was carried out. The pit support was part of the construction of an 80 m high hotel (A-Tower Ljubljana project). The total excavation depth was about -14.6 m. The approximated monitored anchor location is visualised in Fig. 103, which shows the terrain before the excavation works started.

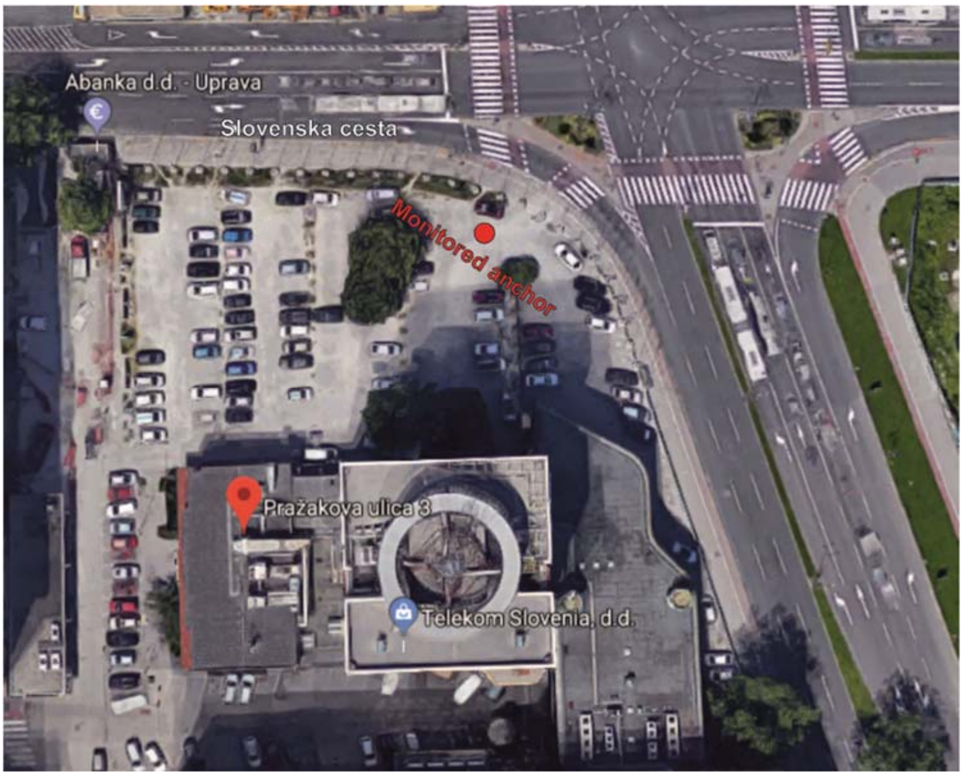

Fig. 103: Approximate location of the monitored anchor (Google Maps 2013)

The excavation was supported by means of overlapping Soilcrete columns and temporary anchors. The fibre optic monitored anchor was installed between two temporary anchor columns and between the first and the second rows, from the top to the bottom of the wall. The horizontal distance between two temporary anchors was 3.4 m and the vertical distance was 3 m. The monitored anchor inclination in relation to the horizontal axis was 10°.

The monitored anchor was 6 m long at the free length and 6 m long at the fixed length. 8 strands were employed (8 x 15.7 mm using high grade steel Y1860), 2 of which were monitored with fibre optic sensors. The borehole diameter was 200 mm. The fibres were glued along the entire anchor length on January 17 2019 and the cables for the grout measurements were installed on February 11 2019 (Fig. 104).

Fig. 104: Fibre optic sensors for grout measurements

Also on February 11, the anchor was installed and primary grouting was carried out. Additional grout under pressure was injected to fill in the space between the soil and the corrugated pipe along the fixed length. During grouting, approximately 200 L of cement were injected and the pressure was about 38 bar. Post-grouting occurred some hours after the anchor was installed, when 153 L of cement were applied under a pressure of about 12 bar. The pullout test was performed on February 28 2019.

A cross-section showing the fibre optic monitored anchor and the temporary anchors is presented in Fig. 105 and the vertical distance between the monitored anchor and the top of the excavation level was about 6 m.

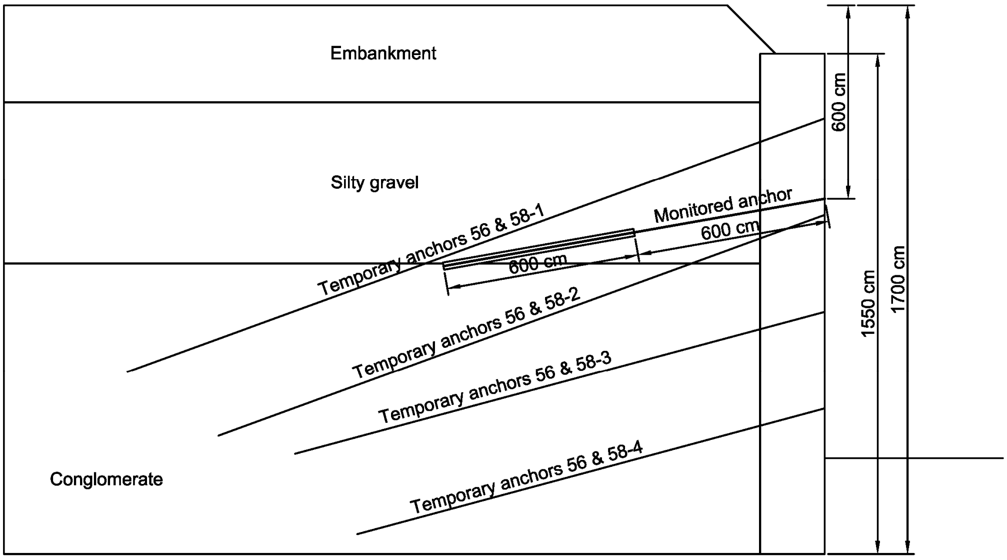

Fig. 105: Cross-section showing the monitored and the temporary anchors

8.2 Soil description and calibration

Soil investigations were carried out on 7 different locations at the excavation area. Standard penetration tests and pressuremeter tests were performed. The boreholes were identified as V-1, V-2, V-3, V-4, V-5, V-6 and V-7 (Fig. 106), and boreholes V-4 and V-6 were the closest to the monitored anchor. The distance between V-4 and V-6 to the monitored anchor was approximately 15 m.

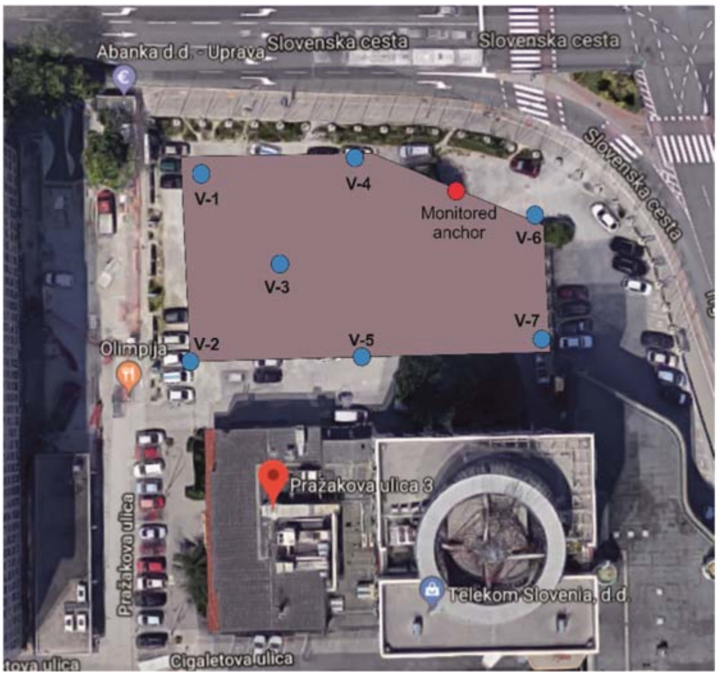

Fig. 106: Boreholes position

The soil investigation indicated the predominance of coarse-grained soil and the presence of conglomerate layers along the borehole. The position of these layers varied in each borehole, but in all cases it started below the depth of -7 m. The layers distribution for boreholes V-4 and V-6 is shown in Tab. 31.

Tab. 31: Soil layers distribution

Soil layer	Depth (V-4)	Depth (V-6)
Fill	0 to -2.3 m	0 to -2.7 m
Silty gravel	-2.3 to -9.5 m	-2.7 to -8.0 m
Conglomerate	-9.5 to -17.5 m	-8.0 to -16.9 m
Clayey sand and gravel	-17.5 to -30.0 m	-16.9 to -30.0 m

The water table was at -20 and -21 m depth for boreholes V-4 and V-6, respectively. Since the fibre optic monitored anchor was 12 m long and had an inclination of 10°, considering the borehole V-6 which was closer to the monitored anchor, almost the entire anchor can be assumed to be positioned within the silty gravel soil layer, as shown in Fig. 105.

Tab. 32 shows the grain size distribution for all boreholes. In general, it can be observed that the fine content increases with increasing depth, except for the sample V-4 located between -8.3 and -8.5 m, which shows a decrease in the fine content in comparison to the sample between -5.5 and -5.7 m.

Tab. 32: Grain size distribution

Borehole	**Depth**	**Fines**	**Sand**	**Gravel**
V-1	-3.5 to -3.7 m	6.5%	18.5%	75.0%
	-6.3 to -6.5 m	13.1%	31.9%	55.0%
V-2	-3.7 to -3.9 m	5.4%	26.6%	68.0%
	-6.5 to -6.7 m	14.5%	34.5%	51.0%
V-3	-4.8 to -5.0 m	9.6%	21.4%	69.0%
	-8.5 to -8.7 m	18.3%	24.7%	57.0%
V-4	-5.5 to -5.7 m	14.3%	26.7%	59.0%
	-8.3 to -8.5 m	9.0%	18.0%	73.0%
V-5	-5.5 to -5.7 m	15.1%	28.9%	56.0%
	-7.2 to -7.5 m	17.0%	30.0%	53.0%
V-6	-6.2 to -6.5 m	13.5%	28.5%	58.0%
	-18.2 to -18.5 m	15.3%	25.7%	59.0%
V-7	-6.0 to -6.2 m	11.1%	23.9%	65.0%

Since the pressuremeter tests were performed for deep foundation design, all the tests were carried out below -17 m. The pressuremeter tests were performed only for the holes V-5 and V-6 and below the water table, except for the test V-6-1. The test results are shown in Tab. 33, where E_M is the pressuremeter modulus and E_R is the reloading modulus. These test results were used to determine the soil stiffness parameters employed in the numerical prediction of the anchor pullout test.

Tab. 33: Pressuremeter tests results

Identification	**Depth (m)**	**E_M (MPa)**	**E_R (MPa)**	**E_R/E_M**
V-5-1	20.9	85	380	4.5
V-5-2	23.4	45	340	7.6
V-5-3	25.4	110	1000	9.1
V-5-4	27.3	45	150	3.3
V-6-1	17.9	20	65	3.3
V-6-2	22.4	12	67	5.6
V-6-3	23.6	26	250	9.6

Three soil types were considered for the pressuremeter tests calibration and were based on the core drilling performed at the location where the tests were carried out. The first layer is a fill and is identified between 0 and -3 m. The second layer is a silty gravel layer, observed between -3 and -8 m. The following layer is a conglomerate, between -8 and -17 m and the last soil layer is a gravel layer between -17 and -40 m with the same material parameters as the second layer. The position at the centre of the measuring cell varies for each test, but in all cases the cell is located within the last gravel layer. The water table is considered at -20.4 m. An overview of the soil layers is presented in Fig. 107a.

The pressuremeter tests selected for the calibration were the tests identified as V-5-1 and V-5-2. These tests were selected due to the presence of conglomerate and sand layers observed in the other tests, which probably affected the in situ results. The pressuremeter tests were carried out with a slotted steel tube. It is important to mention that, considering the test V-5-1, a pre-bored hole (diameter of 66 mm) was performed and, for the test V-5-2, the hole was not pre-drilled. In fact, initially an attempt to pre-drill was carried out but the hole collapsed.

The 2D numerical model was axisymmetric and the axis of symmetry was the vertical one. The pressure was applied by a uniform distributed load along 66 cm, which was the total length of the cell (measuring cell and guard cells). For simulating the test V-5-1, due to the pre-bored hole, an excavation phase with lateral restrained displacements was performed before the pressure was applied. The restrained displacement condition was not performed along the membrane length, where the soil was free to move. Fig. 107b shows the prescribed load and the restrained displacement detail.

The pressuremeter tests were performed at higher depths in comparison with the anchor depth, which was installed at about -6 m from the ground surface. However, the grain size distribution in Tab. 32 for the borehole V-6 indicates that the sample located between -18.2 and -18.5 m shows very similar grain size distribution in comparison to the sample identified between -6.2 and -6.5 m. For this reason, the same material type identified during the tests was considered for the soil layer where the anchor was installed.

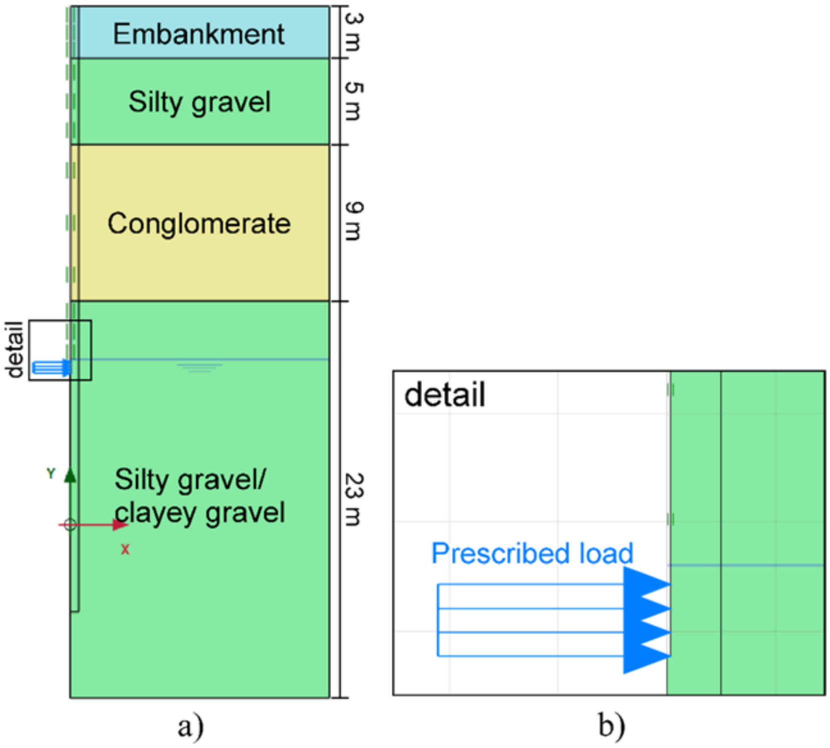

Fig. 107: Pressuremeter test geometry – a) soil layers and b) prescribed load detail

Presssuremeter test V-5-1

The first attempt to calibrate the pressuremeter test V-5-1 (calibration 1) was conducted by back calculating the stiffness parameters of the gravel layer. The HSsmall model was employed for this layer. The ratio between the Ménard modulus (E_M) and the oedometer modulus (E_{oed}) was given by the in situ result and was 0.5. The oedometer modulus at -20.9 m depth was then determined as 170 MPa (85 MPa/0.5). The reference oedometer stiffness ($E_{oed,ref}$) which should be employed in the HSsmall model was back calculated as follows (Eq. 5):

$$E_{oed} = E_{oed,ref} \left(\frac{c' \cos \varphi' - \sigma'_1 \sin \varphi'}{c' \cos \varphi' + p_{ref} \sin \varphi'} \right)^m \tag{5}$$

In Eq. 5, c' is the effective cohesion, φ' is the effective friction angle, σ'_1 is the major effective principal stress, p_{ref} is a reference pressure equal to 100 kPa and m is the amount of stress dependency (power). The effective cohesion, the effective friction angle and the power for the gravel were assumed as 10 kPa, 35° and 0.6, respectively. The high value of the cohesion intercept is justified by the significant amount of fines identified (Tab. 32). The major principal stress was calculated as -434 kPa, leading to $E_{oed,ref}$ = 75 MPa.

The reference secant triaxial stiffness ($E_{50,ref}$) was adopted approximately as $E_{oed,ref}/1.125$ and the reference unloading/reloading stiffness was equal to 4.5 x $E_{oed,ref}$. This assumption was based on the pressuremeter test ratio between E_R and E_M (Tab. 33). As a first approximation, the shear modulus at very small strains (G_0) was adopted equal to 4 x G_{ur}, where G_{ur} is the unloading/reloading shear modulus, leading to G_0 = 562.5 MPa. One additional simulation was performed assuming G_0 = 2.5 x G_{ur} and keeping all other parameters the same (calibration 2). For this assumption, $G_{0,ref}$ was set as 352 MPa instead of 562.5 MPa. The soil parameters for the conglomerate and the fill were assumed based on experience. The parameters are shown in Tab. 34 and Tab. 35.

Because during the pressuremeter tests a slotted steel tube was employed, the calibration of the test curves was not straightforward. The initial part of the in situ test curve is related to the volume required to fill in the space between the membrane and the slotted tube, which was approximately 300 cm^3. Due to the fact that the load in the numerical model was applied directly to the soil, this gap between the membrane and the tube was not reproduced numerically. For this reason, in order to compare the in situ with the numerical results, this initial part of the in situ curve is not shown and the results are compared after the membrane was fully filled. Fig. 108a shows the in situ curve with the initial part and with unloading steps and Fig. 108b shows the curve without the initial part and without unloading steps.

Tab. 34: Gravel and conglomerate parameters – test V-5-1 (HSsmall model)

Parameter	**Gravel: V-5-1**	**Conglomerate**
	Value	**Value**
$E_{50,ref}$ (MPa)	67	150
$E_{oed,ref}$ (MPa)	75	150
$E_{ur,ref}$ (MPa)	337.5	350
ν'_{ur}	0.2	0.2
c' (kN/m²)	10	10
φ' (°)	35	40
m	0.6	0.5
K_0^{nc}	0.43	0.36
$G_{0,ref}$ (MPa)	562.5[1]/352[2]	580
$\gamma_{0.7}$	0.15e-3	0.15e-3

[1] $G_{0,ref}$ employed for calibration 1

[2] $G_{0,ref}$ employed for calibration 2

Tab. 35: Fill parameters – test V-5-1 (Mohr-Coulomb model)

Parameter	**Value**
E (MPa)	15
ν'	0.3
c' (kN/m²)	2
φ' (°)	30

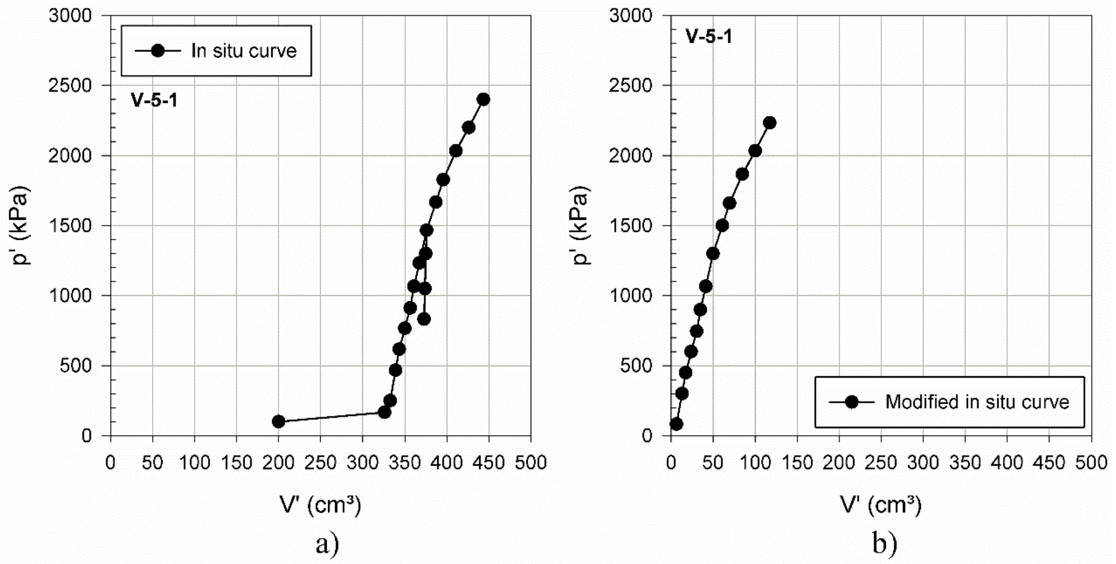

a) b)

Fig. 108: In situ pressuremeter test (V-5-1) result – a) with initial part and unloading steps and b) without initial part and unloading steps

The first calibration result is shown in Fig. 109a (calibration 1). At the first load steps, the numerical curve is slightly steeper than the in situ curve. From approximately 1400 kPa onwards both curves show very similar slope. The second calibration results (calibration 2) and the comparison between the in situ curve is presented in Fig. 109b (calibration 2). Although initially the numerical behaviour is stiffer than the in situ one, from 1000 kPa onwards the numerical curve shows a softer behaviour, which characterises the transition between the small strain state to the large strain state.

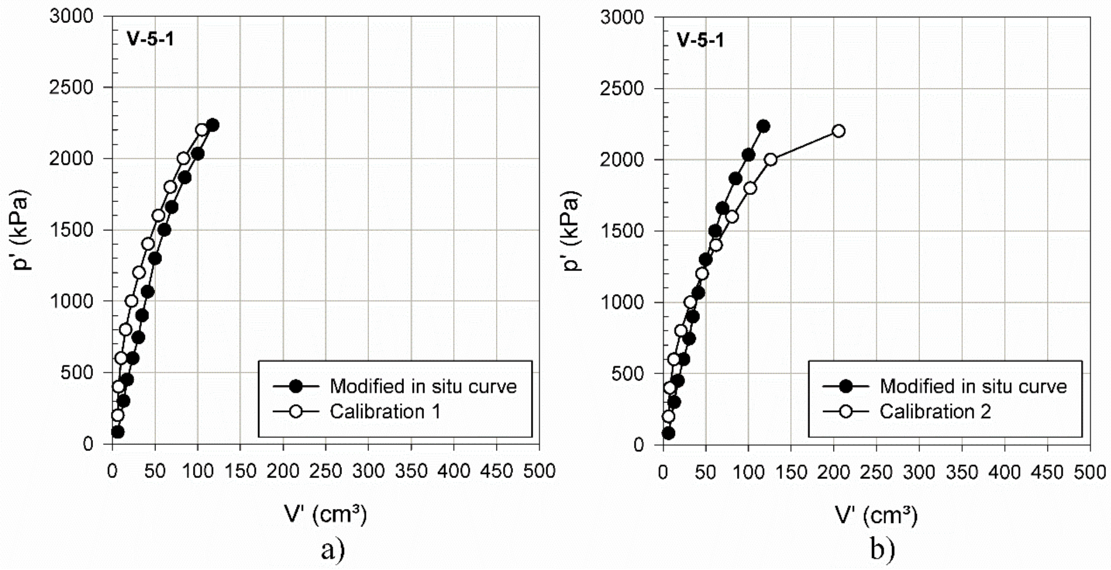

a) b)

Fig. 109: Numerical model calibration (V-5-1) – a) calibration 1 and b) calibration 2

<u>Presssuremeter test V-5-2</u>

The same procedure employed for calibrating test V-5-1 was applied for test V-5-2. The oedometer modulus at -23.4 m depth was determined as 90 MPa (45 MPa/0.5). The reference oedometer stiffness ($E_{oed,ref}$) calculated according to Eq. 5 was 38 MPa. $E_{50,ref}$ was 34 MPa and $E_{ur,ref}$ was 288.8 MPa, thus leading to $E_{ur,ref} \approx 7.6 \times E_{oed,ref}$, as shown in Tab. 33 for E_R/E_M. Finally, G_0 was assumed as 4 x G_{ur} (calibration 3) and 2.5 x G_{ur} (calibration 4), resulting in G_0 = 481.3 and 300.8 MPa, respectively. Tab. 36 shows the gravel parameters employed for calibrating the test V-5-2. The conglomerate and the fill parameters were kept as in Tab. 34 and Tab. 35.

Tab. 36: Gravel parameters – test V-5-2 (HSsmall model)

Parameter	**Gravel: V-5-2**
	Value
$E_{50,ref}$ (MPa)	34
$E_{oed,ref}$ (MPa)	38
$E_{ur,ref}$ (MPa)	288.8
ν'_{ur}	0.2
c' (kN/m²)	10
φ' (°)	35
m	0.6
K_0^{nc}	0.43
$G_{0,ref}$ (MPa)	$481.3^1/300.8^2$
$\gamma_{0.7}$	0.15e-3

$^1G_{0,ref}$ employed for calibration 3

$^2G_{0,ref}$ employed for calibration 4

As for test V-5-1, the initial part of the in situ curve, which is related to the volume required to fill in the space between the membrane and the slotted tube, is not compared with the numerical calibration and a modified curve is employed for this purpose (Fig. 110). The calibration results are shown in Fig. 111. Whist calibration 3 exhibited a stiffer behaviour than the in situ results up to 1600 kN, calibration 4 initially showed a good agreement and at this load step presented a slightly softer behaviour in comparison with the in situ curve.

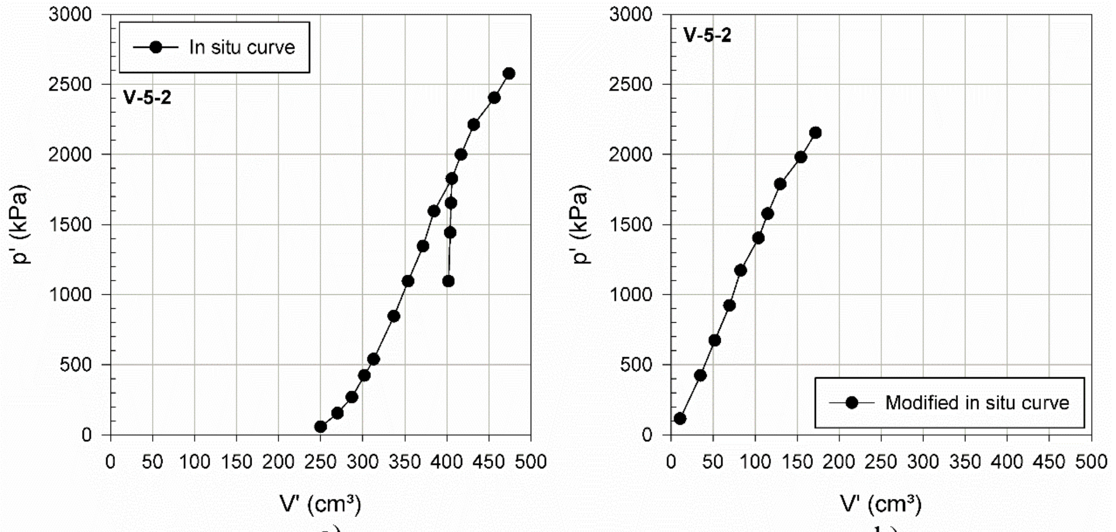

a) b)

Fig. 110: In situ pressuremeter test (V-5-2) result – a) with initial part and unloading steps and b) without initial part and unloading steps

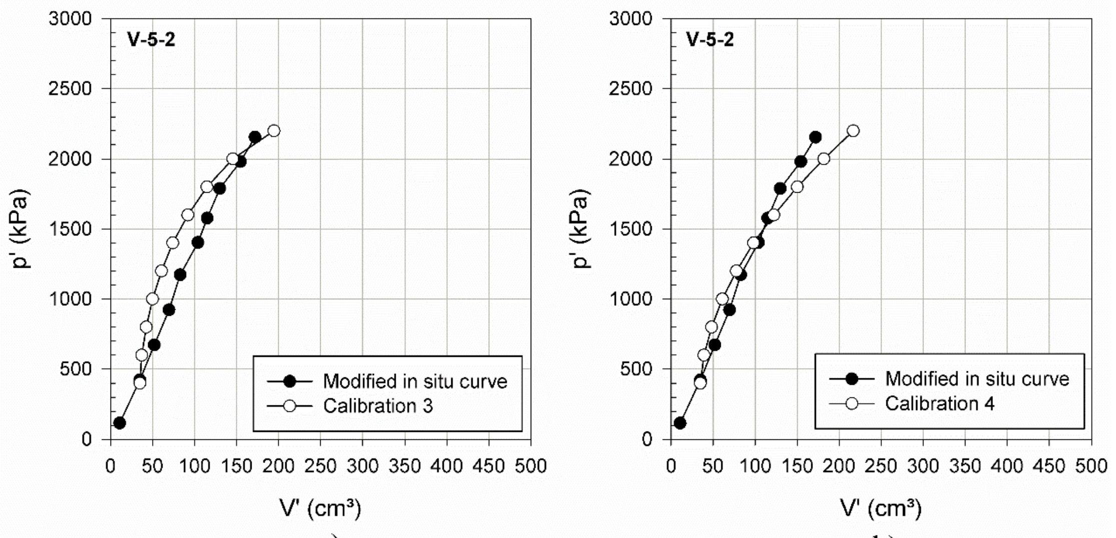

a) b)

Fig. 111: Numerical model calibration (V-5-2) – a) calibration 3 and b) calibration 4

8.3 Grout laboratory results

On the same day of the anchor installation, three cement samples were prepared for laboratory tests (Fig. 112). The tests were performed after about 15 days of curing time, which was the cement age at the time of the pullout test. The density of the cement mixture was 1.87 g/cm³ and the back calculated water/cement ratio was 0.44.

Fig. 112: Cement samples for laboratory tests

Two uniaxial compression tests (ÖNORM EN 12390-3:2012) and one splitting tension test (ÖNORM EN 12390-6:2010) were carried out at the Institute of Rock Mechanics and Tunnelling of the Graz University of Technology. The splitting tensile strength was 2.92 MPa and the uniaxial compression test results are shown in Tab. 37. The uniaxial compression tests showed a very brittle failure and therefore the post-peak behaviour could not be monitored. For this reason, no information on the compression fracture energy was available. Photos of the cement specimens before and after the tests are shown in Fig. 113, Fig. 114 and Fig. 115.

Tab. 37: Uniaxial compression tests results

	Density (kg/dm³)	**Young's modulus (GPa)**	**Poisson's ratio**	**UCS (MPa)**
Test 1	1.95	15.70	0.26	59.9
Test 2	1.95	16.24	0.24	56.5

When the results from the uniaxial compression tests of the grout became available, the grout parameters were numerically calibrated. The calibration results were used to refine the numerical pullout test simulations. The tests were simulated using a numerical model with the real dimensions of the samples. Distributed prescribed displacements were applied at the top of the sample and an axisymmetric model was employed. The Concrete model was employed as constitutive model for the grout.

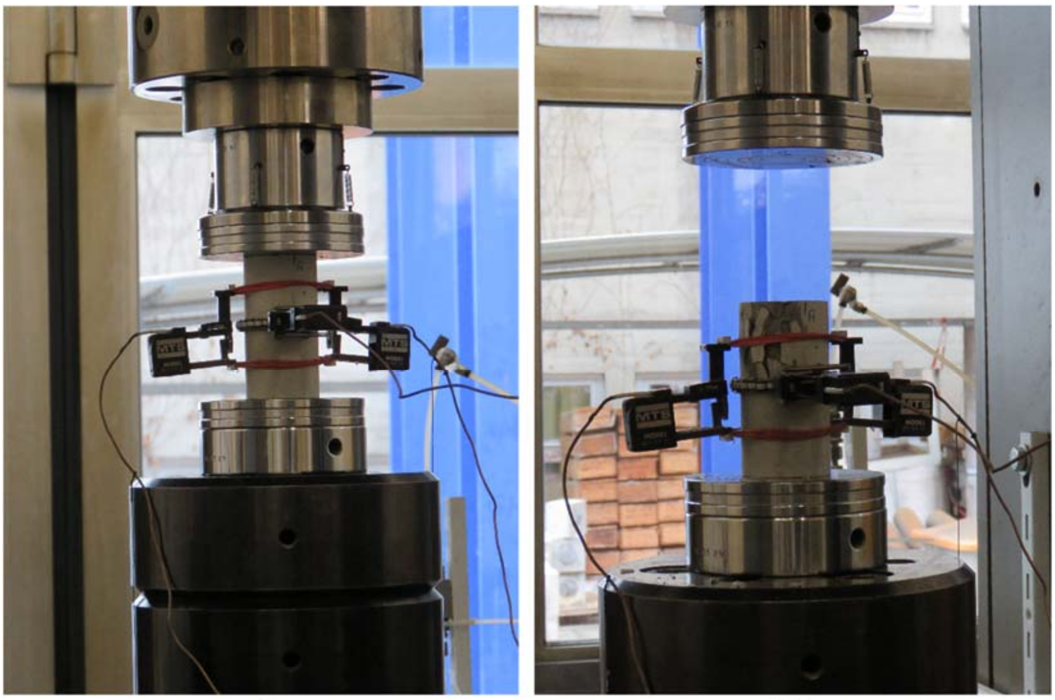

a) b)

Fig. 113: Uniaxial compression test 1 – a) before the test and b) after failure

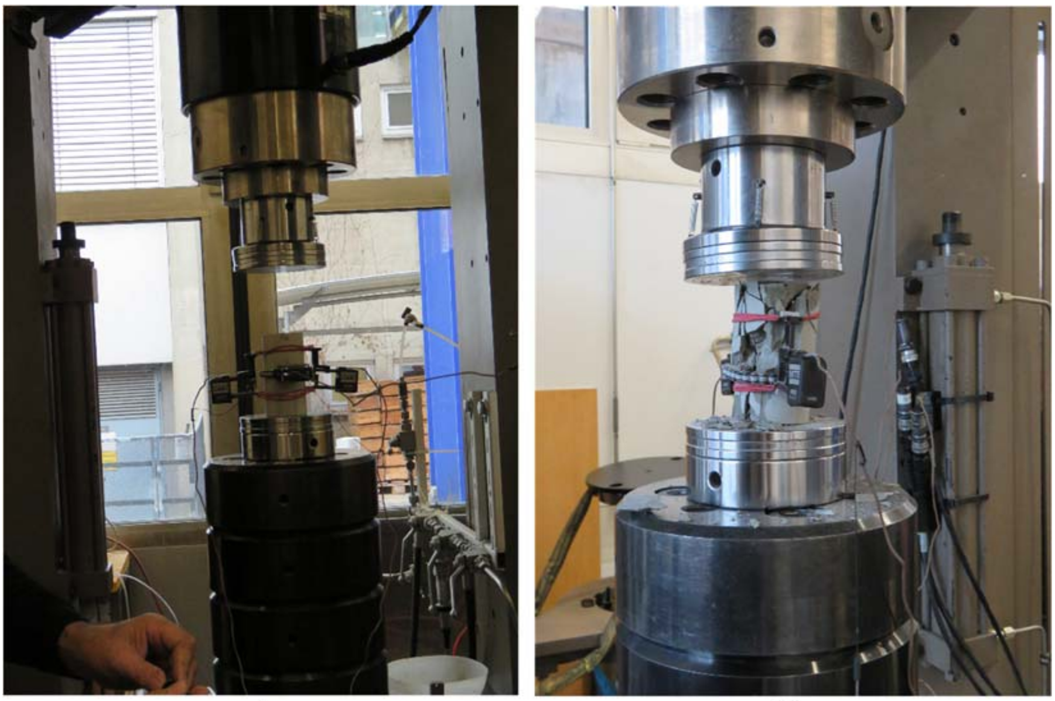

a) b)

Fig. 114: Uniaxial compression test 2 – a) before the test and b) after failure

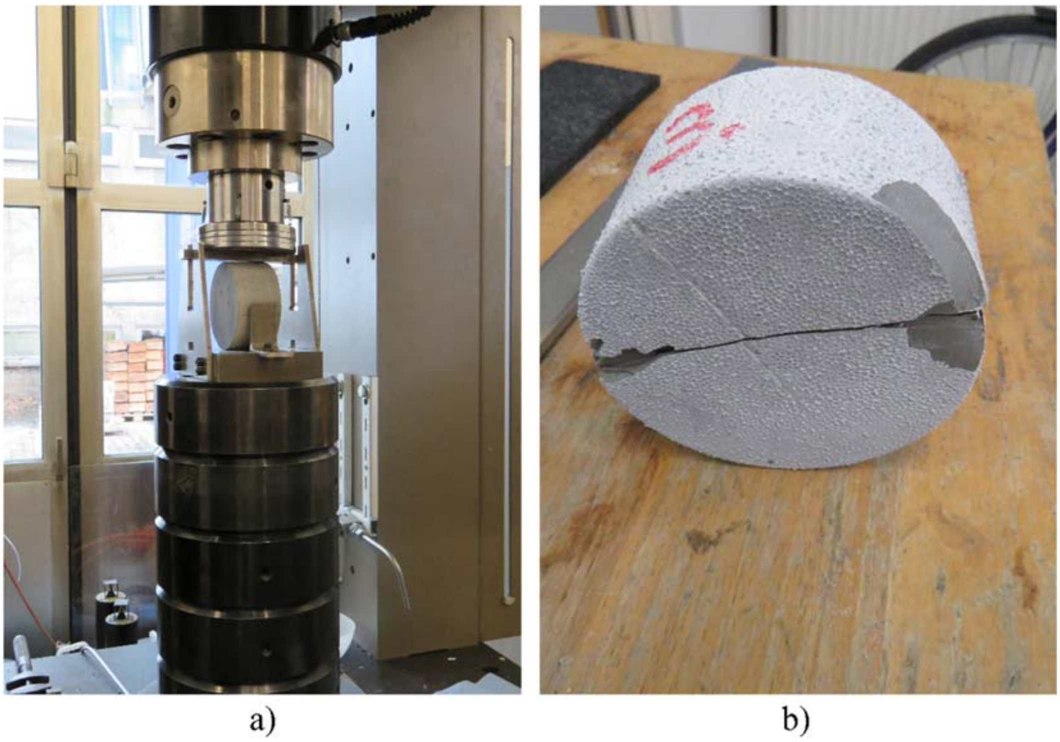

Fig. 115: Splitting tension test – a) before the test and b) after failure

Only the pre-peak behaviour was calibrated and the softening parameters were assumed. In order to capture the brittle behaviour of the sample observed during the laboratory tests, G_c was set as 0.1 kN/m and residual stress state was reached almost immediately after peak. Fig. 116 shows the numerical calibration against the laboratory results (test 1 and test 2). The parameters that were employed in the numerical simulations and those that were considered after calibration are shown in Tab. 38.

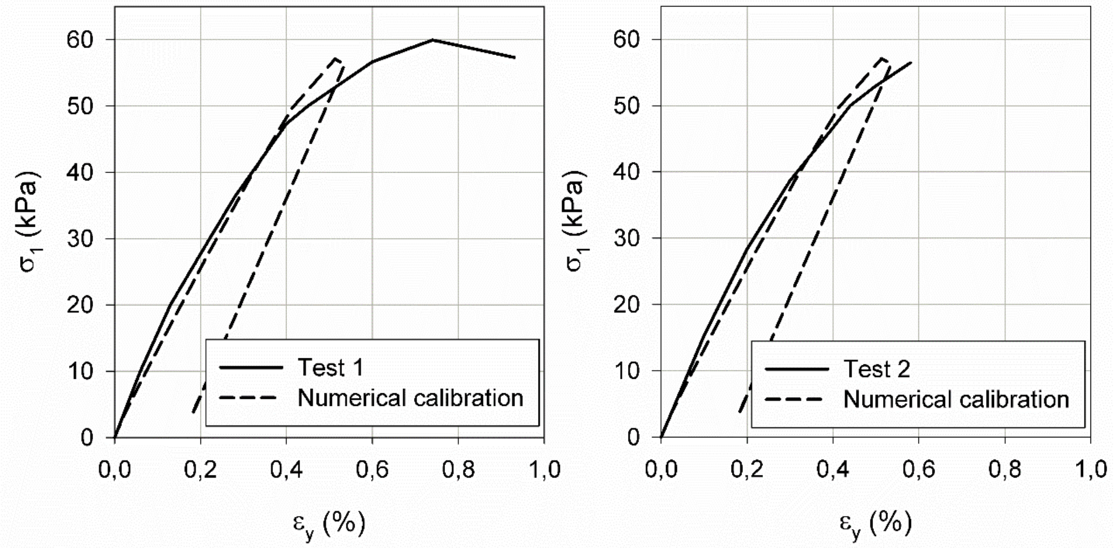

a)

b)

Fig. 116: Numerical calibration of the uniaxial compression test – a) calibration of test 1 and b) calibration of test 2

Tab. 38: Previous and new grout parameters

Parameter	**Previous grout parameters**	**New grout parameters**
E (GPa)	16.5	15.0
ν	0.20	0.20
f_c (MPa)	32.0	56.45
f_t (MPa)	2.0	2.9
f_{c0n}	0.05	0.05
f_{cfn}	0.95	0.95
f_{cun}	0.10	0.10
$\varepsilon_{cp}{}^{p}$	-0.0013	-0.0013
G_c (kN/m)	3	0.1
f_{tun}	0.05	0.05
G_t (kN/m)	0.01	0.01
a	19	19
φ_{max} (°)	48	48

8.4 In situ pullout test results

The load-displacement curve, considering the displacements at the anchor head at the loading and unloading/reloading steps, is presented in Fig. 117. The failure criterion was achieved at the 1710 kN load step. Fig. 118 shows the load-displacement curve considering the displacements at the top of the fixed length and only the loading steps. It is worth mentioning that, after the 1456 kN load step, the displacements increase significantly with increasing pullout load: from 1456 to 1710 kN and from 1710 to 1801 kN the displacements at the top of the fixed length almost doubled in value.

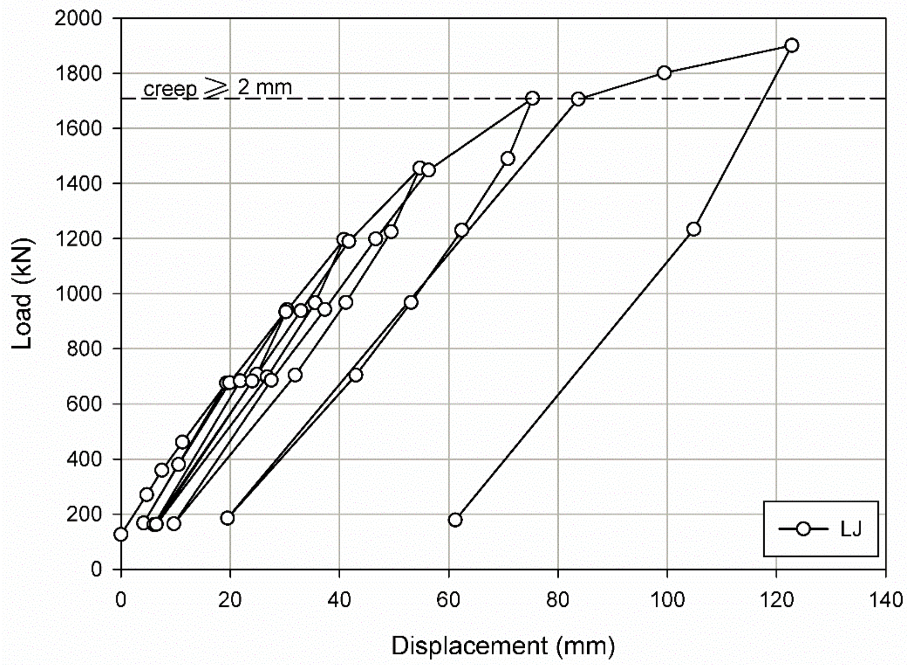

Fig. 117: Load-displacement curve (tendon end displacements)

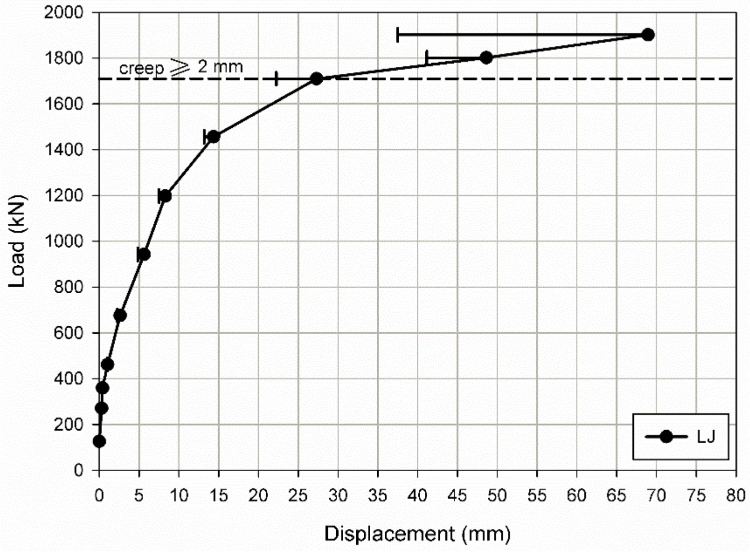

Fig. 118: In situ load-displacement curve

The fibre optic strain measurements are shown below. The load steps of 1800 and 1900 kN were not plotted because the data showed some disturbance. Both measurements performed along the tendon were similar and, for this reason, only the results referred as "measurement 2" are shown in Fig. 119.

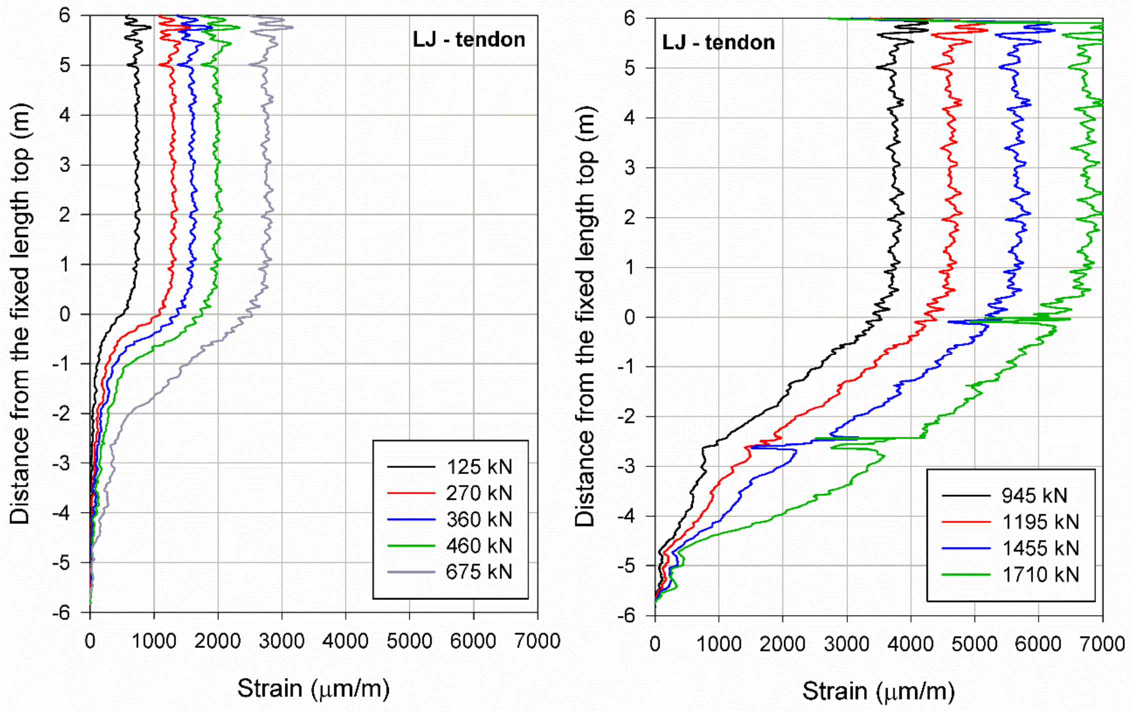

Fig. 119: Strains along the tendon

The grout measurements performed with the thin fibres are shown in Fig. 120. Although the free length is mainly subjected to compressive stresses and the fixed length to tensile stresses, it is remarkable that the compressive stresses along the free length extend significantly towards the fixed length as the pullout load increases. At the in situ ultimate capacity of 1710 kN, compressive stresses developed up to -4.5 m, thus reaching almost the entire anchor length.

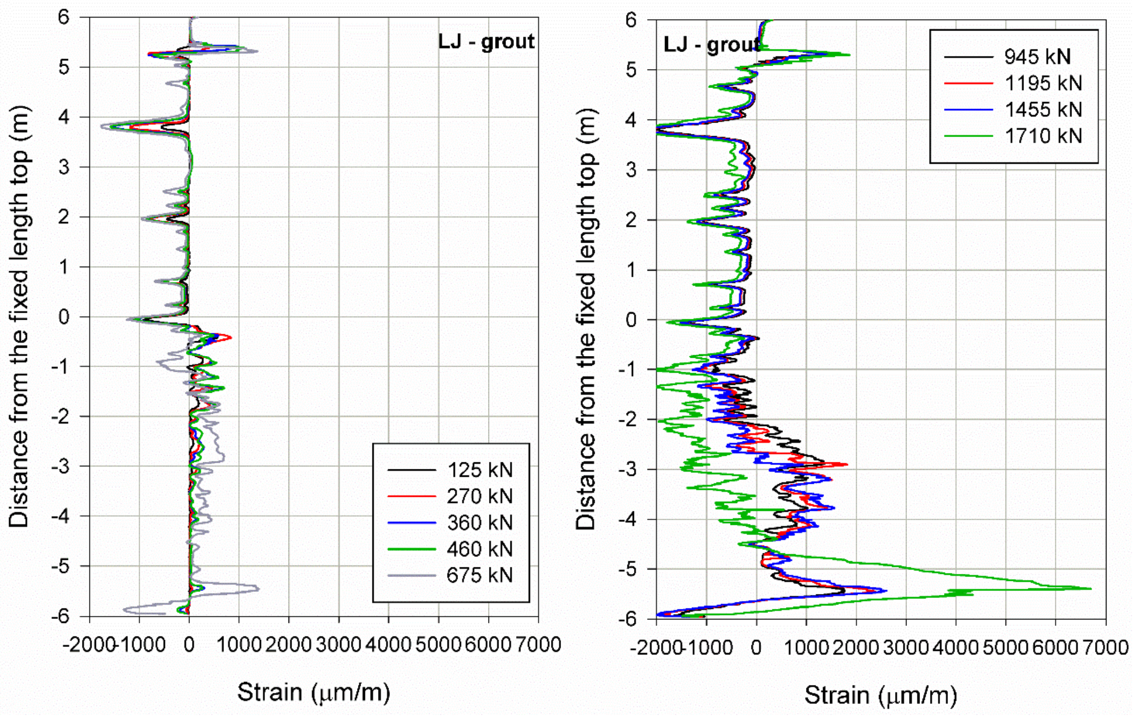

Fig. 120: Strains along the grout

The development of compressive stresses along the fixed anchor length in the grout is better illustrated in Fig. 121. In this figure, the transition zone is identified and its width increases significantly during the pullout test. Additionally, Fig. 121 shows that the strains along the tendon develop significantly with both, the spread of the transition zone and of cracking in the grout.

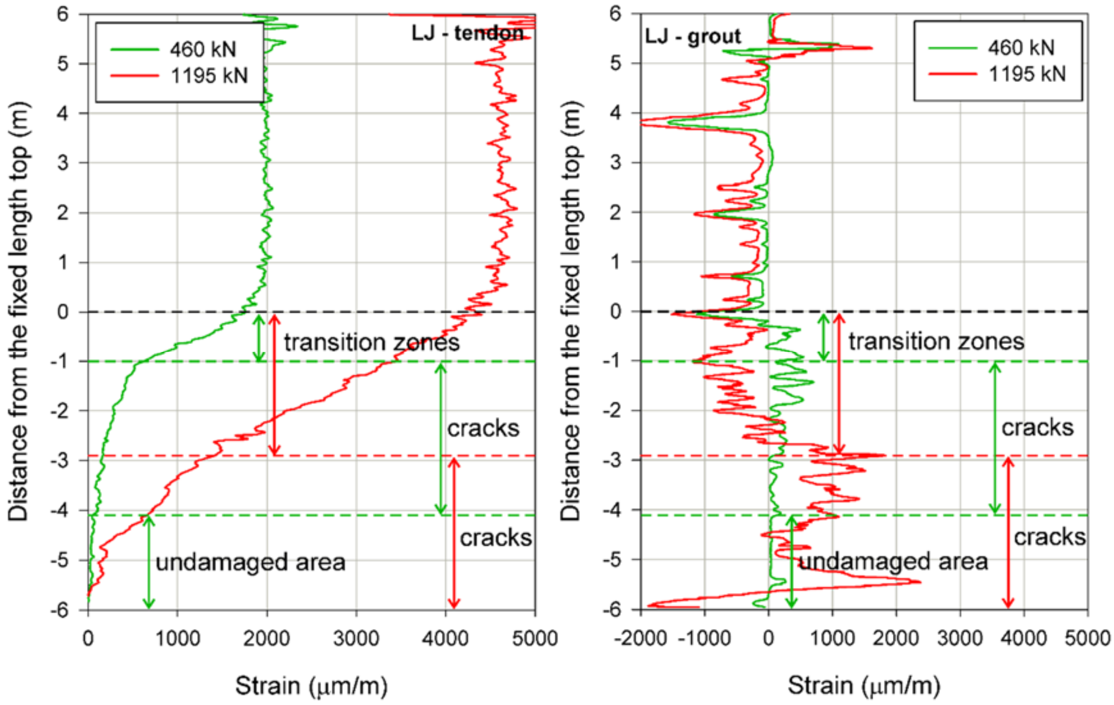

Fig. 121: Strain distribution along the tendon and the grout – different grout conditions

From 675 kN onwards the measurements performed along the grout with the thin fibre show that, at about -4.5 m below the proximal end of the fixed length, the strains drop significantly becoming even negative (compressive strains). The development of compressive strains along the grout at the distal end of the fixed length was also observed in the anchor 1A in St Kanzian and in the Söding-test.

Fig. 122 compares the strains along the grout measured in the St Kanzian-test (anchor 1A) and in the Ljubljana-test, considering the thin fibre and the load steps of 270-280 kN and 900-945 kN. In this figure, although the anchor free and fixed length in St Kanzian were 12 and 8 m, respectively, in order to facilitate the comparison only 6 m of the free and of the fixed length are shown. Some remarks can be made from Fig. 122:

- The measurements performed in Ljubljana at the 270 kN load step showed high peaks along the anchor free length in the grout. These peaks can be attributed to inhomogeneities in the soil or in the grout;
- The peaks observed along the grouted body regarding the Ljubljana test are wider than the peaks observed in the St Kanzian test. This is partially attributed to the gage length employed during data processing, which was 3 cm instead of 1 cm as it was employed for the anchors in St Kanzian and in A10. Increasing the gage length and selecting a proper reference measurement eliminate the spikes caused by vibrations at the construction site;
- The peaks measured in Ljubljana at the 270 kN load step extend towards about -3.5 m of the fixed length, whereas in St Kanzian the peaks are observed within the first -2 m. If the peaks are interpreted as cracks, this is somehow unexpected, because the tensile strength of the cement obtained from splitting tension tests in St Kanzian was about 1.2 MPa and, considering the cement in Ljubljana, the tensile strength was 2.9 MPa;
- Regarding the load step of 945 kN for the test in Ljubljana, it is remarkable that the compressive strains in the grout along the fixed length start to decrease only at about -1 m depth, whereas for St Kanzian it started at the top of the fixed length. This suggests that, at the proximal end of the fixed length, cracks develop and debonding occurs between the tendon and the grout. It is also worth noting that, from 1455 to 1710 kN, the compressive strains start to decrease only at about -2 m below the top of the fixed length.

Debonding between tendon and grout at the proximal end of the anchor is probably related to the transition zone increase. This aspect will be further discussed when the numerical results are evaluated and in section 9.1.

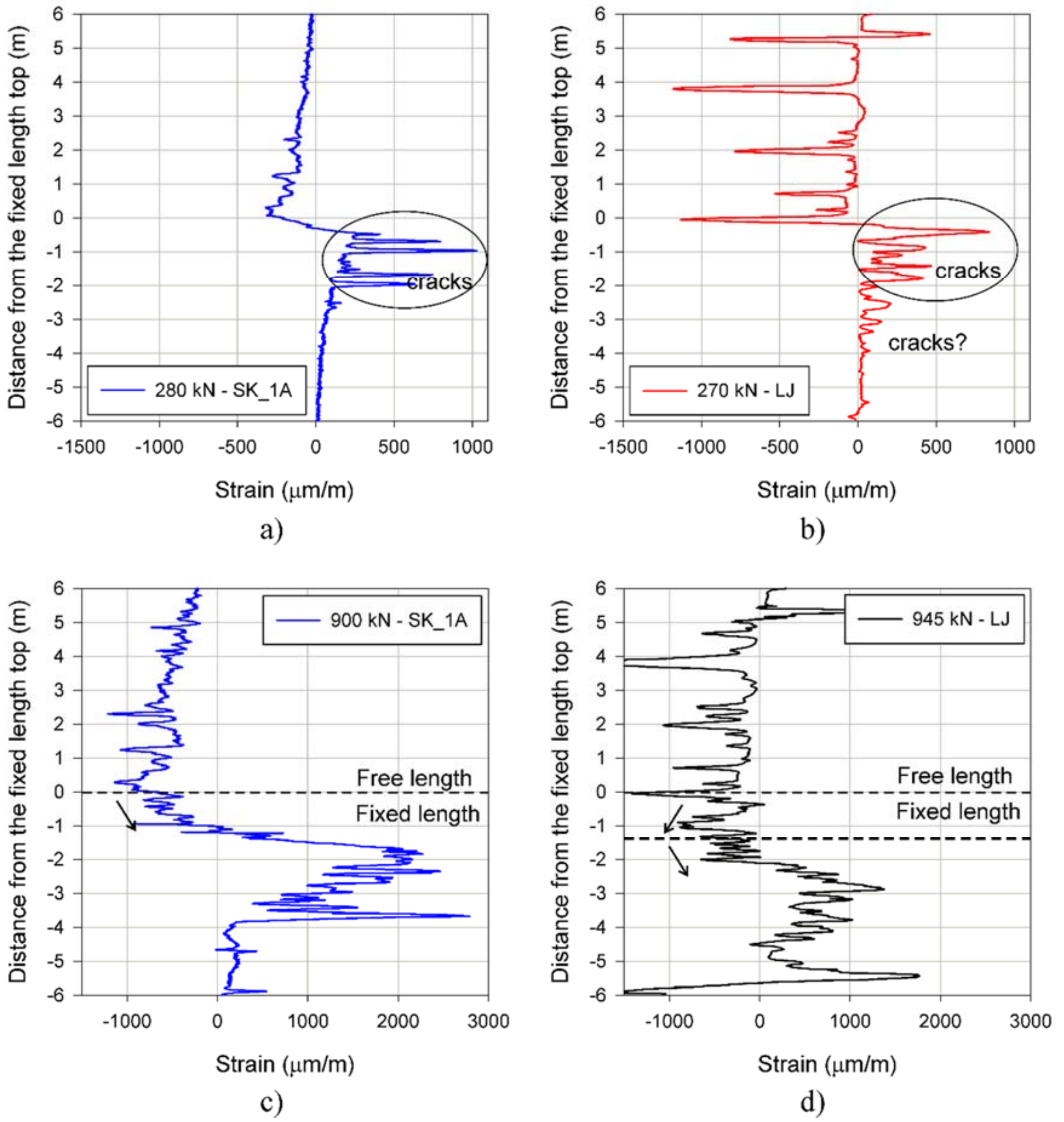

Fig. 122: Strains along the grout for the St Kanzian-test (anchor 1A) and for the Ljubljana-test – a) 280 kN load step (St Kanzian); b) 270 kN load step (Ljubljana); c) 900 kN load step (St Kanzian) and d) 945 kN load step (Ljubljana)

8.5 Numerical simulations

The pullout test was simulated with a 3D model using Plaxis 3D 2018 (Brinkgreve et al. 2018). The domain of the 3D model was selected so that not only the fibre optic monitored anchor was considered, but also the temporary anchors on the right and on the left side of the monitored anchor. The entire excavation depth was modelled. The height of the retaining wall was 15.5 m and it was modelled as a 2 m thick plate element. The monitored anchor was simulated with volume elements, the tendon being a linear elastic material and the grout an elastoplastic material simulated with the Concrete model. The temporary anchors, installed before the anchor pullout test, were simulated with node-to-node anchors. The node-to-node anchors were modelled only along the free length, thus the load was transferred to the soil at the end of the free length.

Prescribed displacements were applied directly at the top of the fixed length and the tendon along the free length was not simulated. The grout was considered along the free and the fixed length. The soil layers distribution is considered as in Fig. 107 and because the last silty/clayey gravel layer was below the excavation depth, this layer was not taken into account. An overview of the pullout test geometry is shown in Fig. 123. Fig. 124 shows the temporary anchors and the fibre optic monitored anchor. In Fig. 124a the tendon (fixed length) and the prescribed displacement are presented, Fig. 124b shows the grout along the free and the fixed length, Fig. 124c and Fig. 124d show the cylindrical soil clusters for mesh refinement.

A mesh sensitivity test was performed in which about 350 000 elements were employed and the results were compared with a simulation carried out with approximately 200 000 elements. Both simulations showed very similar behaviour. Tab. 39 shows the Plaxis version, the number of elements and the element type used in the numerical simulations.

Tab. 39: General information of the numerical simulations

Simulation	Software	Number of elements	Element type
Prediction 1	Plaxis 3D – 2018	148 557	10-noded
Prediction 2	Plaxis 3D – 2018	206 926	10-noded
Refinement 1	Plaxis 3D – 2018	148 557	10-noded
Refinement 2	Plaxis 3D – 2018	206 926	10-noded
Refinement 3	Plaxis 3D – 2018	170 142	10-noded

The anchor bond length was simulated with two different diameters: the first assumption was that the grout diameter along the fixed length was the same as along the free length and equal to the borehole diameter (200 mm); the second assumption accounted for an increase in diameter along the fixed length based on the volume of cement injected under pressure outside the corrugated pipe (200 L lead to a diameter of 270 mm). The different assumptions are shown in Fig. 125.

The lateral earth pressure coefficient at rest was not increased to account for the increase on the radial stresses due to the grouting procedure. According to Xanthakos (1991), for soils with high permeability such as sand and gravel, the injected pressure that remains locked in the soil tends to dissipate more than in fine-grained materials.

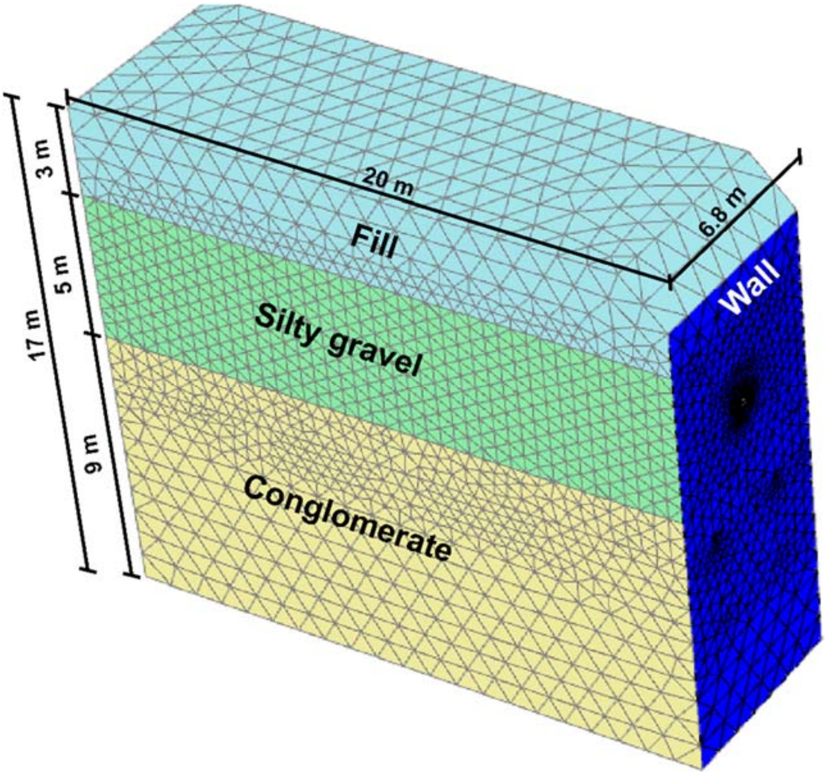

Fig. 123: Overview of the soil layers and retaining wall

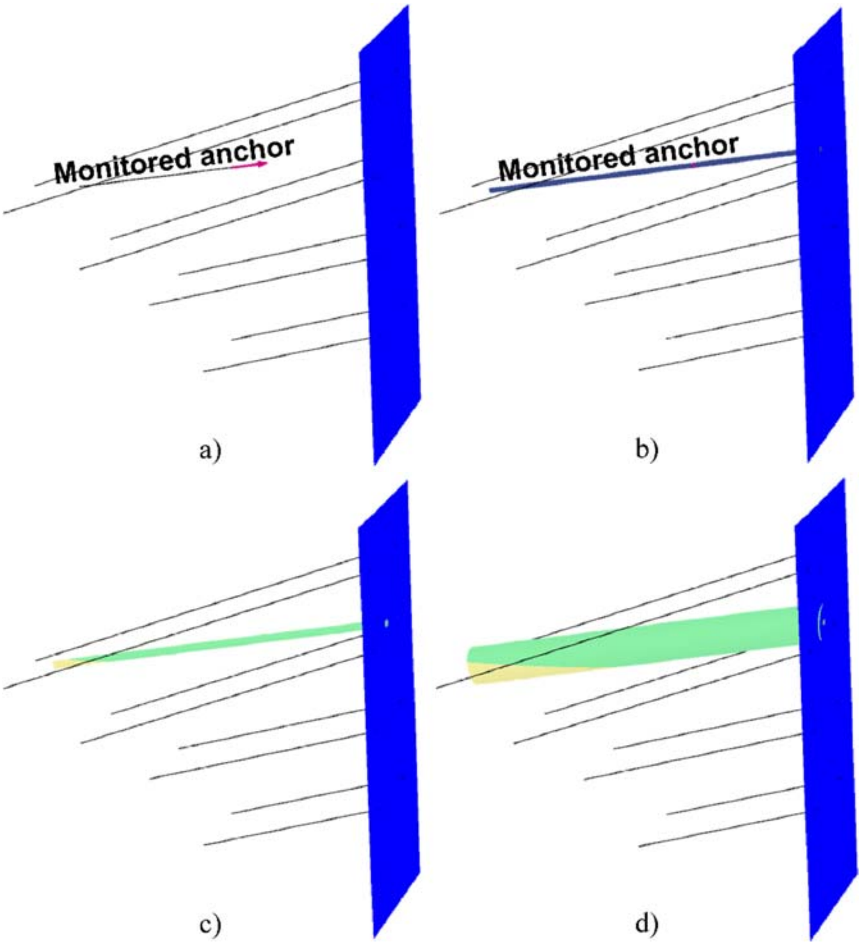

a) b) c) d)

Fig. 124: Anchor detail – a) tendon and prescribed displacement; b) grout; c) soil cluster (1) and d) soil cluster (2)

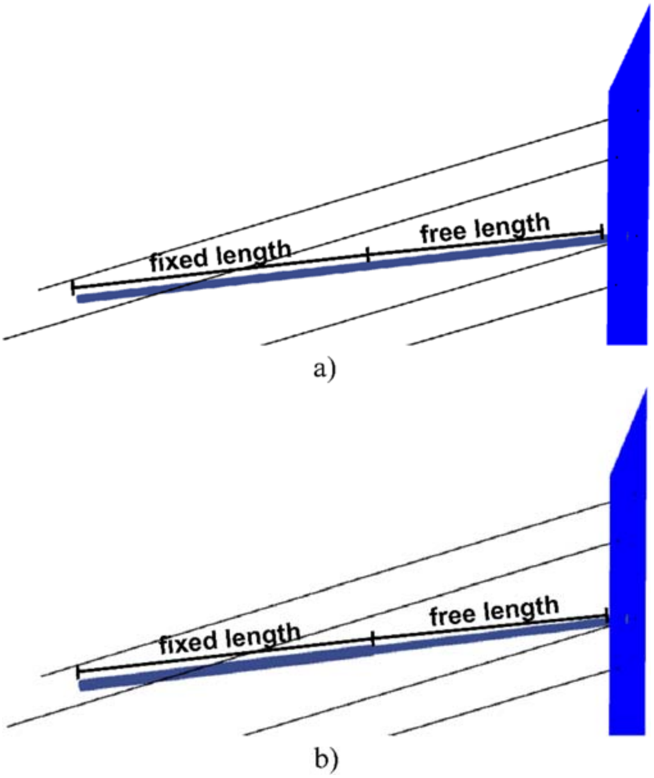

Fig. 125: Different grout assumptions – a) same diameter at the fixed length and b) diameter increased at the fixed length

8.5.1 Material parameters

The soil parameters were already described previously in section 8.2. The silty gravel and the conglomerate parameters are shown in Tab. 34 and the fill parameters in Tab. 35. The grout parameters were presented in section 8.3 in Tab. 38. The plate parameters are shown in Tab. 40 and the node-to-node anchors normal stiffness (EA) was 123900 kN. The tendon stiffness was 160 GPa. The soil unit weight in all cases was 21 kN/m³, the grout unit weight was considered as 25 kN/m³ and the tendon as 78.5 kN/m³.

Tab. 40: Material parameters (Plate, wall)

Parameter	**Value**
d (m)	2
E_1 (GPa)	30
E_2 (GPa)	30

8.5.2 Numerical results

Numerical predictions were performed prior to the anchor pullout test and the simulations were refined after the laboratory results of the grout were available. The numerical predictions were performed considering the soil parameters obtained with calibration 1. The calibration of the V-5-1 test was selected due to difficulties encountered during insertion of the membrane for the test V-5-2, which could be the reason for the lower Ménard modulus observed for this test in comparison with test V-5-1. The numerical load-displacement curves compared with the in situ curve are shown in Fig. 126.

The numerical predictions are referred as “prediction 1” and “prediction 2” and the difference between both is the grouted body diameter, as shown in Fig. 125: the same diameter along the free and the fixed length was considered for prediction 1 and, regarding prediction 2, the diameter was increased along the fixed length. With respect to the numerical refinements, i.e. “refinement 1” and “refinement 2”, they were undertaken considering the calibrated grout parameters and, as for predictions 1 and 2, the difference between the simulations was only the fixed length diameter.

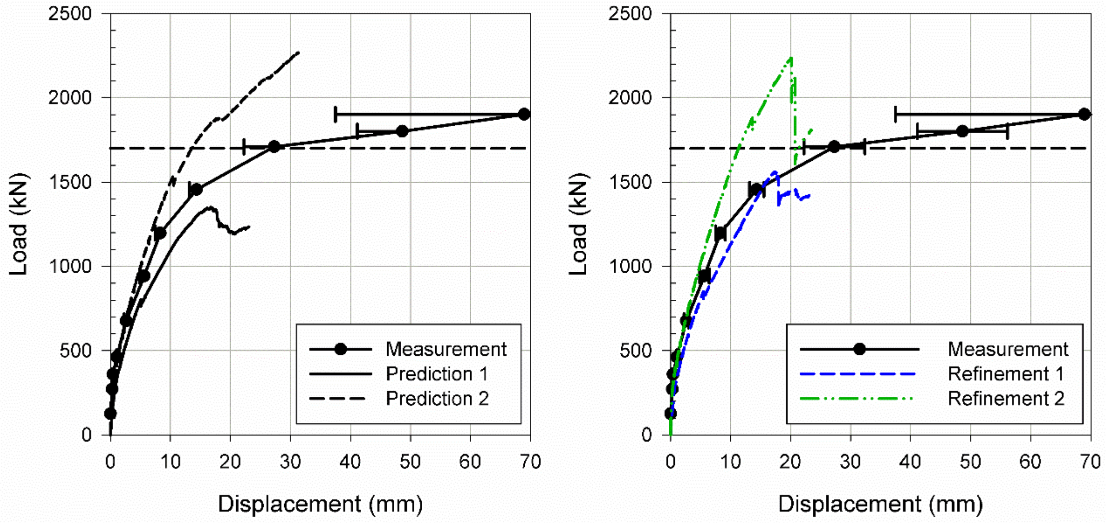

Fig. 126: In situ and numerical load-displacement curves

Comparing prediction 1 with refinement 1 and prediction 2 with refinement 2, that differ only in the grout parameters, the load-displacement behaviour was not significantly different. Up to 1500 kN the slope of refinement 1 agreed very well with the in situ curve, whereas refinement 2 showed stiffer behaviour. The kink observed at about 20 mm for refinement 2 occurs when residual state in compression starts in the grouted body. At this displacement, the pullout load achieved with this simulation is larger than the in situ ultimate capacity.

The strain distribution along the fixed length is compared with the numerical calculation in Fig. 127. Only the numerical results of refinement 1 are shown. If numerical and in situ results are compared, the main differences are related to the extension of the transition zone, leading to an unsatisfactory agreement between the strain profiles. Numerically, the transition zone extends up to about -1.3 m below the proximal end of the fixed length for the last load step shown in Fig. 127. Considering the in situ load of 1455 kN, this zone increases throughout about half of the fixed anchor length. The differences observed between the in situ measurements and the numerical refinement 1, with respect to the transition zone for the load steps of 460 and 1195 kN, are shown in detail in Fig. 128. As the in situ transition zone increases the agreement becomes poorer.

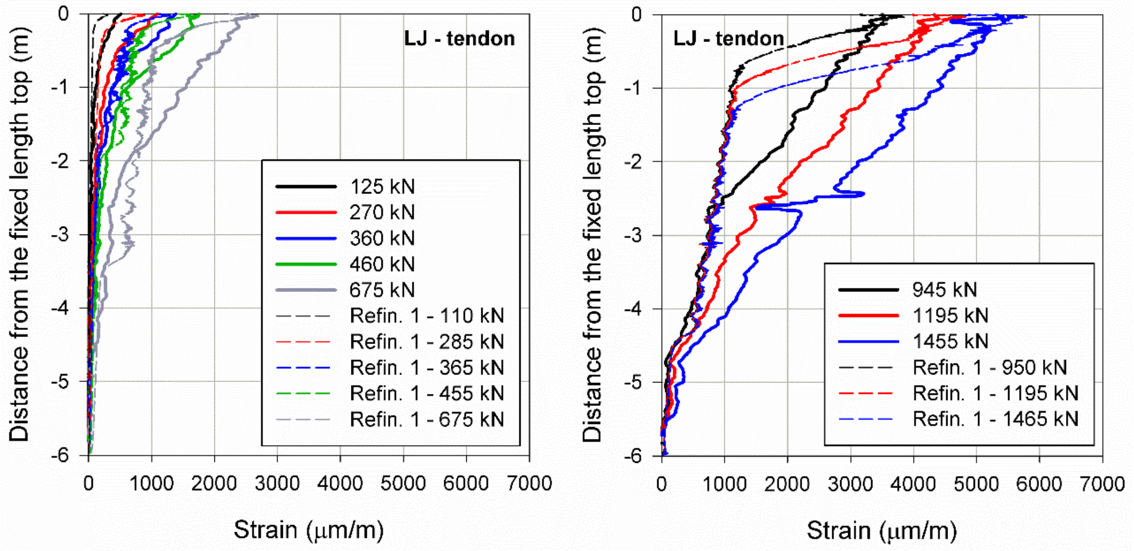

Fig. 127: Strain distribution along the tendon – in situ *vs* refinement 1

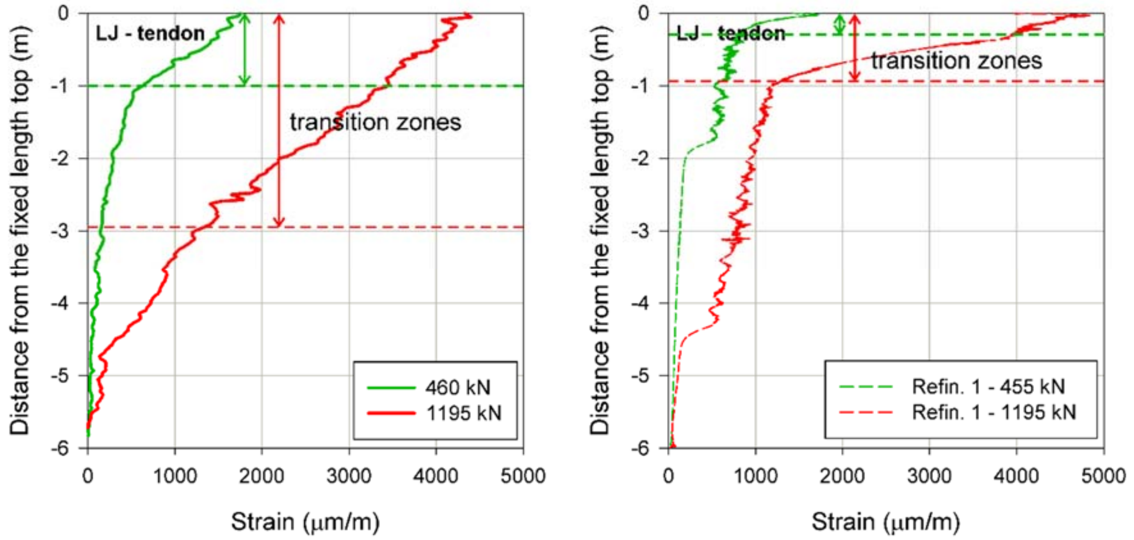

Fig. 128: Transition zone – a) in situ measurements and b) refinement 1

Assuming that the stress-strain behaviour of the cement sample can be extrapolated to the anchor grout and considering that the 200 L of cement injected along the fixed length formed a cylindrical body, it was expected that the best agreement would be achieved with refinement 2. Due to the differences observed between refinement 2 and the in situ result, one additional simulation was performed (refinement 3).

In order to capture the spread of the compressive stresses in the transition zone, an interface between the tendon and the grout was added. The interface was modelled using volume elements and the grout strength and stiffness parameters were reduced. The interface length was increased as the pullout load increased and it extended up to 3.3 m below the proximal end of the fixed length. The interface activation is shown in Fig. 129 for different load steps. The idea behind the interface activation is that, once the shear strength at the contact between tendon and grout is reached, the pullout load is transferred to the grouted body below the damaged interface, thus compressing the region surrounding the debonded grout.

For this simulation, the only modified parameter in comparison with refinements 1 and 2 was the silty gravel cohesion intercept that was decreased to 5 kPa. The grouted body diameter was 270 mm. The stiffness and strength parameters of the interface were reduced to one sixth of the grout original values.

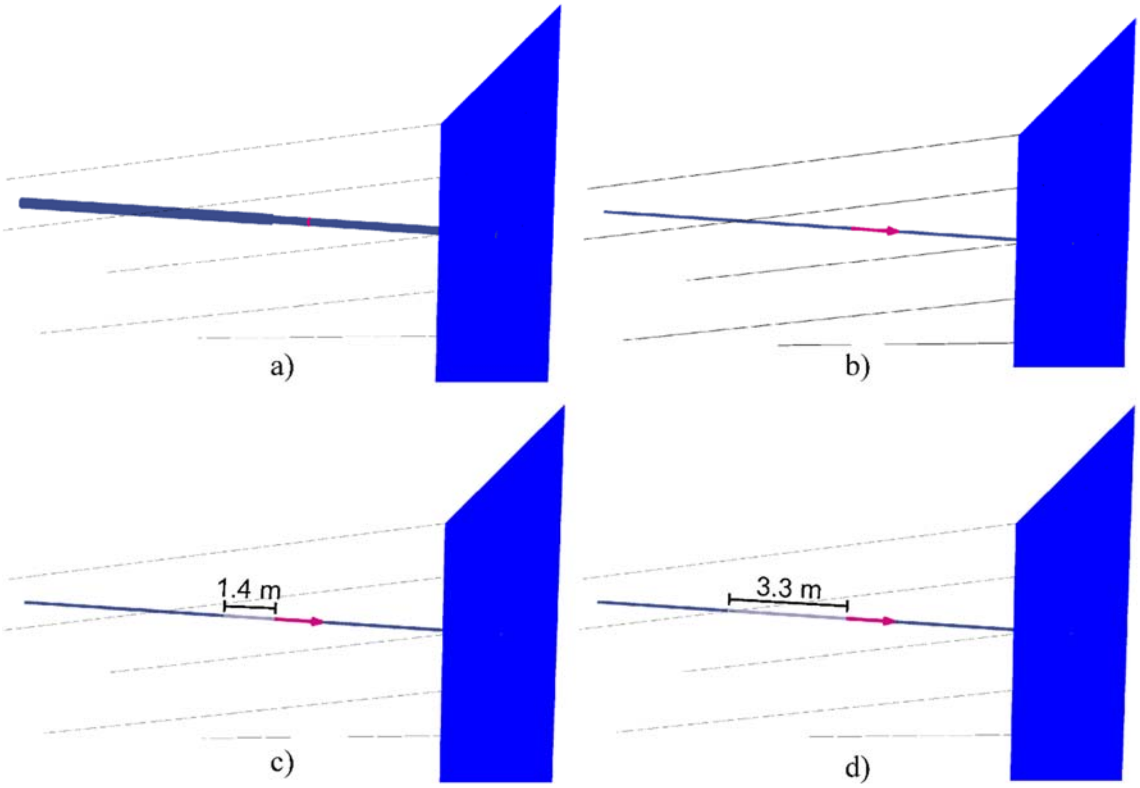

Fig. 129: Interface activation – a) grouted body; b) no tendon-grout interface; c) tendon-grout interface (1.4 m) and d) tendon-grout interface (3.3 m)

Before the interface activation shown in Fig. 129c, tensile cracks spread along the grouted body. After the interface is activated, shear failure occurs between the tendon and the grout and therefore debonding is taken into account. Without introducing the interface manually, the grout would crack in tension but shear failure in the tendon-grout interface would not develop significantly. This occurs because the Concrete model employs a Mohr-Coulomb failure envelope for deviatoric loading and a tension cut-off surface for the tension regime and, if the tensile strength is reached, it decreases during softening but the compressive strength remains unaffected.

The load-displacement curve is shown in Fig. 130. Up to 1900 kN the ultimate capacity was not reached during the numerical simulation. After failure in the tendon-grout interface at the proximal end of the anchor occurs, compressive stresses evolve within the transition zone. Therefore, although the grout is cracked, the tendon is still capable of transmitting the load to the grout even at high stress levels. This situation also occurs in reality when tensile cracks close due to the development of compressive stresses. The strains along the tendon are compared with the in situ measurements in Fig. 131. Because the numerical transition zone increased, the agreement between measurements and numerical results improved.

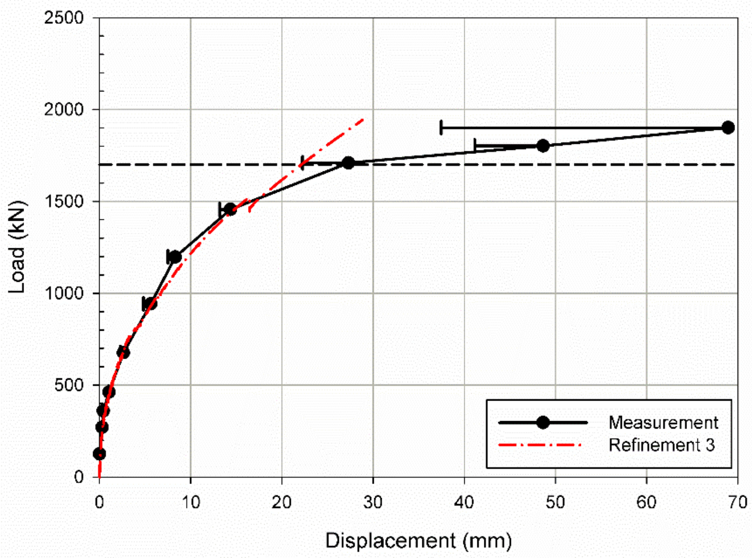

Fig. 130: In situ and numerical (refinement 3) load-displacement curves

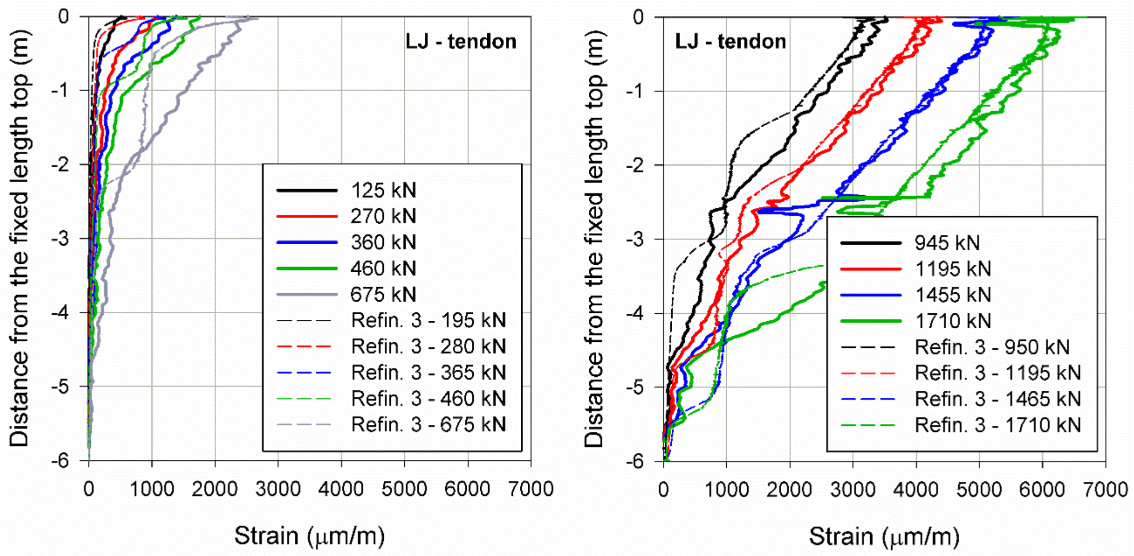

Fig. 131: Strain distribution along the tendon – in situ *vs* refinement 3

8.6 Summary

The last anchor pullout test was carried out in Ljubljana in February 2019. The main soil layer where the anchor was installed was a silty gravel. The soil parameters were calibrated against pressuremeter tests. Prior to the pullout test numerical predictions were carried out and after the test new numerical simulations were performed. The grout parameters were calibrated against uniaxial compression tests and one splitting tension test.

The in situ fibre optic measurements along the grout showed significant compressive stresses evolvement at the bond length, therefore the transition zone increase was pronounced during the test. It is believed that debonding at the proximal end of the fixed length in the tendon-grout interface occurred, thus contributing to the compressive stress development in the grout.

Two numerical predictions were carried out: the first assumed no increase in the bond length diameter due to injection of cement after the anchor was installed; the second assumed an increase in the diameter due to the additional injection. The simulation that accounted for the diameter increase compared well with the in situ load-displacement curve up to 1200 kN.

Numerical refinements were then performed after analysing the in situ pullout test results and considering the grout parameters calibration. The load-displacement curve of the numerical refinement that considered the diameter increase at the bond length showed stiffer behaviour than the in situ result. The strain distribution along the tendon showed that the transition zone observed in the in situ measurements was significantly larger than the numerical one.

Finally, an additional simulation was performed to account for debonding between the tendon and the grout. For this purpose, an interface was included between both materials with reduced grout strength and stiffness parameters. Failure in shear occurred in the contact between tendon and grout and the grout at the vicinity of the interface was subjected to compressive stresses, thus increasing the transition zone. After the interface assumption, the strain distribution along the tendon agreed well with the measurements, suggesting that the spreading of compressive stresses in the grout is indeed related to debonding in the tendon-grout interface.

9 Additional discussion

This chapter provides additional discussion on aspects influencing anchor pullout tests performance. Section 9.1 summarises the different debonding mechanisms observed during the in situ pullout tests and their effect on the fibre optic measurements. Section 9.2 discusses the influence of the retaining wall on the load transfer behaviour of anchors. In sections 9.3 and 9.4 new simulations were undertaken and compared with the refined simulation performed for anchor 1A in St Kanzian. Anchor 1A was selected because it showed the best numerical agreement with the in situ pullout test and it is referred as "reference simulation".

9.1 Debonding

Due to stress concentration at the proximal end of the fixed length, debonding in the tendon-grout interface at this position is more prone to occur. The numerical simulations indicated that, in this case, local shear failure occurs between the tendon and the grout at the fixed length top and the load is mainly transferred from the tendon to the grout below the debonded section. Due to debonding in the tendon-grout interface, the region in the grout surrounding the debonded area undergoes compressive stresses, thus increasing the transition zone. As the pullout load increases, local failure in the tendon-grout interface progresses but, in general, the fibre optic measurements suggested global anchor failure in the grout-ground interface. Moreover, increasing the ground stiffness leads to higher stress concentration at the proximal end of the fixed length. Therefore, tendon-grout detachment is more likely observed in stiff soils and rocks.

The results of the in situ pullout tests of the anchors in St Kanzian type 1A (SK_1A), in Ljubljana (LJ) and in Söding (SÖ) suggested that local debonding due to shear failure occurred during the tests. In Fig. 132 to Fig. 134, the strain profile is plotted at the load steps of 900 kN (SK_1A), 945 kN (LJ) and 1000 kN (SÖ). On the left side, an anchor sketch is presented showing debonding in the tendon-grout interface (vertical red line) and normal tensile cracks (horizontal red lines). It is clear that compressive stresses develop significantly in the grout along the anchor bond length and the spreading of the transition zone is more pronounced for the anchor in Ljubljana, which had stiffer ground.

In addition to the above-mentioned debonding mechanism due to shear failure, another type of debonding was identified during the anchor pullout tests. It was already discussed that vertical strains along the tendon indicate no load transfer to the grout. Fig. 132 to Fig. 134 show that, where large cracks in the grout occur, the slope of the strain distribution along the tendon decreases with respect to the vertical axis. The position of these large cracks is indicated by the red solid rectangles in the anchor sketch. Therefore, the load transfer decrease must be related to debonding due the normal tensile cracks: whilst the damaged grout in compression is still able to transfer the load when the cracks close, the load transfer of the cracked grout in tension is substantially reduced.

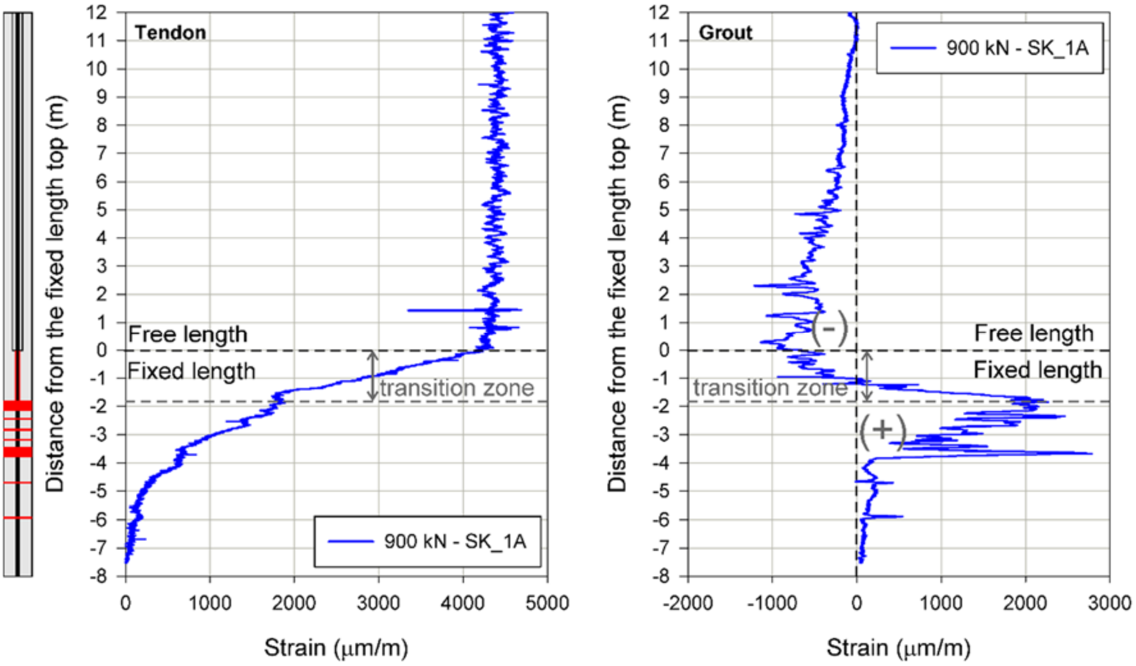

Fig. 132: Debonding mechanism (St Kanzian-test, anchor 1A)

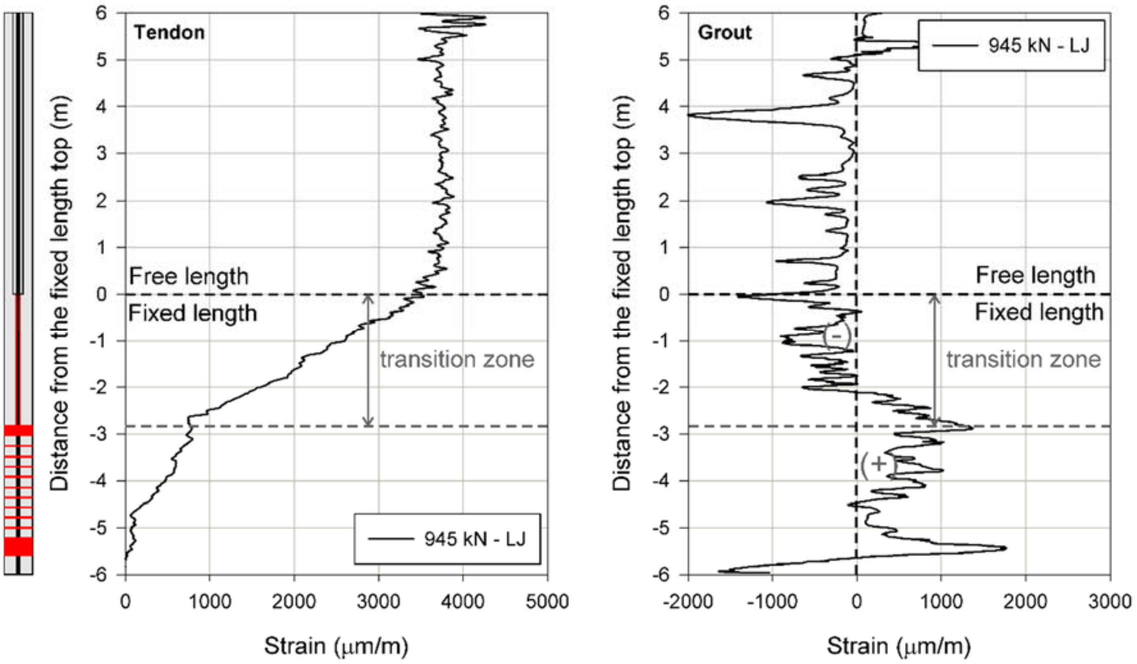

Fig. 133: Debonding mechanism (Ljubljana-test)

Reduction of load transfer was easily identified in the fibre optic measurements of the anchor in Söding: in this case, the first metre of the grout in the fixed length undergoes compressive stresses (and possibly debonding in the tendon-grout interface) and, below this area, the grout undergoes tensile stresses and the strains along the tendon are approximately vertical. A second debonding area due to tensile cracks develops between approximately -3.4 and -5.6 m.

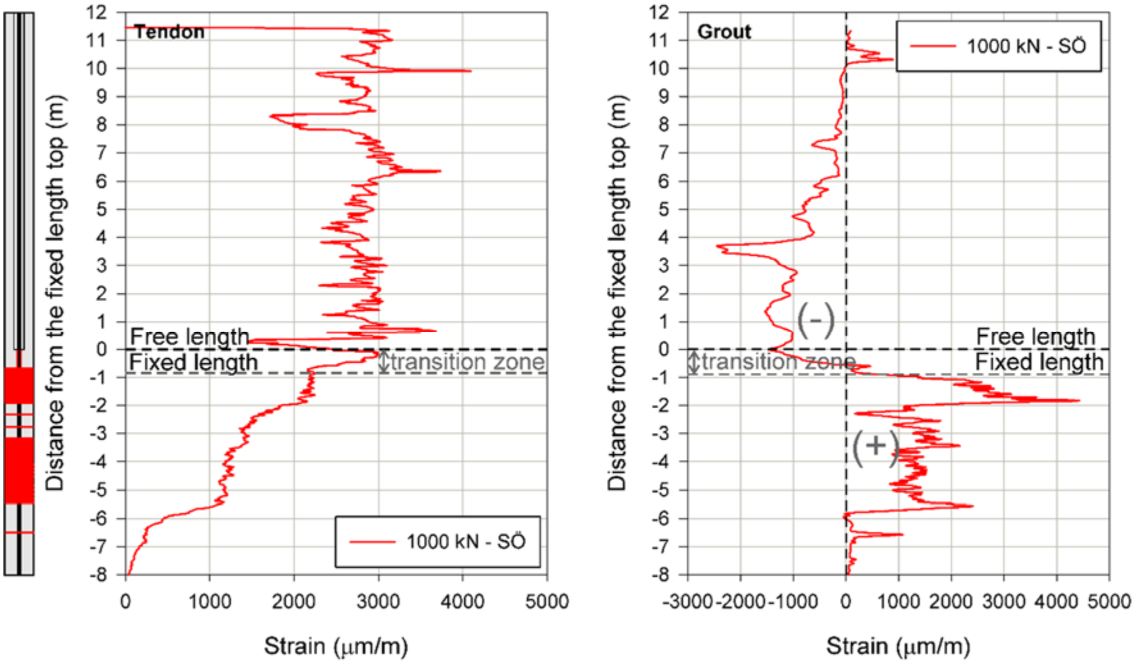

Fig. 134: Debonding mechanism (Söding-test)

Regarding anchor SK_2A (Fig. 135), the grout strain measurements showed low strain values at the fixed length, thus suggesting that load transfer from the tendon to the grout was very low at the position where the fibre optic cable was installed. The fibre optic strain measurements along the tendon provided two important information: first, that the pullout load was not equally distributed between the strands; second, that detachment from the grout occurred during the test. Therefore, it is possible that in this case failure in shear occurred along the entire tendon-grout interface and not only locally, as it was observed for the other anchors shown from Fig. 132 to Fig. 134.

Because anchor SK_2A was only 3 m at the fixed length, debonding in the tendon-grout interface at the proximal end of the fixed length is more likely to result in global failure of the anchor than in the cases that the fixed length is longer. The in situ strain distribution for the 475 kN load step is shown in Fig. 135, where the data of only one monitored strand is plotted, namely measurement 2. Regarding the tendon measurements, because the slope of the strain profile with respect to the vertical axis within the first 1.3 m of the fixed length is higher than the slope at the distal end of the fixed length, this area is probably a transition zone and debonding in the tendon-grout interface can be assumed.

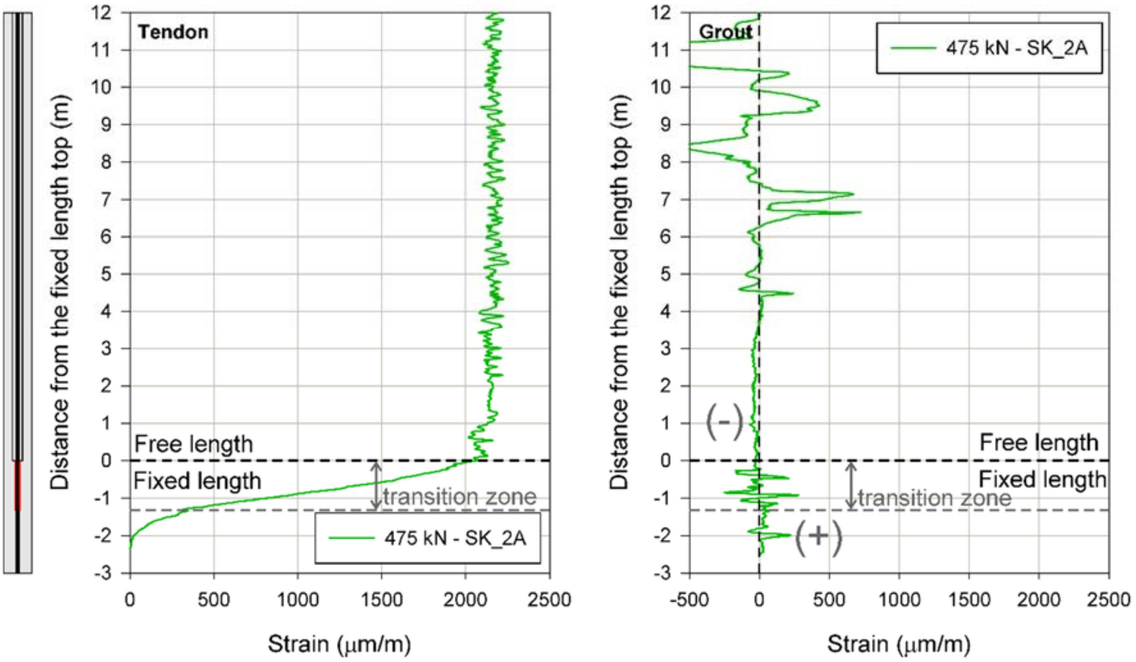

Fig. 135: Debonding mechanism (St Kanzian-test, anchor 2A)

9.2 Retaining wall

In order to investigate the retaining wall influence on the anchors behaviour, a 2D axisymmetric geometry of the anchor in Ljubljana was developed. Fig. 136 shows the model geometry employed. The 6 m depth overburden above the anchor was taken into account as a unique fill layer. The soil unit weight was 21 kN/m³ and the Mohr-Coulomb model was employed. The material parameters are shown in Tab. 35. The retaining wall was modelled as a 2 m thick linear elastic material (E = 30 GPa and $\nu = 0.2$). Because the in situ retaining wall was vertical, its self-weight was not acting on the anchor and, for the 2D simulation, the wall unit weight was set as 1 kN/m³.

The entire anchor was modelled within the silty gravel layer and below this layer the conglomerate material followed. The silty gravel and conglomerate parameters were set according to calibration 1 (Tab. 34) and the HSsmall model was selected. In order to consider approximately the same overburden pressure acting on the anchor as in the 3D geometry, for the 2D model the unit weight of these last two layers was decreased to 3.65 kN/m³. Therefore, the vertical stress acting at the middle of the anchor fixed length was about 160 kPa for the 2D and 3D simulations.

The normal stresses acting along the anchor in the 3D model are approximately the vertical stresses, whereas in the 2D geometry the normal stresses are the horizontal stresses. For this reason, in the axisymmetric model K_0 was set as 1 along the entire silty gravel and conglomerate layers and the horizontal stresses at the initial phase were the same as the vertical stresses. Increasing K_0 to 1 leads to approximately the same shear strength along the slip surface in the grout-soil interface for the 2D and 3D simulations.

The tendon was modelled as a linear elastic material (E_{tendon} = 160 GPa and ν = 0.2). The grout parameters were employed according to Tab. 38 (new grout parameters). The silty gravel and the grout parameters were selected to enable the comparison with the 3D simulation referred in chapter 8 as “refinement 2”.

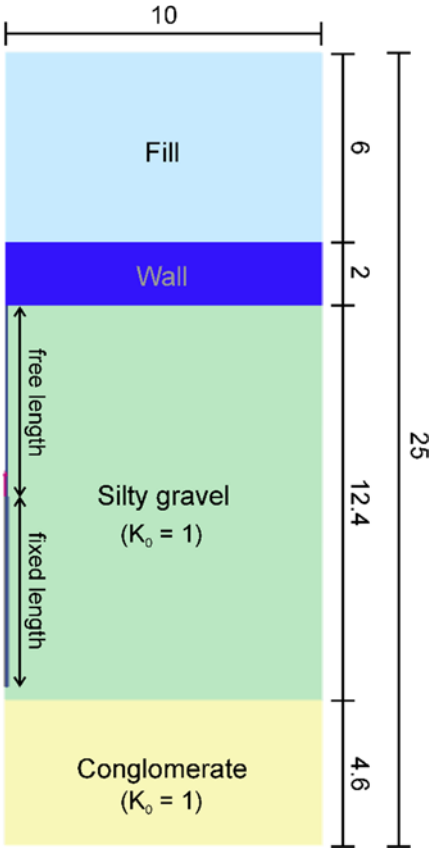

Fig. 136: 2D geometry of the Ljubljana-test (dimensions in metres)

The 2D simulation is referred as “2D_LJ simulation 1”. The load-displacement curves are shown in Fig. 137, where the 3D numerical refinement 2 is also depicted. The 2D simulation led to higher ultimate capacity in comparison with the 3D result, probably due to the K_0 increase performed in the former case. At approximately 1300 kN shear stresses are fully mobilised along the grout-soil interface at the fixed length but the pullout load still increases.

Fig. 138 shows tensile cracking in the grout and relative shear stresses for different load steps, considering the 2D_LJ simulation 1. If the anchor is loaded to 1000 kN, cracks are observed along the same anchor segment as shear failure in the grout-soil interface at the fixed length. At approximately 1300 kN, when shear strength is reached along the entire anchor fixed length, cracking spreads up to 4.4 m of the bond length. After full mobilisation of the skin friction at the fixed length, tensile cracks do not evolve significantly along the bond length. For this reason, cracking at 1500 and 2000 kN occurs along the same anchor section.

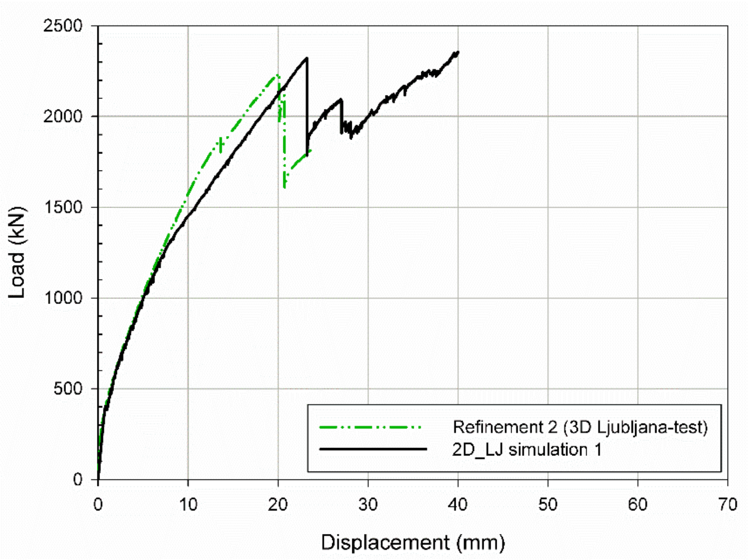

Fig. 137: Load-displacement curves (Ljubljana-test – 2D and 3D model)

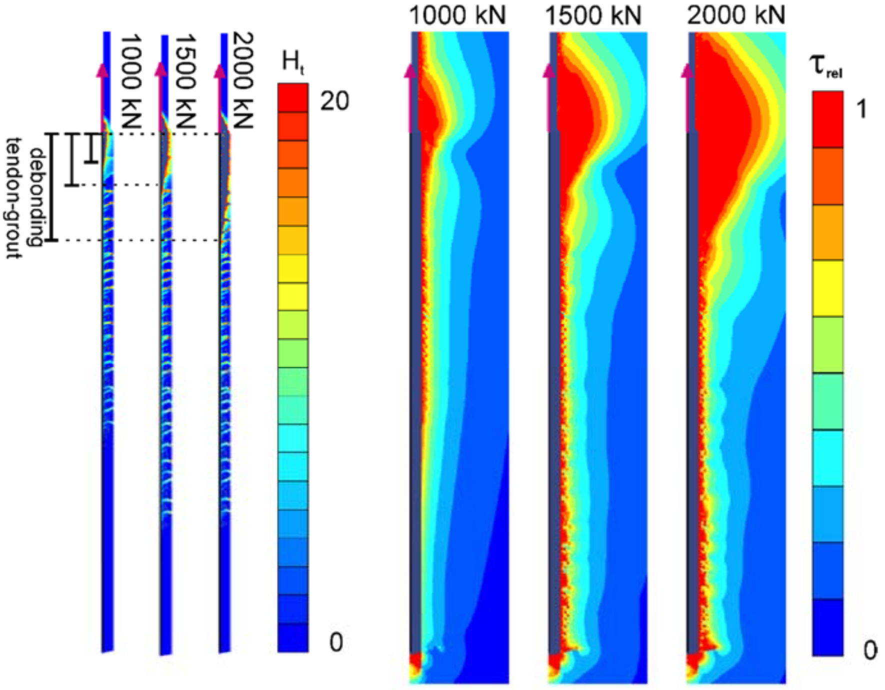

a) b)

Fig. 138: Grout condition and stresses in the soil (2D_LJ simulation 1) – a) cracking evolution at the fixed length and b) relative shear stresses in the soil

Because the movement of the grout at the free length is restrained, stress concentration occurs at the proximal end of the fixed length and the transition zone increases, i.e. shear failure in the tendon-grout interface evolves (Fig. 138a). The stress concentration is more pronounced after shear strength along the entire grout-soil interface at the fixed length is reached.

Within the transition zone the grouted body transfers load to the soil despite full shear stress mobilisation in the grout-soil interface at the bond length. This is shown in Fig. 138b for the 1500 and 2000 kN load steps, where the area at which the soil shear strength is reached increases at the proximal end of the anchor. The load increase after 1300 kN observed in Fig. 137 occurs due to this load transfer mechanism between the grout and the soil. At about 2320 kN numerical snap-back instability occurs due to compression softening of the grout.

It is important to mention that, if the ground stiffness is within the rock range, the stiff ground can act in a similar way as a retaining wall. In order to investigate this effect, another 2D simulation was performed and, for this simulation, the same geometry employed in the St Kanzian-test (anchor 1A) was adopted. The Mohr-Coulomb model was assigned for all soil layers and the Young's modulus was set as 5000 MPa. No retaining wall was considered.

The load-displacement curve is shown in Fig. 139. At approximately 3000 kN, the shear stresses in the grout-ground interface at the fixed length are fully mobilised but the anchor is still able to sustain higher loads. From about this load onwards the anchor fixed length moves upwards but, close to the ground surface, the grout at the free length does not move. The restrained movement leads to stress concentration at the proximal end of the fixed length, which results in local failure in the tendon-grout interface where stresses concentrate. Due to local bond failure in the tendon-grout interface, the load is transferred from the tendon to the grout below the damaged area, thus compressing the grout region where bond failure occurs. Although the skin friction at the fixed length in the grout-ground interface is fully mobilised, the grout under compressive stresses is able to transfer load to the ground. Fig. 140 shows failure points in the tendon-grout interface and vertical stresses surrounding and below the failure points, for a pullout load of 2500 kN.

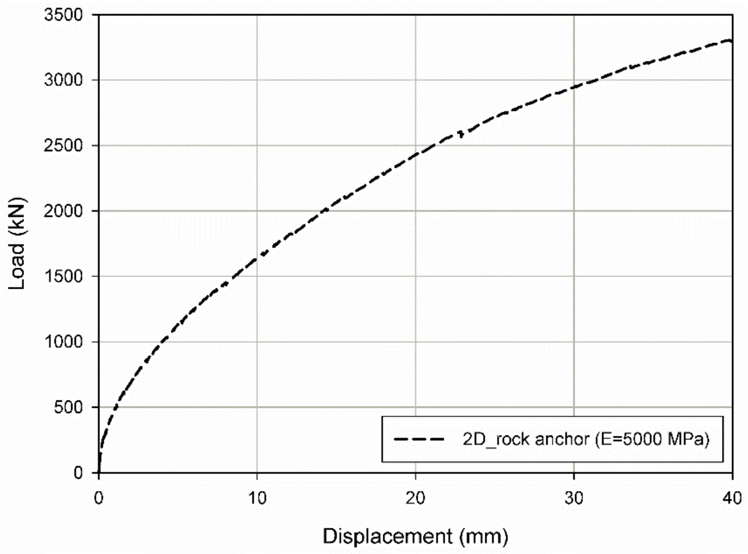

Fig. 139: Load-displacement curve (2D_rock anchor)

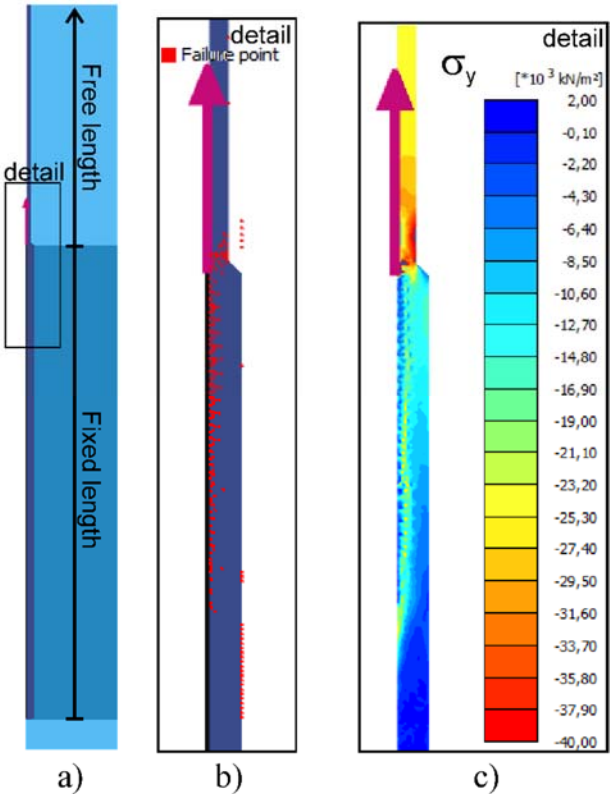

a) b) c)

Fig. 140: Debonding along the tendon-grout interface (2D_rock anchor) – a) fixed length overview; b) failure points and c) vertical stresses in the grout

Therefore, a major difference is observed in comparison with the simulations where the grout movement was not restrained. If complete slipping in the grout-ground interface is not observed, load is still transferred at the proximal end of the anchor even after the skin friction at the fixed length is fully mobilised. If complete slipping occurs, the entire anchor moves upwards and the ultimate capacity is reached.

9.3 Grout in the free length

For permanent anchors, it is common practice to inject grout around the tendon in the anchor free length to increase protection against corrosion. However, although the grout in the free length is intended only for corrosion protection, numerical simulations of anchor pullout tests indicated that the anchor bearing capacity can change significantly if this procedure is carried out.

In this respect, a 2D numerical simulation was undertaken in which no grout was considered in the free length. For this simulation, the same geometry and material data set as the reference simulation were considered, the only difference being the anchor free length that was not grouted. The geometry of the numerical simulations, with and without grout in the free length, is shown in Fig. 141. In the case that the free length was not grouted, the soil horizontal displacement was restrained at the borehole position (Fig. 141c).

The load-displacement curves are shown in Fig. 142. The grouted free length contributed to about 25% of the anchor ultimate capacity. In order to allow for a better insight into this result, the relative shear stresses contours along the grout-soil interface are plotted in Fig. 143 for the prescribed displacement of 10 mm. Once the grout is considered in the free length, load transfer is observed along the free length and the system behaves stiffer than if the free length is not grouted. In the last case, the stresses concentrate only along the fixed length and the ultimate capacity is achieved after shear strength is reached at the entire bond length.

It is noteworthy that the load transfer between the grout and the soil starts at the proximal end of the fixed length and moves upwards towards the free length. This reflects the actual in situ situation if the tendon is perfectly isolated from the grout in the free length. Moreover, if the grout is applied in the free length, the shear strength in the entire grout-soil interface along the free length is reached before the shear stresses along the fixed length are fully mobilised. Therefore, in both cases the ultimate capacity is reached after full mobilisation of the skin friction along the fixed length.

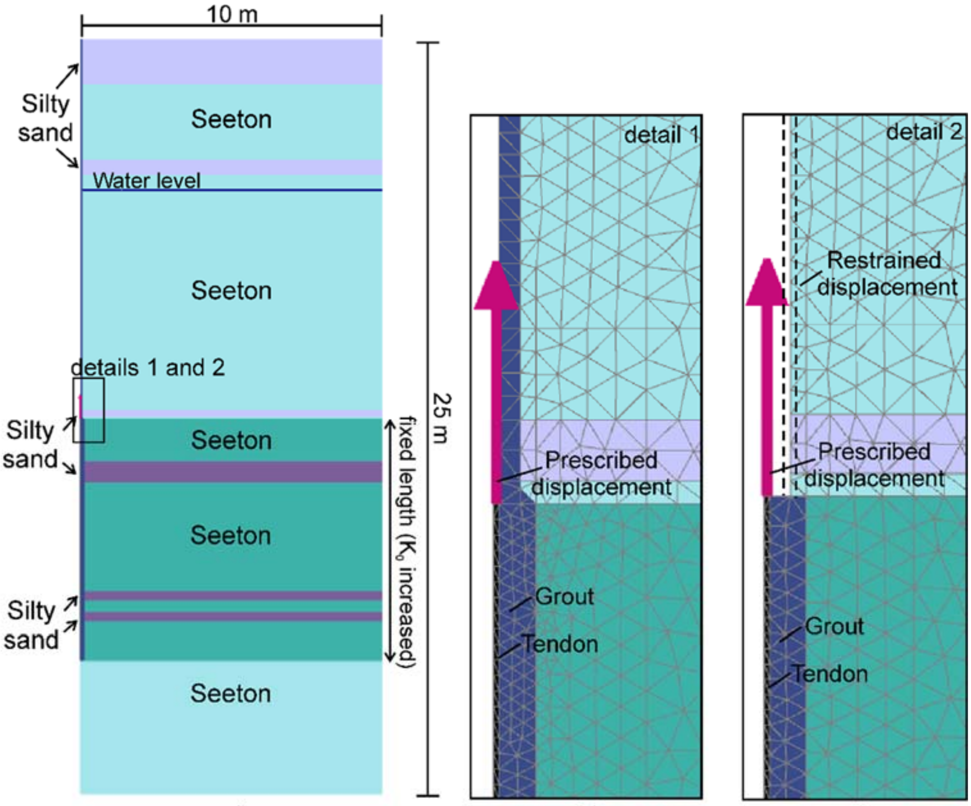

a) b) c)

Fig. 141: Geometry of the numerical simulation – a) free length grouted (reference simulation) and b) free length not grouted

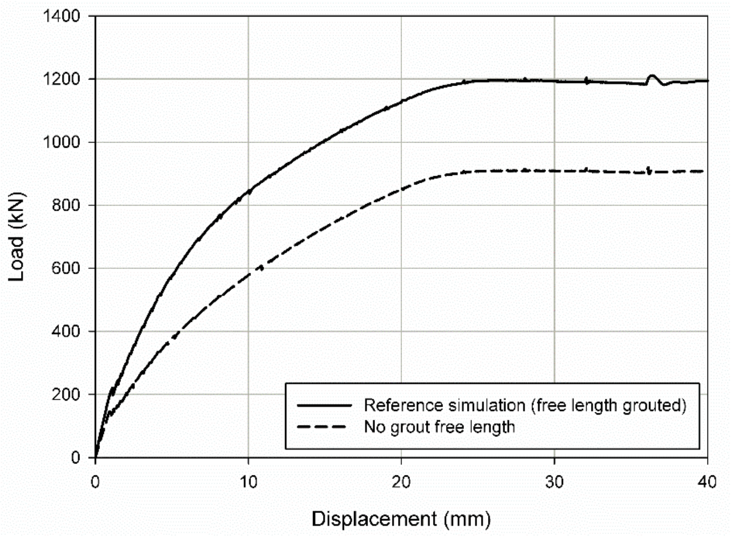

Fig. 142: Load-displacement curves with and without grout in the free length

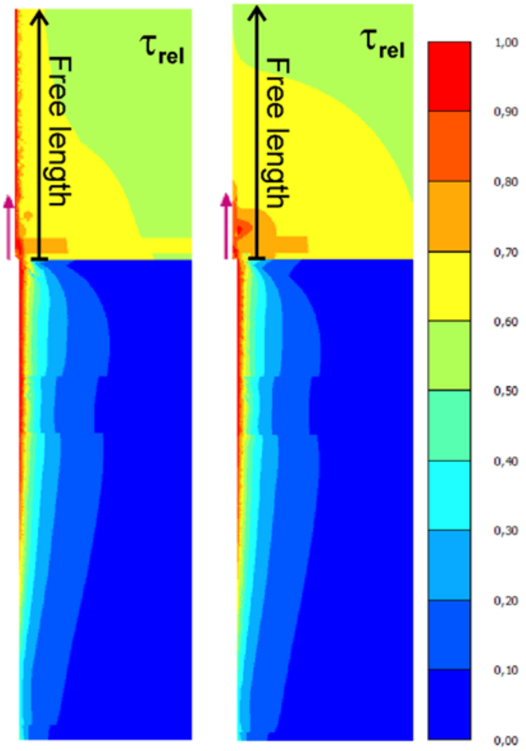

a) b)

Fig. 143: Relative shear contours (10 mm displacement) – a) free length grouted and b) free length not grouted

The strain distribution along the tendon at the fixed length is compared in Fig. 144. Due to the stiffer behaviour if the grout is applied in the free length, the tendon activation is larger in the strain profile obtained with the simulation that did not account for the grout in the free length. Regarding the transition zone, the sharp strain decreased observed in the simulation that considered the free length grouted was not verified in the simulation that the grout in the free length was not modelled. This was expected because compressive stresses in the grout are transferred from the free length to the fixed length.

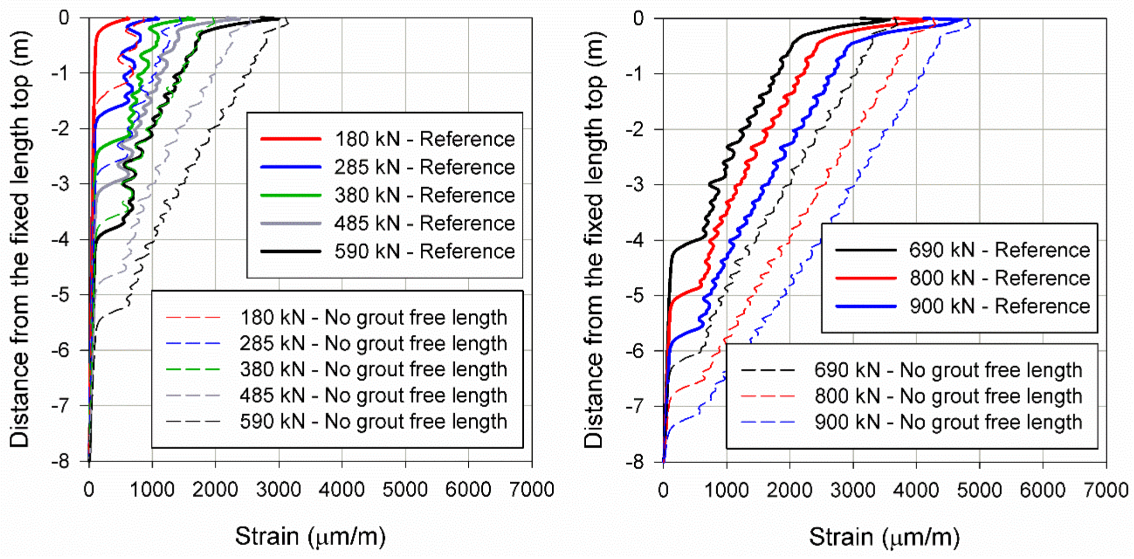

Fig. 144: Strain distribution along the tendon – free length grouted (reference simulation) *vs* free length not grouted

The same procedure of removing the grout in the free length was simulated for the A10-test and the load-displacement curves are shown in Fig. 145. Simulation 3 (section 7.4.2) was considered for the comparison. As observed in Fig. 142, the anchor behaves significantly stiffer when the grout is considered in the free length. If a comparison at the same displacement is made, the load is about 20% lower than the load obtained if the grout in the free length is simulated. Because the ground stiffness was larger for the A10-test, relative movement between grout and rock is reduced in comparison with the soil anchor that showed a contribution of approximately 25%.

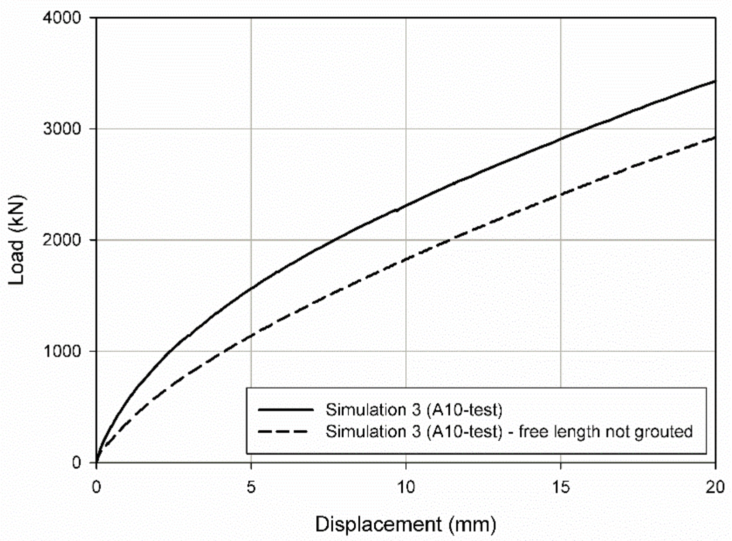

Fig. 145: Load-displacement curves with and without grout in the free length (A10-test)

9.4 Anchor length

During the pullout test of the anchor A10, it was verified that, at the permanent load, less than 30% of the anchor fixed length was activated. In this respect, an additional simulation was performed changing the fixed length. The aim was to evaluate if increasing the non-activated anchor length affects the numerical results significantly with respect to the load-displacement behaviour and the tendon strain distribution.

The reference numerical simulation (St Kanzian-test, anchor 1A) was 8 m at the fixed length. Regarding the additional simulation, the fixed length was increased to 10 m. The load-displacement curves are presented in Fig. 146. As expected, increasing the anchor fixed length leads to an increase in the ultimate pullout load by increasing the grout-soil interface where failure occurs. However, it is remarkable that the slope of both curves is almost identical up to the ultimate capacity of the reference anchor, thus indicating that, although the anchor in the additional simulation is stiffer than the reference anchor, the load-displacement behaviour is almost unaffected.

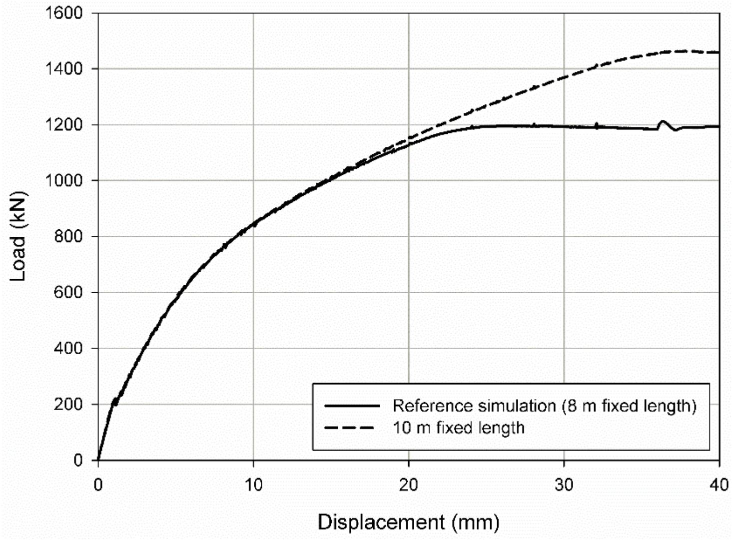

Fig. 146: Load-displacement curves (8 and 10 m long at the fixed length)

The strains along the tendon for both simulations are plotted in Fig. 147. After increasing the fixed anchor length, the differences observed between the numerical results are not significant. The last load step depicted in Fig. 147 showed that, for the simulation with increased length, the active portion of the anchor is only slightly larger than the active portion of the reference simulation. Therefore, if the same load step is analysed, the load distribution along the tendon is almost independent regardless of the fixed length size.

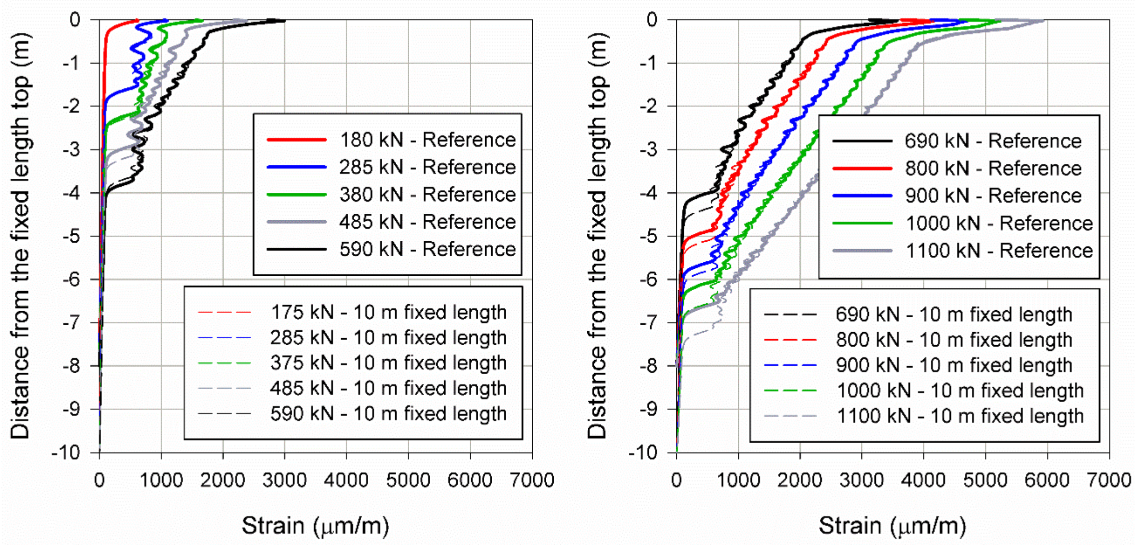

Fig. 147: Strain distribution along the tendon – 8 m long at the fixed length (reference simulation) *vs* 10 m long at the fixed length

9.5 Summary

After evaluating numerical and in situ results, further investigations were carried out to allow for a better insight into specific aspects influencing anchor pullout tests. At the beginning of this section, debonding and its effect on the fibre optic strain profile are discussed. Furthermore, numerical simulations were undertaken in order to evaluate separately how the retaining wall, the grout in the free length and the anchor length influence the anchors behaviour. The following conclusions can be drawn:

- Different debonding mechanisms were observed during the in situ tests. At the proximal end of the fixed length the compressive stresses observed in the grout probably occur due to local shear failure between tendon and grout. When failure in the interface develops, the load is mainly transferred to the grout below the debonded section. Therefore, the grout region surrounding the debonded interface undergoes compressive stresses, i.e. the transition zone increases. Within this debonded area crack closure occurs and load transfer between tendon and grout is observed. Another debonding mechanism, which might be related to the development of normal tensile cracks, was identified when the grout undergoes tensile stresses. In this case, if the grout is significantly damaged, the contact between tendon and grout is reduced and the load transfer decreases significantly;
- The influence of the retaining wall was analysed with a 2D axisymmetric model of the Ljubljana test. The inclination of the in situ anchor was 10° with respect to the horizontal axis and, in order to simulate the test on a 2D model, the soil weight was modified to achieve approximately the same overburden pressure acting along the anchor. Moreover, the lateral earth pressure coefficient at rest was increased to 1 to obtain a similar stress distribution acting perpendicular to the anchor. The simulation showed that, because the retaining wall restrains the anchor movement at the free length, the pullout

load increases significantly even after full mobilisation of shear stresses at the fixed length in the grout-soil interface. Stress concentration occurs at the proximal end of the anchor leading to local failure in the tendon-grout interface. The same load transfer behaviour was observed if the ground stiffness is within the range expected for rocks and, in this case, the stiff ground acted in a similar way as a retaining wall;

- If the grout in the free length was not considered during the numerical analysis, the anchor ultimate capacity decreased by about 20-25% in comparison with simulations that accounted for a grouted free length. This difference occurs because load transfer in the grout-soil interface is not restricted to the fixed length but it also expands towards the free anchor length. Because compressive stresses in the grout are transferred from the free to the fixed length, the sharp strain decrease in the transition zone along the tendon was not verified if the free length was not grouted;
- Increasing the anchor fixed length led to an increase in the anchor ultimate capacity by increasing the area where shear failure develops. However, if the same load step is analysed, the active portion of the tendon was almost the same regardless of the fixed length size.

10 Conclusions

In order to evaluate the load transfer behaviour of ground anchors, in situ anchor pullout tests were performed under different ground conditions. The anchors were monitored at the anchor head with a linear transducer and, for each ground type, at least one anchor was monitored with distributed fibre optic sensors. The fibre optic system, based on Rayleigh scattering and Optical Frequency Domain Reflectometry, was installed along the tendon and embedded in the grout. High spatial resolution measurements were obtained and the load transfer behaviour during the pullout tests was assessed.

The in situ tests were simulated using the finite element method. In some cases, if sufficient information on the ground and grout characteristics was available, numerical class-A predictions were undertaken. The load-displacement curves and the strain profiles were then compared with the numerical results. The simulations were refined after analysing the in situ measurements and after new laboratory test results were available.

During the tests, on site, the fibre optic measurements gave a clear indication of the tendon activation and of the crack development in the grout. Therefore, pullout tests monitored with fibre optic sensors could be carried out in advance on pre-selected anchors and, combined with numerical simulations, the results could be employed to optimise anchor design. Furthermore, the information obtained through the fibre optic measurements and the numerical simulations provided important findings and the main conclusions are summarized below.

The load transfer varies over depth at the fixed length: the strain profile along the tendon indicated that the load is not transferred from the tendon to the grout at the same rate, i.e. the inclination of the strain profile changes with increasing depth.

The load transfer is highly affected by the grout conditions. Within the transition zone, where the grout undergoes compressive stresses at the fixed length, the load transfer is usually high. Below the transition zone tensile cracks evolve and, before the anchor approaches the ultimate capacity, at the distal end the grout is not cracked. In comparison with the undamaged grout section, along the section where the grout is cracked the strains in the tendon are significantly larger. It was also verified that at the position where large cracks develop the load transfer in the tendon-grout interface was reduced, thus suggesting debonding between tendon and grout. This behaviour was clearly identified in the Söding-test measurements.

Regarding anchor 1A (St Kanzian-test), the strain profile was used to calculate shear stresses along the grout-ground interface. The skin friction obtained was in general larger at the proximal end of the fixed length and decreased with crack development, leading to a non-uniform distribution of skin friction in the grout-soil interface.

The in situ measurements usually indicated failure in the grout-ground interface: when the anchor was brought to failure, the tendon was fully activated or almost fully activated at the fixed length. In general the failure mechanism developed along the grout-ground interface and, in this case, high peaks along the grout strain profile were verified, thus indicating cracking. Regarding anchors 2A and 3A (St Kanzian-test), the strains along the grout did not develop significantly, suggesting that load transfer from the tendon to the grout was very low at the position where the fibre optic cable was installed. Therefore, in these cases the failure mechanism was possibly between tendon and grout and not between grout and ground.

The increase of the transition zone is probably related to debonding in the tendon-grout interface: The width of the transition zone increases as the pullout test proceeds and it varies for different ground stiffness. The spread of compressive stresses in the grout at the fixed length was very pronounced for the Ljubljana-anchor. The strain profile of the pullout tests monitored with the fibre optic cables showed that stress concentration occurs at the proximal end of the fixed length, within the transition zone. Due to this stress concentration, it is believed that debonding in the tendon-grout interface occurred along this section.

Assuming shear failure between tendon and grout at the proximal end of the fixed length, the pullout load is transferred from the tendon to the grout below the debonded area. Therefore, the grout at the fixed length surrounding this debonded region is subjected to compressive stresses and, below the debonded section, to tensile stresses. This load transfer mechanism was confirmed with a numerical simulation that accounted for local failure in the tendon-grout interface.

It is important to mention that tensile cracks in the grout were observed before the spreading of compressive stresses. As compressive stresses evolve at the fixed length, tensile cracks close and the transition zone increases. Whereas the load transfer between the tendon and the grout reduces if the grout is cracked and subjected to tensile stresses, after crack closure the transfer is regained.

The ground stiffness influences significantly the anchor behaviour: in situ results and numerical simulations showed that the load-displacement behaviour and the strain distribution along the tendon and the grout are significantly different for soil and rock anchors. In this respect, the active portion of the anchor installed in rock (A10-test) was only 2 m for the 1050 kN load step and, considering the anchor installed in a clayey silt material (St Kanzian-test, anchor 1A), the active portion was 6 m for a pullout load of 1000 kN. Moreover, considering the same load, shear failure in the grout-ground interface and cracking in the grout occur along a smaller section for stiff materials in comparison with a softer ground condition.

The numerical results indicated that, if the ground stiffness is within the range expected for rocks, the movement of the grout at the free length top might be restrained and complete slipping in the grout-ground interface does not occur. The same was observed if a retaining wall was considered in the simulations. Under this condition, stress concentration is observed at the proximal end of the fixed length. Therefore, local shear failure in the tendon-grout interface develops and the transition zone increases.

The grout in the free length contributes to the anchor ultimate capacity: although the grout in the free length is intended only for corrosion protection, numerical simulations of anchor pullout tests indicated that the anchor bearing capacity increased about 20-25% if grout is assumed in the free length. This difference occurs because load transfer in the grout-soil interface spreads from the fixed length towards the free anchor length. In the case that the free length is grouted, compressive stresses in the grout are transferred from the free to the fixed length. Therefore, the sharp strain decrease within the transition zone along the tendon was not verified for the simulation that did not account for the grout in the free length.

The Concrete model is able to simulate cracking evolution during anchor pullout tests: in situ cracking evolution was compared with the tension softening parameter distribution, which is an output of the Concrete model. The tensile crack development was well captured by the constitutive model. However, due to the smeared crack approach, the model did not simulate the load transfer reduction observed in the in situ measurements when tensile cracks increased significantly.

Shear failure between the tendon and the grout developed during the numerical simulations when significant stress concentration at the proximal end of the fixed length took place. However, the spreading of the transition zone occurred along a smaller section in comparison with the in situ tests. This limitation possibly occurs because tension and compression softening are treated independently in the Concrete model. For this reason, when tensile cracks evolve, the grout tensile strength reduces but the compressive strength remains unaffected.

11 Bibliography

Akisanya, A. R. & Ivanović, A., 2014. Debonding along the fixed anchor length of a ground anchorage. *Engineering Structures, Vol. 74*, pp. 23-31.

American Association of State Highway and Transportation Officials, 2002. *Standard Specifications for Highway Bridges.* Washington, DC: American Association of State Highway and Transportation Officials.

Austrian Standards Institute, 1978. *ÖNORM B 4416:1978: Erd- und Grundbau; Untersuchung von Bodenproben; Grundsätze für die Durchführung und Auswertung von Scherversuchen.* Vienna: Austrian Standards Institute.

Austrian Standards Institute, 1989. *ÖNORM B 4420:1989: Erd- und Grundbau; Untersuchung von Bodenproben; Grundsätze für die Durchführung und Auswertung von Kompressionsversuchen.* Vienna: Austrian Standards Institute.

Austrian Standards Institute, 2005. *ÖNORM CEN ISO/TS 17892-4:2005: Geotechnische Erkundung und Untersuchung - Laborversuche an Bodenproben - Teil 4: Bestimmung der Korngrößenverteilung.* Vienna: Austrian Standards Institute.

Austrian Standards Institute, 2008. *ÖNORM B 4411:2008: Geotechnik - Untersuchung von Bodenproben - Bestimmung von Fließ-, Plastizitäts- und Schrumpfgrenzen unter Einbeziehung der VORNORM ÖNORM CEN ISO/TS 17892-12.* Vienna: Austrian Standards Institute.

Austrian Standards Institute, 2009. *ÖNORM B 4411:2009: Geotechnik - Untersuchung von Bodenproben - Bestimmung von Fließ-, Plastizitäts- und Schrumpfgrenze unter Einbeziehung der VORNORM ÖNORM CEN ISO/TS 17892-12.* Vienna: Austrian Standards Institute.

Austrian Standards Institute, 2010. *ÖNORM EN 12390-6:2010: Prüfung von Festbeton - Teil 6: Spaltzugfestigkeit von Probekörpern.* Viena: Austrian Standards Institute.

Austrian Standards Institute, 2012. *ÖNORM EN 12390-3:2012: Prüfung von Festbeton - Teil 3: Druckfestigkeit von Probekörpern.* Vienna: Austrian Standards Institute.

Austrian Standards Institute, 2013. *ÖNORM B 1997-1-1:2013. Eurocode 7: Entwurf, Berechnung und Bemessung in der Geotechnik - Teil 1: Allgemeine Regeln - Nationale Festlegungen zu ÖNORM EN 1997-1 und nationale Ergänzungen.* Vienna: Austrian Standards Institute.

Austrian Standards Institute, 2014. *ÖNORM EN 1997-1:2014: Eurocode 7: Geotechnical design. Part 1: General rules.* Vienna: Austrian Standards Institute.

Austrian Standards Institute, 2014. *ÖNORM EN ISO 17892-4:2014: Geotechnische Erkundung und Untersuchung - Laborversuche an Bodenproben - Teil 4: Bestimmung der Korngrößenverteilung.* Vienna: Austrian Standards Institute.

Austrian Standards Institute, 2015. *ÖNORM EN 1537:2015: Execution of special geotechnical works - ground anchors.* Vienna: Austrian Standards Institute.

Austrian Standards Institute, 2019. *ÖNORM EN ISO 22477-5:2019: Geotechnical investigation and testing - Testing of geotechnical structures. Part 5: Testing of grouted anchors.* Vienna: Austrian Standards Institute.

Bao, X. & Chen, L., 2012. Recent Progress in Distributed Fiber Optic Sensors. *Sensors, Vol. 12*, pp. 8601-8639.

Barrias, A., Casas, J. R. & Villalba, S., 2016. A review of distributed optical fiber sensors for civil engineering applications. *Sensors, Vol. 16*.

Bažant, Z. P., 1986. Mechanics of distributed cracking. *Applied Mechanics Review, Vol. 39, No. 5*, pp. 675-705.

Bažant, Z. P. & Oh, B. H., 1983. Crack band theory for fracture of concrete. *Materials and Structures, Vol. 16*, pp. 155-177.

Bažant, Z. P. & Oh, B. H., 1986. Efficient Numerical Integration on the Surface of a Sphere. *Zeitschrift für Angewandte Mathematik und Mechanik, Vol. 66*, pp. 37-49.

Benmokrane, B., Chekired, M. & Xu, H., 1995. Monitoring Behavior of Grouted Anchors Using Vibrating-Wire Gauges. *Journal of Geotechnical Engineering, Vol. 121*, pp. 466-475.

Bennett, P. J., Klar, A., Vorster, T. E. B., Choy, C. K., Mohamad, H., Soga, K., Mair, R. J., Tester, P. D. & Fernie, R., 2006. Distributed optical fibre strain sensing in piles. In: *Proceedings of the International Conference on Reuse of Foundations for Urban Sites.* Watford. Bracknell: BRE Press, pp. 71-78.

Benz, T., 2007. *Small-Strain Stiffness of Soils and its Numerical Consequences.* Ph.D. Thesis, Stuttgart: Universität Stuttgart.

Berenbaum, R. & Brodie, I., 1959. Measurement of the tensile strength of brittle materials. *British Journal of Applied Physics, Vol. 10*, pp. 281-287.

Bersan, S., Bergamo, O., Palmieri, L., Schenato, L. & Simonini, P., 2018. Distributed strain measurements in a CFA pile using high spatial resolution fibre optic sensors. *Engineering Structures, Vol. 160*, pp. 554-565.

Brinkgreve, R. B. J., Kumarswamy, S. & Swolfs, W. M., 2017a. *Plaxis 2017.* Delft: Plaxis bv.

Brinkgreve, R. B. J., Kumarswamy, S. & Swolfs, W. M., 2018. *Plaxis 2018 (3D).* Delft: Plaxis bv.

Brinkgreve, R. B. J., Kumarswamy, S., Swolfs, W. M. & Foria, F., 2017b. *Plaxis 2017 (3D).* Delft: Plaxis bv.

Brinkgreve, R. B. J., Kumarswamy, S., Swolfs, W. M., Zampich, L. & Manoj, N. R., 2019a. *Plaxis 2D 2019 - Material Models Manual 2019.* Delft: Plaxis bv.

Brinkgreve, R. B. J., Kumarswamy, S., Swolfs, W. M., Zampich, L. & Manoj, N. R., 2019b. *Plaxis 2D 2019 - Reference Manual 2019.* Delft: Plaxis bv.

Carpinteri, A. & Colombo, G., 1989. Numerical analysis of catastrophic softening behaviour (snap-back instability). *Computers and Structures, Vol. 31, No. 4*, pp. 607-636.

Fang, Y. -S., Liao, J. -J. & Sze, S. -C., 1994. An empirical strength criterion for jet grouted soilcrete. *Engineering Geology, Vol. 37, Issues 3-4*, pp. 285-293.

Galavi, V. & Schweiger, H. F., 2010. Nonlocal multilaminate model for strain softening analysis. *International Journal of Geomechanics, Vol. 10, No. 1*, pp. 30-44.

Google Maps, 2013. *Google Maps.* [Online] [Accessed 02 10 2019].

Hauswirth, D., Puzrin, A. M., Carrera, A., Standing, J. R. & Wan, M. S. P., 2014. Use of fibre-optic sensors for simple assessment of ground surface displacements during tunnelling. *Géotechnique, Vol. 64, No. 10*, pp. 837-842.

International Organization for Standardization, 2004. *ISO 17892-12:2004: Geotechnical investigation and testing — Laboratory testing of soil - Part 12: Determination of Atterberg limits.* Geneva: International Organization for Standardization.

International Organization for Standardization, 2004. *ISO/TS 17892-10:2004: Geotechnical investigation and testing — Laboratory testing of soil — Part 10: Direct shear tests.* Geneva: International Organization for Standardization.

International Organization for Standardization, 2004. *ISO/TS 17892-5:2004: Geotechnical investigation and testing — Laboratory testing of soil - Part 5: Incremental loading oedometer test.* Geneva: International Organization for Standardization.

International Organization for Standardization, 2016. *ISO 17892-4:2016: Geotechnical investigation and testing — Laboratory testing of soil — Part 4: Determination of particle size distribution.* Geneva: International Organization for Standardization.

Iten, M., Puzrin, A. M. & Schmid, A., 2008. Landslide monitoring using a road-embedded optical fiber sensor. In: *Smart Sensor Phenomena, Technology, Networks, and Systems 2008. Proceedings of SPIE.* San Diego. Bellingham: SPIE, p. 6933 15.

Ivanović, A. & Neilson, R. D., 2009. Modelling of debonding along the fixed anchor length. *International Journal of Rock Mechanics & Mining Sciences, Vol. 46*, pp. 699-707.

Lambe, T. W. & Whitman, R. V., 1969. *Soil Mechanics.* New York: John Wiley & Sons.

Lee, S. A., 2014. *Characterization and modelling of cement-treated soil column used as cantilever earth retaining structure.* Ph.D. Thesis, Singapore: National University of Singapore.

Leung, C. K. Y., Wan, K. T., Inaudi, D., Bao, X., Habel, W., Zhou, Z., Ou, J., Ghandehari, M., Wu, H. C. & Imai, M., 2015. Review: optical fiber sensors for civil engineering applications. *Materials and Structures, Vol. 48*, pp. 871-906.

Lin, Z. & Wood, L., 2003. Concrete uniaxial tensile strength and cylinder splitting test. *Journal of Structural Engineering, Vol. 129*, pp. 692-698.

Littlejohn, G. S., 1980. Design estimation of the ultimate load-holding capacity of ground anchors. *Ground Engineering, Vol. 13*, pp. 25-39.

Luna, 2014. *Data Sheet: Optical Backscatter Reflectometer (Model OBR 4600), Ver. LTOBR4600 REV. 004 02/13/2014.* Roanoke: Luna Technologies Inc..

Marchetti, S., 1980. In situ tests by flat dilatometer. *Journal of the Geotechnical Engineering Division, Vol. 106, No. GT3*, pp. 299-321.

Mohamad, H., Bennett, P. J., Soga, K., Mair, R. J. & Bowers, K., 2010. Behaviour of an old masonry tunnel due to tunnelling-induced ground settlement. *Géotechnique, Vol. 60, No. 12*, pp. 927-938.

Mohamad, H., Soga, K., Pellew, A. & Bennett, P., 2011. Performance Monitoring of a Secant-Piled Wall Using Distributed Fiber Optic Strain Sensing. *Journal of Geotechnical and Geoenvironmental Engineering, Vol. 137*, pp. 1236-1243.

Monsberger, C. M., Lienhart, W., Kluckner, A., Wagner, L. & Schubert, W., 2018. Continuous strain measurements in a shotcrete tunnel lining using distributed fibre optic sensing. In: *Proceedings of the 9th European Workshop on Structural Health Monitoring.* Manchester.

Monsberger, C., Woschitz, H. & Hayden, M., 2016. Deformation measurement of a driven pile using distributed fibre-optic sensing. *Journal of Applied Geodesy, Vol. 10*, pp. 61-69.

Ostermayer, H., 1975. Construction, carrying behaviour and creep characteristics of ground anchors. In: *Proceedings of Conference on Diaphragm Walls and Anchorages.* London: Institute of Civil Engineers, pp. 141-151.

Ostermayer, H. & Scheele, F., 1978. Research on ground anchors in non-cohesive soils. *Revue Française de Géotechnique, No. 3*, pp. 92-97.

Ostermeyer, H. & Barley, T., 2003. Fixed Anchor Design Guidelines. In: *Geotechnical Engineering Handbook 2.* Berlin: Ernst & Sohn.

Palmieri, L. & Schenato, L., 2013. Distributed optical fiber sensing based on rayleigh scattering. *The Open Optics Journal, Vol. 7*, pp. 104-127.

Pande, G. N. & Sharma, K. G., 1983. Multilaminate model of clays – a numerical evaluation of the influence of rotation of principal stress axes. *International Journal for Numerical and Analytical Methods in Geomechanics, Vol. 7, No. 4*, pp. 397-418.

Rabaiotti, C. & Malecki, C., 2018. In situ testing of barrette foundations for a high retaining wall in molasse rock. *Géotechnique, Vol. 68, No. 12*, pp. 1056-1070.

Racansky, V., Roman, W., Lienhart, W., Monsberger, C., Woschitz, H. & Schweiger, H. F., 2016. Überwachung eines Ankerausziehversuches mittels Glasfasersensoren. In: *Tagungsband zur 34. Baugrundtagung.* Bielefeld: DGGT, pp. 315-322.

Ren, F. F., Yang, Z. J., Chen, J. F. & Chen, W. W., 2010. An analytical analysis of the full-range behaviour of grouted rockbolts based on a tri-linear bond-slip model. *Construction and Building Materials, Vol. 24*, pp. 361-370.

Schädlich, B., 2012. *A Multilaminate Constitutive Model for Stiff Soils.* Ph.D. Thesis, Graz: Technische Universität Graz.

Schädlich, B. & Schweiger, H. F., 2014a. A new constitutive model for shotcrete. In: *Proceedings of the 8th European Conference on Numerical Methods in Geotechnical Engineering.* Delft. Leiden: Balkema, pp. 103-108.

Schädlich, B. & Schweiger, H. F., 2014b. Modelling the shear strength of overconsolidated clays with a Hvorslev surface. *Geotechnik, Vol. 37*, pp. 45-56.

Schädlich, B., Schweiger, H. F., Marcher, T. & Saurer, E., 2014. Application of a novel constitutive shotcrete model to tunnelling. In: *Rock Engineering and Rock Mechanics: Structures in and on Rock Masses.* Leiden: CRC Press.

Schanz, T., Vermeer, P. A. & Bonnier, P. G., 1999. The Hardening Soil model – formulation and verification. In: *Proceedings of the International Symposium Beyond 2000 in Computational Geotechnics.* Amsterdam. Rotterdam: Balkema, pp. 281-296.

Schnaid, F., Belloli, M. V. A., Odebrecht, E. & Marchetti, D., 2018. Interpretation of the DMT in Silts. *Geotechnical Testing Journal, Vol. 41, No. 5*, pp. 868-876.

Schweiger, H. F., Sedighi, P., Henke, S. & Borchert, K. -M., 2014. Numerical modelling of ground improvement techniques considering tension softening. In: *Proceedings of the 8th International Symposium on Geotechnical Aspects of Underground Construction in Soft Ground.* Seoul. Leiden: CRC Press, pp. 209-214.

Schweiger, H. F., Wiltafsky, C., Scharinger, F. & Galavi, V., 2009. A multilaminate framework for modelling induced and inherent anisotropy of soils. *Géotechnique, Vol. 59, No. 2*, pp. 87-101.

Smet, J., Huybrechts, N., van Lysebetten, G., Verstraelen, J. & François, S., 2019. Optical fiber strain measurements and numerical modeling of load tests on grouted anchors. *Journal of Geotechnical and Geoenvironmental Engineering, Vol. 145, No. 12.*

Taylor, D. W., 1948. *Fundamentals of Soil Mechanics.* New York: John Wiley & Sons.

Taylor, G. I., 1938. Plastic strain in metals. *Journal of the Institute of Metals, Vol. 62*, pp. 307-324.

Terzaghi, K. & Peck, R. B., 1948. *Soil mechanics in engineering practice.* New York: John Wiley & Sons.

Toraldo, C., Modoni, G., Ochmanski, M. & Croce, P., 2018. The characteristic strength of jet-grouted material. *Géotechnique, Vol. 68, No. 3*, pp. 262-279.

Van Mier, J. G. M., 1984. *Strain-softening of concrete under multiaxial loading conditions.* Ph.D. Thesis, Eindhoven: Eindhoven University of Technology.

Vonk, R. A., 1992. *Softening of concrete loaded in compression.* Ph.D. Thesis, Eindhoven: Eindhoven University of Technology.

Weerasinghe, R. B. & Littlejohn, G. S., 1997. Load Transfer and Failure of Anchorages in Weak Mudstone. In: *Proceedings of the International Conference on ground anchorages and anchored structures.* London: Thomas Telford, pp. 34-44.

Wernick, E., 1978. Stresses and strains on the surface of anchors. *Revue Française de Géotechnique, No. 3*, pp. 113-119.

Woschitz, H., Monsberger, C. & Hayden, M., 2016. Distributed fibre-optic strain measurements on a driven pile. In: *Proceeding of the 6th European Workshop on Optical Fibre Sensors.* Limerick.

Xanthakos, P. P., 1991. *Ground anchors and anchored structures.* New York: John Wiley & Sons.

Appendix

In order to facilitate the visualisation of the results obtained with the fibre optic cables, the strain profiles are shown herein separately and in larger dimensions. The measurements of the Söding-test are shown in Fig. A1 and Fig. A2. The St Kanzian results of anchor 1A are presented in Fig. A3 and Fig. A4. The results of anchor 2A are shown in Fig. A5 (measurement 1), Fig. A6 (measurement 2) and in Fig. A7. In Fig. A8 the results of anchor 3A are depicted. The strain profiles obtained during the A10-test are shown in Fig. A9 and Fig. A10. The Ljubljana measurements are presented in Fig. A11 and Fig. A12.

Söding-test

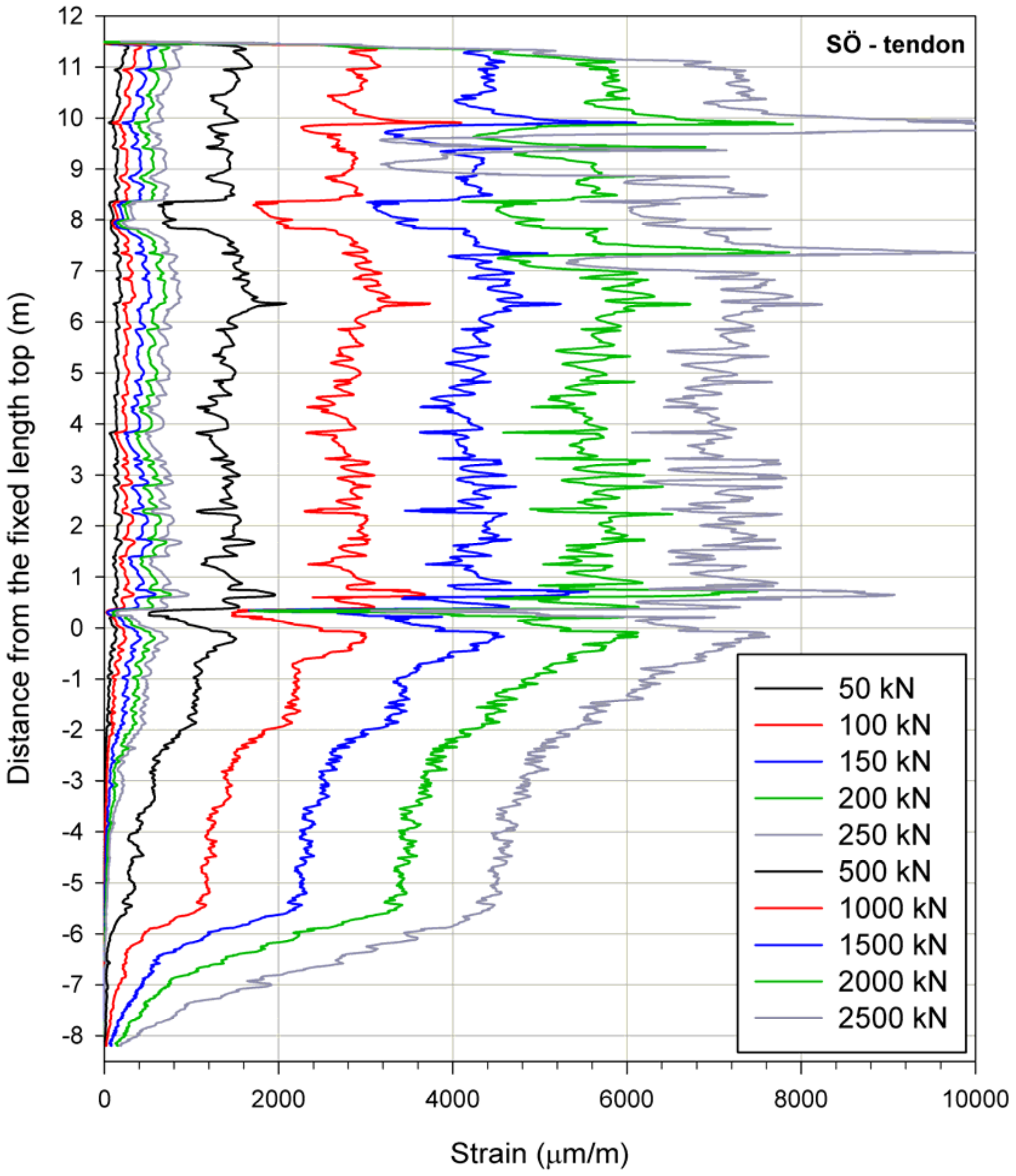

Fig. A1: Strains along the tendon (Söding-test)

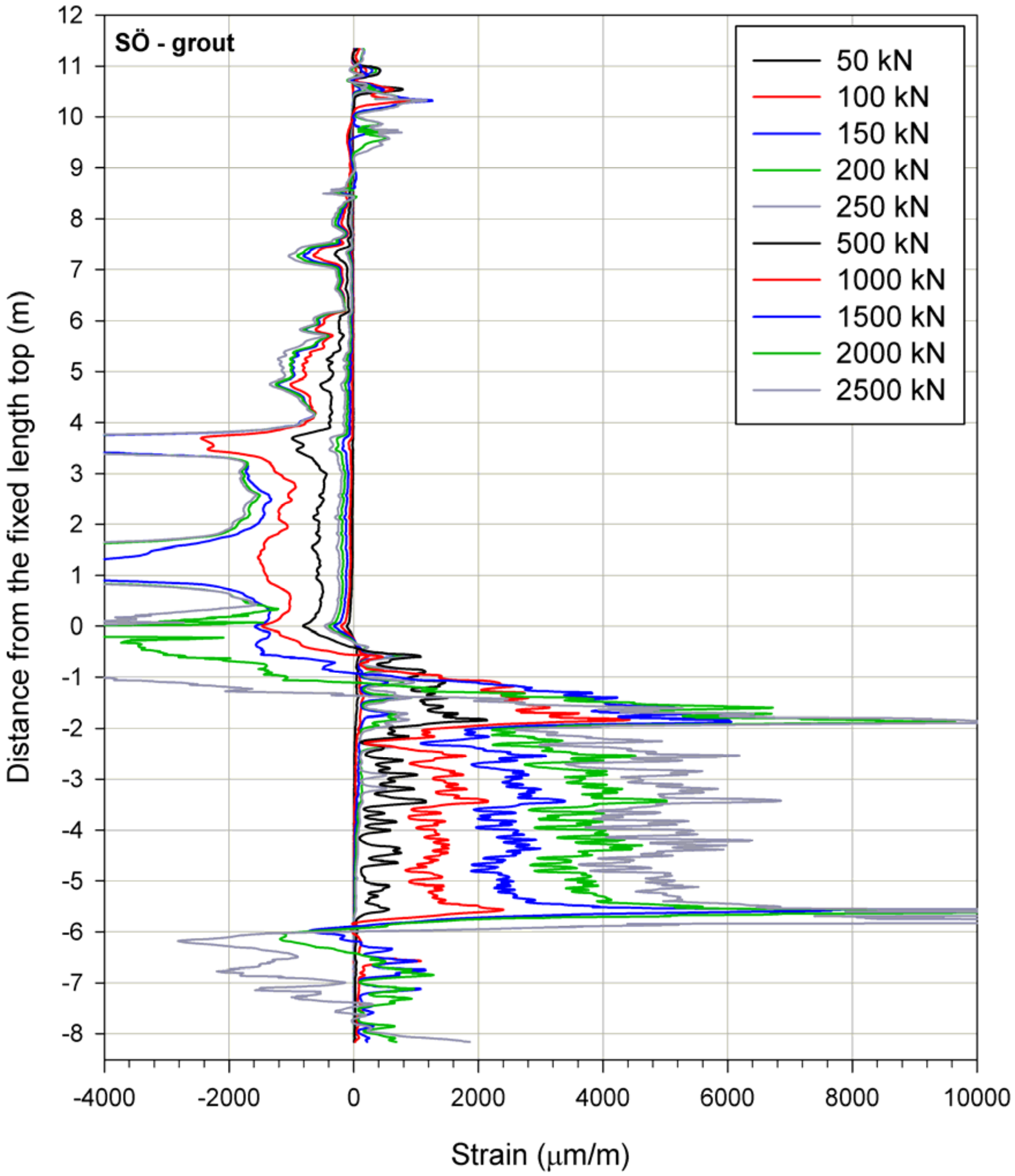

Fig. A2: Strains along the grout (Söding-test)

St Kanzian-tests

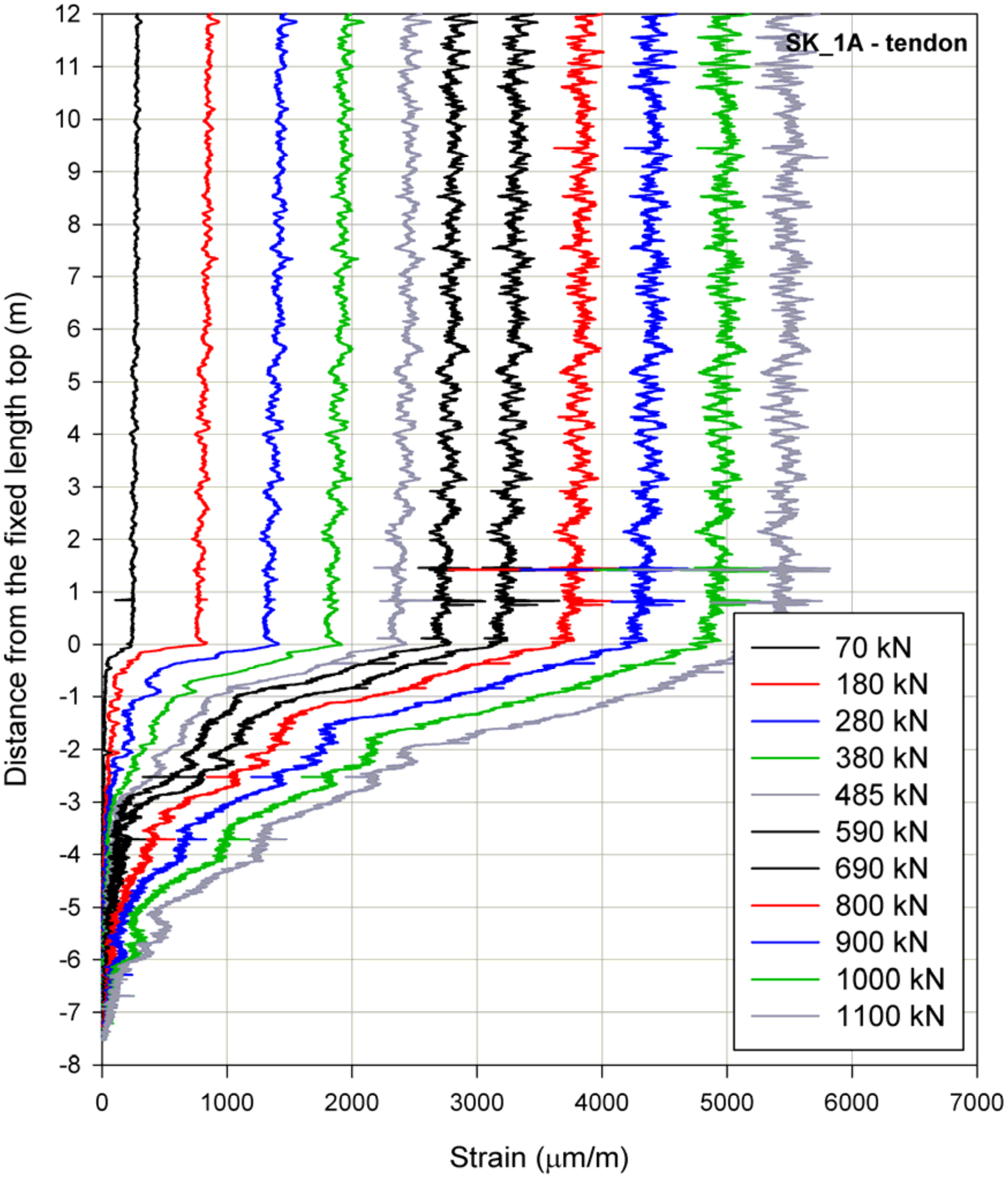

Fig. A3: Strains along the tendon (St Kanzian-test, anchor 1A)

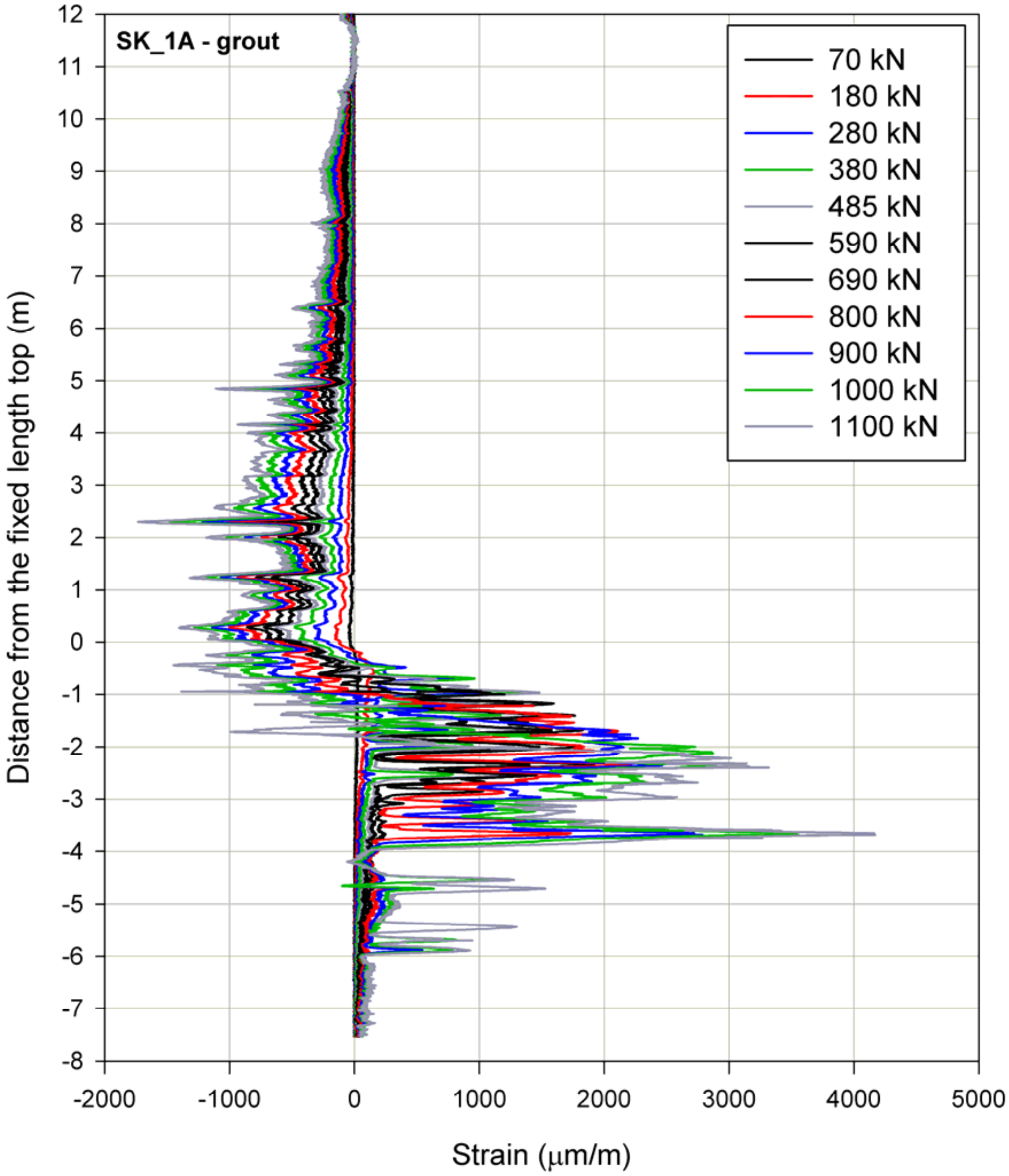

Fig. A4: Strains along the grout (St Kanzian-test, anchor 1A)

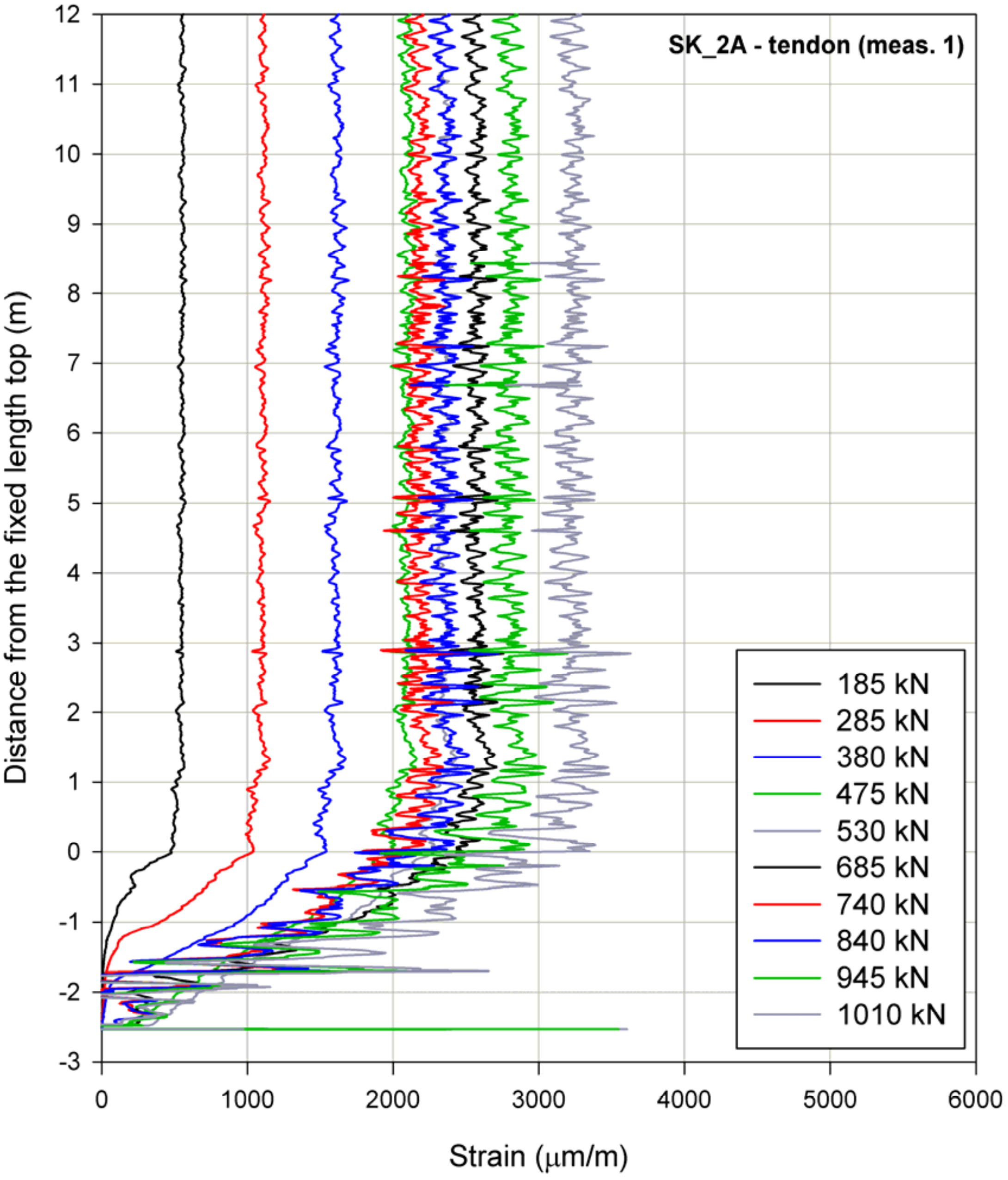

Fig. A5: Strains along the tendon (St Kanzian-test, anchor 2A, measurement 1)

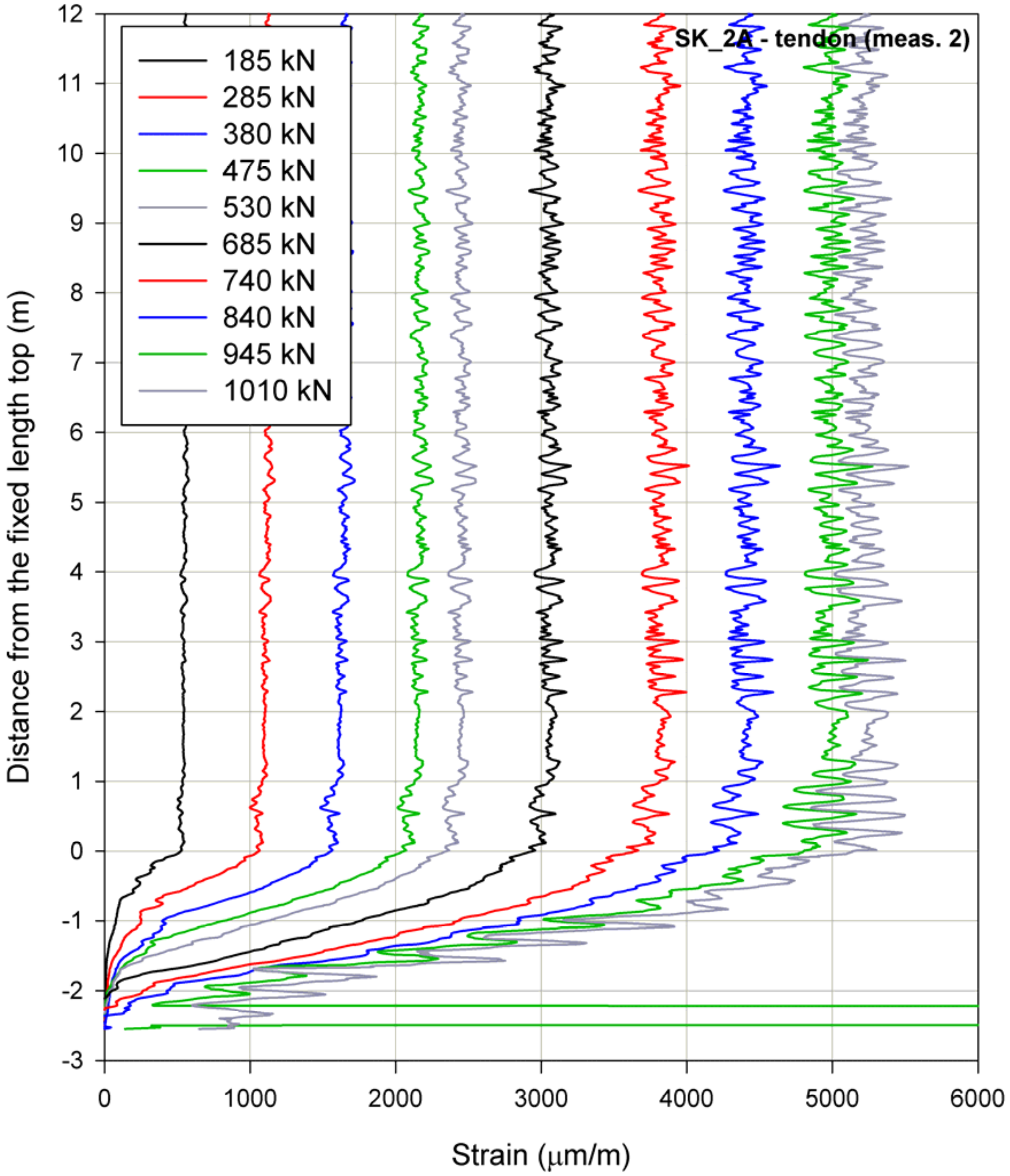

Fig. A6: Strains along the tendon (St Kanzian-test, anchor 2A, measurement 2)

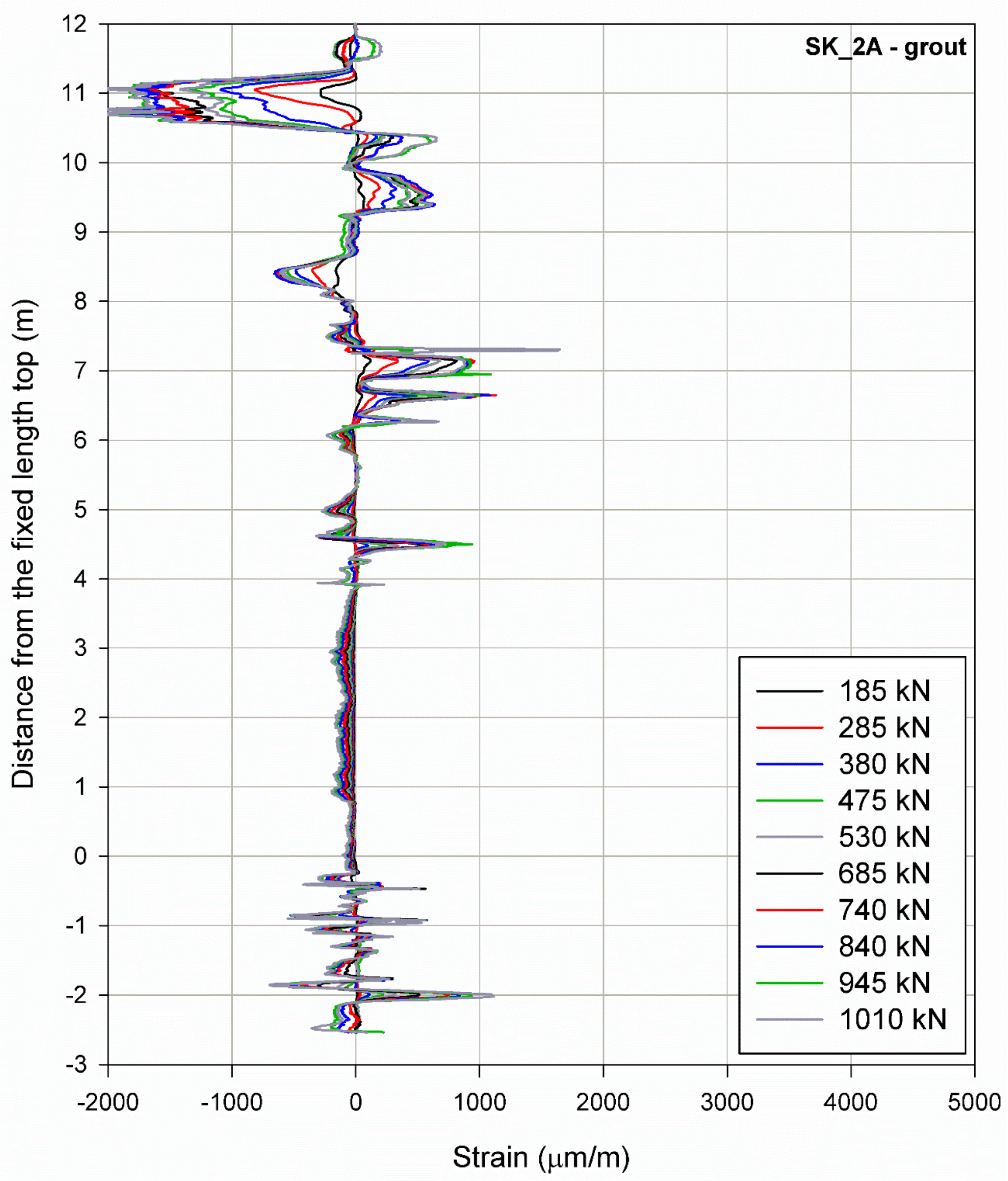

Fig. A7: Strains along the grout (St Kanzian-test, anchor 2A)

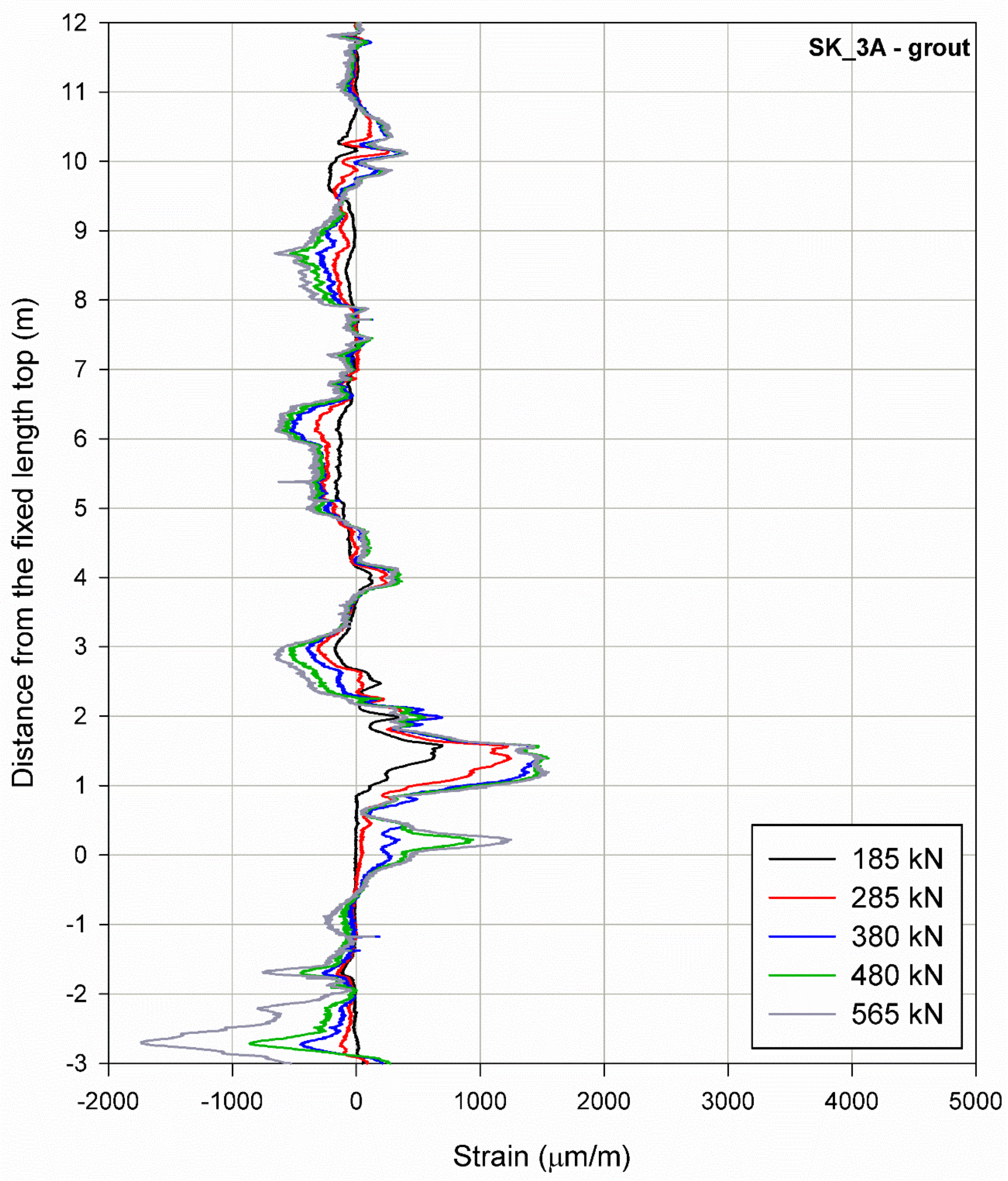

Fig. A8: Strains along the grout (St Kanzian-test, anchor 3A)

A10-test

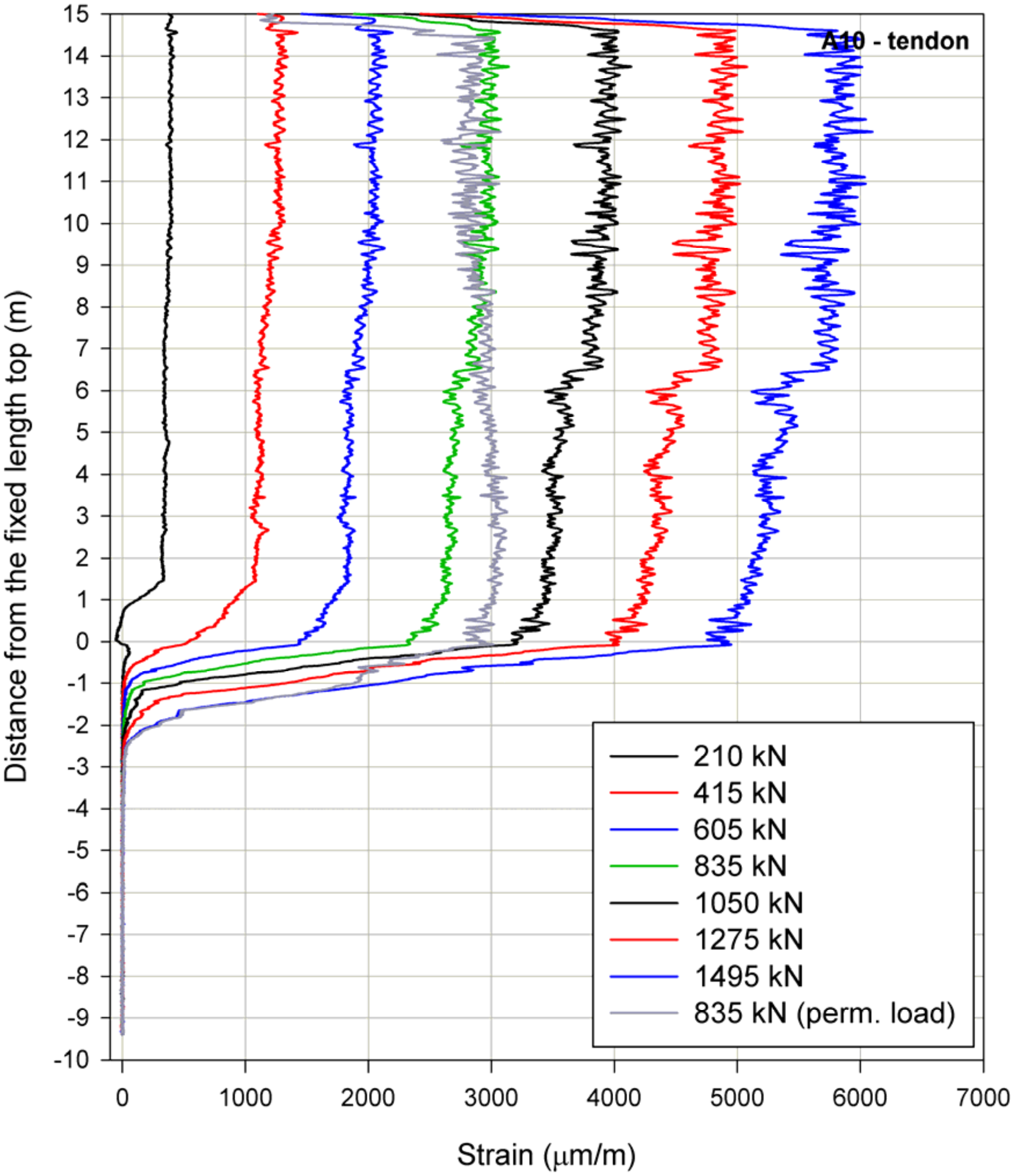

Fig. A9: Strains along the tendon (A10-test)

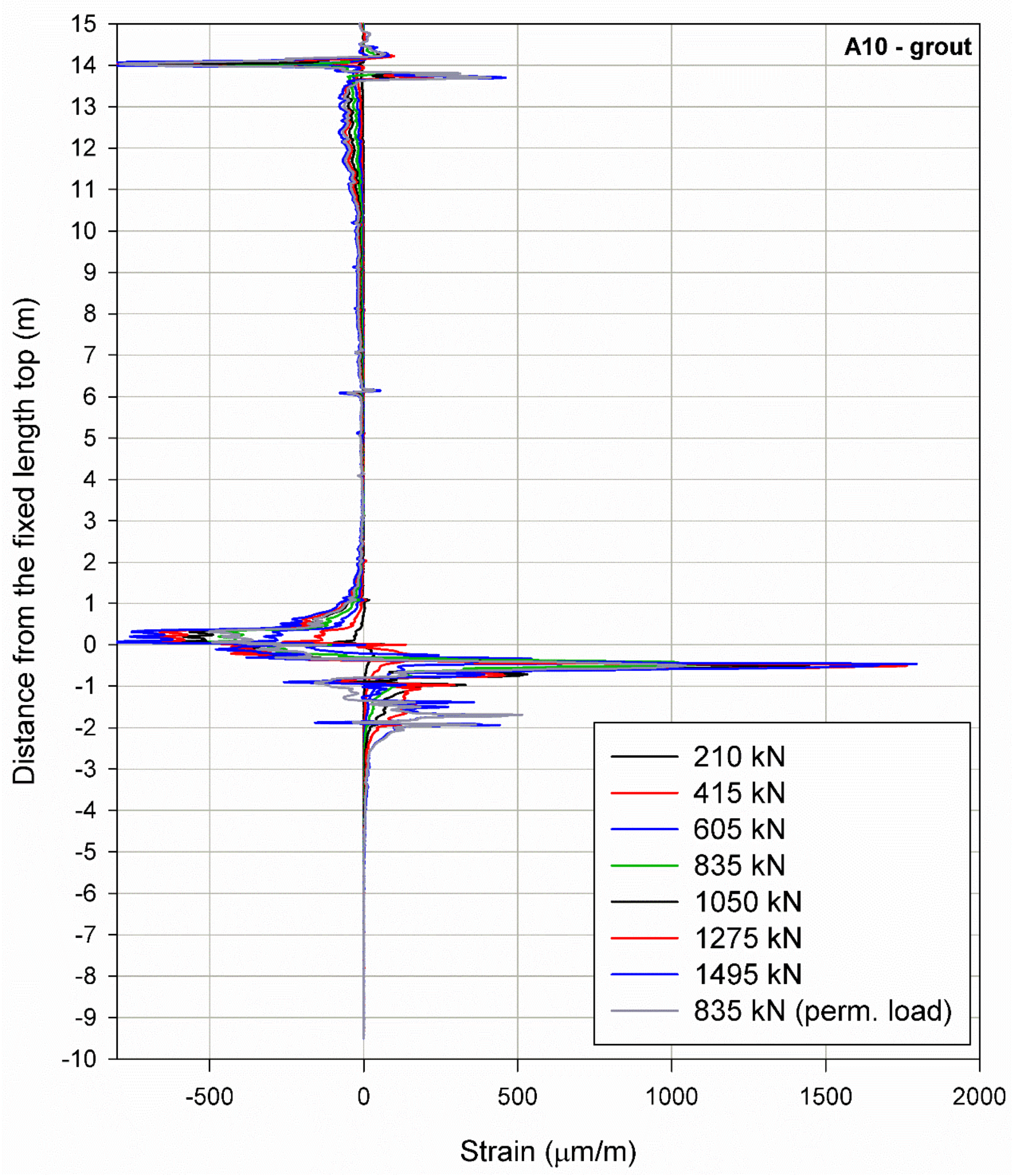

Fig. A10: Strains along the grout (A10-test)

Ljubljana-test

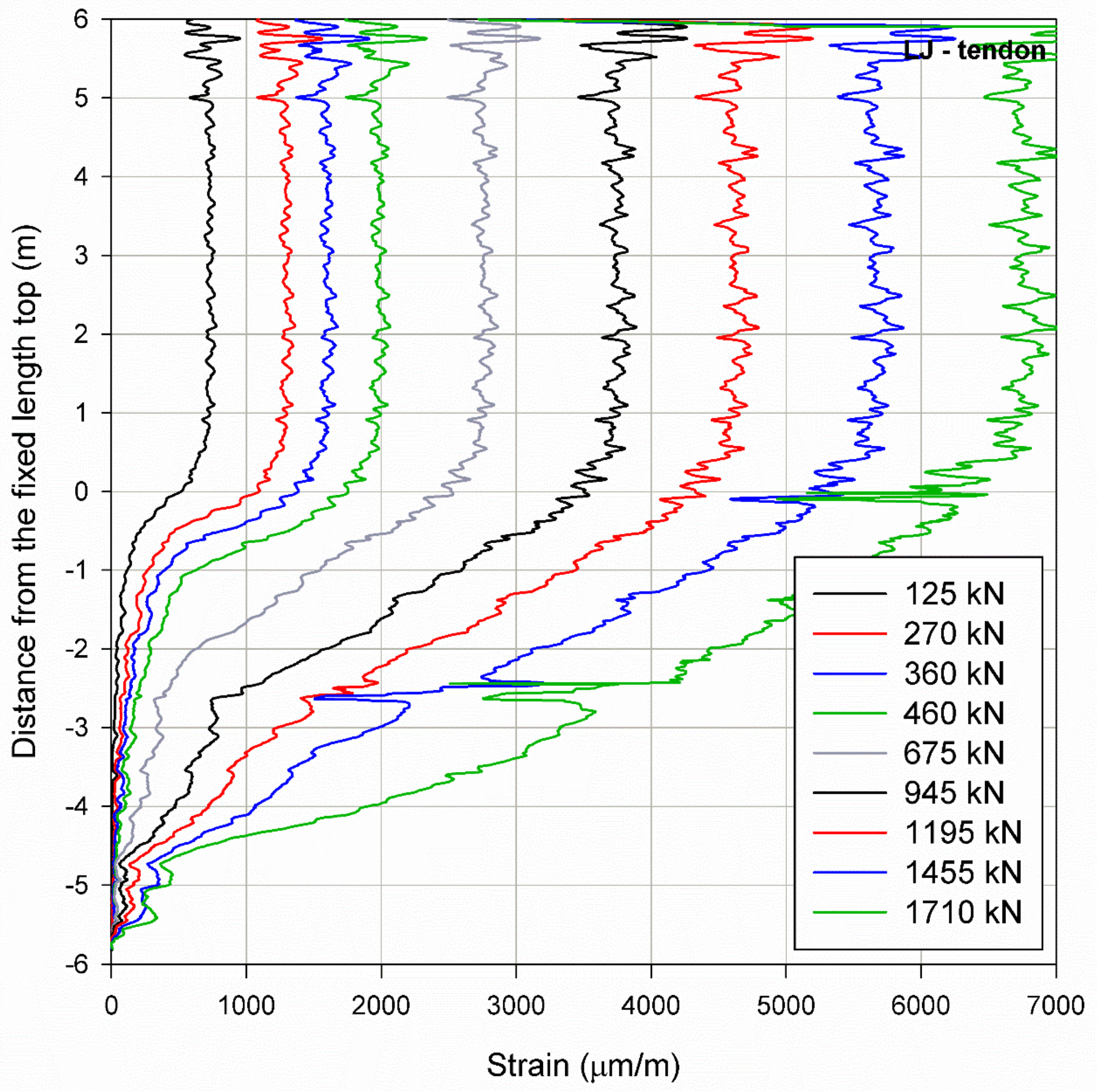

Fig. A11: Strains along the tendon (Ljubljana-test)

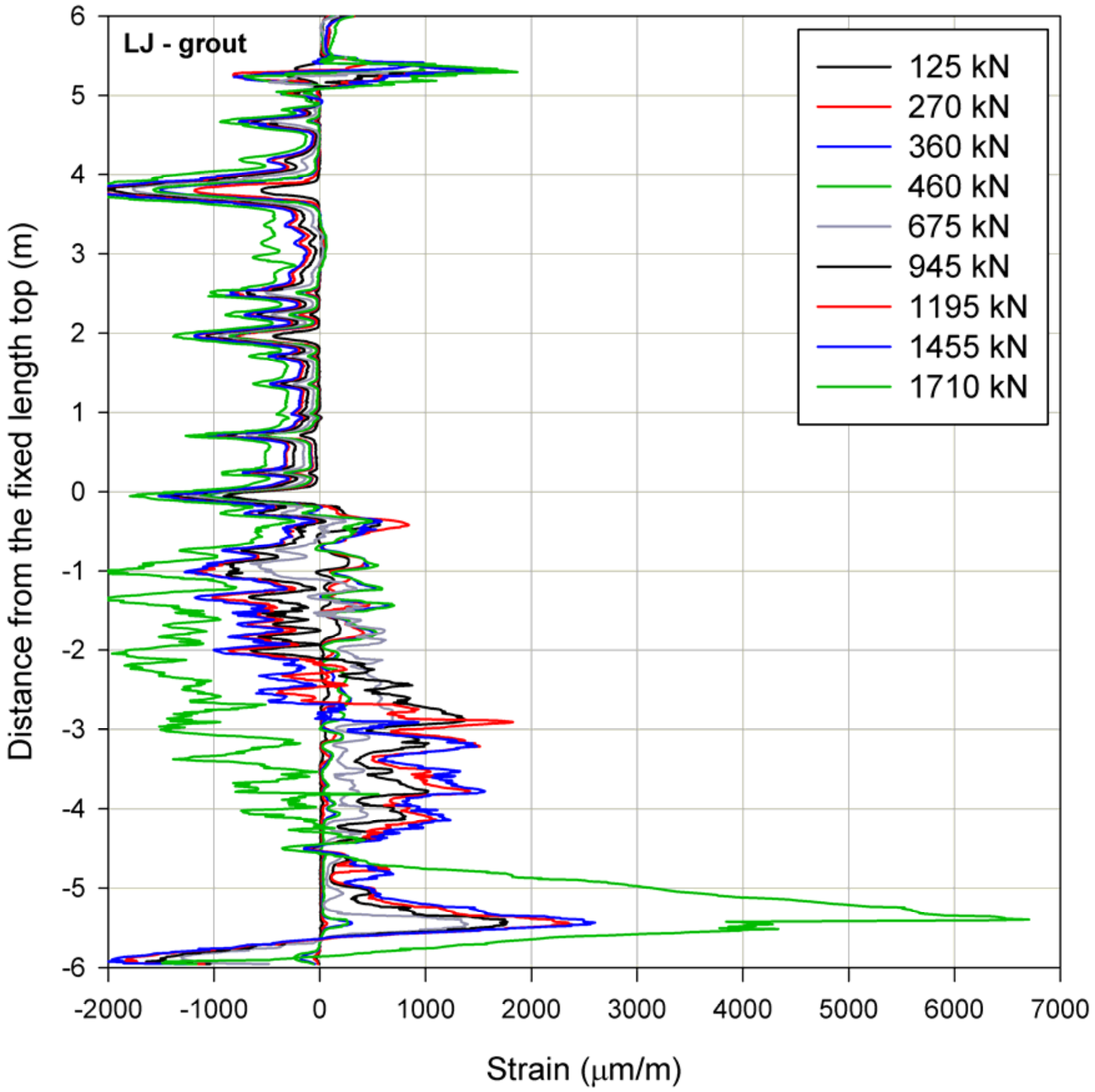

Fig. A12: Strains along the grout (Ljubljana-test)